SHEAR MODE FRACTURE TOUGHNESS OF ROCK WITH DIFFERENT CORE-BASED SPECIMEN GEOMETRIES

A THESIS SUBMITTED TO
THE GRADUATE SCHOOL OF APPLIED AND NATURAL SCIENCES
OF
MIDDLE EAST TECHNICAL UNIVERSITY

BY

KIVANÇ HET

IN PARTIAL FULFILLMENT OF THE REQUIREMENTS
FOR
THE DEGREE OF DOCTOR OF PHILOSOPHY
IN
MINING ENGINEERING

FEBRUARY 2014

Approval of the thesis:

SHEAR MODE FRACTURE TOUGHNESS OF ROCK WITH DIFFERENT CORE-BASED SPECIMEN GEOMETRIES

submitted by **KIVANÇ HET** in partial fulfillment of the requirements for the degree of **Doctor of Philosophy in Mining Engineering Department, Middle East Technical University** by,

Prof. Dr. Canan Özgen _____
Dean, Graduate School of **Natural and Applied Sciences**

Prof. Dr. Ali İhsan Arol _____
Head of Department, **Mining Engineering**

Assoc. Prof. Dr. Levend Tutluoğlu _____
Supervisor, **Mining Engineering Dept., METU**

Examining Committee Members:

Prof. Dr. Celal Karpuz _____
Mining Engineering Dept., METU

Assoc. Prof. Dr. Levend Tutluoğlu _____
Mining Engineering Dept., METU

Prof. Dr. Bahtiyar Ünver _____
Mining Engineering Dept., Hacettepe University

Assoc. Prof. Dr. Hakan Başarır _____
Mining Engineering Dept., METU

Assoc. Prof. Dr. Hasan Öztürk _____
Mining Engineering Dept., METU

Date: 05.02.2014

I hereby declare that all information in this document has been obtained and presented in accordance with academic rules and ethical conduct. I also declare that, as required by these rules and conduct, I have fully cited and referenced all material and results that are not original to this work.

Name, Last Name: KIVANÇ HET

Signature :

ABSTRACT

SHEAR MODE FRACTURE TOUGHNESS OF ROCK WITH DIFFERENT CORE-BASED SPECIMEN GEOMETRIES

HET, Kıvanç

Ph.D., Department of Mining Engineering

Supervisor: Assoc. Prof. Dr. Levend Tutluoğlu

February 2014, 294 pages

Shear mode fracture toughness tests on core specimens of gabbro rock were conducted. Tests were conducted under three-point bending and Brazilian type indirect compression load. In order to investigate the reasons for having different fracture toughness values with the different testing methods and geometries, modeling with ABAQUS software was conducted. Stress distributions around the mode II notches were analyzed. In order to assess which specimen geometry results in similar stress distributions as in the stress state of a plate under pure mode II, stress distributions along some paths were compared. Effect of the thickness of the notches on the stress intensity factor was analyzed. In experiments, core specimens had 100 mm diameter and 60 mm thickness, were used.

Mode II fracture toughness results were $K_{IIc(CSTBD)}$=2.35MPa√m and $K_{IIc(CSTBD)}$=1.76 MPa√m for the Brazilian type CSTBD specimens with notches of 32 mm and 72 mm in length, respectively. Mode II fracture toughness decreased as the notch length increased. This was attributed to the effect of boundary influence on the fracture toughness.

Mode I and mode II fracture toughness values for the three-point bend SCB geometry were lower with $K_{Ic(SCB)}$=1.77 MPa√m and $K_{IIc(SCB)}$=0.92 MPa√m. Another three-point bend circular plate type SNDB geometry method produced closer results to the CSTBD method with $K_{Ic(SNDB)}$=2.10 MPa√m and $K_{IIc(SNDB)}$=1.18 MPa√m. Reasons for lower fracture toughness with three-point bending loading were explained in terms of having larger yield zones ahead of the notch and cracks, and the boundary influence issue.

Keywords: Rock fracture, toughness, core specimens, stress intensity modeling, ABAQUS

ÖZ

ÇEŞİTLİ KAROT BAZLI KAYA NUMUNE GEOMETRİLERİNİN
MAKASLAMA MODU ÇATLAK TOKLUKLARI

HET, Kıvanç
Doktora, Maden Mühendisliği Bölümü
Tez Yöneticisi: Doc. Dr. Levend Tutluoğlu

Şubat 2014, 294 sayfa

Makaslama modu çatlak tokluğu testleri karot bazlı gabbro nunumeleri ile yürütülmüştür. Testler, üç noktadan eğme altında ve Brazilyan tipi direkt olmayan yükleme ile test edilmiştir. Farklı geometri tiplerinden elde edilen farklı çatlak tokluğu değerlerinin nedenlerinin incelenmesi için modellemeler ABAQUS yazılımı ile gerçekleştirilmiştir. Mod II çentiği çevresindeki gerilme dağılımları analiz edilmiştir. Hangi numune geometrisinin plaka tipi saf mod II modeli ile aynı gerilme dağılımına sahip olduğunu belirlemek için değişik patikalar üzerinden alınan gerilme değerleri kıyaslanmıştır. Çentik kalınlığının gerilme şiddeti faktörü üzerine etkisi analiz edilmiştir. Deneylerde 100 mm çapa ve 60 mm kalınlığa sahip karot numuneleri kullanılmıştır.

Başlangıç çentik uzunluğu 32 mm ile 72 mm olan Düz Çentikli Brezilyan Disk numuneleri için mod II çatlak tokluğu değerleri sırasıyla $K_{IIc(CSTBD)}$=2.35 MPa√m ve $K_{IIc(CSTBD)}$=1.76 MPa√m olarak saptanmıştır. Makaslama modu çatlak tokluğu değeri çentik uzunluğu arttıkça düşmüştür. Bu çatlak tokluğundaki düşüşün nedeni olarak, numune sınırının çatlak tokluğu üzerindeki etkisi olduğu sonucuna varılmıştır.

SCB geometrisine ait mod I ve mod II çatlak tokluğu değerleri düşerek $K_{Ic(SCB)}$=1.77 MPa√m and $K_{IIc(SCB)}$=0.92 MPa√m olarak belirlenmiştir. Diğer üç noktandan eğme altındaki disk tipi numunesi (SNDB), CSTBD methodu ile elde edilen sonuçlara $K_{Ic(SNDB)}$=2.10 MPa√m and $K_{IIc(SNDB)}$=1.18 MPa√m yakın değerler üretmiştir. Üç noktadan eğme altında yüklenen numune geometrilerinin düşük çatlak tokluğu değerlerine sahip olmasının nedeni olarak, çentik ucu çevresinde oluşan büyük yenilme bölgesi ile numune sınırının çatlak üzerine etkisi olarak açıklanmıştır.

Anahtar Kelimeler: Kaya çatlak, tokluğu, karot numuneleri, gerilme şiddeti modellemesi, ABAQUS

To My Family…

ACKNOWLEDGEMENTS

Foremost, I would like to express my sincere appreciation and gratitude to my supervisor Assoc. Prof. Dr. Levend Tutluoğlu for his continuous support, patience, enthusiasm, and immense knowledge throughout in this study.

Besides my advisor, I would also like to thank the rest of my examining committee: Prof. Dr. Celal Karpuz, Prof. Dr. Bahtiyar Ünver, Assoc. Prof. Dr. Hakan Başarır and Assoc. Prof. Dr. Hasan Öztürk for their invaluable comments, suggestions and contributions.

I would like to give my great thanks to General Director of Turkish Coal Enterprises Mr. Mustafa Aktaş, Deputy General Director Mr. Mustafa Özdingiş and also Project Manager Ms. Şahika Yürek for their continuous support, help and patience during this study.

My sincere thanks and deepest love also go to my parents, Şenay Het and Timur Het for their morale support and patience during my entire life. I also would like to thank all my family, whom I have not written their names here.

In addition, I thank to Tahsin Işıksal and Hakan Uysal for their help during my experimental studies.

TABLE OF CONTENTS

ABSTRACT v
ÖZ vii
ACKNOWLEDGEMENTS x
TABLE OF CONTENTS xi
LIST OF TABLES xvi
LIST OF FIGURES xviii
LIST OF SYMBOLS AND ABBREVIATIONS xxxiii
CHAPTERS
1. INTRODUCTION 1
1.1 Historical development of fracture mechanics 2
1.2 Statement of the problem 5
1.3 Objective of the thesis 6
1.4 Methodology 6
1.5 Sign convention 10
1.6 Von mises stress and yield criterion 13
1.7 Outline of the thesis 16
2. APPLICATION OF FRACTURE TOUGHNESS IN HYDRAULIC FRACTURING AND ROCK FRAGMENTATION 19
2.1 Hydraulic fracturing 20
2.2 Fracturing for rock fragmentation 23
3. BASICS OF ROCK FRACTURE MECHANICS 27
3.1 Linear elastic fracture mechanics (LEFM) 28
3.1.1 Stress intensity factor and fracture toughness 28
3.1.2 Crack tip stresses for mode I and mode II 29

3.1.3 Crack tip stresses and displacements for mode I and mode II 30
3.2 Elasto-plastic fracture mechanics 32
3.2.1 J integral 32
3.2.2 Crack tip opening displacements (CTOD) 33
4. MODE II FRACTURE TOUGHNESS TESTING METHODS 35
4.1 Punch through shear test 35
4.2 Shear box test 38
4.3 Double edge cracked Brazilian disc (DECBD) 41
4.4 Cracked straight through Brazilian disc (CSTBD) 42
4.5 Semi-circular specimen under three point bending (SCB) 48
5. FINITE ELEMENT MODELING & PROGRAM STRUCTURE 55
5.1 Finite element method 55
5.2 Origins of the finite element method 56
5.3 ABAQUS finite element program package 57
5.4 ABAQUS main windows and modules 58
5.4.1 Part module 60
5.4.2 Property module 60
5.4.3 Assembly module 60
5.4.4 Step module 60
5.4.5 Interaction module 62
5.4.6 Load module 62
5.4.7 Mesh module 62
5.4.8 Job module 62
5.4.9 Visualization module 62
5.4.10 Sketch module 63

5.5 Definition of some ABAQUS terms 63

5.6 Fracture mechanics calculation techniques used in ABAQUS software . 64

5.7 Fracture criteria and crack propagation direction 69

6. VERIFICATION EFFORTS AND MODELING IMPROVEMENT 71

6.1 Pure shear plate model under mode II type loading 71

6.2 Convergence study for seam cracks 78

6.3 Pure shear plate verification model with blunted cracks 81

6.4 Effect of notch thickness on K_{II} SIF analyses 85

6.5 Inclined crack in tension – mixed mode verification model 87

6.6 Inclined crack in tension with blunted notch 96

7. MODELING WORK FOR VARIOUS CORE-BASED SPECIMEN GEOMETRIES 99

7.1 Stress intensity factor computation for SCB (semi-circular specimen under three-point bending) specimen 99

7.2 Stress intensity factor computation for SNDB (straight notch disc bending method) specimen 103

7.3 Proposed 2D plane strain simplification of the 3D modeling work for SNDB geometry 112

7.4 Stress intensity factor calculations for CSTBD (cracked straight through Brazilian disc) specimen 122

7.5 Undeformed and deformed shapes of different core-based specimen geometries 128

8. EXPERIMENTAL WORK & FRACTURE TOUGHNESS DETERMINATION 133

8.1 Rock properties 134

8.2 Fracture toughness testing 139

8.2.1 Mode II fracture toughness determination with SCB specimen 140

8.2.2 Mode II fracture toughness determination with SNDB specimen 144

8.2.3 Mode II fracture toughness determination with CSTBD specimen .. 148

9. STRESS ANALYSES AROUND THE NOTCHES OF DIFFERENT SPECIMEN GEOMETRIES 165

9.1 Geometrical details and the critical load levels for the stress analyses of the specimen models 166

9.2 Comparison of the results with different geometries and the loading methods 169

9.3 Analyses of the distribution of stresses around the notches of the different geometries 172

9.3.1 Stress distributions along Path 1 for the different core-based specimen geometries 174

9.3.2 Stress distributions along Path 2 for different core-based specimen geometries 180

9.3.3 Stress distributions along Path 3 for the different core-based specimen geometries 184

9.3.4 Stress distributions along Path 4 for the various specimen models .. 192

9.4 Stiffness comparison for different core-based specimen geometries 198

9.5 Comparison of stress distributions along the paths between different core-based specimen models and pure shear plate model 199

9.5.1 Stress distribution comparisons between CSTBD and pure shear plate model on Path 1 201

9.5.2 Stress distribution comparisons between CSTBD and pure shear plate model on Path 2 206

9.5.3 Stress distribution comparisons between CSTBD and pure shear plate model on Path 3 210

9.5.4 Stress distribution comparisons between CSTBD and pure shear plate model on Path 4 214

9.5.5 Stress distribution comparisons between SCB and pure shear plate model on path 1 218

9.5.6 Stress distribution comparisons between SCB and pure shear plate model on path 2 222

9.5.7 Stress distribution comparisons between SCB and pure shear plate model on path 3 226

9.5.8 Stress distribution comparisons between SCB and pure shear plate model on path 4 230

9.5.9 Stress distribution comparisons between SNDB and pure shear plate model on path 1 234

9.5.10 Stress distribution comparisons on path 2 between SNDB and pure shear plate model 238

9.5.11 Stress distribution comparisons on path 3 between SNDB and pure shear plate model 242

9.5.12 Stress distribution comparisons between SNDB and pure shear plate model on Path 4 246

9.6 Stress distribution on path 3 and path 4 for CSTBD specimens with initial notch length varying between 32 mm and 72 mm 250

10. CONCLUSIONS & RECOMMENDATIONS 271

REFERENCES 275

APPENDICES

A. PETROGRAPHICAL ANALYSIS 285

B. SPECIMEN PHOTOS AFTER EXPERIMENTS 289

VITA 294

LIST OF TABLES

TABLES

Table 4.1 Fracture toughness values for different rock types..... 38
Table 4.2 Fracture toughness test results determined by Shear Box Test 41
Table 4.3 Mode I and mode II fracture toughness values of different materials... 44
Table 4.4 Fracture toughness results 47
Table 4.5 Effect of notch radius on fracture toughness results 48
Table 6.1 Dimensions of the model and mechanical properties related to the central crack on an infinite plate under pure shear mode loading 72
Table 6.2 Effect of Notch Thickness on K_{II} Stress Intensity Factor 86
Table 6.3 Dimensions and mechanical properties of the inclined crack in tension 89
Table 6.4 Effect of different crack propagation criteria on CPD 95
Table 7.1 Geometric details of 2D plane strain SCB models for K_I and K_{II} computations..... 100
Table 7.2 Dimensional entries and mechanical properties of the SNDB specimen model 106
Table 7.3 SNDB stress intensity factor results 110
Table 7.4 Comparison between dimensionless stress intensity factors 111
Table 7.5 3D SNDB disc model SIF results..... 117
Table 7.6 3D modified SNDB prismatic model SIF results 117
Table 7.7 2D modified SNDB rectangular model SIF results..... 118
Table 7.8 Dimensionless stress intensity factors for 3D SNDB disc model 118
Table 7.9 Dimensionless stress intensity factors for 3D modified SNDB prismatic model 119
Table 7.10 Dimensionless stress intensity factors for 2D modified SNDB rectangular model 120

Table 7.11 Dimensional and mechanical properties of the 2D and 3D CSTBD models 123
Table 7.12 K_I, K_{II} and SIF results for the various notch thicknesses on the CSTBD specimen models 126
Table 7.13 Dimensionless SIF values for the various notch thicknesses on the CSTBD specimen models 127
Table 8.1 Results of indirect Brazilian type tensile strength tests 134
Table 8.2 Uniaxial compression and deformability test data and the results..... 137
Table 8.3 Dimensions of SCB gabbro specimens used for pure mode I and pure mode II fracture toughness tests..... 141
Table 8.4 Fracture toughness results for tests on SCB specimens..... 143
Table 8.5 Dimensions of SNDB gabbro specimens used for pure mode I and pure mode II fracture toughness tests..... 146
Table 8.7 Fracture toughness results for SNDB specimens..... 147
Table 8.8 CSTBD specimen dimensions 151
Table 8.9 Representative CSTBD 2D model dimensions for each notch length group 152
Table 8.10 CSTBD 2D Model's Y_{II} results compared to the previous work 154
Table 8.11 SIF and fracture toughness results for CSTBD specimens 157
Table 8.12 Average P_{cr}, SIF and fracture toughness results for CSTBD specimens 158
Table 9.1 Summary of the results of the fracture toughness tests on the gabbro rock with the different specimen geometries 170
Table 9.2 Stiffness values for different core-based specimen geometries..... 199
Table 9.3 Dimensions and the loading levels applied to the 2D centrally notched plate under pure mode II loading 200
Table 9.4 Average P_{cr}'s for CSTBD specimens 251

LIST OF FIGURES

FIGURES

Figure 1.1 Brief summary of the methodology in a flowchart 8
Figure 1.2 Positive stress state in solid mechanics 11
Figure 1.3 Transformed or rotated stress state in local primed coordinate system of a stress path 12
Figure 1.4 Crack opening and positive mode I stress intensity factor K_I sign convention at the notch tip illustrated for SNDB specimen geometry 12
Figure 1.5 Illustration of shear stress state at the vicinity of the notch tip for a SNDB specimen model 13
Figure 1.6 Von Mises yield surface in principal stress space 15
Figure 1.7 3D and 2D Mohr Coulomb yield surface in principal stress space 15
Figure 2.1 Directional drilling and hydraulic fracturing 20
Figure 2.2 Position of the bedding planes for the oil shale samples subjected to the three-point bending for mode I fracture toughness tests 22
Figure 2.3 Mechanical rock breakages with the indenter and the drag bit actions 24
Figure 3.1 Fracture modes 27
Figure 3.2 Crack tip stress components 29
Figure 3.3 Displacement of the original crack tip and the 90° intercept 33
Figure 4.1 Sample geometry and principle loading for the PTS-test 37
Figure 4.2 Shear Box Testing 39
Figure 4.3 Double edge cracked Brazilian disc (DECBD) 42
specimen and loading position 42
Figure 4.4 CSTBD specimen and loading configuration 43
Figure 4.5 SCB specimen and loading configuration 49
Figure 5.1 Components of the main ABAQUS window 59
Figure 5.2 Seeds and partitions to improve modeling accuracy 64
Figure 5.3 Seam crack in 2D 66

Figure 5.4 Seam crack in 3D 66
Figure 5.5 V and U shaped notches in 2D with their crack front selection 67
Figure 5.6 V and U shaped notches in 3D with their crack front selection 67
Figure 5.7 Crack tip singularity definitions for 2D and 3D linear elastic analysis 68
Figure 5.8 Illustration of one-sided collapse for the crack tip second-order quadratic elements 69
Figure 5.9 Illustration of crack propagation direction angle definition in ABAQUS 70
Figure 6.1 Schematic view of the 2D plane strain model with traction directly applied to the upper boundary 73
Figure 6.2 Applied Horizontal Force and Coupling 74
Figure 6.3 Schematic views of the seam crack in the (a) un-deformed and 75
(b) deformed state of the model part 75
Figure 6.4 Crack tip elements and crack tip subtend angles 79
Figure 6.5 Different mesh intensities at the contour integral region 80
(Number of contours in the contour integral region = 4, 6, 10, 14, 17 and 24 respectively) 80
Figure 6.6 K_{II} Stress intensity factor variations according to number of contours in contour integral region 80
Figure 6.7 Size of the elements around blunted notch 82
Figure 6.8 Crack front, crack surface and crack tip definition for blunted notches in ABAQUS 82
Figure 6.9 Selection of crack front, crack tip and direction of *q* vector for blunted notch model 83
Figure 6.10 Fine meshing around blunted notch tips 84
Figure 6.11 $K_{II}/K_{II\ Analytical}$ versus t_n/a 87
Figure 6.12 Inclined crack in tension 88
Figure 6.13 Dimensions and boundary conditions of inclined crack in tension model 90

Figure 6.14 Schematic views of crack extension directions for each crack and the crack fronts 91
Figure 6.15 Schematic view of mesh controls for inclined crack in tension model 92
Figure 6.16 Schematic views of the seam crack and the whole model after meshing 92
Figure 6.17 Schematic views of new mesh controls and concentric tubes for inclined crack in tension model 94
Figure 6.18 Schematic view of fine meshing inside the concentric tubes and contour integral region 94
Figure 6.19 Schematic view of blunted notch before and after meshing 96
Figure 6.20 Schematic views of blunted crack and the whole model before and after meshing 97
Figure 7.1 SCB specimen model frame under three-point bending load configuration 101
Figure 7.2 Boundary conditions for SCB specimen 102
Figure 7.3 Geometry of SNDB specimens under three-point bending load 103
Figure 7.4 Mid-Central Section for the selection of crack extension direction and expected crack propagation direction 104
Figure 7.5 SNDB model mesh and rigid roller loading configuration through the reference point of the first boundary condition case 105
Figure 7.6 Schematic view of expected shear stress state over the preliminary notch of SNDB specimen mode 107
Figure 7.7 Load transfer to the SNDB model through the reference point and coupling to distribute the load vertically 108
Figure 7.8 Second boundary condition scenario for SNDB geometry 108
Figure 7.9 SNDB Y_I results compared to Karakaş, 2011 111
Figure 7.10 SNDB Y_{II} comparison of this work and Karakaş, 2011 112
Figure 7.11 Creating modified 2D SNDB specimen model geometry 113
Figure 7.12 Representative prism of the modified SNDB model in 3D 114

Figure 7.13 Plane strain mid-section and the geometric parameters of the 2D modified SNDB model 114
Figure 7.14 Section view of the 2D modified SNDB model with blunted and seam crack 116
Figure 7.15 Graphical representations of Y_I results for different SNDB geometries 120
Figure 7.16 Graphical representations of Y_{II} results for different SNDB geometries 121
Figure 7.17 3D CSTBD model geometry 122
Figure 7.18 2D CSTBD model geometry 124
Figure 7.19 Normalized *SIF* Y_{II} results versus t_n/a 128
Figure 7.20 Undeformed shape of the SCB (semi-circular disc) specimen model 129
Figure 7.21 Deformed shape of the SCB (semi-circular disc) specimen model . 129
Figure 7.22 Undeformed shape of the SNDB (circular plate disc) specimen model 130
Figure 7.23 Deformed shape of the SNDB (circular plate disc) specimen model 130
Figure 7.24 Undeformed shape of the CSTBD (Brazilian disc) specimen model 131
Figure 7.25 Deformed shape of the CSTBD (Brazilian disc) specimen model .. 131
Figure 8.1 Brazilian disc specimen in the indirect tensile strength test 135
Figure 8.2 Brazilian disc specimens after the tests 135
Figure 8.3 Specimen under uniaxial compression equipped with circumferential extensometer 138
Figure 8.4 A typical stress-strain curve for a gabbro specimen under uniaxial compression 139
Figure 8.5 SCB specimen coding 141
Figure 8.6 Configuration for pure mode I and pure mode II loading of SCB specimens 143

Figure 8.7 Edge notch machining with angle setter and digital caliper 144
Figure 8.8 SNDB specimen coding 145
Figure 8.9 Position of SNDB core specimens under pure mode I and pure mode II loading 146
Figure 8.10 Preparation of CSTBD core specimens with high-pressure water jet 148
Figure 8.11 Positioning and alignment of the internally notched CSTBD disc with respect to the compressive load application axis 149
Figure 8.12 Coding for notched CSTBD specimen discs 150
Figure 8.13 Example section views of 2D models for some notch length groups 153
Figure 8.14 Y_{II} comparisons between the modeling work here and Fowell & Xu (1993) 155
Figure 8.15 P_{cr} versus notch length 159
Figure 8.16 Average P_{cr} values versus grouped *a/R* entries 159
Figure 8.17 K_{IIc} versus *a/R* for all CSTBD Tests 160
Figure 8.18 Averaged K_{IIc} versus group averaged *a/R* ratios 161
Figure 9.1 Position and geometric details of Path 1 on the semi-circular disc (SCB) specimen model 175
Figure 9.2 Position and geometric details of Path 1 on circular plate type (SNDB) specimen model 175
Figure 9.3 Position and geometric details of Path 1 on the Brazilian disc type (CSTBD) specimen model 176
Figure 9.4 Dimensionless S_{11}' normal stress distribution vs. *d / a* (Distance / Notch Length) ratio along Path 1 177
Figure 9.5 Dimensionless S_{22}' stress distribution vs. *d* (Distance) / *a* (Notch Length) along Path 1 177
Figure 9.6 Dimensionless S_{33}' stress distribution vs. *d* (Distance) / *a* (Notch Length) along Path 1 178

Figure 9.7 Dimensionless S_{12}' stress distribution vs. *d* (Distance) / *a* (Notch Length) along Path 1 178
Figure 9.8 Dimensionless *Mises* stress distribution vs. *d* (Distance) / *a* (Notch Length) along Path 1 179
Figure 9.9 Position and geometric details of Path 2 on SCB specimen model ... 180
Figure 9.10 Position and geometric details of Path 2 on SNDB specimen model 181
Figure 9.11 Position and geometric details of Path 2 on CSTBD specimen model 181
Figure 9.12 Dimensionless S_{11}' stress distribution vs. *d* (Distance) / *a* (Notch Length) along Path 2 182
Figure 9.13 Dimensionless *Mises* stress distribution vs. *d* (Distance) / *a* (Notch Length) along Path 2 183
Figure 9.14 Position and geometric details of Path 3 on SCB specimen model . 184
Figure 9.15 Position and geometric details of Path 3 on the SNDB specimen model 184
Figure 9.16 Position and geometric details of Path 3 on the CSTBD specimen model 185
Figure 9.17 Dimensionless S_{12}' stress distribution vs. *d* (Distance) / *a* (Notch Length) along Path 3 186
Figure 9.18 Dimensionless S_{11}' stress distribution vs. *d* (Distance) / *a* (Notch Length) along Path 3 after the data refinement 187
Figure 9.19 Dimensionless S_{22}' stress distribution vs. *d* (Distance) / *a* (Notch Length) along Path 3 after the data refinement 188
Figure 9.20 Dimensionless S_{33}' stress distribution vs. *d* (Distance) / *a* (Notch Length) along Path 3 after the data refinement 188
Figure 9.21 Dimensionless S_{12}' stress distribution vs. *d* (Distance) / *a* (Notch Length) along Path 3 after the data refinement 189
Figure 9.22 Dimensionless Mises stress distribution vs. *d* (Distance) / *a* (Notch Length) along Path 3 after the data refinement 192

Figure 9.23 Position and geometric details of the Path 4 on the SCB specimen model 193
Figure 9.24 Position and geometric details of the Path 4 on the SNDB specimen model 193
Figure 9.25 Position and geometric details of the Path 4 on the CSTBD specimen model 194
Figure 9.26 Dimensionless S_{11}' stress distribution vs. *d* (Distance) / *a* (Notch Length) along Path 4 194
Figure 9.27 Dimensionless S_{22}' stress distribution vs. *d* (Distance) / *a* (Notch Length) along Path 4 195
Figure 9.28 Dimensionless S_{33}' stress distribution vs. *d* (Distance) / *a* (Notch Length) along Path 4 195
Figure 9.29 Dimensionless S_{12}' stress distribution vs. *d* (Distance) / *a* (Notch Length) along Path 4 196
Figure 9.30 Dimensionless *Mises* stress distribution vs. *d* (Distance) / *a* (Notch Length) along Path 4 196
Figure 9.31 Stiffness comparisons between different core-based specimens 198
Figure 9.32 Position and geometric details of Path 1 on CSTBD specimen model 201
Figure 9.33 Position and geometric details of Path 1 on pure shear plate model 202
Figure 9.34 Dimensionless S_{11}' stress distribution vs. *d* (Distance) / *a* (Notch Length) along Path 1 203
Figure 9.35 Dimensionless S_{22}' stress distribution vs. *d* (Distance) / *a* (Notch Length) along Path 1 203
Figure 9.36 Dimensionless S_{33}' stress distribution vs. *d* (Distance) / *a* (Notch Length) along Path 1 204
Figure 9.37 Dimensionless S_{12}' stress distribution vs. *d* (Distance) / *a* (Notch Length) along Path 1 204
Figure 9.38 Dimensionless *Mises* stress distribution vs. *d* (Distance) / *a* (Notch Length) along Path 1 205

Figure 9.39 Position and geometric details of Path 2 on CSTBD specimen model 206
Figure 9.40 Position and geometric details of Path 2 on Pure Shear Plate Model 206
Figure 9.41 Dimensionless S_{11}' stress distribution vs. *d* (Distance) / *a* (Notch Length) along Path 2 207
Figure 9.42 Dimensionless S_{22}' stress distribution vs. *d* (Distance) / *a* (Notch Length) along Path 2 208
Figure 9.43 Dimensionless S_{33}' stress distribution vs. *d* (Distance) / *a* (Notch Length) along Path 2 208
Figure 9.44 Dimensionless S_{12}' stress distribution vs. *d* (Distance) / *a* (Notch Length) along Path 2 209
Figure 9.45 Dimensionless *Mises* stress distribution vs. *d* (Distance) / *a* (Notch Length) along Path 2 209
Figure 9.46 Position and geometric details of Path 3 on CSTBD specimen model 210
Figure 9.47 Position and geometric details of Path 3 on Pure Shear Plate Model 210
Figure 9.48 Dimensionless S_{11}' stress distribution vs. *d* (Distance) / *a* (Notch Length) along Path 3 211
Figure 9.49 Dimensionless S_{22}' stress distribution vs. *d* (Distance) / *a* (Notch Length) along Path 3 212
Figure 9.50 Dimensionless S_{33}' stress distribution vs. *d* (Distance) / *a* (Notch Length) along Path 3 212
Figure 9.51 Dimensionless S_{12}' stress distribution vs. *d* (Distance) / *a* (Notch Length) along Path 3 213
Figure 9.52 Dimensionless *Mises* stress distribution vs. *d* (Distance) / *a* (Notch Length) along Path 3 213
Figure 9.53 Position and geometric details of Path 4 on CSTBD specimen model 214

Figure 9.54 Position and geometric details of Path 4 on Pure Shear Plate Model 214
Figure 9.55 Dimensionless S_{11}' stress distribution vs. *d* (Distance) / *a* (Notch Length) along Path 4 215
Figure 9.56 Dimensionless S_{22}' stress distribution vs. *d* (Distance) / *a* (Notch Length) along Path 4 216
Figure 9.57 Dimensionless S_{33}' stress distribution vs. *d* (Distance) / *a* (Notch Length) along Path 4 216
Figure 9.58 Dimensionless S_{12}' stress distribution vs. *d* (Distance) / *a* (Notch Length) along Path 4 217
Figure 9.59 Dimensionless *Mises* stress distribution vs. *d* (Distance) / *a* (Notch Length) along Path 4 217
Figure 9.60 Position and geometric details of Path 1 on SCB specimen model . 218
Figure 9.61 Position and geometric details of Path 1 on Pure Shear Plate Model 218
Figure 9.62 Dimensionless S_{11}' stress distribution vs. *d* (Distance) / *a* (Notch Length) along Path 1 219
Figure 9.63 Dimensionless S_{22}' stress distribution vs. *d* (Distance) / *a* (Notch Length) along Path 1 220
Figure 9.64 Dimensionless S_{33}' stress distribution vs. *d* (Distance) / *a* (Notch Length) along Path 1 220
Figure 9.65 Dimensionless S_{12}' stress distribution vs. *d* (Distance) / *a* (Notch Length) along Path 1 221
Figure 9.66 Dimensionless *Mises* stress distribution vs. *d* (Distance) / *a* (Notch Length) along Path 1 221
Figure 9.67 Position and geometric details of Path 2 on SCB specimen model . 222
Figure 9.68 Position and geometric details of Path 2 on Pure Shear Plate Model 222
Figure 9.69 Dimensionless S_{11}' stress distribution vs. *d* (Distance) / *a* (Notch Length) along Path 2 223

Figure 9.70 Dimensionless S_{22}' stress distribution vs. *d* (Distance) / *a* (Notch Length) along Path 2 224
Figure 9.71 Dimensionless S_{33}' stress distribution vs. *d* (Distance) / *a* (Notch Length) along Path 2 224
Figure 9.72 Dimensionless S_{12}' stress distribution vs. *d* (Distance) / *a* (Notch Length) along Path 2 225
Figure 9.73 Dimensionless *Mises* stress distribution vs. *d* (Distance) / *a* (Notch Length) along Path 2 225
Figure 9.74 Position and geometric details of Path 3 on SCB specimen model. 226
Figure 9.75 Position and geometric details of Path 3 on Pure Shear Plate Model 226
Figure 9.76 Dimensionless S_{11}' stress distribution vs. *d* (Distance) / *a* (Notch Length) along Path 3 227
Figure 9.77 Dimensionless S_{22}' stress distribution vs. *d* (Distance) / *a* (Notch Length) along Path 3 228
Figure 9.78 Dimensionless S_{33}' stress distribution vs. *d* (Distance) / *a* (Notch Length) along Path 3 228
Figure 9.79 Dimensionless S_{12}' stress distribution vs. *d* (Distance) / *a* (Notch Length) along Path 3 229
Figure 9.80 Dimensionless *Mises* stress distribution vs. *d* (Distance) / *a* (Notch Length) along Path 3 229
Figure 9.81 Position and geometric details of Path 4 on SCB specimen model. 230
Figure 9.82 Position and geometric details of Path 4 on Pure Shear Plate Model 230
Figure 9.83 Dimensionless S_{11}' stress distribution vs. *d* (Distance) / *a* (Notch Length) along Path 4 231
Figure 9.84 Dimensionless S_{22}' stress distribution vs. *d* (Distance) / *a* (Notch Length) along Path 4 232
Figure 9.85 Dimensionless S_{33}' stress distribution vs. *d* (Distance) / *a* (Notch Length) along Path 4 232

Figure 9.86 Dimensionless S_{12}' stress distribution vs. *d* (Distance) / *a* (Notch Length) along Path 4 233
Figure 9.87 Dimensionless *Mises* stress distribution vs. *d* (Distance) / *a* (Notch Length) along Path 4 233
Figure 9.88 Position and geometric details of Path 1 on SNDB specimen 234
Figure 9.89 Position and geometric details of Path 1 on Pure Shear Plate Model 234
Figure 9.90 Dimensionless S_{11}' stress distribution vs. *d* (Distance) / *a* (Notch Length) along Path 1 235
Figure 9.91 Dimensionless S_{22}' stress distribution vs. *d* (Distance) / *a* (Notch Length) along Path 1 236
Figure 9.92 Dimensionless S_{33}' stress distribution vs. *d* (Distance) / *a* (Notch Length) along Path 1 236
Figure 9.93 Dimensionless S_{12}' stress distribution vs. *d* (Distance) / *a* (Notch Length) along Path 1 237
Figure 9.94 Dimensionless *Mises* stress distribution vs. *d* (Distance) / *a* (Notch Length) along Path 1 237
Figure 9.95 Position and geometric details of Path 2 on SNDB specimen model 238
Figure 9.96 Position and geometric details of Path 2 on Pure Shear Plate Model 238
Figure 9.97 Dimensionless S_{11}' stress distribution vs. *d* (Distance) / *a* (Notch Length) along Path 2 239
Figure 9.98 Dimensionless S_{22}' stress distribution vs. *d* (Distance) / *a* (Notch Length) along Path 2 240
Figure 9.99 Dimensionless S_{33}' stress distribution vs. *d* (Distance) / *a* (Notch Length) along Path 2 240
Figure 9.100 Dimensionless S_{12}' stress distribution vs. *d* (Distance) / *a* (Notch Length) along Path 2 241

Figure 9.101 Dimensionless *Mises* stress distribution vs. *d* (Distance) / *a* (Notch Length) along Path 2 241
Figure 9.102 Position and geometric details of Path 3 on SNDB specimen..... 242
Figure 9.103 Position and geometric details of Path 3 on Pure Shear Plate Model 242
Figure 9.104 Dimensionless S_{11}' stress distribution vs. *d* (Distance) / *a* (Notch Length) along Path 3 243
Figure 9.105 Dimensionless S_{22}' stress distribution vs. *d* (Distance) / *a* (Notch Length) along Path 3 244
Figure 9.106 Dimensionless S_{33}' stress distribution vs. *d* (Distance) / *a* (Notch Length) along Path 3 244
Figure 9.107 Dimensionless S_{12}' stress distribution vs. *d* (Distance) / *a* (Notch Length) along Path 3 245
Figure 9.108 Dimensionless *Mises* stress distribution vs. *d* (Distance) / *a* (Notch Length) along Path 3 245
Figure 9.109 Position and geometric details of Path 4 on SNDB specimen..... 246
Figure 9.110 Position and geometric details of Path 4 on Pure Shear Plate Model 246
Figure 9.111 Dimensionless S_{11}' stress distribution vs. *d* (Distance) / *a* (Notch Length) along Path 4 247
Figure 9.112 Dimensionless S_{22}' stress distribution vs. *d* (Distance) / *a* (Notch Length) along Path 4 248
Figure 9.113 Dimensionless S_{33}' stress distribution vs. *d* (Distance) / *a* (Notch Length) along Path 4 248
Figure 9.114 Dimensionless S_{12}' stress distribution vs. *d* (Distance) / *a* (Notch Length) along Path 4 249
Figure 9.115 Dimensionless *Mises* stress distribution vs. *d* (Distance) / *a* (Notch Length) along Path 4 249
Figure 9.116 Dimensionless S_{11}' stress distribution vs. *d* (Distance) / *a* (Notch Length) along Path 3 252

Figure 9.117 Dimensionless S_{11}' stress distribution vs. *d* (Distance) / *a* (Notch Length) along Path 4 253
Figure 9.118 Dimensionless S_{11}' stress distribution vs. *d* (Distance) / *a* (Notch Length) along Path 3 after data refinement 254
Figure 9.119 Dimensionless S_{11}' stress distribution vs. *d* (Distance) / *a* (Notch Length) along Path 4 after dropping problematic stress values..... 254
Figure 9.120 Dimensionless S_{22}' stress distribution vs. *d* (Distance) / *a* (Notch Length) along Path 3 255
Figure 9.121 Dimensionless S_{22}' stress distribution vs. *d* (Distance) / *a* (Notch Length) along Path 4 256
Figure 9.122 Dimensionless S_{22}' stress distribution vs. *d* (Distance) / *a* (Notch Length) along Path 3 after data refinement 256
Figure 9.123 Dimensionless S_{22}' stress distribution vs. *d* (Distance) / *a* (Notch Length) along Path 4 after data refinement 257
Figure 9.124 Dimensionless S_{33}' stress distribution vs. *d* (Distance) / *a* (Notch Length) along Path 3 258
Figure 9.125 Dimensionless S_{33}' stress distribution vs. *d* (Distance) / *a* (Notch Length) along Path 4 258
Figure 9.126 Dimensionless S_{33}' stress distribution vs. *d* (Distance) / *a* (Notch Length) along Path 3 after data refinement 259
Figure 9.127 Dimensionless S_{33}' stress distribution vs. *d* (Distance) / *a* (Notch Length) along Path 4 after data refinement 259
Figure 9.128 Dimensionless S_{12}' stress distribution vs. *d* (Distance) / *a* (Notch Length) along Path 3 261
Figure 9.129 Dimensionless S_{12}' stress distribution vs. *d* (Distance) / *a* (Notch Length) along Path 4 261
Figure 9.130 Dimensionless S_{12}' stress distribution vs. *d* (Distance) / *a* (Notch Length) along Path 3 after data refinement 262
Figure 9.131 Dimensionless S_{12}' stress distribution vs. *d* (Distance) / *a* (Notch Length) along Path 4 after data refinement 263

Figure 9.132 Dimensionless S_{12}' stress distribution vs. *d* (Distance) / *a* (Notch Length) along Path 3 264
Figure 9.133 Dimensionless *Mises* stress distribution vs. *d* (Distance) / *a* (Notch Length) along Path 3 265
Figure 9.134 Dimensionless *Mises* stress distribution vs. *d* (Distance) / *a* (Notch Length) along Path 4 265
Figure 9.135 Dimensionless *Mises* stress distribution vs. *d* (Distance) / *a* (Notch Length) along Path 3 after data refinement 267
Figure 9.136 Dimensionless *Mises* stress distribution vs. *d* (Distance) / *a* (Notch Length) on Path 4 after data refinement 267
Figure 9.137 Dimensionless *Mises* stress distribution vs. *d* (Distance) / *a* (Notch Length) on Path 3 268
Figure 9.138 Dimensionless *Mises* stress distribution vs. *d* (Distance) / *a* (Notch Length) along Path 4 269
Figure A.1 General views of thin section and ophitic texture 286
Figure A.2 Pyroxene, plagioclase and opaqued biotite minerals observed in thin section 286
Figure A.3 Plagioclase and opaqued biotite minerals that have zones in textures 287
Figure A.4 Amphibol generation after uralitization that is observed in pyroxenes 287
Figure B.1 CSTBD specimens (fine grained gabbro) after experiments 289
Figure B.2 Shear surfaces on CSTBD gabbro specimen after experiment 290
Figure B.3 CSTBD gabbro specimen with 2a=52 mm initial notch after experiment 290
Figure B.4 CSTBD gabbro specimen fractured along desired path 291
Figure B.5 CSTBD gabbro specimen fractured along undesired path 291
Figure B.6 SNDB gabbro specimens after mode I experiments 292
Figure B.7 SNDB gabbro specimens after mode II experiments 292
Figure B.8 SCB gabbro specimens after mode I experiments 293

Figure B.9 SCB gabbro specimens after mode II experiments 293

LIST OF SYMBOLS AND ABBREVIATIONS

2D : Two Dimensional

3D : Three Dimensional

a : Crack Length

B : Specimen Thickness

C3D8R : Continuum Three Dimensional Eight Node with Reduced integration

CCNBD : Cracked Chevron-Notched Brazilian Disc

CPE8 : Continuum Plane Strain Eight Node

CSTBD : Cracked Straight through Brazilian Disc

D : Specimen Diameter

E : Young's Modulus

EPFM : Elastic Plastic Fracture Mechanics

G : Strain Energy Release Rate

H : Height

ISRM : International Society for Rock Mechanics

I_1 : Fist Stress Invariant

J : J-Integral

J_2 : Second deviatoric stress invariant

K : Stress Intensity Factor

k_f : Stiffness

K_{Ic} : Mode I Fracture Toughness

K_{IIc} : Mode II Fracture Toughness

K_I : Stress Intensity Factor in Mode I

K_{II} : Stress Intensity Factor in Mode II

L : Specimen Length

LEFM : Linear Elastic Fracture Mechanics

LVDT : Linear Variable Differential Transformer

ρ : Notch Tip Radius

P_y : Applied Load

P_{cr} : Critical Load

PTS : Punch through Shear

R : Specimen Radius

S : Support Span

S_{11} : Stress Component in x-direction

S_{22} : Stress Component in y-direction

S_{33} : Stress Component in z-direction

S_{12} : Shear Stress Component in xy-direction

SCB : Semi-Circular Specimen under Three-Point Bending

SNDB : Straight-Notched Disc Specimen under Three-Point Bending

T_0 : Tensile Strength

UCS : Uniaxial Compressive Strength

Y_I : Normalized Stress Intensity Factor in Mode I

Y_{II} : Normalized stress intensity factor in Mode II

ε : Strain

μ : Shear modulus

σ : Stress

σ_y : Yield Strength

σ_c : Uniaxial Compressive Strength

α : a/R

τ : Shear stress

υ : Poisson's ratio

θ : Crack propagation angle

CHAPTER 1

INTRODUCTION

Rock is not an ideally homogenous material; inherently it contains small flaws, pores, and/or micro cracks and fractures in its internal structure. In engineering problems, rock mass involves macro-scale discontinuities in the form of joints, faults and bedding planes. Behavior of these discontinuities shows differences under applied loads. The problem begins with fracture initiation, which depends on an important material property, called as fracture toughness. Rock fracture toughness is a rock material parameter that determines the crack resistance at the onset of the crack growth. This material property plays a vital role in analyzing the safety issues and production rates in the earth sciences related research work and projects.

Conventional design procedures were based on the failure mechanics in a continuum sense. If applied stress exceeded the yield strength of the continuous material forming the internal structure of a part, material failed, regardless of any flaws, cracks and micro-scale defects in the internal structure. No material is perfectly continuous and homogenous. Accepting the unavoidable existence of such discontinuities, a new discipline in mechanics was needed to investigate and figure out the mechanisms of fracture process in many complex engineering materials like metals, rocks, concrete and ceramics. In order to find out the solutions for crack problems that were encountered in various engineering materials, a state of art called as Fracture Mechanics emerged in 1950’s and 1960’s.

Rock Fracture Mechanics deals with the initiation and propagation of micro-and macro-scale cracks, fractures and other characteristic discontinuities such as joints and faults, which are common in earth sciences applications. Predicting the attitude of fractures in geological rock mass units is attractive in applications such as hydraulic fracturing, rock slope analyses, earthquake mechanics, rock fragmentation, in-situ stress determination, geological disposal of radioactive wastes, terrestrial carbon dioxide sequestration, underground coal gasification, hot dry rock geothermal energy extraction, shale gas & shale oil production, solution mining and in many other similar practical problems of earth sciences.

By using rock fracture mechanics and rock fracture toughness concepts, producers of drilling equipment, rock fragmentation machines and explosives can improve their fracturing based efficiency for rock types of different origin.

1.1 Historical development of fracture mechanics

Before the development of fracture mechanics approaches, conventional design was based on the failure mechanics in a continuum sense. According to this, if stress exceeded the yield strength of the continuous material forming the part, material failed. A safety factor based design was conducted to remain on the safe side. In late 1800's, although designed sufficiently on the safe side, railway parts, aircraft parts, pipes, welded joints, ships and similar structures failed. It was not possible to explain failure mechanisms with the possible usual mechanisms of the conventional design approaches.

The establishment of fracture mechanics is closely related to some well-known disasters in recent history. Several hundred liberty ships fractured extensively during World War II. The failures occurred primarily because of the change from riveted to welded construction and the major factor was the combination of the poor weld properties with stress concentrations and poor choice of brittle

materials in the construction, (Wang, 1996). There were 2,751 Liberty Ships manufactured between 1941 and 1945. Cracks propagated in 400 of these ships including 145 catastrophic failures; and some broke completely into two. Today only two of these ships still exist, (Banks, 2003).

First major step in the direction of quantification of the effects of crack like defects was taken by Inglis (1913). He published an article on stress analysis for an elliptical hole in an infinite linear elastic plate loaded at its outer boundaries. However, theory of fracture mechanics is commonly believed to begin with Griffith's analytical model and elasticity solution for stresses around an elliptical cavity in a uniformly loaded infinite plate.

In Griffith (1921) and Griffith (1924), the condition under which a small elliptical crack in a solid became unstable was established. He evaluated the decrease of energy when a crack of length a existed in the plate. In addition, at the point of incipient fracture this amount of energy must be equal to the energy required to form new crack surfaces. Introducing cracks of different lengths in a specific material and recording the various loads at incipient fracture, he showed that the product $\sigma_c(a)^{1/2}$ remained essentially constant.

Later, the symbol K_c was assigned to represent this material constant in the form of $\sigma_c(a)^{1/2}$and was called the fracture toughness of that material. σ_c corresponded to the critical stress and a was the crack length.

Cornerstone of fracture prediction by testing was Irwin's (1957) work in a series of publications in the late 1950's. According to his work, surface energy characteristics of cracks in materials could be defined and could be measured in fracture tests. Irwin defined the work required to create a unit increase in crack area by fracture. G_c is a material property and is defined as the critical energy release rate. G is energy release rate per unit increase in crack area and is

sometimes named as crack driving force. If $G<G_c$ the crack is stable; $G=G_c$ is meta-stable equilibrium or limiting condition; if $G>G_c$ the crack is unstable and it propagates.

Decades coming after 1960's, scientists began to focus on the plasticity of crack tips. Fracture criterion was set in terms of critical values of crack opening displacement (COD) by Cottrell (1960) and Wells (1961). To account for contribution of crack tip plasticity and nonlinearities resulting in additional opening of crack surfaces, Wells developed a criterion called as Crack Tip Opening Displacement (CTOD) in 1961. In 1968, Rice generalized and extended the energy release method to include crack tip plasticity and non-linear behavior; he introduced a path independent contour integral around the crack tip, which would account for both linear and non-linear parts of the energy release rate. Development in the energy approach to fracture prediction involved in examining a relatively small size arbitrary contour integral region around the tip of the crack rather than considering the energy changes of entire specimen. Elastic-plastic fracture mechanics concepts attracted attention following Rice's work related to this contour integral. Rice defined a path independent integral namely J-integral for two-dimensional non-linear elasticity and for deformation theory of plasticity.

As an alternative to the energy approach, stress intensity factor concept was developed by Barrenblatt (1962) to examine the fracture prediction using the stress field near the tip of the crack. K within the limits of linear elastic fracture mechanics is the stress intensity factor (SIF) which provides a description of the elastic stress field. K depends on the magnitude of the applied stress σ over a part and crack length a in the part. By measuring the critical value σ_c for a part with a crack of length a, fracture toughness K_c which is a material property like strength can be determined experimentally. Extensive compilation of stress intensity factors for different loading and crack configurations are available in SIF handbooks like Sih (1973) and Tada et al., (1973).

In linear elastic fracture mechanics, the energy and stress intensity factor approaches are equivalent. This was first shown by Irwin (1957). By showing that the energy release rate in a cracked body depended only on the conditions at the tip of the crack, Irwin unified the two approaches to fracture prediction.

With the improvement of numerical modeling techniques, working with stress intensity approach is more attractive; stress intensity factor for an arbitrary loading and geometry can be evaluated conveniently by the numerical contour integration around the crack tip. Based on this J-integral, SIF value can be easily computed and presented as part of the output, since energy approaches and SIF approaches are equivalent as long as the material remains linear elastic.

1.2 Statement of the problem

In geo-mechanical applications, earth material is mostly under compressive stress state due to overburden loads. Shear type of fracture is an important failure mechanism in rocks under compression. Shear type loading mode is called as mode II in fracture mechanics. In mode II type shear loading, crack faces slide relative to each other; displacements of the crack surfaces are in the crack plane and in the plane that is perpendicular to the crack front as opening or closure type movements due to shearing action. Crack initiation in shear mode takes place when the mode II crack tip stress intensity factor K_{II} reaches a critical value. This critical value is called mode II plane strain fracture toughness and symbolized as K_{IIc}.

For measuring K_{IIc} different testing geometries and methods have been proposed by researchers. Rock testing is conventionally conducted on core type specimen geometries, since core-based specimens can be prepared easily from the contents of the boxes gathered from investigation boreholes. Core-based specimen geometries and testing methods for K_{IIc} determination are attractive in this sense.

In current practice, not a single K_{IIc} testing method has been suggested and widely accepted for determining mode II fracture toughness of rocks. A thorough comparison among the available core-based geometries and methods is necessary to assess the applicability and limitations of these to K_{IIc} measurements.

1.3 Objective of the thesis

Pure shear mode, which is named as mode II, is originally defined for an infinite plate loaded at the ends by shear stresses parallel to the faces of the internal crack. Plate is assumed to be either in plane stress or plane strain condition.

Pure mode II testing with plate type rock specimens is difficult to conduct, considering the preparation of specimens and appropriate experimental set up. Hard rocks are brittle and machining of small holes to attach shearing fixtures around the upper and lower boundaries is not practically possible. Holes can tear apart. Glueing the shear loading fixtures to the boundaries will not work, since the glueing material at the plate ends tears off before the crack shears apart.

For the reasons stated, mode II fracture toughness testing with core-based geometries is the logical alternative currently. Objective is to figure out which core-based mode II fracture testing geometry and method result in a mode II fracture toughness that realistically represents the pure mode II fracture toughness that would have been obtained by testing with a plate under pure mode II loading.

1.4 Methodology

Shear mode (mode II) fracture toughness tests on core-based specimen geometries of Semi-Circular Disc specimens (SCB) and Circular plate (SNDB) specimens under three-point bending, and Brazilian Disc (CSTBD) specimens under concentrated compressive loads were conducted on a brittle fine-grained gabbro

rock type. Because of relatively homogeneous structural nature, majority of the test program was conducted on commercially labeled Absolute Black Indian Granite (Fine-Grained Gabbro) core-based specimens that were imported from India quarries. Apart from challenges of machining an initial notch to this rock, this high strength rock type was preferred being very brittle, fine-grained, and noticeably homogeneous.

Load application configuration is three-point bending type compression for SCB and SNDB geometries. Bending load application span between the two bottom roller type platens affects the results for such specimen geometries.

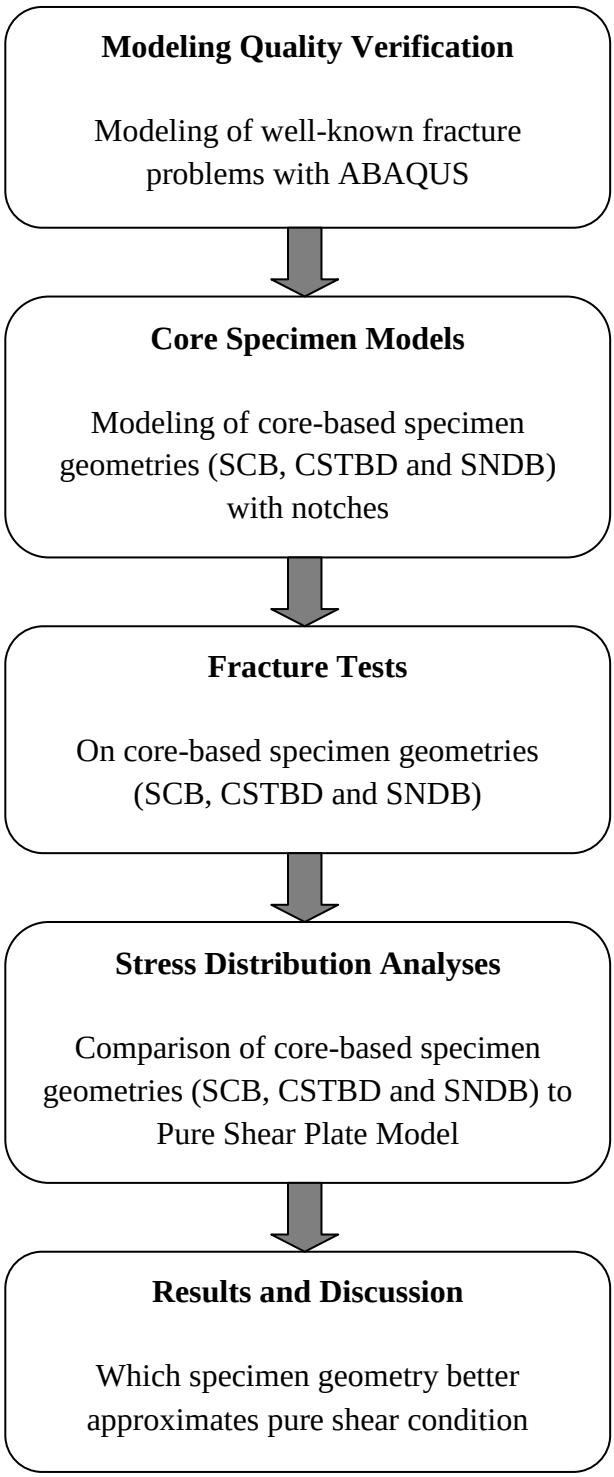

Figure 1.1 Brief summary of the methodology in a flowchart

For all geometries considered, angle of initial notch inclination that produced pure shear mode condition with respect to the applied compressive load axis was computed numerically with models of various notch length, specimen thickness and loading span prior to testing of relevant specimen geometries.

For testing with CSTBD method, core specimens of fine-grained gabbro were prepared by machining of initial internal notches with high-pressure water jet cutting. Notches with varying length were machined through with an angle of initial notch inclination to assure the pure mode II condition as figured out from modeling work.

Stress distributions around the notch, ahead of the notch tip and crack propagation direction were investigated by assigning stress paths around these critical regions in ABAQUS finite element software. In modeling work for the determination of stress intensity factors and the stress distributions around the notch and initiating crack, the different specimen geometries were generated by ABAQUS (Three dimensional finite element software). Models were in either 2D (two dimensional) plane strain sections or 3D (three dimensional blocks), according to the need for proper structural simulation of the core-based geometry.

In order to simulate pure mode II condition for SNDB specimen geometry with blunted notches, modeling was conducted with the same specimen diameter, initial notch length, notch thickness, specimen thickness and loading span as the testing specimens under various relevant loading angles. SCB specimens were modeled in the same manner.

On the other hand, different initial notch lengths were employed for CSTBD specimen models that had the same notch thickness, specimen diameter and specimen thickness as the ones tested.

In order to compare stress distributions and yielding condition based on von Mises yield stress around the initial notches of different specimen geometries under pure mode II loading, some model paths with local coordinate systems were assigned around and ahead of the notch front.

1.5 Sign convention

On the contrary, to the general rock mechanics sign convention, compressive stresses are taken, as negative and tensile stresses are positive throughout this study as in general solid mechanics, (Figure 1.2). ABAQUS finite element software is used in whole modeling applications in this thesis. Coordinate axes marked with 1, 2 and 3 in ABAQUS corresponds *x*, *y* and *z* axes, respectively following the general tensor notation. For instance, S_{11} stress output of ABAQUS models corresponds to S_{xx} or σ_{xx} which is the normal stress component along x-direction. *x-y-z* system is referred as the global reference system of the whole specimen model. In ABAQUS field output visualization module, transforming or rotating the stress state to a notch-related local primed (x'-y'-z') coordinate system (Figure 1.3) relevant to the stress paths with different angles, stress component S_{11} is now S_{11}' or σ_x' which is the normal stress component parallel to the plane of the notch. σ_{22}' or S_{22}' is the normal stress perpendicular to the notch plane in the rotated primed system.

Sign convention for stress intensity factors K_I and K_{II} in ABAQUS is as follows. K_I is positive when the crack is opened under tensile stresses, as depicted in Figure 1.4. The sign of K_{II} depends on the sign of shear stress that is effective over the notch or crack plane. Shear stresses are taken to be positive as in Figure 1.2. However, when this stress state is transformed to counterclockwise direction with respect to the applied loading and notch position of SNDB specimen model as shown in Figure 1.5, shear stress state acting on the square element around the notch front is in a negative form. Resulting K_{II} is computed as negative (–).

For a notch shown in Figure 1.5, initiating crack kinks and propagates upward towards the application point of concentrated load P when K_{II} is negative and angle of crack propagation is computed as (+). If K_{II} is computed as positive in the global coordinate system, then the angle of crack propagation is computed as negative and crack initiates and kinks downward towards the bottom boundary of specimen model.

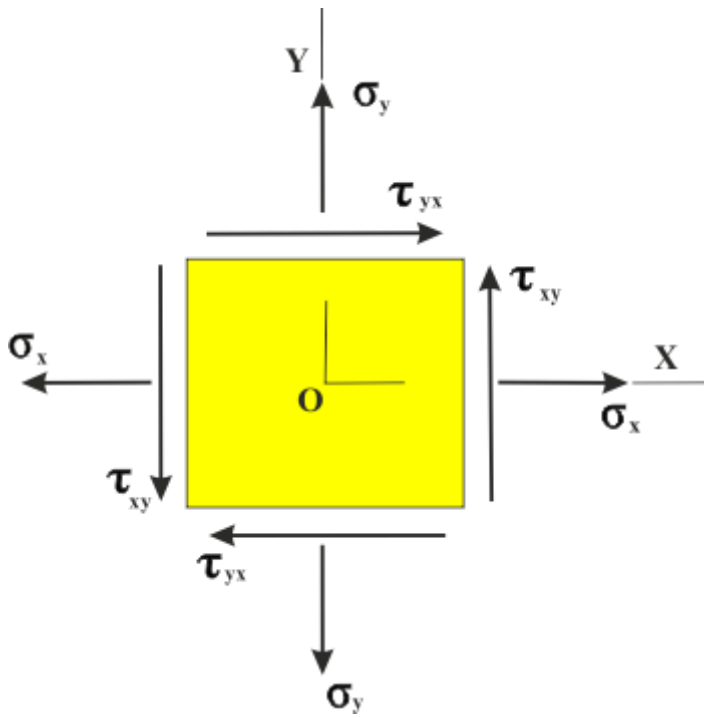

Figure 1.2 Positive stress state in solid mechanics

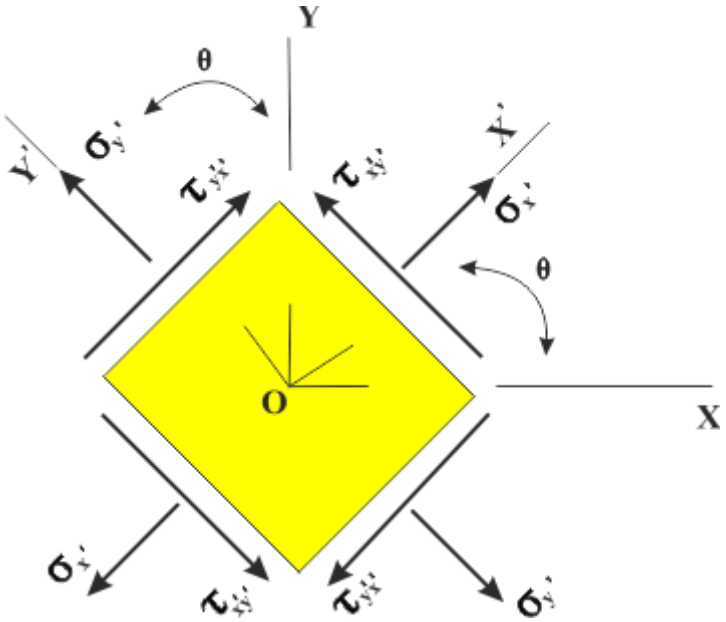

Figure 1.3 Transformed or rotated stress state in local primed coordinate system of a stress path

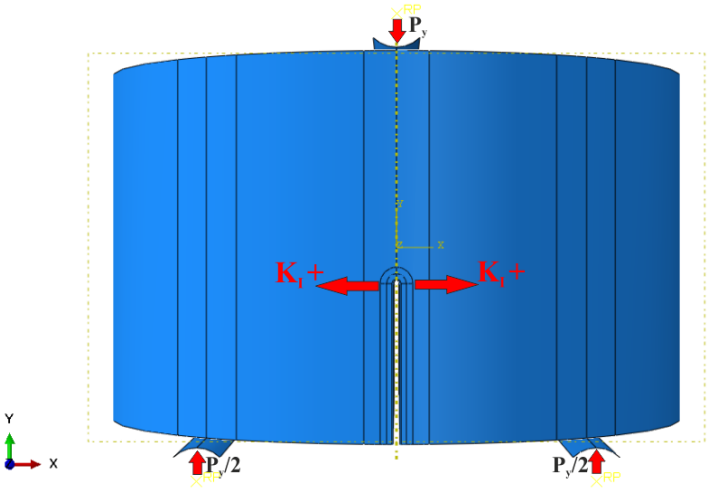

Figure 1.4 Crack opening and positive mode I stress intensity factor K_I sign convention at the notch tip illustrated for SNDB specimen geometry

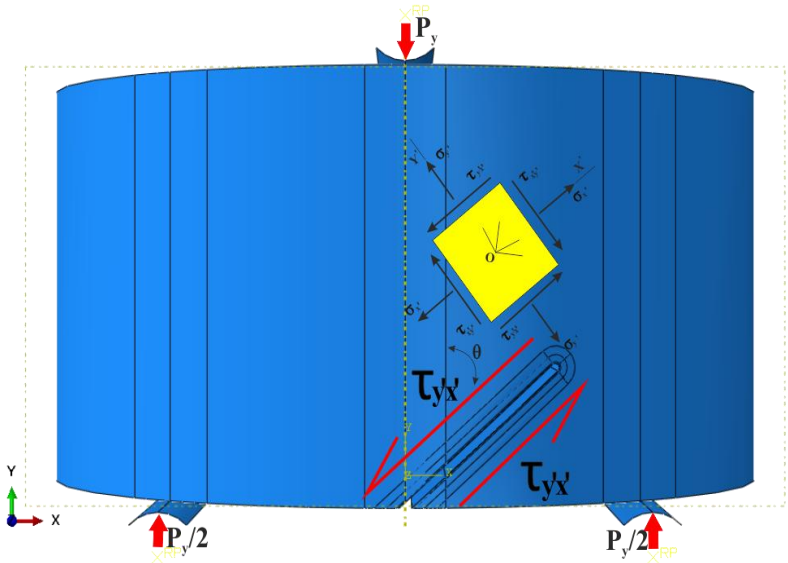

Figure 1.5 Illustration of shear stress state at the vicinity of the notch tip for a SNDB specimen model

1.6 Von mises stress and yield criterion

Specified as ABAQUS field output in the pre-computation modeling steps, user can investigate and analyze all stress components such as S_{11}, S_{22}, S_{33}, S_{12}, etc., and displacement components u_1, u_2, and u_3 of the model block after the computation. In addition, von Mises stress is another readily available parameter as part of the same output scheme.

According to von Mises yield criterion, material starts to yield when the second deviator stress invariant called as J_2 reaches to a critical value. This is called as von Mises stress in the program output and yielding occurs as it reaches to a critical value known as the yield strength, σ_y. Magnitude of the yielding stress is the same under tension and compression, since this criterion is developed to be used for elastic-perfectly plastic or ductile materials like aluminum, steel, copper, saturated clay and the other similar materials. Before the plastic flow, material response against stress is assumed to remain elastic.

Von Mises stress criterion is independent of the hydrostatic stress or first stress invariant I_1. This yield criterion is a 3D form involving all three principal stress components. Graphically, it is represented by a cylindrical surface (Figure 1.6) in the principal stress space with the meridians being parallel with the hydrostatic axis, (Mises, 1913). Von Mises Stress σ_y is used to predict yielding of materials in multi axial loading conditions involving the combined influence of all three principal stress components. It is defined as:

$$\pm\sigma_y = \sqrt{3J_2} \tag{1.1}$$

In terms of principal stresses invariant J_2 is expressed as:

$$J_2 = -{}^{1}/_{6}\,[(\sigma_1 - \sigma_2)^{\,2} + (\sigma_2 - \sigma_3)^{\,2} + (\sigma_1 - \sigma_3)^{\,2}] \tag{1.2}$$

In ABAQUS user' manuals, von Mises stress is described with a different equivalent form in terms of deviatoric stress tensor of s_{ij} as in Equation 1.3 below:

$$\sigma_v = \sqrt{{}^{3}/_{2}\, s_{ij}s_{ij}} \tag{1.3}$$

In the model output interpretation in terms of von Mises stress, a positive value for von Mises stress represents a yield condition in tension, and a negative value corresponds to yielding in compression.

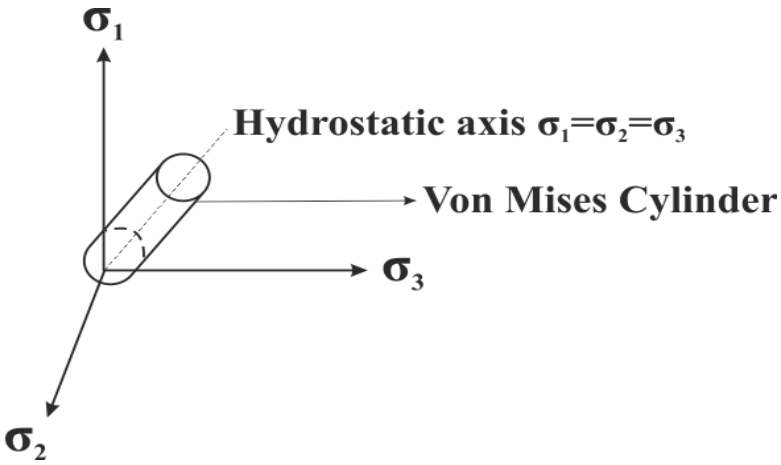

Figure 1.6 Von Mises yield surface in principal stress space

For brittle materials under increasing confining pressure reflected by increasing σ_2 and σ_3, mean stress or I_1 invariant increases the strength. For materials like concrete, brittle soil and rock different tensile and compressive yield strengths are observed. In fact, tensile strengths of such materials can be significantly lower than the compressive strengths. Then, Mohr–Coulomb yield criterion is widely used to describe and analyze the yield phenomenon. Yield surface in the three-dimensional space of principal stresses is graphically represented by a hexagonal pyramid. (Figure 1.7)

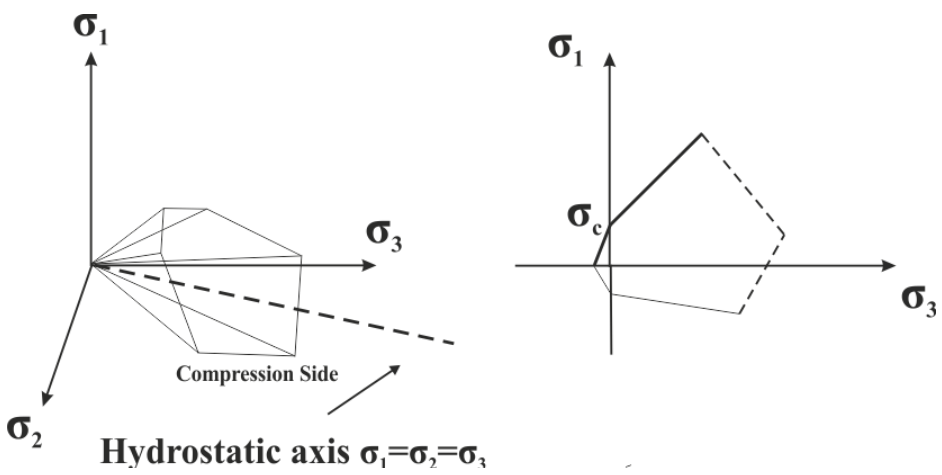

Figure 1.7 3D and 2D Mohr Coulomb yield surface in principal stress space

Yield function involving all three principal stresses in the Mohr-Coulomb criterion is expressed below in terms of I_1, internal friction angle $\emptyset$, cohesion c, and the most important entry, which is the invariant J_2:

$$f_s = -\frac{I_1}{3} sin\emptyset + \sqrt{J_2} cos\theta + \frac{\sqrt{J_2}}{\sqrt{3}} sin\theta sin\emptyset - ccos\emptyset = 0 \tag{1.4}$$

Here, θ is called as Lode Angle (Lode, 1926) or deviator polar angle that is controlled by the relationship of the intermediate principal stress to the major and minor principal stresses and it is given by: (Phase 2 user's manual, 2010)

$$\theta = \frac{1}{3} sin^{-1}\left(\frac{3\sqrt{3}J_3}{2{J_2}^{3/2}}\right) \; where - \pi/6 \leq \theta \leq \pi/6 \tag{1.5}$$

No matter which yield criterion is used to analyze crack or yielding initiation location, the important controlling parameter is always the invariant J_2, which is strongly dependent on the differences in principal stresses around the notch and crack front. As the invariant J_2, increases in magnitude brittle Mohr-Coulomb material approaches the yield surface more and more.

1.7 Outline of the thesis

After a brief introduction to rock fracture mechanics in Chapter 1, Chapter 2 is devoted to application areas of rock fracture mechanics in enhanced recovery of hydrocarbons from deep levels of earth crust by using hydraulic fracturing technique and rock fragmentation. Fracture modes, stress intensity factor, fracture toughness and LEFM (Linear Elastic Fracture Mechanics) concepts are described in Chapter 3. In Chapter 4, previous studies that involve pure mode II stress intensity estimation and measurement work for mode II fracture toughness K_{IIc} are reviewed.

Finite element modeling and program structure of ABAQUS are defined in Chapter 5. Verification analyses and numerical modeling details of SCB, SNDB and CSTBD specimen geometries are described in Chapter 6 and 7 respectively. In Chapter 8, details of laboratory work including experimental set up and procedures are presented. In Chapter 9, stress distributions around the notch for SCB, SNDB and CSTBD specimen geometries are investigated and compared to the pure mode II condition of the plate problem. Finally, conclusions and recommendations for further studies are given in Chapter 10.

CHAPTER 2

APPLICATION OF FRACTURE TOUGHNESS IN HYDRAULIC FRACTURING AND ROCK FRAGMENTATION

Due to the global energy crises faced off during the last three decades, unconventional energy production methods were reevaluated by the developed countries. Among the energy production methods, enhanced recovery of hydrocarbons from deep levels of the earth crust is the main title that includes various types of the novel production techniques. Shale gas, shale oil, enhanced oil recovery (EOR), coal bed methane (CBM), underground coal gasification (UCG) and microbiological coal conversion are the best-known novel production applications under consideration today. In all these novel methods, fracturing in rocks for increasing the energy production is nowadays very popular worldwide.

Because of working at the deep levels of the earth crust, enhanced drilling techniques including the directional drilling and hydraulic fracturing are the most important parts of these novel production methods. Production capacities of the drill-holes can be attractively improved by applying the directional drilling and the hydraulic fracturing.

Fracturing associated with the directional drilling commonly require the availability of the mode I and mode II fracture toughness entries in the energy input computations of the novel applications.

In rock breaking, estimates of the energy input are needed to create broken rock with new crack surfaces. Both mode I and mode II fracture toughness entries are important in such computations. Based on such computations, design of the cutting tools can be improved. Or the mixture of the blasting agents and the blast

hole geometries can be improved depending on the rock type. In rock cutting and drilling work with the tools like the disc cutters and the polycrystalline diamond compact type bits, fracture toughness used in the form of the energy input estimation to create the fresh surfaces can prove to be a useful parameter.

2.1 Hydraulic fracturing

Hydraulic fracturing (Figure 2.1), commonly known as the hydraulic fracking is a modern technology that is used in petroleum production, unconventional natural gas and oil production, geothermal energy extraction, and carbon capture and sequestration applications. It is also a modern technique applied in mining through the boreholes. Highly pressurized mixture of ingredients such as water, sand and chemicals are pumped into the boreholes to form fractures in the valuable deposits. Then, the production and fluid transfer with the valuable ingredients from the borehole can be enhanced tremendously.

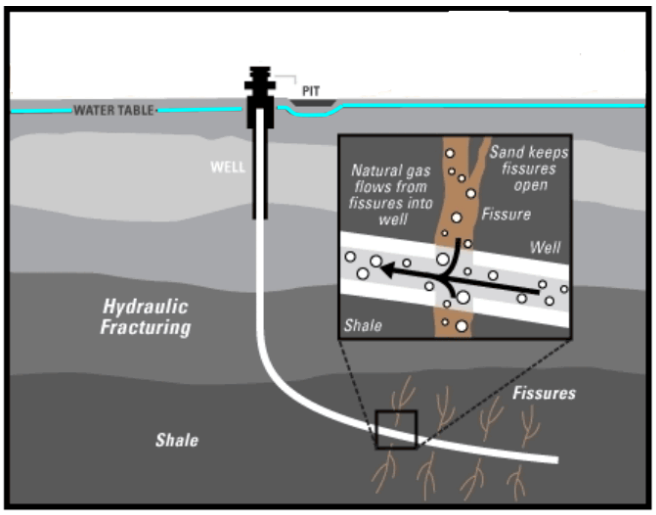

Figure 2.1 Directional drilling and hydraulic fracturing
(Modified from http://bradleydibble.authorsxpress.com/tag/hydraulic-fracturing/)

First hydro-fracking trials were made in 1947 and the commercial application of this technique was employed in 1949. Vertical and horizontal fractures in the mixed-mode fracturing states were generated during these initial applications of hydraulic fracturing. By using these fractures, targeted hydrocarbons were recovered from the relatively great depths of the earth crust. Issues regarding the contamination of the ground water were detected and publicized in different applications at those times. Public claims related to those issues lead to the enforcement of new environmental regulations.

Regarding the fracture mechanics perspective of the hydro-fracking, fracture propagation is greatly influenced by the mode II fracture toughness, since this is one of the important factors, which controls whether a fracture diverts, (Jin et al., 2011). During hydraulic fracturing, fracture toughness increases with confining pressure and it decreases with exposure of the rock to fluids. Therefore, fracture toughness values that are determined in the laboratory conditions are much smaller than the ones observed at in-situ conditions, (Thiercelin et. al., 1989).

One of the novel application areas of hydraulic fracturing is in-situ shale gas and in-situ tight shale oil production. In order to enhance the gas or oil production and reduce the risks regarding the desired manner of fracture propagation, the fracture propagation under the existing in-situ stress conditions should be understood in detail. The majority of these fractures are under pure mode I loading state. Chandler et al., 2013 conducted a series of pure mode I experiments on Mancos shale in the three principle mode I crack orientations (arrester, divider and short-transverse) by using the short rod method under a variety of confining pressures representing the in-situ stress state. It was found that a very substantial anisotropy was observed in the loading curves and K_{Ic} values for the three crack orientations and the divider type crack orientation has 25% higher K_{Ic} value than the other crack orientations.

Schmidt, R. A. (1977) tested Colorado oil shale to determine the effects of the orientation of the bedding planes classified as arrester, divider and short transverse on the mode I fracture toughness, (Figure 2.2). Three-point bending type loading was applied to the dog-boned shape rectangular specimens. It was found that the highest mode I fracture toughness was attained for the divider geometry and the lowest was for the short transverse geometry. In addition, it was determined that mode I fracture toughness of the oil shale that had low kerogen content (80 ml/kg) was %40 higher than the fracture toughness of the oil shale samples that had high kerogen content with 160 ml/kg. Kerogen content is described as amount of organic compounds that are inherently present in the shale formations. Suitability for the extraction operations and the economical production from the oil shale formations can be projected based on this amount.

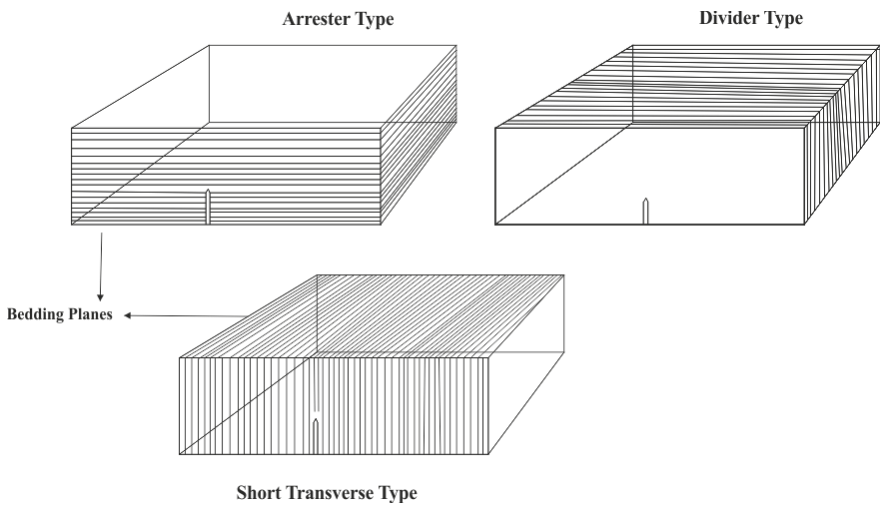

Figure 2.2 Position of the bedding planes for the oil shale samples subjected to the three-point bending for mode I fracture toughness tests
(Modified from Schmidt, R.A., 1977)

Senseny and Pfeifle, 1984 conducted mode I fracture toughness tests on oil shale, sandstone, mudstone and siltstone that were originated from Piceance basin by using the short rod fracture toughness testing method. Core specimens that had 100 mm diameter were machined by the diamond saws. It was determined that mode I fracture toughness of the sandstone unit resulted in an average toughness of 1.27 MPa√m with ranges from 0.69 to 2.40 MPa√m, while for oil shale, mudstone and siltstone the average toughness was around 1.46 MPa√m with ranges from 0.17 to 2.61 MPa√m.

Hydraulic fracturing is commonly used in the exploitation of Coal Bed Methane (CBM) to enhance the permeability of coal seams. Increasing the overburden load also increases the in-situ pressure and the permeability of coal seams decreases because of the closing cleats and fractures. Jeu et al., 1988 investigated the effect of different hydraulic fracture techniques for the enhanced recovery of the coal seams that are located in Piceance Basin, Colorado and San Juan Basin around New Mexico sites. It was concluded that higher operating pressures for fracturing can result in shorter but wider cracks.

2.2 Fracturing for rock fragmentation

One of the rock fragmentation techniques that can be applied for the excavation of the rock is mechanical breakage. Mechanical breakage in rock can be imposed by using the indentation action with high thrust or shearing dominated action of the drag bits (chips). Difference related to the breaking mechanisms of these can be explained as the indenters apply higher normal force that is perpendicular to the rock surface whereas the drag bit tools apply shearing dominated forces that are parallel to the surface of the rock to be excavated.

Indenter type cutting elements like disc cutters are used for the hard and brittle rock types and high-energy need is a characteristic feature for such cutting units

compared to the shearing action of the drag bits. While indenter type cutting units are generally used for penetrating through the competent rocks, shearing action dominated drag bits are used< in relatively weaker rocks such as coal and evaporates. Both breakage systems make use of dominantly the tensile stress fields and the shear stress fields around the cutting units to form rock chips. Pure mode I and the mixed mode fractures initiate in the cutting region to be excavated. These fractures incorporate to form the chips as the excavated material.

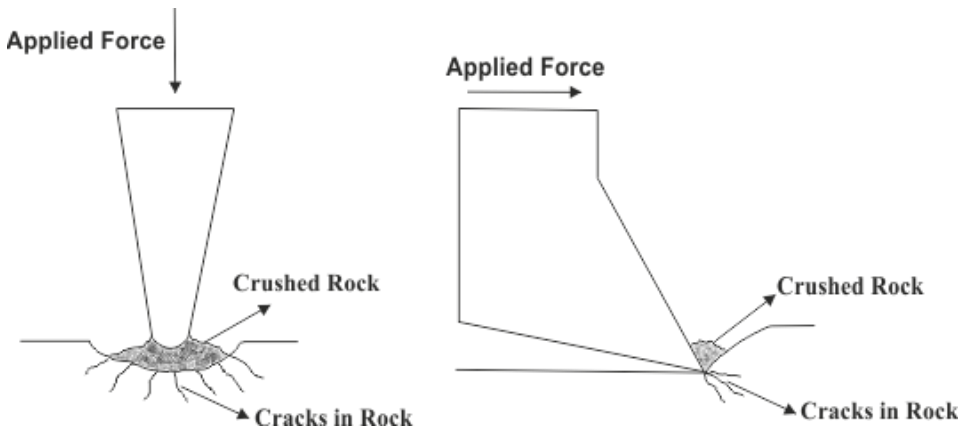

Figure 2.3 Mechanical rock breakages with the indenter and the drag bit actions (Modified from Hood and Roxborough, 1992)

A popular fragmentation method that can be applied in excavation of any rock type is blasting. In rock blasting, fragmentation is dominantly controlled by the energy input of the explosives to the formation of the new surfaces. Energy input can be assessed in terms of the relationship between the fracture toughness and the critical energy release rate or the energy needed to create new cracks or surfaces.

In drilling and cutting operations on rock, specific energy is an important controlling parameter of the penetration rate of the cutting and drilling tools. Energy input to the breaking process and the resulting chip formation with new cracks and surfaces are related to the mode I, mode II and the mixed rock fracture toughness.

Fracture toughness is an intrinsic property, which is related to the energy needed for the rupture. Guo (1990) conducted penetration rate versus rock fracture toughness tests and investigations on five different rock types (sandstone, white limestone, fine grain marble, coarse grain marble and basalt). Fracture toughness of rocks was found to be related to the penetration rates in these rock units with a correlation coefficient of 0.90. However, the rock fracture toughness was not the only parameter that governs the penetration rate. Therefore, another important parameter called as rock hardness was proposed in the same study for the determination of the penetration rate in these rock types.

$$Penetration\ rate\ of\ Drilling\ Machine = 776.21 \times K_{Ic}^{-2.9109} \tag{2.1}$$

In Deliac (1986), a relationship between mean peak cutting force (MPFC) and fracture toughness regarding the chipping efficiency by the drag tool cutting was proposed as:

$$MPFC = C' \times K_{Ic} \times d^{3/2} \tag{2.2}$$

where;

C' = Coefficient depending on the rock type

K_{Ic}= Mode I fracture toughness

d = Depth of the cut

Donovan (2003) conducted a series of experiments on rock fracture toughness and rock comminution to be used in discovering the breaking mechanisms and in designing the jaw crushers. Close relationship was observed between the fracture toughness and the specific comminution energy. When the fracture toughness increases, required specific comminution energy increases. It was surprising that this relationship more dominantly represented the mechanisms of crushing than any other rock material property such as the tensile strength. The relationship

between fracture toughness and the specific comminution energy for determining the parameters of the jaw crusher action was given by:

$$P_c = \sum_{i=1}^{j} [-0.511 + 0.511RR_i]\, K_{Ic} C_i x_i + P_n \;\; for\; 1 \leq RR < 1.5 \tag{2.3}$$

$$P_c = \sum_{i=1}^{j} [0.215RR_i^{0.428}]\, K_{Ic} \tag{2.4}$$

$$333C_i x_i + P_n \;\; for \;\; \geq 1.5 \tag{2.5}$$

where;

P_c = Power consumption of the crusher in kW

RR_i = Reduction ratio for a particle size i

K_{Ic} = Mode I fracture toughness of the rock (MPa√m)

C_i = Probability of breakage for particle size i

x_i = Mass flow of particle size *i in* metric tons per hour

P_n = Power drawn by the crusher under no load in kW.

Closing this chapter about the important application areas of the fracture toughness, it can be stated that fracture toughness can usefully be related to the energy input estimations of the field fracturing processes in efforts to increase the yield of the natural energy sources. Fracture toughness being related to the critical energy release rate of rock material can be used as an important entry in the energy input estimations to create the fresh surfaces in rock breaking processes.

CHAPTER 3

BASICS OF ROCK FRACTURE MECHANICS

In general, cracks can initiate and propagate in three basic modes of loading. These loading types that shown in Figure 3.1 are classified and called as Mode I, Mode II and Mode III. If the combination above-mentioned modes can be taken into consideration, generated new type of loading condition is called as Mixed Mode.

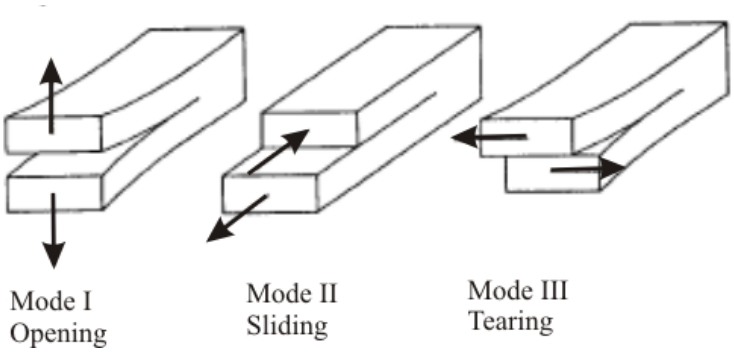

Figure 3.1 Fracture modes

Mode I is the tensile or opening mode. In Mode I, crack propagates along the crack plane direction.

Mode II is the sliding or in-plane shearing mode.

Mode III is the tearing mode or out-of plane shear mode.

3.1 Linear elastic fracture mechanics (LEFM)

LEFM assumes that the material is homogeneous and linear elastic and plastic deformation around the crack tip is negligible. Isotropic and linear elastic mean that the material properties are independent of direction and these materials have only two independent elastic constants, which are elastic modulus (*E*), and Poisson's ratio (υ). (Alkılıçgil, 2010) The objective of LEFM is to predict the critical loads that will cause a crack to grow in a brittle material.

3.1.1 Stress intensity factor and fracture toughness

LEFM uses and characterizes the local tip stress fields by using the parameter called as stress intensity factor, *K* (SIF). *K* depends upon the applied stress, the size, and placement of the crack, as well as the geometry of the specimen. The stress intensity factor is calculated as:

$$K = \sigma\sqrt{\pi x a} x f({}^{a}/_{w}) \tag{3.1}$$

where:

σ : remote stress applied to component

a : crack length

$f(a/w)$: correction factor that depends on specimen and crack geometry

w : specimen width

When the SIF reaches a critical stress state, the crack starts to propagate, and the material fails, this critical stress state denoted as K_c and it is known as fracture toughness. Fracture toughness is a material property that can vary with temperature, loading rate, thickness and the composition of the material.

3.1.2 Crack tip stresses for mode I and mode II

Early crack tip stress and displacement solutions that are depicted in Figure 3.2 for Mode I were identified by in Westergaard's (1934) study. Then, Williams (1957) developed the crack tip stress and displacement solutions for mode II and mode III.

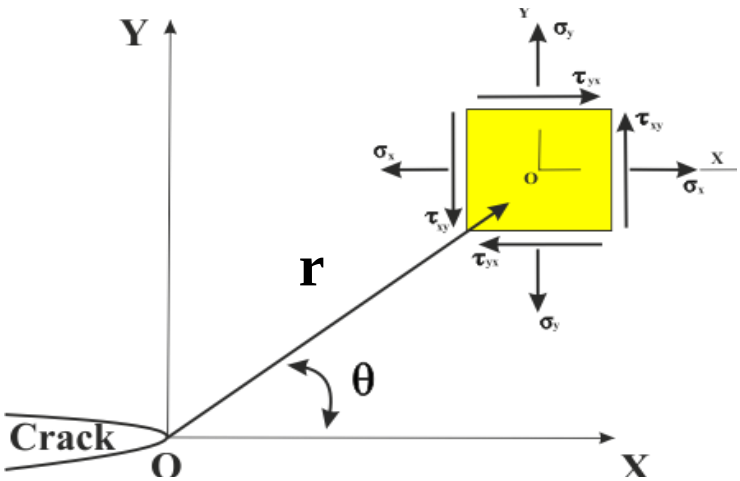

Figure 3.2 Crack tip stress components

The predicted stress state for linear elastic material at the crack tip possesses square root of singularity. ($\sigma \sim {}^{1}/_{\sqrt{r}}$) The stress fields near a crack tip of an isotropic material can be expressed as a product $1/\sqrt{r}$ and a function of θ with a scaling factor K:

The simple form of stress and displacement functions for different Modes near the tip of the crack (as r→0) that are listed below, were established by Westergaard in 1934.

$$\lim_{r\to 0} \sigma_{ij}^{(I)} = \frac{K_I}{\sqrt{2\pi r}} f_{ij}^{(I)}(\theta) \tag{3.2}$$

$$\lim_{r\to 0} \sigma_{ij}^{(II)} = \frac{K_{II}}{\sqrt{2\pi r}} f_{ij}^{(II)}(\theta) \tag{3.3}$$

$$\lim_{r\to 0} \sigma_{ij}^{(III)} = \frac{K_{III}}{\sqrt{2\pi r}} f_{ij}^{(III)}(\theta) \tag{3.4}$$

where:

σ_{ij} = Stress tensor in Cartesian coordinates,

f_{ij} = Geometric stress factor depending solely on angle θ.

3.1.3 Crack tip stresses and displacements for mode I and mode II

Mode I
Stress Components

$$\sigma_{11} = \frac{K_I}{\sqrt{2\pi r}} cos\frac{\theta}{2}\left[1 - sin\frac{\theta}{2} sin\frac{3\theta}{2}\right] \tag{3.5}$$

$$\sigma_{22} = \frac{K_I}{\sqrt{2\pi r}} cos\frac{\theta}{2}\left[1 + sin\frac{\theta}{2} sin\frac{3\theta}{2}\right] \tag{3.6}$$

$$\sigma_{33} = \begin{cases} 0 \quad Plane\ Stress \\ v\ (\sigma_{11} + \sigma_{22})\ Plane\ Strain \end{cases} \tag{3.7}$$

$$\tau_{12} = \frac{K_I}{\sqrt{2\pi r}} \cos\frac{\theta}{2} \sin\frac{\theta}{2} \cos\frac{3\theta}{2}\ ; \tau_{13} = 0;\ \tau_{23} = 0 \tag{3.8}$$

Displacement Components

$$\boldsymbol{u_1 = \frac{K_I}{2\mu}\sqrt{\frac{r}{2\pi}}cos\frac{\theta}{2}\left[\kappa - 1 + 2sin^2\frac{\theta}{2}\right]}$$

(3.9)

$$\boldsymbol{u_2 = \frac{K_I}{2\mu}\sqrt{\frac{r}{2\pi}}sin\frac{\theta}{2}\left[\kappa + 1 - 2cos^2\frac{\theta}{2}\right]}$$

(3.10)

$$\boldsymbol{u_3 = 0}$$

(3.11)

where;

$$\boldsymbol{\kappa = \begin{cases} \frac{3 - v}{1 + v} & \text{Plane Stress} \\ 3 - 4v & \text{Plane Strain} \end{cases}}$$

(3.12)

$$\boldsymbol{\mu = Shear\ Modulus}$$

(3.13)

Mode II
Stress Components

$$\sigma_{11} = -\frac{K_{II}}{\sqrt{2\pi r}}sin\frac{\theta}{2}\left[2 + cos\frac{\theta}{2}cos\frac{3\theta}{2}\right]$$

(3.14)

$$\sigma_{22} = \frac{K_I}{\sqrt{2\pi r}}sin\frac{\theta}{2}\ cos\frac{\theta}{2}cos\frac{3\theta}{2}$$

(3.15)

$$\sigma_{33} = \begin{cases} 0 & Plane\ Stress \\ v\ (\sigma_{11} + \sigma_{22}) & Plane\ Strain \end{cases}$$

(3.16)

$$\tau_{12} = \frac{K_{II}}{\sqrt{2\pi r}}cos\frac{\theta}{2}\left[1 - sin\frac{\theta}{2}sin\frac{3\theta}{2}\right]; \tau_{13} = 0;\ \tau_{23} = 0$$

(3.17)

Displacement Components

$$u_1 = \frac{K_{II}}{2\mu}\sqrt{\frac{r}{2\pi}}\,sin\frac{\theta}{2}\left[\kappa + 1 + 2sin^2\frac{\theta}{2}\right] \tag{3.18}$$

$$u_2 = \frac{K_{II}}{2\mu}\sqrt{\frac{r}{2\pi}}\,cos\frac{\theta}{2}\left[\kappa - 1 - 2sin^2\frac{\theta}{2}\right] \tag{3.19}$$

$$u_3 = 0 \tag{3.20}$$

3.2 Elasto-plastic fracture mechanics

In general, LEFM is used when the nonlinear behavior of crack tip is small enough that can be neglected. This situation is impossible in many materials. Thus, to characterize the time-dependent nonlinear behavior of the crack tip that are encountered in many materials such as metals, Elasto-Plastic Fracture Mechanics (EPFM) concept is used. In order to define crack tip conditions, CTOD (Crack Tip Opening Displacement) and J integral approaches can be used as a fracture criterion. EPFM fracture criteria assumes that material is isotropic and elasto-plastic.

3.2.1 J integral

J integral is an energy based nonlinear fracture criterion for determining the onset of the crack front. It can be related with stress intensity factor if the material response is linear at the crack tip. In small-scale yielding, J integral can be interpreted as in terms of stress intensity factor for isotropic, perfectly brittle, linear elastic materials if the crack extends along the crack plane direction. For plane strain, under mode I, mode II, and mode III conditions, below equations can be used.

$$J_{IC} = G_{IC} = K_{IC}^2 \left(\frac{1 - \upsilon^2}{E}\right) \tag{3.21}$$

$$J_{IIC} = G_{IIC} = K_{IIC}^2 \left(\frac{1 - \upsilon^2}{E}\right) \tag{3.22}$$

$$J_{IIIC} = G_{IIIC} = K_{IIIC}^2 \left(\frac{1 + \upsilon}{E}\right) \tag{3.23}$$

3.2.2 Crack tip opening displacements (CTOD)

In 1961, Wells found that LEFM is not applicable when characterizing the tough materials. He observed that before the sharp crack initiates noticeable crack blunting was occurred. This observation led Wells to propose a new fracture criterion CTOD (Crack Tip Opening Displacement), that depends on the degree of blunting while examining the fracture toughness of the material. This fracture criterion is generally used for determining the fracture toughness of ductile materials. Most common definitions for this criterions are: Displacement of the original crack tip and the 90° intercept.

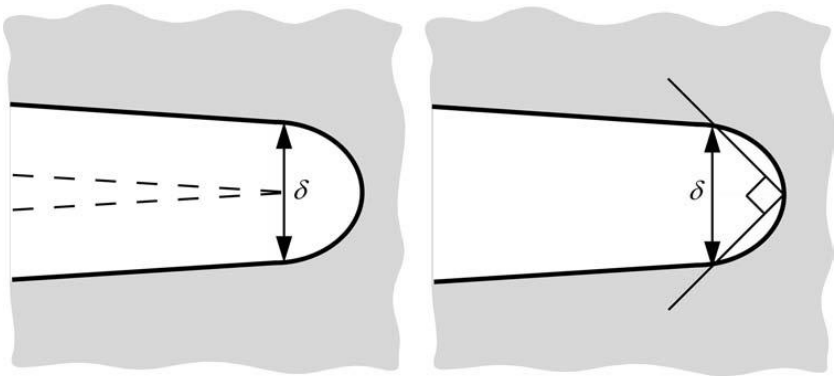

Figure 3.3 Displacement of the original crack tip and the 90° intercept (Anderson, 1991)

CHAPTER 4

MODE II FRACTURE TOUGHNESS TESTING METHODS

Drillings that are conducted in mining industry for mineral and deposit explorations generally have been made with wire-line systems and drill jigs for recovery of undisturbed core samples. Those core samples have been used in determination of rock properties such as rock strength (deformability tests) and fracture parameters.

In order to reduce specimen preparation time cost, scientist generally used core-based specimens in their experimental testing program for solving many engineering problems.

Although, core-based pure mode I testing methods have been used widely and some common types have been accepted by ISRM (International Society of Rock Mechanics), no suggested core-based fracture toughness testing method has been developed and adopted for pure mode II and mixed mode fracture toughness testing. Therefore, various experimental programs have been conducted on different types of specimen geometries for determining pure mode II and mixed mode fracture toughness of rocks. For that reason to inform the reader about the previous studies, upcoming part of this thesis was devoted some of the pure mode II fracture toughness testing methods.

4.1 Punch through shear test

Punch through Shear Test (PTS), illustrated in Figure 4.1, was firstly introduced by Watkins (1983) to analyze shear properties of soil-cement. In addition, Watkins (1983) employed finite element analyses to study fracture behavior of

soil-cement specimens. 100 mm x 100 mm cubic specimens that are mold into together by hand were used pure mode II experiments.

Then, Backers et al. (2002) applied PTS test for rock materials to determine pure mode II fracture toughness. In Backers study, distinctly from Watkins (1983) core-based rock samples that are equal in length to diameter with circular notches drilled into centered end surfaces were used. The main advantage of this testing method, during loading axially (σ) for implementing pure mode II condition, confining pressures (P) can be applied independently from the shear force to the outer surface of the specimens.

Prior to testing procedure, finite element software called as Phase 2 was used to determine the optimum specimen dimensions. Firstly, 95 specimens for three different rock types (limestone, granite and marble) were tested. During testing program, influence of initial notch length, notch diameter, notch symmetry and confining pressures up to 70 MPa on mode II fracture toughness were investigated. It was concluded that pure mode II fracture toughness increases with confining pressure, higher than 30 MPa confining pressure, pure mode II fracture toughness value reaches a constant value for different rock types. In addition, fracture initiation and propagation were differed for particular rock type and this situation was interpreted as: grain size distribution has a strong influence on the mechanism of micro fracturing and failure. (Backers et. al., 2002)

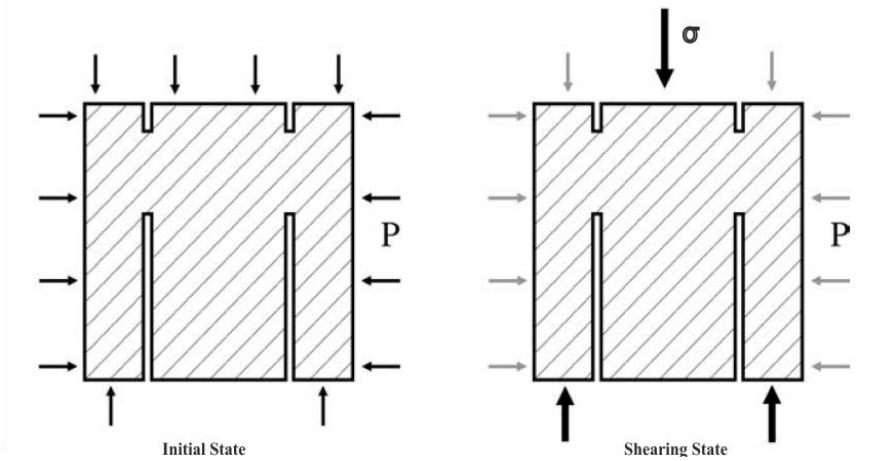

Figure 4.1 Sample geometry and principle loading for the PTS-test
(Modified from Backers et al., 2002)

In addition, six different rock types were again tested by Backers et al., 2004 to investigate the influence of high confining pressure on pure mode II fracture toughness on different rock types. In 2012, updated pure mode II rock fracture toughness values that were determined by using PTS test under high confining pressures (>30 MPa) and low confining pressures were presented in the final paper. According to this paper, pure mode I and pure mode II fracture toughness values of some different rock types are summarized in Table 4.1.

Table 4.1 Fracture toughness values for different rock types
(Modified from Backers et. al., 2012)

Rock Type	Origin	K_{Ic} MPa $\sqrt{m}$	K_{IIc} (low P) MPa $\sqrt{m}$	K_{IIc} (high P) MPa $\sqrt{m}$
Avrö Granite, medium grained	Sweden	3.8	4.7	11.5
Aue Granite, coarse grained	Germany	1.6	4.2	10.5
Mizunami Granite, medium grained	Japan	2.4	4.2	10.9
Seoul Granite fine grained	Korea	1.6	4.0	-
Carrara Marble	Italy	2.4	3.1	6.7
Flechtingen Sandstone, fine grained	Germany	1.2	2.1	5.3
Bentheim Sandtone, fine grained	Germany	0.9	-	-
Ruedersdorf Limestone, mudstone	Germany	1.1	3.1	4.2

Note: Pure mode I fracture toughness values were determined by using ISRM suggested Chevron Bend Method

4.2 Shear box test

Rao et al. (2003) introduced Shear Box Test, illustrated in Figure 4.2. In this test technique, rock samples were placed between reciprocal beveled dies. Rao et al. (2003) thought that this experimental set up establishes a favorable condition for pure mode II fracture toughness testing. Prior to testing, finite element analyses by using ALGOR FEA3 software were employed to determine pure mode II fracture mechanism in shear box test. Pure mode II fracture toughness tests with single or double notches were conducted on three different rock types (granite, marble and sandstone). During experimental program, specimen thickness (*B*), dimensionless

notch length (*a/W*), notch inclinations with respect to the horizontal direction were investigated.

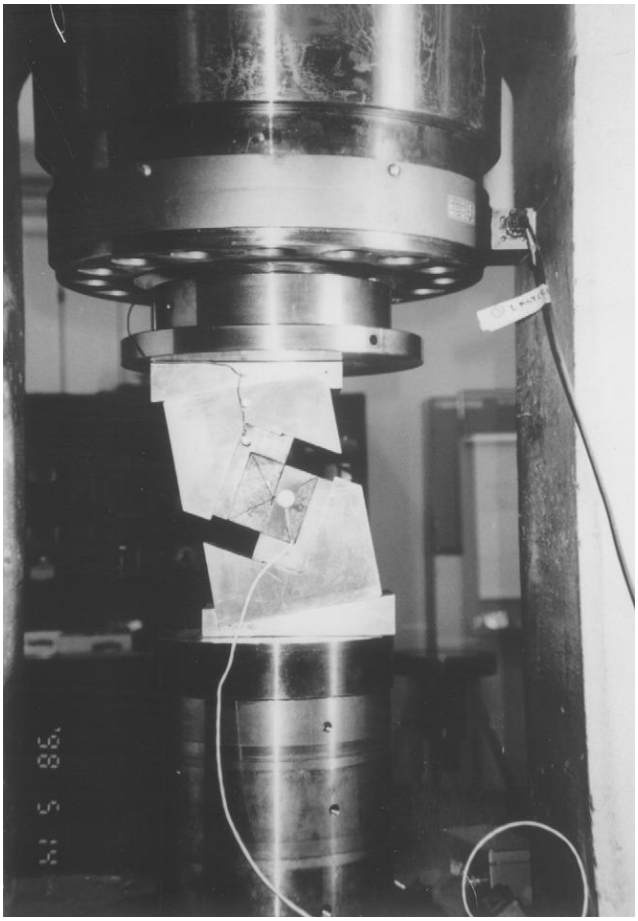

Figure 4.2 Shear Box Testing
(Rao et al., 2003)

For single notched specimens and doubled notched specimens in shear box testing, pure mode II stress intensity (K_{II}) calculated by Equations 4.1 and 4.2 respectively: (Rao et al., 2003)

$$K_{II} = \frac{Q_e}{B\sqrt{W}}\, F\left(\frac{a}{W}\right) \tag{4.1}$$

$$K_{II} = \frac{Q_e}{BW}\sqrt{\pi a}F\left(\frac{2a}{W}\right) \tag{4.2}$$

where:

B = Specimen Thickness (mm)

W = Specimen Width (mm)

a = Notch Length (mm)

$$F\left(\frac{a}{w}\right) = SHAPE\ FACTOR = \frac{2.138 - 5.2\left(\frac{a}{W}\right) + 6.674\left(\frac{a}{W}\right)^{2} - 3.331\left(\frac{a}{W}\right)^{3}}{\sqrt{1 - a/W}} \tag{4.3}$$

$$F\left(\frac{2a}{w}\right) = SHAPE\ FACTOR = 1.780 + 3.095\left(\frac{2a}{W}\right) - 10.559\left(\frac{2a}{W}\right) + 8.167\left(\frac{2a}{W}\right)^{3} \tag{4.4}$$

$$Q_e = P(\sin\alpha - tan\emptyset cos\alpha) \tag{4.5}$$

where:

P= Applied Load

$\emptyset$ = Internal friction angle of rock (^{o})

α = Notch inclination angle (^{o})

It was concluded that, shear-box testing is a potential method for determining pure mode II fracture toughness (K_{IIc}) of cubic rock specimens, since it can create a favorable condition for pure mode II fracture, and in addition this pure mode II testing provides 2-3 times higher K_{IIc} values than K_{Ic} results. Furthermore, because of its simple specimen geometry, loading device and pure mode II fracture toughness calculation, this technique was attributed as an proper pure mode II fracture toughness experiment. (Rao et al., 2003)

Pure mode II fracture toughness results determined by Shear Box Test are tabulated in Table 4.2:

Table 4.2 Fracture toughness test results determined by Shear Box Test (Modified from Rao et al., 2003)

Rock Type	K_{IIc} MPa $\sqrt{m}$	K_{IIc}/K_{Ic}
Granite	4.9	2.6
Marble	6.1	-
Sandstone	5.0	-

4.3 Double edge cracked Brazilian disc (DECBD)

Double Edge Cracked Brazilian Disc (DECBD) specimen (Figure 4.3) was firstly introduced by Chen et al. (2001). In this study, mode I stress intensity factors were attained with weighted function method by using DECBD specimens that are subjected under diametrical compression. Then, in 2005, Chen et al. conducted a new study on mode II stress intensity calculations again using DECBD specimens. It was concluded that semi-analytical formula that was derived by using weighted function method and the results obtained from this method were precisely in harmony with finite element results. In addition, because of its simple specimen preparation for testing and no need a sophisticated loading device, this specimen geometry was proposed as a mode II fracture toughness experiments for brittle materials like rocks, ceramics and concretes. (Chen et al., 2005)

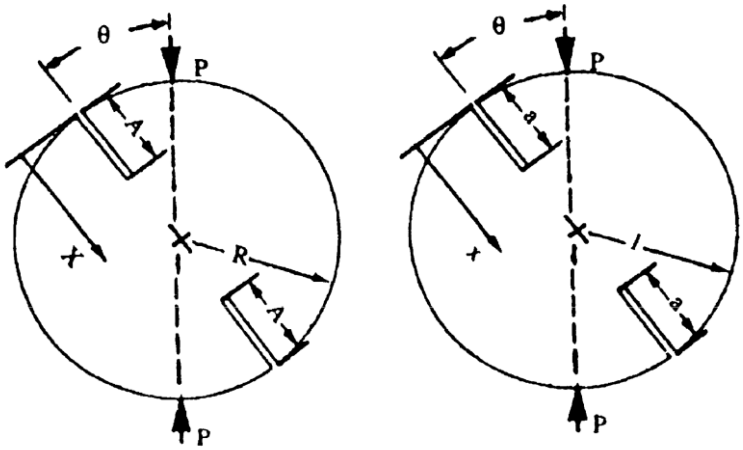

Figure 4.3 Double edge cracked Brazilian disc (DECBD)
specimen and loading position
(Chen et al., 2005)

4.4 Cracked straight through Brazilian disc (CSTBD)

Cracked straight through Brazilian disc (CSTBD) specimen (Figure 4.4) subjected to diametrical compression has been broadly used by many researchers to investigate mode I, mode II and mixed mode fracture toughness of brittle materials such as rocks, ceramics, etc. in many years. Because of many advantages such as: simple geometry, easily extraction from rock cores, simple loading configuration, easily set-up procedure, ability to use both in mode I and mode II fracture toughness testing and the most important one application of compressive loads rather than tensile loads, CSTBD specimen is known as an important mode II fracture toughness specimen. (Ayatollahi and Sistaninia, 2011)

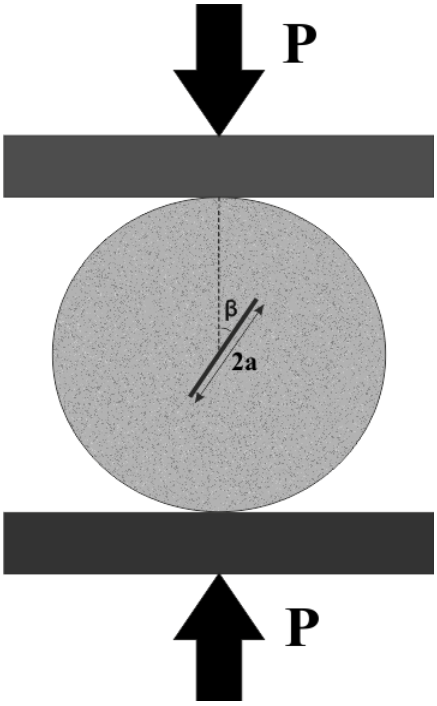

Figure 4.4 CSTBD specimen and loading configuration

CSTBD specimen was firstly used by Libatskii and Kovichick in mode I fracture toughness determination in 1967. Then, Awaji and Sato (1978) used same specimen type in their experimental program for determination of mode I, mode II and mixed mode fracture toughness of marble, plaster and graphite materials. Central cracks that have 0.6 mm notch thickness for marble and the 0.3 mm notch thickness for graphite and plaster, were machined each of the specimen types. In entire testing program, crack Length (a) / specimen radius (R) (a/R =0.5) ratio were kept constant. In addition, they used boundary collocation and dislocation method in numerical analyses. After conducting above-mentioned testing program, fracture toughness values of particular material were found as:

Table 4.3 Mode I and mode II fracture toughness values of different materials (Modified from Awaji and Sato, 1978)

Material	K_{Ic} MPa $\sqrt{m}$	K_{IIc} MPa $\sqrt{m}$	K_{IIc} / K_{Ic}
Marble	0.93	1.05	1.13
Graphite	0.94	1.09	1.16
Plaster	0.13	0.15	1.14

Then in 1982, Atkinson et al., conducted a series of mode I and mode II experiments on PMMA (Polymethyl Methacrylate). Analytical equations were derived for calculations on mode I and mode II normalized stress intensity factors of CSTBD specimens. As a result, they concluded that short cracks that have $l/a \leq 0.3$ (where l = crack length, a = disk radius) ratio, yield reliable results for mixed mode fracture toughness analysis in moderate size specimens.

In 1986, to investigate mixed mode behavior of ceramics, Shetty et al. used CSTBD (diametral compression test) specimens with Knoop indenter surface flaws. They deduced from experiments that CSTBD specimen type provides any combination of mode I and mode II loading in simple specimen geometry.

Because of the SIF equations on mode I and mode II suggested by Atkinson et al., give reliable results only for short cracks (l/a=0.3), Fowell and Xu (1993) proposed new polynomial equations for determination of dimensionless stress intensity factors (Y_I and Y_{II}) and critical inclined angle for satisfying pure mode II condition on CSTBD specimens. According to their paper published in 1993, mode I dimensionless stress intensity factor (Y_I) can be calculated by using Equation 4.6 error within 2% error for $\alpha=a/R$=0.05 - 0.95. (where a= crack length, R=disk radius)

$$Y_I(\alpha) = 0.0354+2.0394\alpha-7.0356\alpha^2+12.8154\alpha^3+8.4111\alpha^4-30.7418\alpha^5-29.4959\alpha^6+62.9739\alpha^7+66.5439\alpha^8-82.1339\alpha^9-73.6742\alpha^{10}+73.8466\alpha^{11} \quad (4.6)$$

In addition to above equation, Fowell and Xu, 1993 suggested Equation 4.7 and Equation 4.8 for determination of critical inclined angle (θ_{II}) that satisfies pure mode II condition and also dimensionless mode II stress intensity factor ($Y_{II}(\alpha)$).

$$\theta_{II} =30.4406-4.6734\alpha-17.6741\alpha^2-9.6827\alpha^3+3.9819\alpha^4+12.9163\alpha^5-13.3222\alpha^6+12.8001\alpha^7-13.1239\alpha^8 \quad (4.7)$$

$$Y_{II}(\alpha)=0.06462+2.8956\alpha-6.8663\alpha^2+9.8566\alpha^3-0.4455\alpha^4-1.0494\alpha^5-13.2492\alpha^6+9.0783\alpha^7-10.7354\alpha^8+28.4775\alpha^9-6.3197\alpha^{10}+10.6626\alpha^{11}-10.0268\alpha^{12}-34.2997\alpha^{13}+1.7292\alpha^{14}+25.2216\alpha^{15} \quad (4.8)$$

In the same study, mode II fracture toughness of the CSTBD specimen was calculated using the Equation 4.9 below:

$$K_{IIc} = \frac{P_{cr}}{B \times \sqrt{R}} Y_{II} \quad (4.9)$$

where P_{cr} is the maximum load that initiates the crack to propagate, B is the thickness of the CSTBD specimen and the R is the radius of the CSTBD specimen.

Krishnan et al., 1998, used CSTBD specimens to investigate mixed mode behavior of soft rock, called as Antler sandstone. Core-based cylindrical specimens, each one has 71.9 mm diameter were tested in mode I, mode II and mixed mode conditions. In all specimens, 10.5 mm notches were machined with two thin cardboard pieces that have 0.1 mm thickness. According to Krishnan et al., 1998, pure mode II condition was achieved around θ=29° inclined notch angle

from vertical and the pure mode II fracture toughness of Antler sandstone was determined as 0.01028 MPa√m. In addition, mixed mode fracture failure envelopes were developed in both tension-shear loading and compression-shear loading conditions.

Al-Shayea et al., (2000) conducted a series of experiments on CSTBD specimens to investigate mode I, mode II and mixed mode fracture toughness of Saudi Arabian limestone at a various elevated temperatures and under effective confining pressures. Initial notches inside each specimen were machined using wire-saw. Specimens that have 98 mm diameter, 22 mm thickness and a/R=0.3 were used in both fracture toughness experiments at a various elevated temperatures and under effective confining pressures. Tri-axial loading cell was used for fracture toughness determination under effective confining stresses. In addition, rectangular box that is fabricated from a heat and electrical insulting material was used in fracture toughness determinations under elevated temperatures. Al-Shayea et al., 2000 concluded that, mode I fracture toughness is substantially increased with confining pressure. However, effect of increasing temperature was measured an increase around 25%.

On the other hand, same trends were observed on mode II fracture toughness values. However, this time, magnitude of increase was followed a lower gradient. To summarize study of Al-Shayea et al., (2000), Table 4.4 was generated.

Table 4.4 Fracture toughness results
(Modified from Al-Shayea et al., 2000)

K_{Ic} at Ambient Conditions MPa $\sqrt{m}$	K_{IIc} at Ambient Conditions MPa $\sqrt{m}$	K_{Ic} at 116°C MPa $\sqrt{m}$	K_{IIc} at 116°C MPa $\sqrt{m}$	K_{Ic} at 28 MPa Confining Pressure MPa $\sqrt{m}$	K_{IIc} at 28 MPa Confining Pressure MPa $\sqrt{m}$
0.42	0.92	0.52	1.00	1.57	2.18

In 2010, Ayatollahi and Torabi tested PMMA and soda-lime glass specimens with blunted notches called as U notched Brazilian Disc specimens under diametrical compression for determination of mode I and mode II fracture toughness. Specimens that have 10 mm disc thickness for PMMA and 6 mm soda-lime glass were prepared as 80 mm diameter and 40 mm notch length. In addition, to investigate notch radius (ρ) effect on mode I and mode II fracture toughness results, specimens that have four different notch radii for PMMA and three different notch radii soda – lime, were prepared by using carefully controlled water-jet. Mode I and mode II fracture toughness results that were obtained after tests are tabulated in Table 4.5.

Table 4.5 Effect of notch radius on fracture toughness results
(Modified from Ayatollahi and Torabi, 2010)

Material	ρ (mm)	K_{Ic} MPa $\sqrt{m}$	K_{IIc} MPa $\sqrt{m}$	K_{IIc} / K_{Ic}
PMMA	0.5	2.23	4.28	1.92
	1	2.83	5.51	1.95
	2	3.77	7.54	2.00
	4	5.10	11.32	2.22
Soda-Lime Glass	1	0.71	1.29	1.82
	2	1.00	1.85	1.85
	4	1.46	2.92	2.00

Aliha et al., 2012 studied mode I fracture toughness experiments on Guiting Limestone. Tests were conducted by using CSTBD and SCB specimens. Results showed that mode I fracture toughness of SCB type specimens are much higher than CSTBD specimens are. Moreover, it is concluded that mode I fracture toughness is significantly dependent on the geometry and the loading type.

4.5 Semi-circular specimen under three point bending (SCB)

Semi-circular specimen under three point-bending (SCB), illustrated in Figure 4.5, was initially introduced by Chong and Kuruppu (1984). For this specimen geometry, they provided a relationship for finding the load line displacement from crack opening displacement by using a rotational factor *r*, which depends on the degree of the nonlinearity of the material. Using the finite element method, Chong and Kuruppu (1984) and Chong et al. (1987) numerically determined the variation of stress intensity factor for mode I and mixed-mode loading for very limited ranges of crack lengths and span lengths.

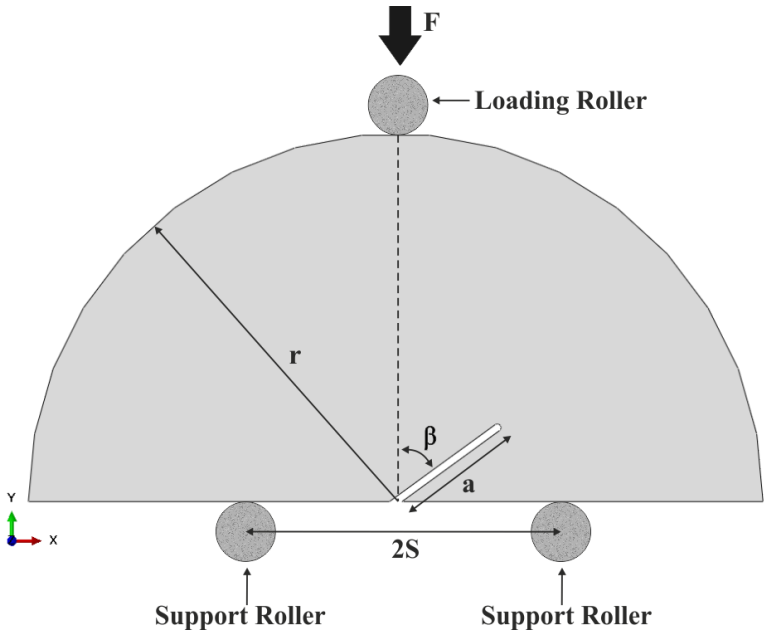

Figure 4.5 SCB specimen and loading configuration

Whittaker et al., 1992 suggested a large crack inclination angle, 63º to obtain pure mode II in SCB specimens and noted that, with such a geometry specimen preparation becomes very difficult due to the damage in the thin wedge zone beneath the crack. In addition, Whittaker et al., 1992 concluded that specimen thickness has insignificant effect on mode II fracture toughness.

Lim et al., 1993 computed stress intensity factors for semi-circular specimens under three-point bending for a range of specimen geometries with the normalized crack length *a/r* changing between 0.1-0.8, crack inclination angles between 0º- 75º, and the normalized span lengths between 0.5-0.8. Results were expected to be accurate within 1% and this was confirmed by comparing the computed stress intensity factors to the results found by the commercial finite element package ABAQUS. Lim et al., 1993 observed that mode II loading becomes increasingly dominant as the support span length is reduced or when the crack angle and length are increased. The use of shorter crack lengths are

suggested for fracture testing as the stress intensity factor‘s less sensitive to any variations in specimen geometry.

Lim et al., 1994 performed mode I fracture toughness tests on SCB specimens of a synthetic mudstone to evaluate SCB technique for fracture testing of rocks. In the first part of this study, mode I fracture toughness values of Johnstone mudstone with various conditions were examined by using SCB specimens. On the other hand, second part of above-mentioned study, mixed mode, and mode II fracture toughness values of Johnstone mudstone were investigated by using SCB specimen. In order to obtain mode I and mixed mode conditions, vertical notches for first case and the angled notches for the second case were employed in the SCB specimens. Specimen diameters were 55, 95, and 144 mm and the specimen thicknesses ranged from 11.9 to 43.9 mm. A notch of approximately 1 mm was machined in the specimens with a rotary diamond-impregnated saw. Keeping with crack preparation procedure recommended by Haberfield and Johnstone (1990), a sharp crack at the tip of the notch was scoured with a razor blade. Fatigue pre-cracking was not employed to avoid the damage in specimens of weak and brittle rock type used here. In fact, in the work of Haberfield and Johnston (1990) it was found that no significant differences were observed in the results with the use of fatigue pre-cracking in a series of tests involving notch tip radii from 0.1 to 0.8 mm. It was concluded by Lim et al., 1994 that semi-circular specimen under three-point bending was the most appropriate due to its versatility, cost-effectiveness, and reliability. On the other hand, regarding the experiments being employed below conclusions were made:

- Mode I fracture toughness (K_{Ic}) decreases with increasing saturated water content exponentially.
- Loading rate have a considerable effect on mode I fracture toughness (K_{Ic}), with high loading rates, increase in mode I fracture toughness was observed.
- Effect of specimen thickness, specimen size and notch length on mode I fracture toughness is insignificant.
- Pure mode II condition was achieved when the initial edge notch has a 54 ^{o} angle from the vertical loading axis. K_{Ic} and K_{IIc} fracture toughness values for Johnstone mudstone were determined as 2.15 MPa√mm and 1.05 MPa√mm, respectively.
- Furthermore, it was observed in the same study that, with increasing notch inclination angle, the region of high tensile stresses spread increasingly over the upper surface of the notch.

Ayatollahi et al., 2006 conducted a series of mode I, mode II, and mixed mode experiments on PMMA (Polymethyl Methacrylate) by using SCB specimens. In this experimental program, specimens that had 100 mm diameter, 5 mm thickness, and 0.3 mm notch thickness were tested with *a/R*=0.3 and *S/R*=0.43 ratios. In order to demonstrate crack growth path and propagation direction, SCB models with consecutive cracks were generated in 20 steps by using ABAQUS finite element package program. It was concluded that the discrepancy between the theoretical and experimental results was more significant for mode II dominated loading conditions.

In addition, Ayatollahi and Aliha (2007) conducted experiments on determination of mode I, mode II and mixed mode fracture toughness of CSTBD and SCB type specimens that are commonly used in fracture toughness determination of brittle rocks. It was deduced that the crack tip parameters (K_I, K_{II}, T-Stress) in either of the SCB and BD test specimens are influenced considerably by the specimen

geometry and loading conditions. Furthermore, it was seen that *T*-stress magnitude (useful indicator of the strength of the crack-tip singularity) in SCB specimen is larger than CSTBD specimen and also opposite *T*-stress signs (SCB (+), CSTBD (-)) were attained for these specimen geometries.

In 2011, Aliha and Ayatollahi investigated the mixed fracture toughness of Iranian White Marble, called as Harsin Marble, by using SCB specimens. Several mixed mode fracture toughness tests were conducted to attain the mixed mode fracture resistance envelope in the complete range from pure mode I to pure mode II. SCB specimens that have 110 mm diameter, 25 mm thickness, and 0.5 mm notch thickness were tested with varying crack inclination angles. (α=0 (pure mode I), 10, 20 , 30 ,40, 43, 47, 50 (pure mode II)) The ratios of *a/R* and *S/R* were kept constant for entire SCB specimens. The average fracture toughness ratio K_{IIc}/K_{Ic} was found around 0.4. In other words, the value of mode II fracture toughness obtained from SCB testing work was noticeably less than the K_{Ic} value.

Ameri et al., 2012 conducted a series of experiments on edge-notched classical SCB type specimens and on the two types of modified SCB specimen to investigate fracture resistance of Hot Mix Asphalt (HMA). ABAQUS finite element package program was used to determine the values of shape factors for the two modified SCB specimens that were proposed for measuring the mixed mode fracture resistance of HMA mixtures. They concluded that although the classical SCB specimen was found to be more suitable, both types of specimens have similar potential for measuring the mixed mode fracture resistance of HMA mixtures.

In 2013, Aliha and Saghafi investigated the effect of specimen thickness and Poisson’s ratio on mixed mode fracture parameters of SCB specimens by using numerical analyses. 2D and 3D models that have 110 mm diameter were developed for investigating the effect of varying specimen parameters. These were

(a/R = 0.2, 0.3, 0.4, and 0.5; $\beta(^{o})$ = 0, 10, 20, 30, 40, 50, and 60; B = 10, 20, 30, and 40 mm, ratio B/R = 0.182, 0.364, 0.545, and 0.727; and υ = 0, 0.1, 0.2, 0.3, and 0.4) As a result of 3D-based SCB specimen geometry modeling, it was found that specimen thickness and Poisson's ratio have an influence on crack tip parameters such as K_I, K_{II}, and T-Stress.

CHAPTER 5

FINITE ELEMENT MODELING & PROGRAM STRUCTURE

In order to calculate stress intensity factors (SIF) of the samples with different geometries, numerical computations are carried out. The commercial finite element package program ABAQUS is preferred for stress and fracture analyses. ABAQUS is a user friendly and powerful finite element-modeling program that is used broadly in many industrial modeling applications.

In this section, development of finite element modeling is briefly reviewed first. Then, an introduction to modeling procedure, terminology, and interpretation of the results in ABAQUS program package is presented as well as crack simulation and fracture mechanics capabilities of the package.

5.1 Finite element method

Many problems in engineering and applied science are governed by differential or integral equations. Complexities in the geometry, properties and in the boundary conditions that exist in most problems usually mean that exact solution cannot be obtained or obtained in a reasonable form in a reasonable amount of time. Current product design cycle times imply that engineers must obtain design solutions in a short amount of time. They are content to obtain approximate solutions that can be readily obtained in a reasonable period, and with reasonable effort. The FEM (Finite Element Method) is one such approximate solution technique. The FEM is a numerical procedure for obtaining approximate solutions to many of the problems encountered in engineering analysis, (Barton & Rajan, 2000).

In the FEM, a complex region defining a continuum is discretized into simple geometric shapes called elements. The properties and the governing relationships

are assumed over these elements and expressed mathematically in terms of unknown values at specific points in the elements called nodes. An assembly process is used to link the individual elements to the given system. When the effects of loads and boundary conditions are considered, a set of linear or nonlinear algebraic equations is usually obtained. Solution of these equations gives the approximate behavior of the continuum or system. The continuum has an infinite number of degrees-of-freedom (DOF), while the discretized model has a finite number of DOF. This is the origin of the name, finite element method, (Barton & Rajan, 2000).

5.2 Origins of the finite element method

The basic concept studies of finite element method were begun approximately 150 years before. The term finite element method was first introduced by Clough in 1960. At this time period engineers used this method for solution of problems such as stress analysis, fluid flow, heat transfer etc. The first written book on a FEM was published in 1967 by Zienkiewicz and Cheung. In the late 1960s and early 1970s, the FEM was applied to a wide variety of engineering problems. The 1970s marked advances in mathematical treatments, including the development of new elements, and convergence studies. Most commercial FEM software packages originated in the 1970s (ABAQUS, ADINA, ANSYS, MARK, PAFEC) and 1980s (FENRIS, LARSTRAN‘80, SESAM‘80). The FEM is one of the most important developments in computational methods to occur in the 20th century. In just a few decades, the method has evolved from one with applications in structural engineering to a widely utilized and richly varied computational approach for many scientific and technological areas, (Barton & Rajan, 2000). Nowadays, ABAQUS, ADINA and ANSYS are the best-known finite element software packages.

5.3 ABAQUS finite element program package

ABAQUS is a simulation program based on a finite element method. The ABAQUS Finite Element Program Package suite offers powerful and complete solutions for both routine and sophisticated engineering problems covering a vast spectrum of industrial applications. It can solve problems ranging from relatively simple linear analyses to the most challenging nonlinear simulations. It includes an extensive library of elements that can model virtually any geometry. ABAQUS can be used to study structural (stress/displacement) problems, heat transfer, mass diffusion, thermal management of electrical components (coupled thermal-electrical analyses), acoustics, soil mechanics (coupled pore fluid-stress analyses and also fully coupled thermal-pore fluid-stress analyses), and piezoelectric analysis. ABAQUS contains an extensive list of engineering materials including metals, rubber, polymers, composites, reinforced concrete, crushable and resilient foams and geotechnical materials such as soils and rock. (ABAQUS 6.11-1 Documentation, 2011)

ABAQUS is easy to use and offers the user a wide range of capabilities. Even the most complicated analyses can be modeled easily. For an instance, problems with multiple components are modeled by associating the geometry defining each component with the suitable material models. On the other hand with ABAQUS contact between the solids are easily modeled. (ABAQUS 6.11-1 Documentation, 2011)

ABAQUS was developed and maintained by Habbitt, Karlson and Sorensen, Inc. (HKS) in 1978. The company has several offices around the world; A-Z Tech. Ltd. in Istanbul ('A to Z Advanced Engineering Technologies') is the Turkey Office.

ABAQUS has some pre- and post-processor units like **ABAQUS/CAE** and **ABAQUS/Viewer**. **ABAQUS/CAE** is a Complete ABAQUS Environment that provides a simple, consistent interface for creating, submitting, monitoring, and evaluating results from ABAQUS simulations. **ABAQUS/CAE** is divided into modules, where each module defines a logical aspect of the modeling process; for example, defining the geometry, defining material properties, generating a mesh, submitting analyses jobs, and interpreting results. **ABAQUS/Viewer** contains only the post-processing capabilities of the Visualization module. It produces the output database in file types with extension .odb to process results from the analyses of models. Therefore, results from an ABAQUS analysis run can be viewed on any other platform supporting **ABAQUS/Viewer**. It provides deformed configuration, contour, vector, and X–Y plots, as well as animation of results, (ABAQUS 6.11-1 Documentation, 2011).

5.4 ABAQUS main windows and modules

ABAQUS main window contains title bar, menu bar, toolbars, context bar, model tree/ results tree, toolbox area, canvas and drawing area, viewport, prompt area, message area, and command line interface. The components of the main window are illustrated in Figure 5.1.

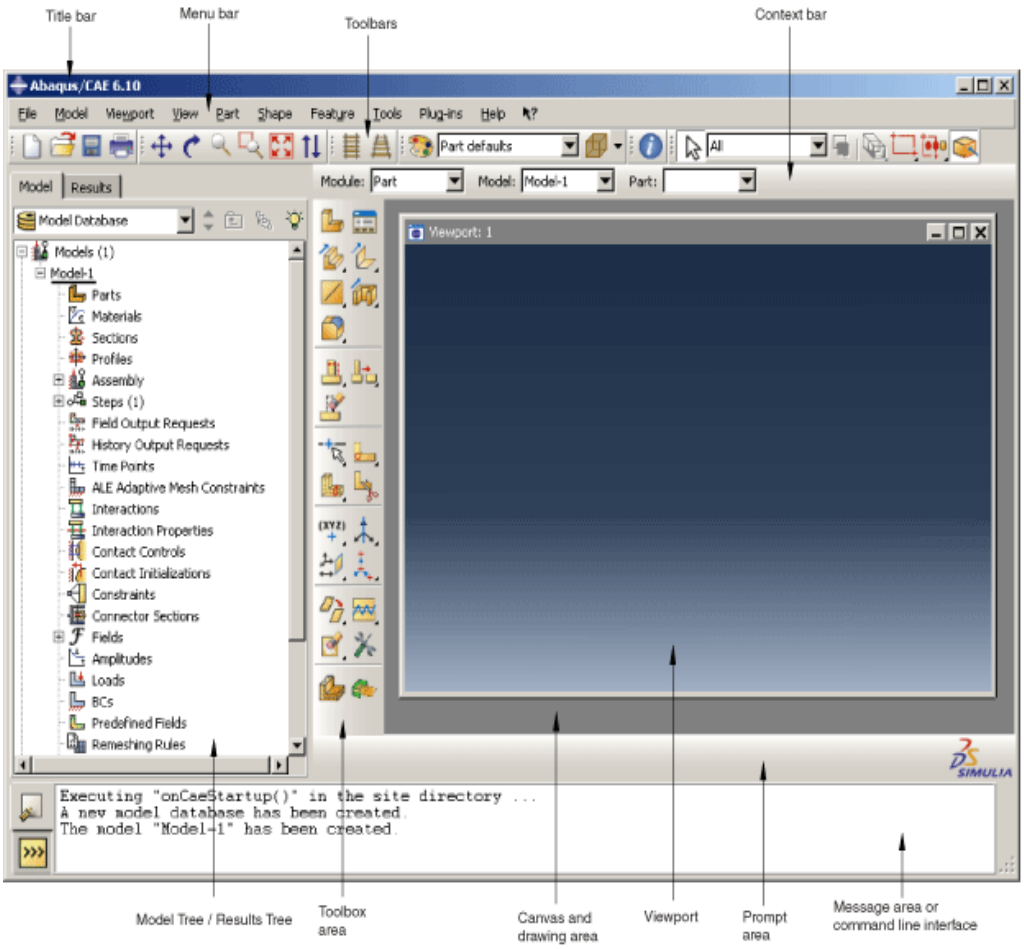

Figure 5.1 Components of the main ABAQUS window

Each ABAQUS module contains only the relevant tools. For example, the Part module contains only the tools needed to create a new part, while the Mesh module contains only the tools for meshing the model. The orders of the modules in the menu are in a logical sequence therefore when creating a model, following the logical sequence is required. Before submitting the model for analyzing the geometry, physical properties, interactions, boundary conditions, and loads of the model must be defined in a hierarchical manner by the following list of modules.

5.4.1 Part module

The Part module allows creating and editing individual parts by sketching their geometry directly in ABAQUS. On the other hand, importing parts that are modeled with other similar programs are accepted.

5.4.2 Property module

Material definitions and material properties of each region of parts are assigned in this module. Some typical material property options involve linear elastic, plastic with Mohr-Coulomb, Drucker Pracker, Clay, and Concrete Damaged & Concrete Smeared Cracking.

5.4.3 Assembly module

Assembly module is used for creating the instances of parts and positioning the instances relative to each other in a global co-ordinate system. Cracks, springs, and dashpots are modeled under the assembly module. In ABAQUS, crack modeling based on either crack modeling with Conventional Finite Element Method or crack modeling with Extended Finite Element Method (XFEM) is embedded in this module. Information on crack-modeling techniques will be described in forthcoming paragraphs.

5.4.4 Step module

Step module is used for creating and configuring analysis steps and associated output requests. Step module provides a sequence of steps to capture changes in a loading and boundary conditions. In ABAQUS, output requests are taken from the step module. Two output requests are available in ABAQUS. One of them is Field Output Request and the other one is History Output Request.

Generally Field Output Request data is generated for the entire model or over a portion of it. Visualization module is used to view field output data using deformed shape, contour, or symbol plots. On the other hand, History Output Request data is generated at the specific points in the model. The rate of output depends on how you want to use the data that is generated by the analysis. In fracture mechanics applications, to calculate the stress intensity factor of a crack, history output request must be defined in the step module.

When assigning the history output request for a crack, firstly contour integral domain type or in other words previously defined name of the crack has to be selected. Three SIF criteria are available under the Stress Intensity Factor type selection window for characterizing the Crack Propagation Direction (CPD). These are:

1) Maximum tangential stress criterion (MTS),
2) Maximum strain energy release rate criterion (MERR)
3) $K_{II} = 0$ criterion.

A typical model regarding above crack propagation criterions was generated for mixed mode problem in Chapter 6. Predicted crack propagation angle differences were observed and this situation will be explained later on.

In order to compute CPD at initiation, one of the criteria must be selected. Number of contours around the crack tip after meshing is written in the number of contours dialog box. These contours are taken into consideration for the computation of the stress intensity factor around the crack tip for the model geometry.

5.4.5 Interaction module

Interaction module is used to specify mechanical and thermal interactions between regions of a model, connections between two points, connections between two edges or connections between point and a surface. In the interaction module, other interactions are defined as constraints (tie, coupling, rigid body, equation) and connectors.

5.4.6 Load module

The Load module is used to specify prescribed conditions, such as applied loads and boundary conditions of the model.

5.4.7 Mesh module

The Mesh module is used to generate finite element meshes of the parts and the assemblies. Seeding, mesh controls, mesh techniques, and element types are defined in the mesh module.

5.4.8 Job module

After determining and defining all of the necessary specifications in the model, the next phase is to finalize the analysis by using Job module. The Job Module is used to submit a job for analysis and monitor its progress. Multiple models and runs can be submitted and monitored simultaneously.

5.4.9 Visualization module

The Visualization Module is used to provide graphical display of finite element models and results. It obtains model and result information from the output database; user can control what information is written to the output database by

modifying output requests in the Step module. User can demonstrate output values of the analysis by using deformed or un-deformed shapes, contours, symbols, vectors, animations, and graphs.

5.4.10 Sketch module

The Sketch Module is used to create and manage two-dimensional profiles that are helped to form the geometry when defining an ABAQUS native part.

5.5 Definition of some ABAQUS terms

In this section, some of the terms that are used widely in FEM analyses are introduced. Some commonly used modeling terms are degrees of freedom, seeding and partitions or partitioning. In mechanics, degrees of freedom (DOF) are broadly described as the number of allowable possible motions for the body or solid. In finite element applications, nodes can have displacements and rotations related to these degrees of freedom. These are typically u_1, u_2, u_3, ur_1, ur_2, ur_3. Faces and edges of the ABAQUS models can be restrained against these displacement and rotational components.

Seeding in ABAQUS is related to the discretization of boundaries and/or partition lines by increasing the number of nodes or vertices along these lines or faces. It is the technique to obtain the desired mesh refinement for the entire model frame or targeted regions in the model.

Partitioning in ABAQUS involves creating additional internal lines, edges, and faces in the model blocks for the purpose of applying different boundary conditions, loads, constraints on and along these partitions. These partitions also serve to refine and improve seeding and mesh intensity. With these partitions, overall model block can be divided into faces or cells, which can be handled

individually to improve the quality and the accuracy of the modeling procedure. The seeding procedure and the typical partitions are illustrated in Figure 5.2.

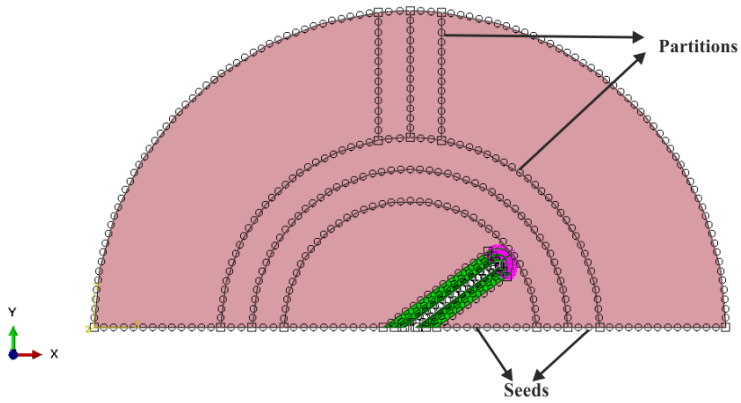

Figure 5.2 Seeds and partitions to improve modeling accuracy

5.6 Fracture mechanics calculation techniques used in ABAQUS software

ABAQUS/Standard offers the evaluation of several parameters for fracture mechanics studies based on either the Conventional Finite Element Method or the Extended Finite Element Method (XFEM). In Conventional Finite Element Method, mesh should be conformed to the cracked geometry, crack front should be defined explicitly, and virtual crack extension direction should be specified. In this type of analysis, detailed focus meshes are generally required for obtaining accurate contour integral results for a crack in a three-dimensional curved surface. In Extended Finite Element Method (XFEM), it does not require the mesh to match the cracked geometry. The presence of a crack is ensured by the special enriched functions in conjunction with additional degrees of freedom. This approach also removes the requirement for explicitly defining the crack front or specifying the virtual crack extension direction when evaluating the contour integral. The data required for the contour integral are determined automatically based on the level set signed distance functions at the nodes in elements.

However, in 2012, Levén and Rickert analyzed and evaluated five different 3D Crack cases that had well-known analytical solution on K_I. In their study, less than 10 percent error existed between XFEM and the benchmark solutions. Besides, errors between 60-100 percent were acquired for the specimens with stress raisers (notches/holes). In Levén and Rickert's study it was concluded that:

XFEM is often proposed to be a mesh-independent method, i.e. the mesh does not have to follow the crack geometry. However, the modeling method showed a higher mesh dependency than expected, where the mesh size at the crack tip showed to be the aspect that affected the accuracy the most. XFEM enables for a relatively simple/flexible crack modeling in terms of mesh construction, but the accuracy is varying with the flexibility. A conformed mesh around the crack tip, similar to what is used in conventional crack modeling, gives very good results within 5 percent error. However, this kind of mesh refinement is hard to accomplish for complex structures. An unstructured mesh is more flexible and easier to model but is shown to give lower accuracy (within 10 percent error).

Because of the XFEM's low accuracy and necessary mesh refinements for complex structures, Conventional Finite Element Method was adopted here in contour integral evaluations.

Before starting the verification problems related to pure mode II and mixed mode fracture analyses with Conventional Finite Element Method, some definitions for contour integral calculations in Conventional Finite Element Method are presented in the upcoming paragraphs.

In ABAQUS, there are two types of cracks that can be introduced to the model during fracture analyses. First one is the seam (sharp) type crack and the second is notch (blunted) type crack. Seam type crack (Figure 5.3 and 5.4) can be defined on an edge or on a face in the models; crack is originally closed but can open during an analysis.

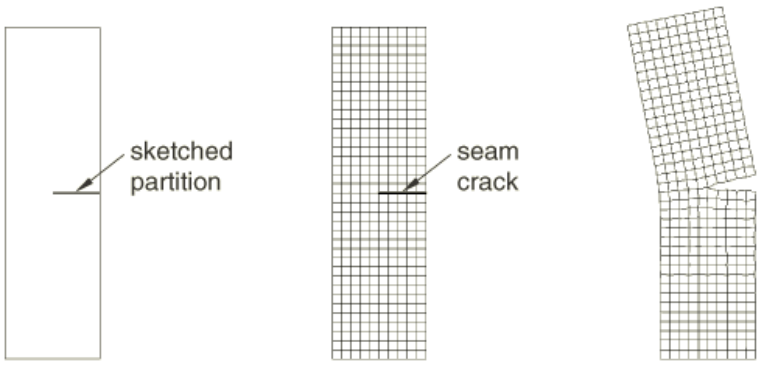

Figure 5.3 Seam crack in 2D
(ABAQUS 6.11-1 Documentation, 2011)

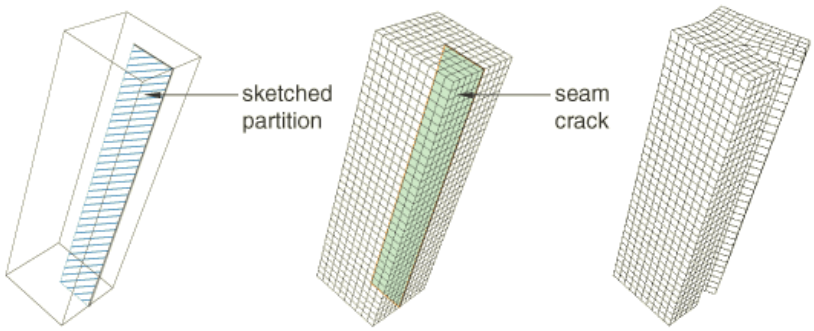

Figure 5.4 Seam crack in 3D
(ABAQUS 6.11-1 Documentation, 2011)

However, in notch type crack, notch is created originally inside the model either as V-shaped or U-shaped (Figure 5.5 and 5.6) structures under part module or subtracting flaw (crack) region from the combination of two original parts with a Boolean operation in the assembly module.

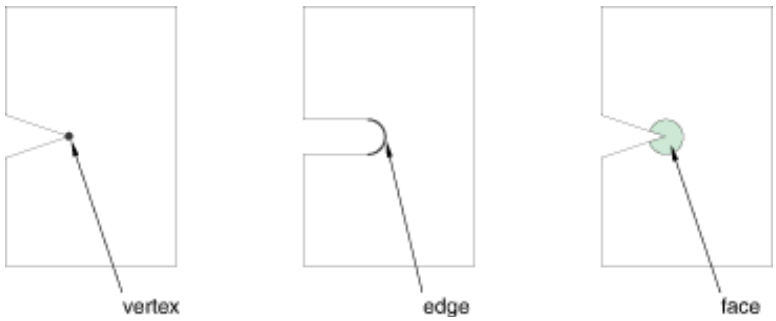

Figure 5.5 V and U shaped notches in 2D with their crack front selection (ABAQUS 6.11-1 Documentation, 2011)

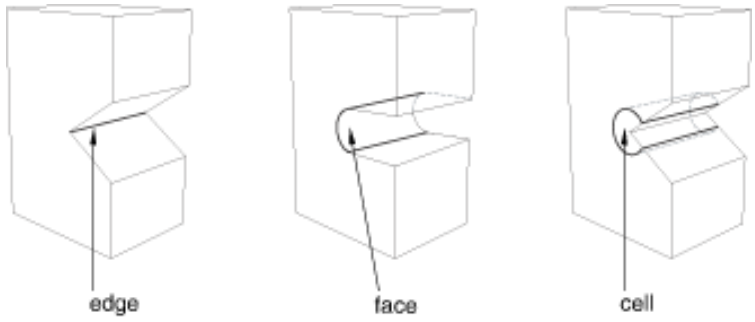

Figure 5.6 V and U shaped notches in 3D with their crack front selection (ABAQUS 6.11-1 Documentation, 2011)

In order to compare and asses the accuracy of the SIF results with seam type cracks and U-shaped notches for mixed mode and pure mode II fracture analyses, these two crack types are employed in the modeling work here.

Other important point for crack modeling with ABAQUS is the determination of Crack Tip Singularity. Normally crack tip singularity for stresses (σ) and thus for strains (ε) is in the form of $1/\sqrt{r}$ in linear elastic solutions as given in section 3.1.3. It is mentioned in ABAQUS 6.11-1 Documentation, 2011 that,

"The singularity at the crack tip should be considered in small-strain analysis (when geometric nonlinearities are ignored). Including the singularity often improves the accuracy of the J-integral, the stress intensity factors, and the stress and strain calculations because the stresses and strains in the region close to the crack tip are more accurate. If r is the distance from the crack tip, the strain singularity in small-strain analysis is determined as":

$$\varepsilon \ \alpha \ r^{-1/2} \text{ for linear elasticity,}$$

$$\varepsilon \ \alpha \ r^{-1} \text{ for perfect plasticity, and}$$

$$\varepsilon \ \alpha \ r^{-\frac{n}{n+1}} \text{ for power-law hardening.}$$

Crack tip singularity application requires attaching some mid-side nodes to increase the modeling accuracy around crack tip. Second-order high accurate mesh is constructed at crack tip. Menu window for this is given in Figure 5.7. Mid-side node is positioned *1/4* of the distance between the native nodes (Linear Elastic or Power Law Hardening case) or *1/2* of between the native nodes (Plastic case). Crack propagation either degenerate removing single node or duplicate nodes at the collapsed element side is simulated with a collapsed element procedure at the crack tip.

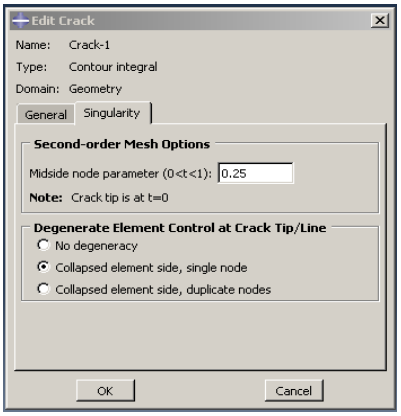

Figure 5.7 Crack tip singularity definitions for 2D and 3D linear elastic analysis

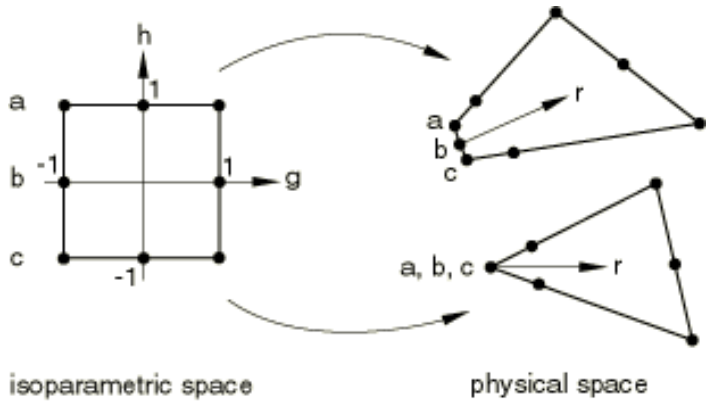

Figure 5.8 Illustration of one-sided collapse for the crack tip second-order quadratic elements
(ABAQUS 6.11-1 Documentation, 2011)

5.7 Fracture criteria and crack propagation direction

The stress intensity factors K_I, K_{II} and K_{III} are usually used in linear elastic fracture mechanics to characterize the local crack-tip/crack-line stress and displacement fields. (ABAQUS 6.11-1 Documentation, 2011) During stress intensity factor computations, crack propagation direction can also be calculated. In Maximum Tangential Stress Criterion (MTS), Crack Propagation Direction (CPD) angle θ is calculated according to formula written in expression 5.1.

$$\theta = cos^{-1}\left(\frac{3K_{II}^2 + \sqrt{K_I^4 + 8K_I^2K_{II}^2}}{K_I^2 + 9K_{II}^2}\right) \tag{5.1}$$

Determination of Crack Propagation Direction Angle is stated in ABAQUS 6.11-1 Documentation that:

Direction of the crack propagation angle is measured with respect to the crack plane. In such a way that, when $\hat{\theta} = 0$*, this situation represents the crack propagation direction is in the straight-ahead direction. Furthermore,* $\hat{\theta}<0$ *if* $K_{II}>0$*, while* $\hat{\theta}>0$ *if* $K_{II}<0$*. The crack propagation direction angle is measured from q to n; i.e., it is measured about the direction –t, or counterclockwise measured from q.*

Above-mentioned situation is illustrated below in Figure 5.9.

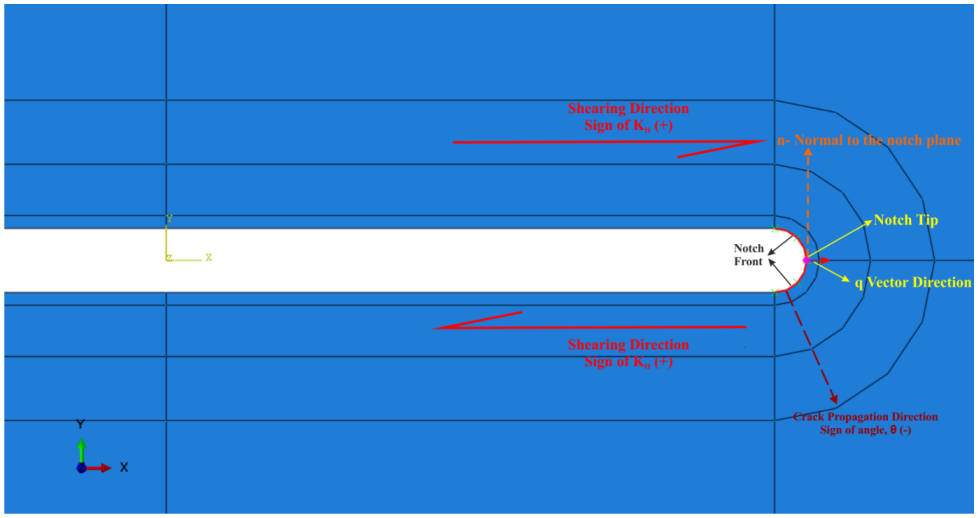

Figure 5.9 Illustration of crack propagation direction angle definition in ABAQUS

CHAPTER 6

VERIFICATION EFFORTS AND MODELING IMPROVEMENT

In order to assess the accuracy of stress intensity factor computations with ABAQUS software, fracture mechanics problems that have well-known analytical solutions, were studied in this verification work. For demonstrating the correct pure shear mode condition, Pure Shear Plate Model was simulated compatible with the original definition of pure mode II shear loading definition.

For the mixed mode loading condition of an inclined crack in a plate, Inclined Crack in Tension Model was investigated in the models. The purpose of investigating such a crack configuration under mixed mode loading state was to assess the prediction ability of various crack propagation criteria such as Maximum Tangential Stress (MTS), Maximum Strain Energy Release Rate (MERR) and $K_{II}=0$.

Stress intensity factor results and crack propagation directions computed by ABAQUS modeling work were compared to the available results of analytical expressions developed in the previous investigations.

6.1 Pure shear plate model under mode II type loading

Stress intensity factors K_I, K_{II} and Crack Propagation Direction (CPD) for a central crack on a plate subjected to uniform shear traction loading are computed with models constructed by ABAQUS program package. This verification problem material is modeled as an isotropic elastic material with two-dimensional (2D) type CPE8 (Continuum Plane Strain Eight Node) kind of elements in the package program.

Crack length in the plate of the problem is *2a*=20 mm. Dimensions of the model and mechanical properties related to the central crack on an infinite plate under pure shear mode loading is given on Table 6.1. Problem frame is in 2D plane strain state (computed based on a sufficiently thick plate with a thickness much higher than in-plane dimension) with a seam crack embedded to the center of the plate.

Table 6.1 Dimensions of the model and mechanical properties related to the central crack on an infinite plate under pure shear mode loading

Dimensions and Mechanical Properties	Values
Width of the plate, 2W	400 mm
Height of the plate, 2H	400 mm
Seam Crack length, 2a	20 mm
Traction Stress on the plate, τ	1 MPa
Young's modulus, E	200 MPa
Poisson's ratio, υ	0.3

Seam crack type with zero thickness is introduced into the model, (Figure 6.1). Seam crack is the crack type that is used in ABAQUS analyses to attach sharp cracks with no thickness. In ABAQUS, seam type crack tip option is available under the Crack Menu.

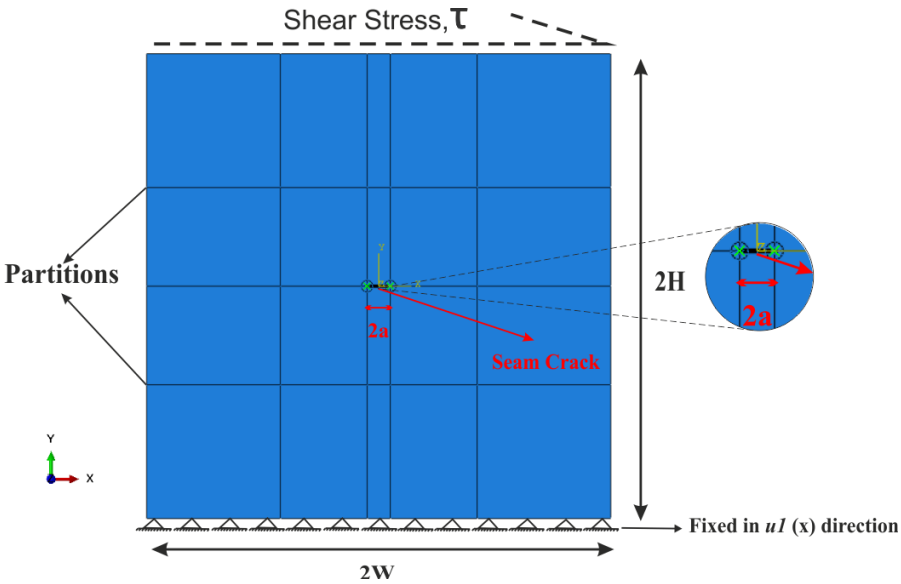

Figure 6.1 Schematic view of the 2D plane strain model with traction directly applied to the upper boundary

For applying the shear load to the upper and lower boundaries of the plate, two different options were tried. In the first case, boundary shear loading was generated by selecting Traction Stress Component (τ) under the Load Module of ABAQUS and applying this shear directly to the upper boundary as the lower boundary was kept fixed, (Figure 6.1). In the second case, shear loading was applied through the reference point located over the upper boundary of the plate while the bottom boundary was kept fixed as in case 1. In order to transfer and distribute the shear load to the upper boundary, horizontal shear force assigned through the reference point was manipulated by the Coupling Constraint process of ABAQUS under the Interaction Module, (Figure 6.2).

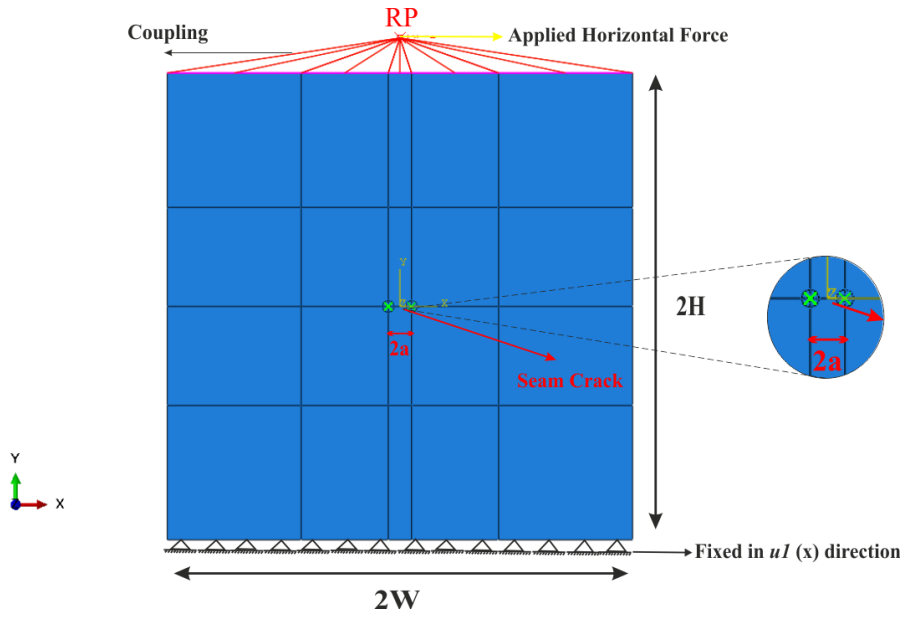

Figure 6.2 Applied Horizontal Force and Coupling

Analytical stress intensity factor solutions for pure mode I and pure mode II for this example are given as K_I = 0 and K_{II} = $\tau\sqrt{\pi a}$. A shear stress of 1 MPa sufficiently far away from the inner crack region is applied to the upper and lower boundaries of the plate model of ABAQUS. The results of computation with ABAQUS are K_I = 0 and K_{II} = 1MPa$\sqrt{\pi x 10mm}$ = 5.605 MPa√mm.

To increase the finite element model computation accuracy, fine meshing should be applied to the whole model and contour integral region (18 Contours). After meshing the model by using proper mesh controls and seeding, fine meshing procedure (47915 Second Order Quadrilateral Plane Strain Elements, CPE8) was applied around the seam crack. Schematic views of un-deformed and deformed contour integral region around the seam crack are illustrated in Figure 6.3 (a) and (b) respectively.

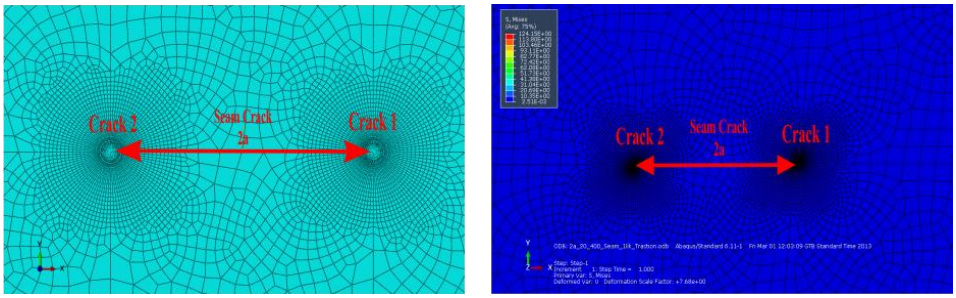

(a) (b)

Figure 6.3 Schematic views of the seam crack in the (a) un-deformed and (b) deformed state of the model part

In ABAQUS finite element code, stress intensity factor computation is implemented on the crack tip nodes that are located in the vicinity of the crack front. For that reason, SIF computation is made by taking averages of these nodes along crack front and called as $K_{I\ av}$. In this study, to prevent confusion, SIF results will be given without av. notation.

After analyzing the problem with case 1 loading condition, average stress intensity factors K_I is zero as expected. K_{II} computed for both ends of the seam crack on the left and right tips and the Crack Propagation direction (CPD) are found as:

$$K_{II} = 5.587 \text{ MPa} \sqrt{mm}$$

Crack Propagation Direction = -70.5^{o}

Percentage difference between the computed and the analytical results can be calculated as:

.

$$Difference\ (\%) = \frac{K_{\ computed} - K_{analytical}}{K_{analytical}} x100 \tag{6.1}$$

Percentage difference is found as 0.32% between the analytical solution and the computed mode II stress intensity factor.

As it is mentioned above, case 2 loading condition, depicted in Figure 6.2, was achieved by using Reference Point and Coupling Constraint for the same model constrained by same boundary conditions. In this type of loading condition, Traction Stress (τ) was generated by using horizontal u_1-direction force that is applied on Reference Point. In addition, Reference Point was coupled to the upper edge of the model. Because of the model was designed as a plane strain model, horizontal force was applied along model's plane strain thickness surface. As a result, Traction Stress (τ) for the case 1 loading was achieved.

However, analytical solution of this analysis a little bit different from case 1 (τ, Traction Stress) loading condition. In this case, Traction Stress (τ) was calculated from Equation 6.2:

$$\tau = \frac{F}{A} \tag{6.2}$$

τ = Traction Stress (MPa)
F= Applied Force (N)
A= Surface Area (mm^2)

For acquiring 1 MPa Traction Stress (τ) by using Equation 6.2, horizontal force was taken as 640000 N that is applied on 640000 mm^2 (Wide-400 mm x Thickness-1600mm) plane strain surface area. Final situation of this formula is:

$$\tau = \frac{640000\ N}{640000\ mm^2} \tag{6.3}$$

$$\tau = 1\ MPa \tag{6.4}$$

After analyzing the above case 2 loading condition with ABAQUS, average stress intensity factors K_I and K_{II} that are computed for both ends of the seam crack on the left and right tips and the Crack Propagation direction (CPD) were found as:

K_I = 0 MPa $\sqrt{mm}$ K_{II} = 5.587 MPa $\sqrt{mm}$

:

Crack Propagation Direction = -70,5^o

Percentage difference was calculated from Equation 6.5 below.

$$Difference\ (\%) \frac{K_{\ computed} - K_{analytical}}{K_{analytical}} x100 \tag{6.5}$$

Comparing these to the analytical solution, percentage difference was calculated as:

Difference of K_{II} = 0.32%

After acquiring similar results with different loading scenarios, because of its simplicity, Traction Stress (τ) was chosen as a loading type in convergence and notch thickness analysis.

In order to investigate the effect of Elastic Modulus on SIF results, Pure Shear Plate Model with seam crack was again computed with 70 GPa Elastic Modulus (*E*). No difference was observed on SIF results between the Pure Shear Plate Models that have 200 MPa Elastic Modulus and 70 GPa Elastic Modulus. One can conclude that SIF results cannot be affected by changing Elastic Modulus.

6.2 Convergence study for seam cracks

In ABAQUS finite element code, stress intensity factors are calculated conventionally by contour integral technique. This technique is applied to the model by using circular region around the crack tip, called as contour integral region.

Contour integral region is the region where stress intensity factor values are computed. It must be large enough that the average of the stress intensity factor in that region could converge. On the other hand, it must be small enough to provide a sufficient area for smaller and larger cracks to achieve a valid mesh. (Alkılıçgil, 2010)

In order to get reliable results in contour integral region around the crack tip, sufficient mesh density (refinement) must be provided. It is described in ABAQUS 6.11 Analysis User's Manual (2011) that:

The size of the crack-tip elements influences the accuracy of the solutions: the smaller the radial dimension of the elements from the crack tip, the better the stress, strain, etc. results will be and, therefore, the better the contour integral calculations will be. The angular strain dependence is not modeled with the singular elements. Reasonable results are obtained if typical elements around the crack tip subtend angles in the range of 10° (accurate) to 22.5° (moderately accurate). The finite element mesh must be refined in the vicinity of the crack to get accurate stresses and strains; however, accurate J-integral results can frequently be obtained even with a relatively coarse mesh.

This means that for getting accurate results from the model, contour integral region should be divided into between minimum 16 pie (α=22,5^o) to maximum 32 pie (α=11,25^o).

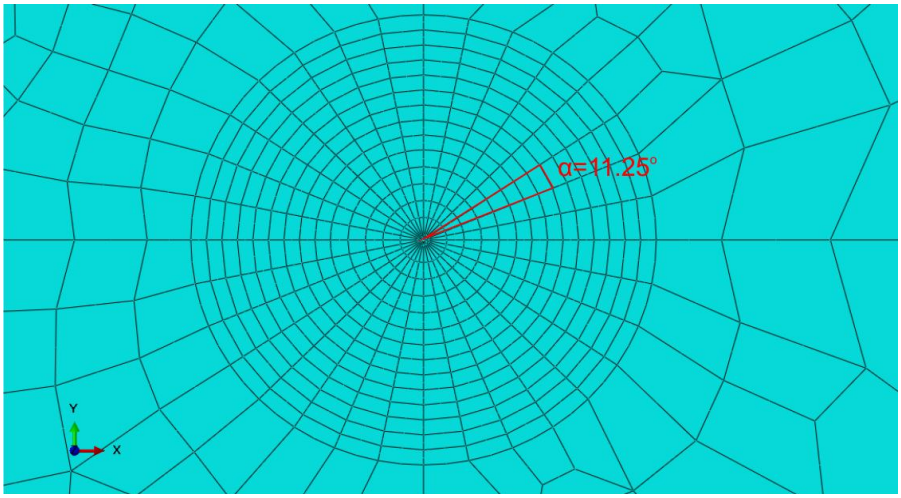

Figure 6.4 Crack tip elements and crack tip subtend angles

In order to get pure mode II condition, distinctly from Figure 6.4 subtend angles were taken approximately as 3.4^o in Figure 6.2 (a). When the subtend angles were taken as 11.25^o as in Figure 6.4, K_I value was calculated as nearly zero (K_I =1x10^{-5} MPa $\sqrt{mm}$). However, when the subtend angles were arranged as 3.4^o, K_I value was calculated as 0. This situation can be defined as smaller subtend angles increase the accuracy of the results.

On the other hand, mesh intensity of the whole model used for stress intensity factor analysis should be consistent with contour integral region mesh intensity. This situation increases the mesh harmony and minimizes the unwanted irregular shape elements.

Besides the crack tip subtend angles, number of contours in the contour integral region is also so important in mesh intensity studies. To understand the number of contours influence on stress intensity factors around the crack tip, number of contours in the contour integral region were changed in between 4 and 24 (4, 6, 10, 14, 17 and 24) as seen in Figure 6.5.

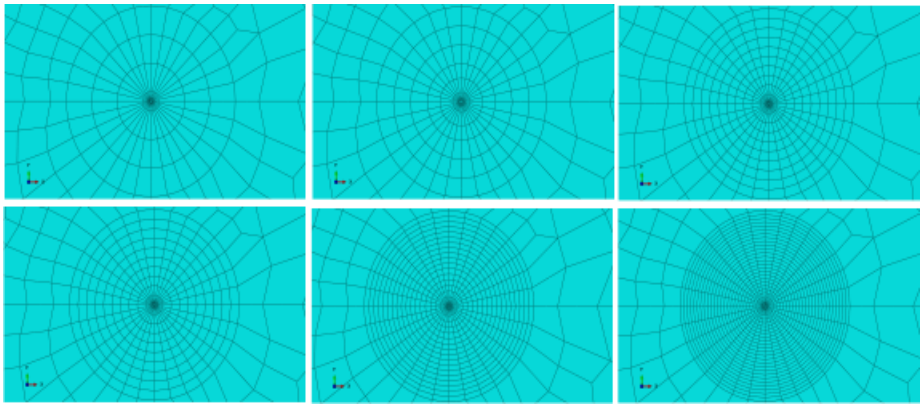

Figure 6.5 Different mesh intensities at the contour integral region
(Number of contours in the contour integral region = 4, 6, 10, 14, 17 and 24 respectively)

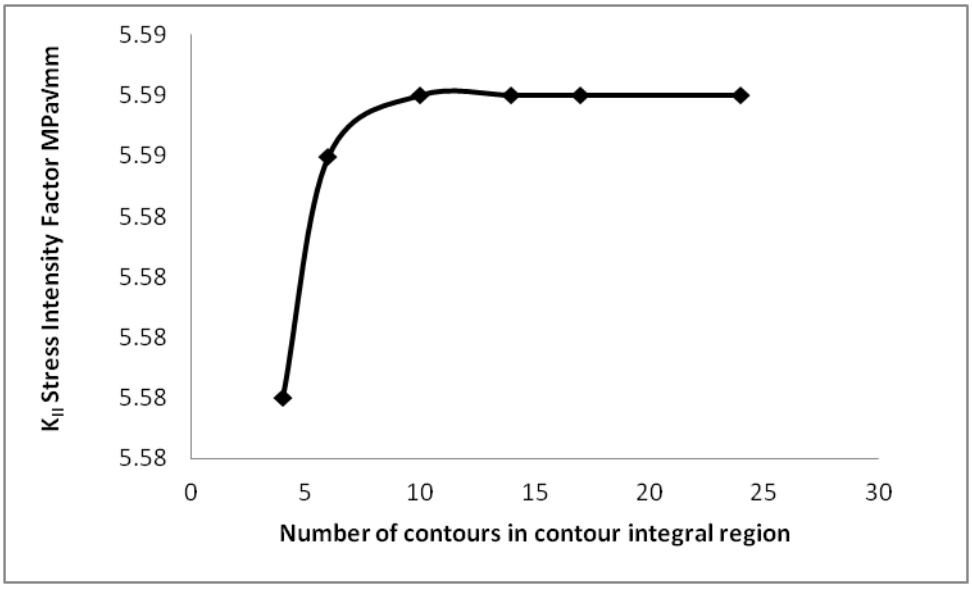

Figure 6.6 K_{II} Stress intensity factor variations according to number of contours in contour integral region

As it is shown in Figure 6.6, when the number of contours in the contour integral region increases, K_{II} stress intensity factor converges to the specific value. In this study, the stress intensity factor difference between the coarsest and the finest mesh was found as 0.09%.

It can be concluded that 10 to 15 contours in the contour integral region are sufficient for the stress intensity factor analysis for seam cracks. Another important issue that shouldn't be forgotten for this analysis, Pure Shear Plate Model was designed wholly in 2D environment with the CPE8 (Continuum Plane Strain Eight Node) elements. This situation increases the accuracy of analysis and decreases the effect of the number of contour integrals on stress intensity factor computation.

6.3 Pure shear plate verification model with blunted cracks

Above studies are based on zero-thickness seam type crack elements in modeling work. However, specimen geometries that are used in SCB, SNDB and CSTBD tests include initial diamond saw-cut notches with finite thicknesses and rounded notch tips. Therefore, in order to examine the effect of notch thickness and materialize the real experimental conditions, blunted notch analyses on pure mode II verification model were carried out.

ABAQUS finite element code has capabilities for this type of modeling on blunted notches. However, it is specified in Modeling Fracture & Failure with ABAQUS Book that: In order to achieve accurate results, some model specifications must be taken into account during modeling work. Such as, during meshing around blunted notch surface, the size of the elements around the blunted notch shouldn't be higher than the $1/10^{th}$ of notch radius. This situation was depicted in Figure 6.7. Element sizes may be increased forthcoming contour integrals by using bias edge seeds.

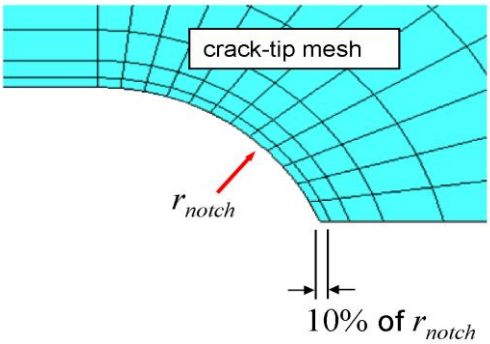

Figure 6.7 Size of the elements around blunted notch
(Modeling Fracture & Failure with ABAQUS)

On the other hand, crack faces must be parallel to each other or parallel to the symmetry plane. In addition, the region on the surface of the blunted notch must be used to define the crack front, shown in Figure 6.8.

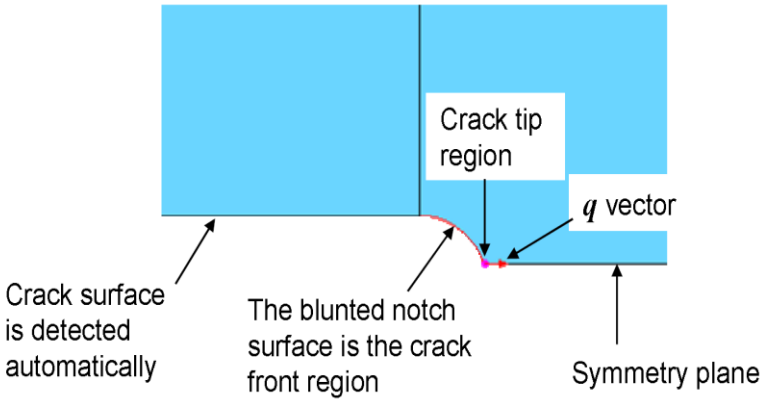

Figure 6.8 Crack front, crack surface and crack tip definition for blunted notches in ABAQUS
(Modeling Fracture & Failure with ABAQUS)

Model specifications, dimensions, and boundary conditions were kept same as in previous seam crack model. However, only the 0.5, 1, 1.5, 2, 2.5 and 3 mm blunted notches were generated behalf of seam crack by using cut module. In order to show effect of real cutting notch thicknesses on different types of pure mode II experiments, above mentioned notch thicknesses were chosen. In whole

notch thickness analyses, notch roundness starting point distance was taken half of the notch thickness. For instance, in 1 mm notch thickness model, notch roundness starting point begins 0.5 mm away from the crack tip.

Selection of crack front, crack tip and direction of *q* vector for blunted notch model is illustrated in Figure 6.9.

Figure 6.9 Selection of crack front, crack tip and direction of *q* vector for blunted notch model

To optimize the finite element computation accuracy, fine meshing should be applied to the whole model and contour integral region (23 Contours). After meshing the model by using proper mesh controls and seed, fine meshing (47378 Second Order Quadrilateral Plane Strain Elements, CPE8) around the blunted notch were obtained and depicted in Figure 6.10.

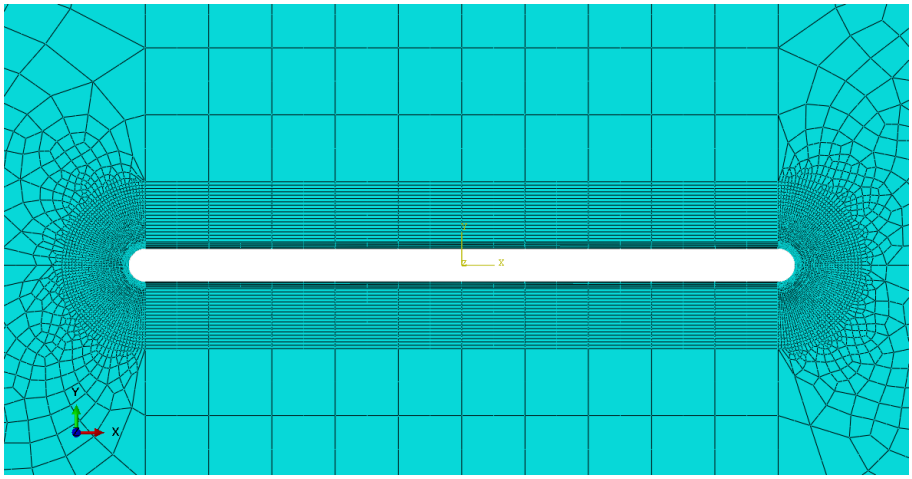

Figure 6.10 Fine meshing around blunted notch tips

After analyzing the above blunted 1 mm notch model with ABAQUS, average stress intensity factors K_I and K_{II} that are computed for both ends of the seam crack on the left and right tips and the Crack Propagation direction (CPD) were found as:

K_I = 1.09 x 10 $^{-5}$ MPa $\sqrt{mm}$ K_{II} = 5.625 MPa $\sqrt{mm}$

Crack Propagation Direction = -70,5^{o}

Percentage difference was calculated from Equation 6.6.

$$Difference\ (\%) = \frac{K_{\ computed} - K_{analytical}}{K_{analytical}} x100 \tag{6.6}$$

Comparing these to the analytical solution, percentage difference was found as:

Difference on K_{II} = 0.35%

Thus, results that were gained from seam crack and blunted notch analyses are compatible with analytical solution of this well-known problem. Both results have few differences that were thought to be coming from effect of meshing.

If we look at the difference on K_{II} between seam crack and blunted notch:

Percentage difference between seam crack and 1 mm blunted notch (%) is:

$$= \frac{K_{II\ blunted} - K_{II\ seam}}{K_{II\ seam}} x100 \tag{6.7}$$

$$= \frac{5.625 - 5.587}{5.587} \tag{6.8}$$

= 0.68% was determined.

6.4 Effect of notch thickness on K_{II} SIF analyses

As it is known, during experimental preparation for pure mode I and pure mode II fracture toughness studies, many researchers use different thickness diamond saws, which have various cutting blunted notch thicknesses. Therefore, researcher should be aware of the effect and deviation of notch thickness during his/her original specimen modeling work.

In order to understand the effect of notch thickness on K_{II} analysis, above mentioned blunted notched verification analyses were again conducted with 0.5, 1, 1.5, 2, 2.5 and 3 mm blunted notch thicknesses.

In this study, all model specifications (Boundary Conditions, Mesh Seeds, Element Type, etc.) for 1 mm blunted notch thickness analysis were kept constant that used in 0.5, 1.5, 2, 2.5 and 3 mm notch thickness analyses. Nevertheless,

some total element differences were occurred because of the element removal inside blunted notch.

After analyzing the above blunted 0.5, 1, 1.5, 2, 2.5 and 3 mm notch models with ABAQUS, average stress intensity factor K_{II} and Crack Propagation Directions (CPD) were found and tabulated as in Table 6.2:

Table 6.2 Effect of Notch Thickness on K_{II} Stress Intensity Factor

Notch Thickness (mm)	Crack or Notch Type	K_{II} Results MPa $\sqrt{mm}$	Crack Propagation Direction ^{o}
-	Seam	5.587	-70.5
0.5	Blunted U Notch	5.604	
1		5.625	
1.5		5.656	
2		5.687	
2.5		5.712	
3		5.748	
Analytical solution of the problem		5.605	

For understanding the effect of notch thickness on K_{II} in graphical form, above tabulated K_{II} results were illustrated with analytical solution in Figure 6.11.

As it can be seen from the graph that, K_{II} stress intensity factor increases with notch thickness. However, percentage difference on K_{II} stress intensity factor between analytical solution of the problem and 3 mm blunted notch thickness result, were determined as 2.55%. On the other hand, result of 0.5 mm notch thickness approximately equals to analytical solution.

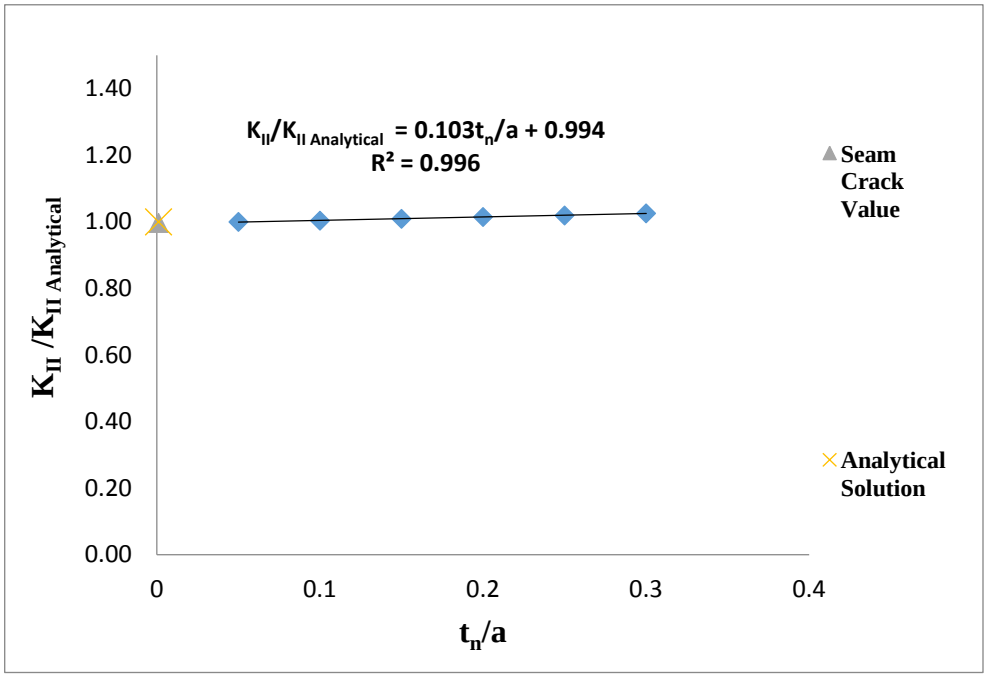

Figure 6.11 $K_{II}/K_{II\ Analytical}$ versus t_n/a

6.5 Inclined crack in tension – mixed mode verification model

Second verification fracture model is an inclined crack in tension. Remote from the crack, model is subjected to a far field uniaxial stress acting in the direction at an angle (β^o) from the crack, as shown below. Analytical solution of stress intensity factors and schematic representation of this model are shown below in Figure 6.12.

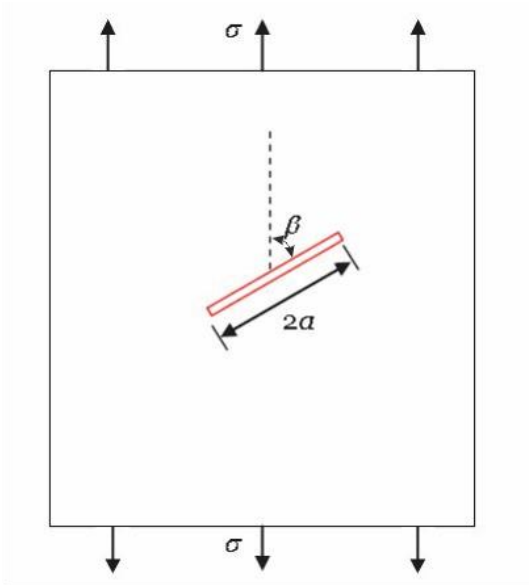

Figure 6.12 Inclined crack in tension
(Modified from Suo)

Analytical solution for stress intensity factor calculations for this example is given in Equation 6.9 and 6.10.

$$K_I = \sigma\sqrt{\pi a}sin^2\beta \tag{6.9}$$

$$K_{II} = \sigma\sqrt{\pi a}sin\beta cos\beta \tag{6.10}$$

On the other hand, for the same mixed mode model, the Crack Propagation Direction (CPD) or in other words direction of the kink can be found as in Equation 6.11. As it is known, the kink direction depends on the relative amount of mode II to mode I load. Erdogan and Sih (1963) showed that the experimentally measured direction of the kink in Plexiglas is well predicted by the criterion that the crack kinks to the plane with the maximum hoop stress. For the stationary crack, the hoop stress near the crack tip is:

$$\sigma_{\theta\theta}(r,\theta) = \frac{K_I}{\sqrt{2\pi r}} cos^3\left(\frac{\theta}{2}\right) - \frac{K_{II}}{\sqrt{2\pi r}} 3cos^2\left(\frac{\theta}{2}\right) sin\left(\frac{\theta}{2}\right) \tag{6.11}$$

The hoop stress maximizes at an angle θ^*, is given by:

$$tan\left(\frac{\theta^*}{2}\right) = -\frac{2K_{II}/K_I}{1+\sqrt{1+8(K_{II}/K_I)^2}} \tag{6.12}$$

When the crack is pure mode I (K_I>0), this criterion predicts that the crack extends straight ahead. When the crack is pure mode II (K_{II}>0 or K_{II}<0) this criterion predicts that the crack kinks at an angle θ^*=70.5 ^{o} that is measured with respect to the crack plane.

For the example above, by using Equations 6.9, 6.10, and 6.12 and using dimensions in Table 6.3, K_I, K_{II} and θ (Crack Propagation Direction) were found as analytically:

K_I = 3,158,300 Pa $\sqrt{m}$ $\qquad$ K_{II} = 3,158,300 Pa $\sqrt{m}$

θ = 53.13^o

Table 6.3 Dimensions and mechanical properties of the inclined crack in tension

Dimensions and Mechanical Properties	Values
Width of the plate, *2W*	254 m
Height of the plate, *2H*	254 m
Crack (seam) length of the plate, *2a*	25.4 m
Crack Angle, β^o	45°
Load on the plate in tension, σ	1 MPa
Young's modulus, *E*	13000 MPa
Poisson's ratio, υ	0.15

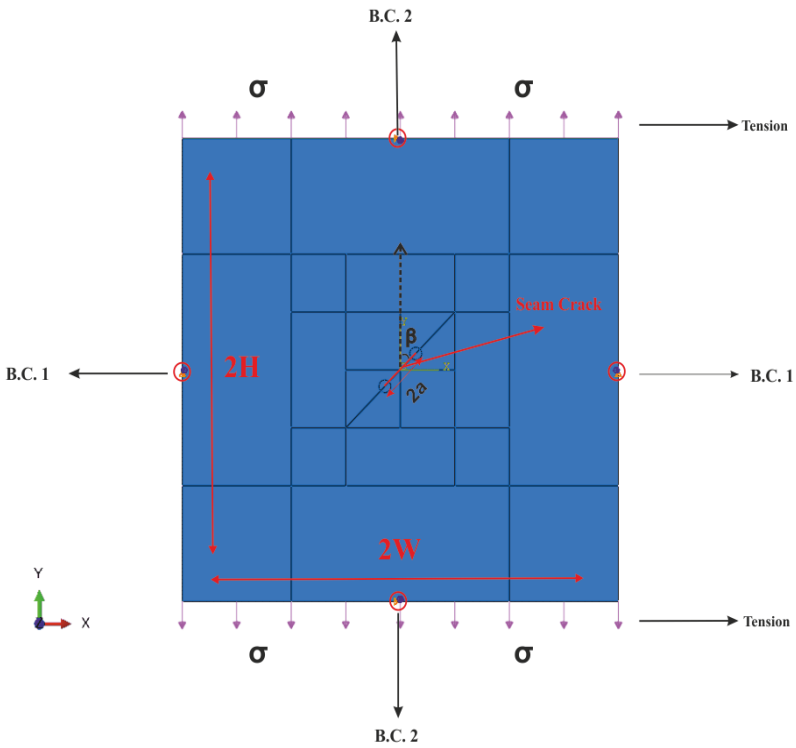

Figure 6.13 Dimensions and boundary conditions of inclined crack in tension model

In order to verify the ABAQUS model with analytical solution, firstly seam crack type was introduced into the model in 2D plane strain environment(computed based on a sufficiently thick plate with a thickness much higher than in-plane dimension). As it was mentioned before, when the crack type is sharp, seam type cracks are used in ABAQUS fracture analysis. In ABAQUS, seam crack type choice is available under the crack menu.

This verification problem was modeled as an isotropic elastic material with 2D CPE8 (Continuum Plane Strain Eight Node) elements. Seam crack, plate dimensions and applied load were shown in Figure 6.13 and the magnitudes of applied tension loading condition and the properties of the isotropic elastic material were given in Table 6.3.

Explanations of the boundary conditions are:

B.C. 1: The model is fixed at *u2 (*y-direction) and *ur3* (rotation of z direction).

B.C. 2: The model is fixed at *u1* (x-direction) and *ur3* (rotation of z direction)

Selection of crack extension directions for each crack and the crack fronts are shown in Figure 6.14.

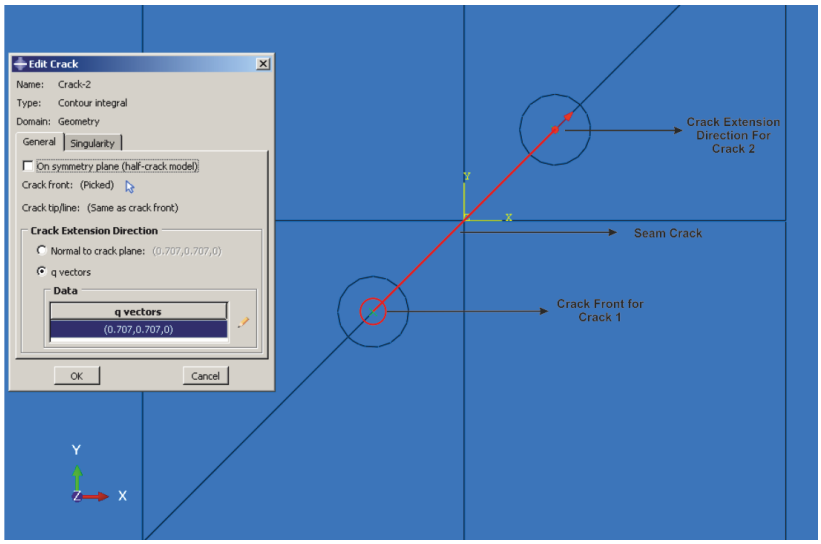

Figure 6.14 Schematic views of crack extension directions for each crack and the crack fronts

In terms of decreasing the finite element calculation errors, fine meshing should be applied to the whole model and contour integral region (7 Contours). After meshing the model by using proper mesh controls and seed, fine meshing (17488 Second Order Quadrilateral Plane Strain Elements, CPE8) around the seam crack and whole model are shown in Figure 6.16.

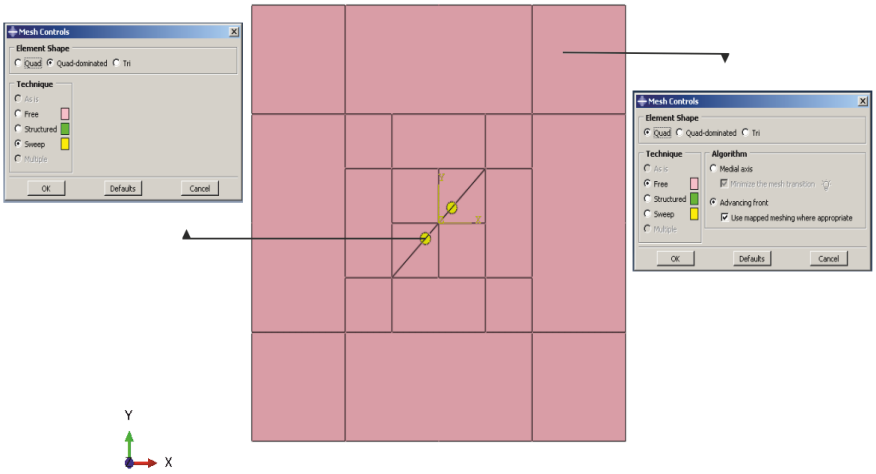

Figure 6.15 Schematic view of mesh controls for inclined crack in tension model

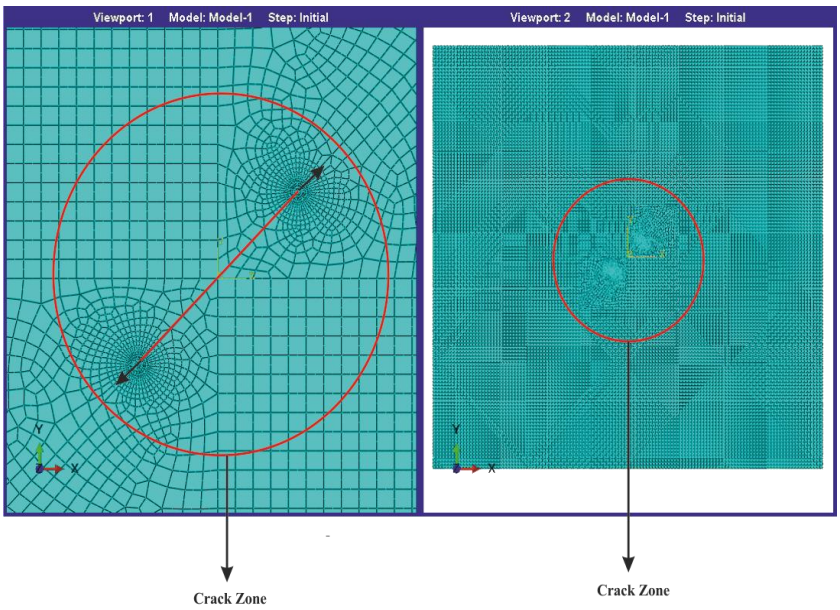

Figure 6.16 Schematic views of the seam crack and the whole model after meshing

After analyzing the model with ABAQUS, average stress intensity factors K_I and K_{II} that are computed for both ends of the seam crack on the left and right tips and the Crack Propagation Direction (CPD) were found as:

K_I = 3,197,350 Pa $\sqrt{m}$ K_{II} = 3,188,150 Pa $\sqrt{m}$

Crack Propagation Direction = -53.1^o

Percentage difference was calculated from Equation 6.13.

$$Difference\ (\%) = \frac{K_{\ computed} - K_{analytical}}{K_{analytical}} x100 \tag{6.13}$$

Comparing these to the analytical solution, percentage differences were calculated as:

Difference of K_I =1.24%

Difference of K_{II} = 0.95%

In order to understand importance of mesh controls during contour integral analysis, another trial was made on again Inclined Crack in Tension Model. In this analysis, mesh controls depicted in Figure 6.15 were changed into Figure 6.17. As it is shown in Figure 6.17, concentric tubes was added into the contour integral region for each crack and the structured meshing techniques was preferred in contour integral region. Hex-dominated mesh technique inside of the concentric tube was kept constant likewise in previous analysis. Moreover, different from the previous analysis, fine meshing (14 contours) that is illustrated in Figure 6.18, was designed inside the contour integral region and for crack front definition concentric tubes were selected as a crack front. After meshing the model by using proper mesh controls and seed, 19736 Second Order Quadrilateral Plane Strain Elements (CPE8) were introduced to the model.

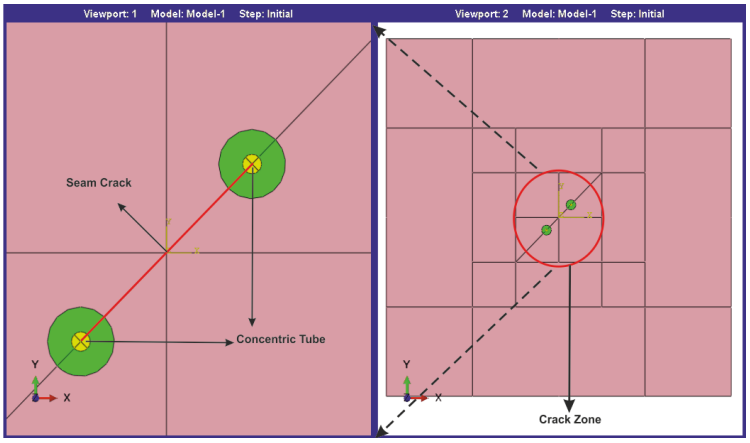

Figure 6.17 Schematic views of new mesh controls and concentric tubes for inclined crack in tension model

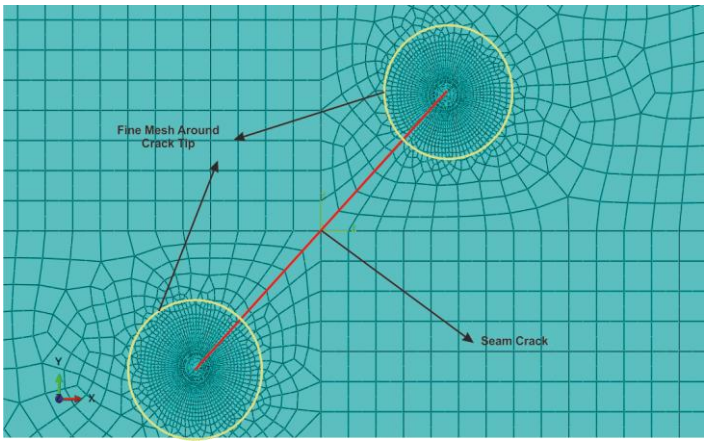

Figure 6.18 Schematic view of fine meshing inside the concentric tubes and contour integral region

After analyzing the model with ABAQUS, average stress intensity factors K_I and K_{II} that are computed for both ends of the seam crack on the left and right tips and the Crack Propagation direction (CPD) were found as:

$$K_I = 3{,}197{,}360 \text{ Pa}\sqrt{m} \qquad K_{II} = 3{,}188{,}150 \text{ Pa}\sqrt{m}$$

Crack Propagation Direction: -53.1 ^{o}

Percentage difference was calculated from Equation 6.18.

$$Difference\ (\%) = \frac{K_{\ computed} - K_{analytical}}{K_{analytical}} x100 \tag{6.14}$$

Again, comparing these to the analytical solution percentage differences were found as:

Difference of K_I = 1.24%

Difference of K_{II} = 0.95%

As a result, no significant difference was observed between two different mesh controls. Both analyses have same differences against analytical solution of the problem. These differences can be explained as; the problem frames are not infinite as in the case of analytical solution, that is why a 2% difference in the computations of K_I and K_{II} is acceptable for whole verification analyses.

On the other hand, in order to assess the prediction ability of various crack propagation criteria, different Crack Propagation Criterions were introduced to the model. As it can be seen from Table 6.4 that, Maximum Tangential Stress criteria has the closest CPD result to the analytical solution.

Table 6.4 Effect of different crack propagation criteria on CPD

Crack Propagation Criteria	Crack 1			Crack 2		
	K_I Pa $\sqrt{m}$	K_{II} Pa $\sqrt{m}$	CPD	K_I Pa $\sqrt{m}$	K_{II} Pa $\sqrt{m}$	CPD
MTS	3,197,360	3,188,150	-53.1 ^{o}	3,197,350	3,188,150	-53.1 ^{o}
MERR	3,197,360	3,188,150	-56.5 ^{o}	3,197,150	3,188,150	-56.5 ^{o}
K_{II} = 0	3,197,360	3,188,150	-56.9 ^{o}	3,197,350	3,188,150	-56.9^o

6.6 Inclined crack in tension with blunted notch

In terms of analyzing the effect of notch thickness on Stress Intensity Factors, K_I and K_{II}, Incline Crack in Tension Model was again developed with 1 mm blunted notch behalf of seam crack. This study aims to observe the effect of blunted notch on Mixed Mode condition. Model specifications, dimensions, and boundary conditions were kept same that are used in the above seam crack model. However, only the 1 mm thickness blunted notch were generated behalf of seam crack by using cut module. As it was mentioned before, notch roundness starting point distance was taken half of the notch thickness.

After meshing the model by using proper mesh controls and seed, 31614 Second Order Quadrilateral Plane Strain Elements (CPE8) were introduced to the model. Schematic view of blunted notch and the whole model before and after meshing are illustrated in Figure 6.19 and 6.20 respectively.

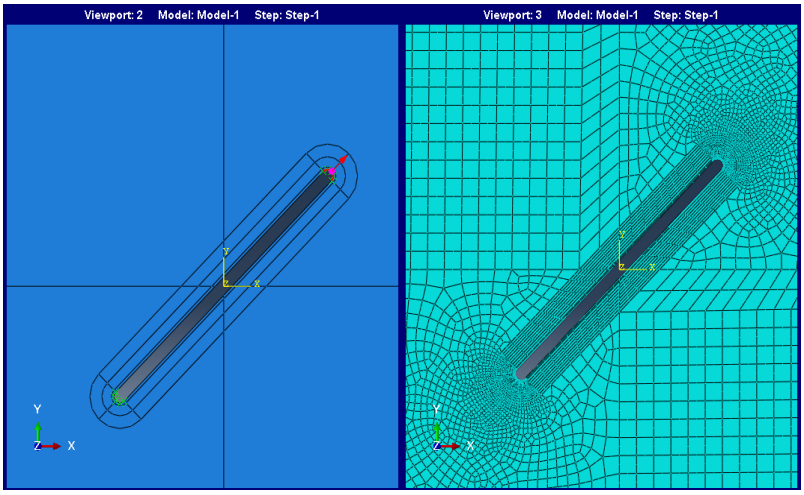

Figure 6.19 Schematic view of blunted notch before and after meshing

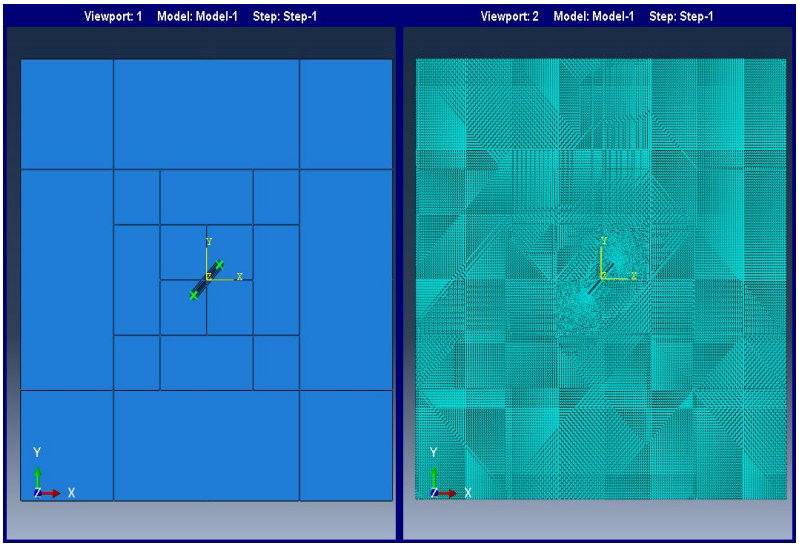

Figure 6.20 Schematic views of blunted crack and the whole model before and after meshing

After analyzing the model with ABAQUS, average stress intensity factors K_I and K_{II} that are computed for both ends of the seam crack on the left and right tips and the Crack Propagation direction (CPD) were found as:

K_I = 3,199,380 Pa $\sqrt{m}$ K_{II} = 3,207,190 Pa $\sqrt{m}$

Crack Propagation Direction: -53.2 ^{o}

Percentage difference was calculated from Equation.

$$Difference\ (\%) = \frac{K_{\ computed} - K_{analytical}}{K_{analytical}} x100 \tag{6.15}$$

Comparing these to the analytical solution percentage differences are found as:

Difference of K_I = 1.30%
Difference of K_{II} = 1.55%

As it was discussed earlier, because of the model were not solved as in an infinite medium, 2% difference between analytical solution and the analyses results are acceptable.

CHAPTER 7

MODELING WORK FOR VARIOUS CORE-BASED SPECIMEN GEOMETRIES

Basically, three specimen geometries namely SCB (Semi-Circular Specimen under Three- Point Bending), SNDB (Straight Notch Disc Bending) and CSTBD (Cracked Straight through Brazilian Disc) are modeled to compute the SIF's (Stress Intensity Factors) under opening and shear modes of loading modes of fracture mechanics. Among these core-based specimen geometries, SCB half-disc type specimens, and SNDB circular plate type specimens are loaded in three-point bending. CSTBD disc type specimens are subjected to Brazilian type compressive loading applied by the concentrated forces at the upper and lower boundaries.

Presented in the results of modeling work, Crack Propagation Direction (CPD) is computed based on the Maximum Tangential Stress Criterion as described in Chapter 5.

7.1 Stress intensity factor computation for SCB (semi-circular specimen under three-point bending) specimen

SCB (Semi-Circular Specimen under Three-Point Bending) specimen geometry, depicted in Figure 7.1, is modeled in 2D section with plane strain assumption. In order to simulate saw cut notch with a finite thickness and blunted tip as in real experimental conditions, blunted notches are inserted to the SCB half disc models. By changing the angle β^o of the preliminary notch from the vertical loading axis, pure mode I ($\beta=0°$) and pure mode II ($\beta=54°$) models are generated for determination SIF's K_I and K_{II}. To assure pure mode II loading state angle used as

$\beta=54°$ was originally found by Lim et al. (1993). Original solution for SIF's of pure mode I and pure mode II states were given in Lim et al. (1993).

In order to compare results of this work to the ones in the original source, specimen dimensions here are kept in compatible ranges close to the dimensions of specimens investigated by Lim et al. (1993). In Table 7.1, geometric differences between K_I and K_{II} models are highlighted. Common properties for both SIF computation models are: diameter D=100 mm, specimen thickness B=60 mm, notch thickness t_n=1 mm and the concentrated load P_y=-1N at the upper boundary. Material properties are also used as E=38.9 GPa (Young's modulus) and υ=0.11 (Poisson's ratio).

Table 7.1 Geometric details of 2D plane strain SCB models for K_I and K_{II} computations

MODEL	K_I Computation	K_{II} Computation
Notch length, a	20 mm	17.6 mm
Span Length, $2S$	60 mm	50 mm
Notch Angle from Vertical, β^o	0°	54°
a/R	0.40	0.35
S/R	0.60	0.50
B/D	0.60	0.60

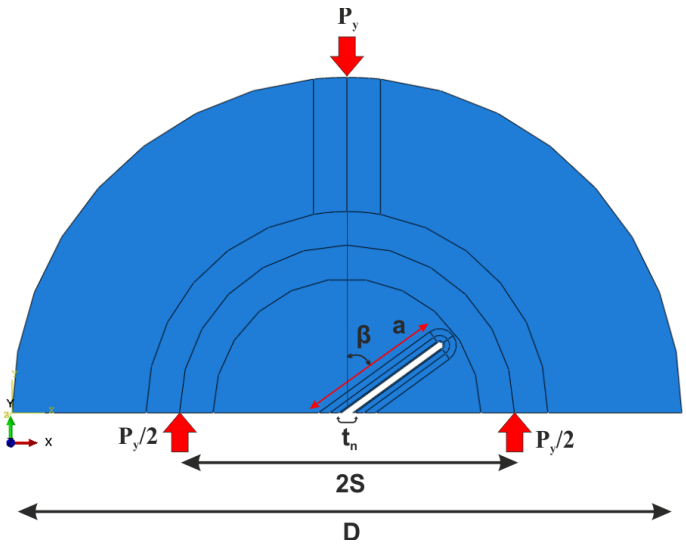

Figure 7.1 SCB specimen model frame under three-point bending load configuration

D: Diameter

a: Crack Length

2S: Span Length

t_n: Notch Thickness

***β*:** Crack angle from vertical

Because of its simplicity, all SCB models are generated in 2D Plane Strain sections with special elements coded as CPE8 (Continuum Plane Strain Eight Node) which are second order quadrilateral elements. In order to increase the computation accuracy approximately 2800 of such plane strain elements in SCB model frame geometries are used. Numbers of contours in the contour integral region around the crack front is set equal to 13 consistently for all SCB models.

Following the computations with the presumed pure K_I and pure K_{II} model conditions, SIF results represented by K_I and K_{II} and Crack Propagation Direction (CPD) for both cases are summarized below.

Pure K_I Model:

K_I = 158.64 Pa $\sqrt{m}$ K_{II} = -0.0020 Pa $\sqrt{m}$

Crack Propagation Direction = 0°

Pure K_{II} Model:

K_I = 1.41 Pa $\sqrt{m}$ K_{II} = -26.78 Pa $\sqrt{m}$

Crack Propagation Direction = 69.52^o

For this specimen geometry boundary conditions (B.C. 1 and B.C. 2) that are shown in Figure 7.2 are applied to achieve pure mode I and pure mode II fracture mechanics loading conditions. B.C. 1 and B.C. 2 coded boundary conditions are defined below as:

B.C.1: Load application points were fixed in u_2 direction.
B.C.2: Load application point was fixed in u_1 direction.

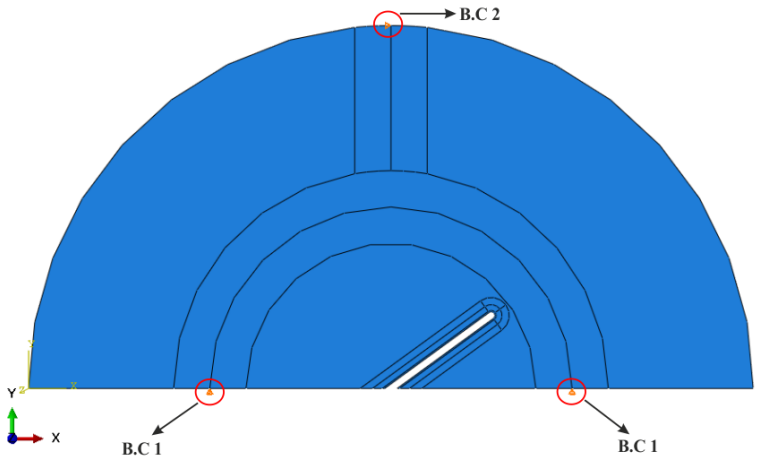

Figure 7.2 Boundary conditions for SCB specimen

7.2 Stress intensity factor computation for SNDB (straight notch disc bending method) specimen

Modeling of straight-notched disc specimen geometry that is used for K_{IIc} testing under three-point bending load is conducted in 3D. Blunted notch used in 3D modeling is assigned to the bottom boundary region between the two load concentrated load application points. Basic model geometry for SNDB specimen is illustrated in Figure 7.3.

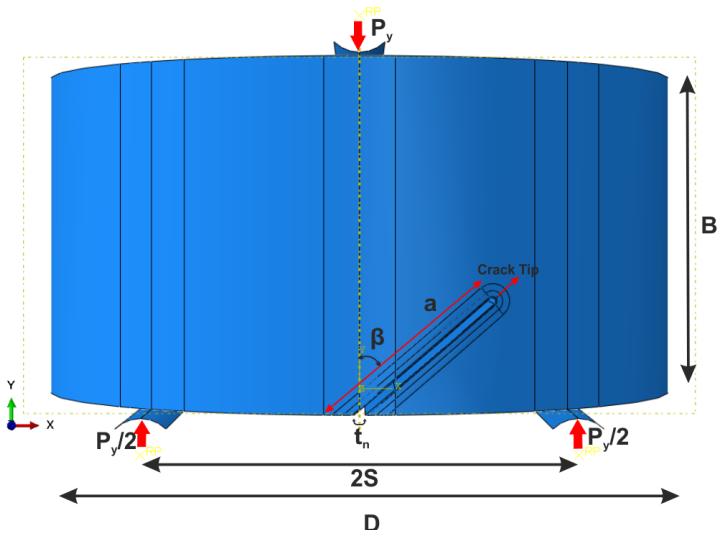

Figure 7.3 Geometry of SNDB specimens under three-point bending load

a: Crack Length

t_n: Notch Thickness

B: Specimen Thickness

D: Diameter

2S: Span Distance

***β*:** Crack Angle from Vertical

R: Radius

Preliminary notches are machined by a circular diamond saw in preparation of disc specimens. The use of a saw type-cutting tool is necessary to insert notches to the core specimen geometries. With the use of a saw, initial notch is naturally expected to have a blunted notch tip and finite thickness.

A blunted notch of a finite thickness of 1 mm is assigned to the 3D models of SNDB specimen geometry models. Blunted notch modeling technique has some specifications and related geometrical selections that have to be implemented in assigning the crack front and crack extension direction as shown in Figure 7.4. Crack front is selected as a curved surface that is inside the blunted notch tip. On the other hand, crack extension direction (*q*-vector) should be selected and marked at the mid central section of the model; not at the outer curved boundary. To reach an accurate result with the expected correct sign for the average K_{II}, special partitions added in the neighborhood of the notch play an important role as shown in Figure 7.4.

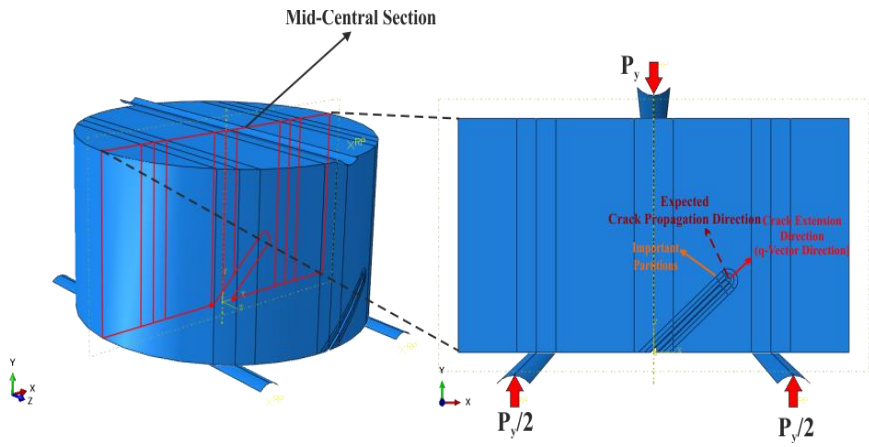

Figure 7.4 Mid-Central Section for the selection of crack extension direction and expected crack propagation direction

Eight node linear brick type finite elements are employed for meshing of SNDB models. In order to increase the computation accuracy, approximately 110,000 brick elements coded as C3D8R are introduced to the models. Number of contours in the contour integral region around the crack front is generally set as 13.

In modeling SNDB geometry, two different boundary conditions and loading scenarios have been tried. The aim is to figure out the effect of differences

regarding the different loading and boundary conditions on stress intensity factor computation.

First boundary condition case involves the application of a unit negative load (P_y = -1N) on the simulated rigid top roller unit. It is done so through a reference point above the upper boundary and the rigid top roller; this distributes the load along the upper rigid element, while bottom roller supports' displacements and their rotations are kept fixed in all directions. Initially at step zero, upper rigid concentrated load application roller is fixed against all degrees of freedom. In the following step called step one; upper rigid roller is set free in y–direction to allow the transfer of 1N unit load application to the specimen model. Rigid body motions and rotations are prevented by fixed roller supports. However, specimen model itself free to deform as desired under applied compression. At the roller-specimen contact a friction coefficient of 0.4 controls the relative movement of the deforming specimen. First boundary condition scenario and typical 3D mesh are illustrated in Figure 7.5.

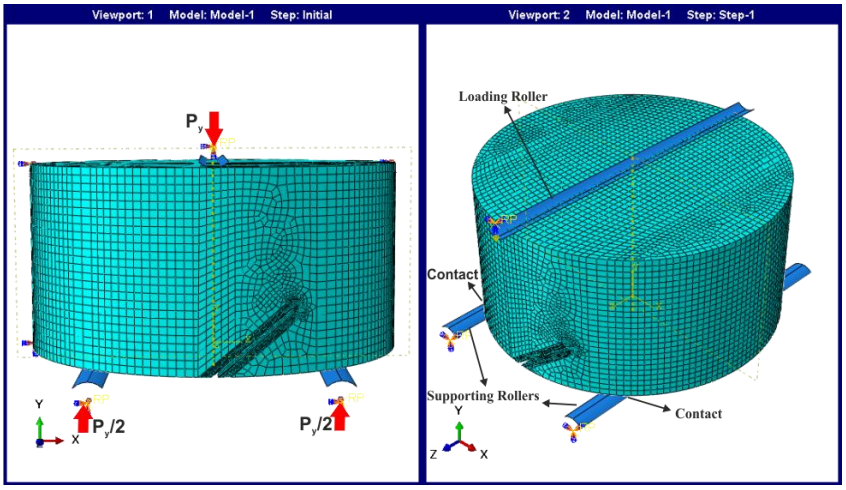

Figure 7.5 SNDB model mesh and rigid roller loading configuration through the reference point of the first boundary condition case

For the load transfer condition of case 1, dimensional entries, and material properties of the SNDB specimen model are given in Table 7.2:

Table 7.2 Dimensional entries and mechanical properties of the SNDB specimen model

Dimensions and Mechanical Properties	**Values**
Radius of the specimen, *R*	50 mm
Diameter of the specimen, *D*	100 mm
Thickness of the specimen, *B*	50 mm
Notch thickness, t_n	1 mm
Notch length, *a*	25 mm
Span Length, *2S*	60 mm
Crack angle from vertical, β^o	51 ^{o}
Load , P_y	-1 N
Young's modulus, *E*	200 MPa
Poisson's ratio, υ	0.3
a/R	0.5
S/R	0.6
B/D	0.5

After analyzing the SNDB model under the case 1 loading and boundary conditions, average stress intensity factors K_I, K_{II} and Crack Propagation Direction (CPD) were found as:

K_I = -0.40 Pa $\sqrt{m}$ $K_{II.}$ = -27.69 Pa $\sqrt{m}$

Crack Propagation Direction = 68.96^o

K_I is close to zero and it can be assumed that pure mode II condition for SNDB specimen is achieved around β=51° angle from vertical. To reach this result with the expected correct sign of average K_{II}, special partitions added in the neighborhood of the notch play an important role. Otherwise, correct negative sign may not be observed in the results for K_{II}. With these efforts in this SNDB analysis, resulting shear stress state represented by the symbol τ around the notch in the Figure 7.6 is expected to be in a negative sense related to the shear direction.

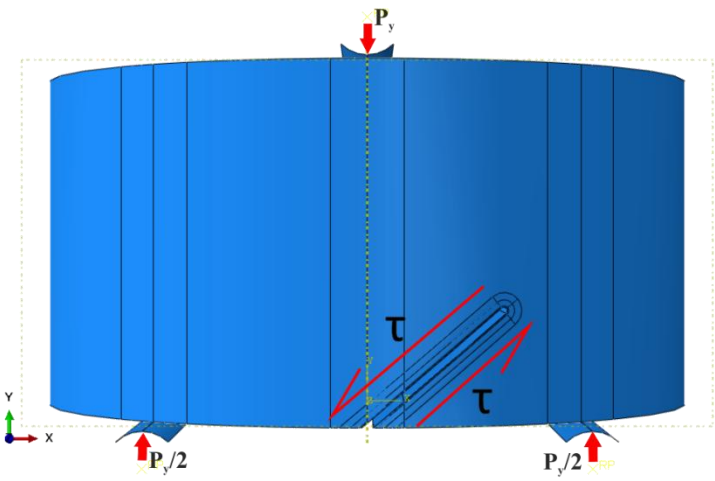

Figure 7.6 Schematic view of expected shear stress state over the preliminary notch of SNDB specimen mode

In second boundary condition and loading scenario, specimen geometry, and the material properties tabulated in Table 7.2 are used again. In this analysis, boundary conditions (Figure 7.8) are applied to the lines on the specimen outer faces and the loading is applied by using a reference point that is located at the center of the upper face of the specimen model. In loading application, reference point is constrained by using coupling tool under interaction module in ABAQUS. Because the loading is distributed along a line at the top and applied vertically to the specimen, coupling is generated only in u_2 direction (y-direction) as shown in Figure 7.7.

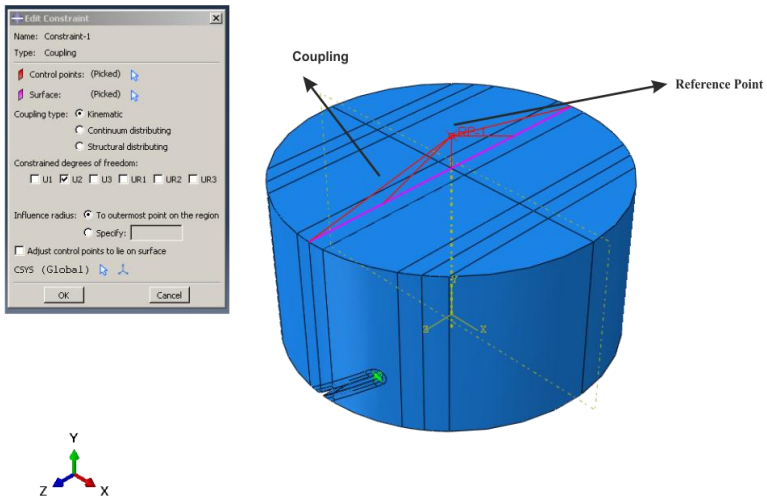

Figure 7.7 Load transfer to the SNDB model through the reference point and coupling to distribute the load vertically

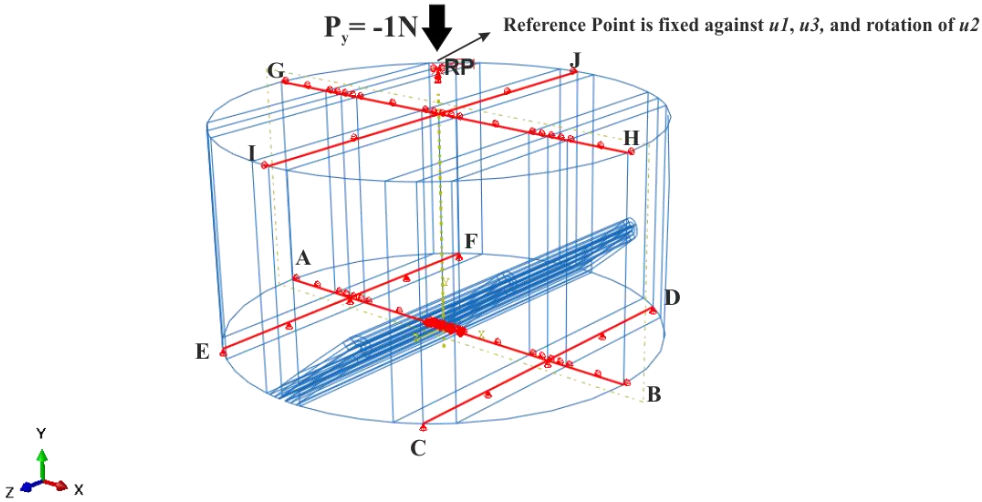

Figure 7.8 Second boundary condition scenario for SNDB geometry

In the second boundary condition scenario (case 2) conditions are listed as:

B.C.1: Along lines CD and EF, displacement component in y (u_2) is fixed.

B.C.2: Along lines AB and GH, displacement component in z (u_3) is fixed.

B.C.3: Along the line GH, displacement component in x (u_1) is fixed.

B.C.4: For point RP (reference point) displacement components along x (u_1), z (u_3) and rotation around y (ur_2) are fixed.

After running problem with case 2 boundary and loading conditions in ABAQUS, results show that new boundary conditions give approximately the same K_I and K_{II} results, as the ones in case 1 as, below:

$$K_I = 0.22 \text{ Pa}\sqrt{m} \qquad K_{II} = -27.86 \text{ Pa}\sqrt{m}$$

$$\text{Crack Propagation Direction} = 68.71^{o}$$

Because of its simplicity and easiness, the load application method of the second case is adopted for further SNDB modeling work.

In order to compare SIF computations of SNDB models to the ones in Karakaş, 2011, SNDB model geometries with 100 mm diameter, 25 mm initial notch length and 50 mm thickness with 1 mm blunted notches were constructed in 3D by using ABAQUS software. Different notches with angles β^{o}=20, 30, 40, 45, 50, 51, 55, 60 in degrees were inserted to various models at constant S/R=0.6 span ratio. Geometric parameters are the same as the ones in Karakaş, 2011 for comparison purposes. Material properties are also kept the same and used as E= 70 GPa (Young's modulus) and υ= 0.32 (Poisson's ratio).

Results in terms of stress intensity factors K_I, K_{II} and Crack Propagation Direction angles for various blunted notch orientations that are computed from the 3D SNDB modeling work are presented in Table 7.3.

Table 7.3 SNDB stress intensity factor results

$\beta°$	K_I Pa $\sqrt{m}$	K_{II} Pa $\sqrt{m}$	Crack Propagation Direction ^{o}
20	84.89	-36.00	36.64
30	53.94	-39.29	47.86
40	25.54	-35.94	57.82
45	13.14	-32.70	62.95
50	2.25	-28.75	67.69
51	0.22	-27.87	68.55
55	-7.21	-24.16	65.02
60	-15.06	-19.06	56.47

In terms of finding the differences between results obtained in Karakaş, 2011, normalized stress intensity factors found by Karakaş, 2011, and this study are tabulated in Table 7.4. During calculation of dimensionless stress intensity factors for each model below normalization equations were used likewise in Karakaş, 2011:

$$Y_{II} = \frac{K_{IIAbaqus}\,\pi DB}{P * \sqrt{\pi a}} \tag{7.1}$$

$$Y_{II} = \frac{K_{IAbaqus}\,\pi DB}{P * \sqrt{\pi a}} \tag{7.2}$$

Table 7.4 Comparison between dimensionless stress intensity factors

$\beta°$	Y_I	Y_{II}	Karakaş, 2011 Y_I	Karakaş, 2011 Y_{II}
20	4.76	-2.02	4.68	-1.86
30	3.02	-2.20	2.95	-2.04
40	1.43	-2.01	1.42	-1.85
45	0.74	-1.83	-	-
50	0.13	-1.61	0.13	-1.45
51	0.01	-1.56	-	-
55	-0.40	-1.35	-	-
60	-0.84	-1.07	-0.83	-0.89

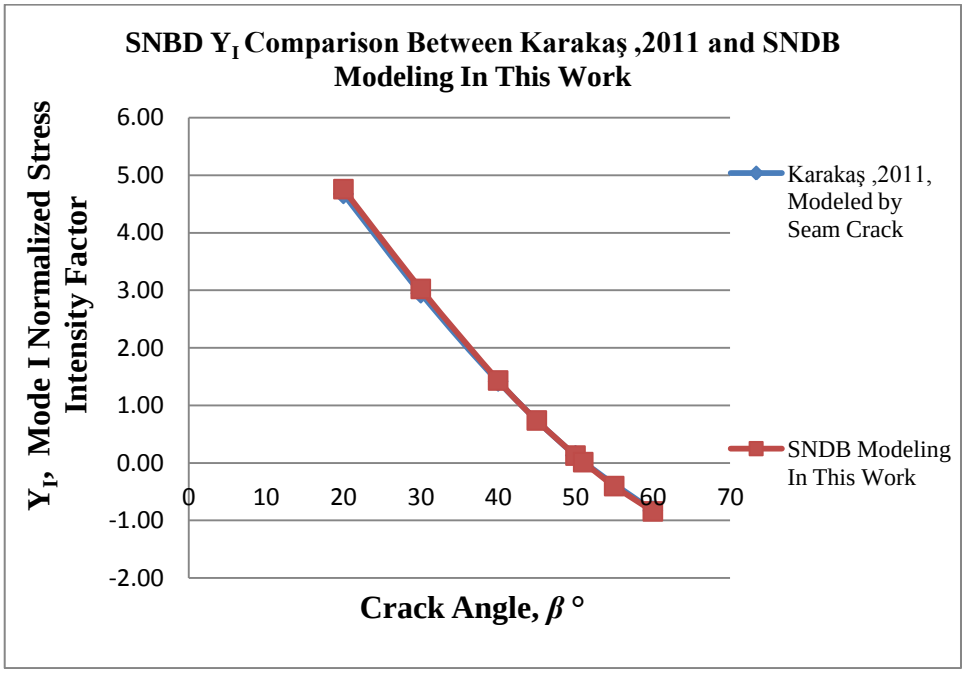

Figure 7.9 SNDB Y_I results compared to Karakaş, 2011

As it can be seen from Table 7.4 and the Figures 7.9 and 7.10, no significant difference was observed on Y_I results. However, approximately 10% difference was obtained on Y_{II} results. Difference on Y_{II} results can be explained by modeling technique such as mesh density, blunted notch type modeling and also accurate crack front and q vector definition in ABAQUS. Nevertheless, Pure K_{II} condition was achieved at 51° in both studies and this situation was depicted on Figure 7.9.

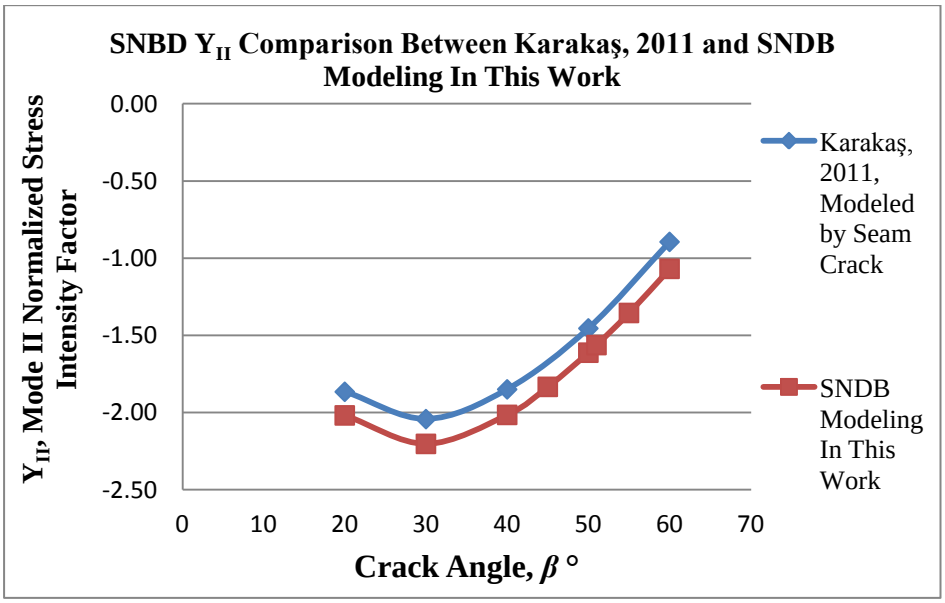

Figure 7.10 SNDB Y_{II} comparison of this work and Karakaş, 2011

7.3 Proposed 2D plane strain simplification of the 3D modeling work for SNDB geometry

In this section, because of the difficulties that are encountered in 3D SNDB modeling, a new 2D modeling procedure called as Modified SNDB 2D Modeling Technique is introduced. In this technique, modeling is carried out on a centrally cut 2D plane strain rectangular section through the 3D disc. Main aim of doing this simplification is to reduce the amount of time that is consumed during partitioning and SNDB model construction because of the curved boundaries

surrounding the circular-plate type geometry. This way, any errors related to the meshing complexity are minimized and different modeling alternatives with various changes in the parameters can be quickly and correctly manipulated in simple 2D models.

As it is seen in bird eye view of Figure 7.11, a square that is tangent to the outer circular boundary of the section of the disc is drawn. After extruding the square in u_2 (y-direction) direction, rectangular prism in Figure 7.12 is expected to represent equivalently the circular plate in a 3D model. However, the purpose here is a serious simplification by reducing the modeling and meshing procedure to a 2D form. So, a 2D rectangular section through the center of the prism is sectioned and modeled to represent the 3D SNDB circular plate type specimen geometry. Geometrical parameters that are used in this modeling technique are presented on the extracted mid-section of Figure 7.13.

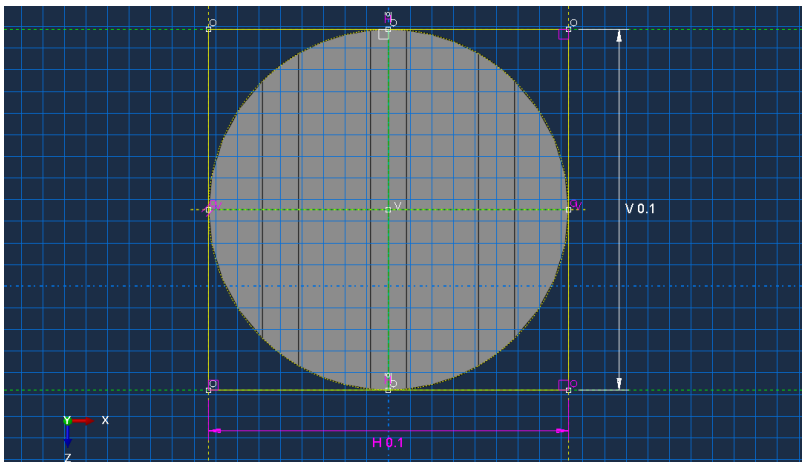

Figure 7.11 Creating modified 2D SNDB specimen model geometry

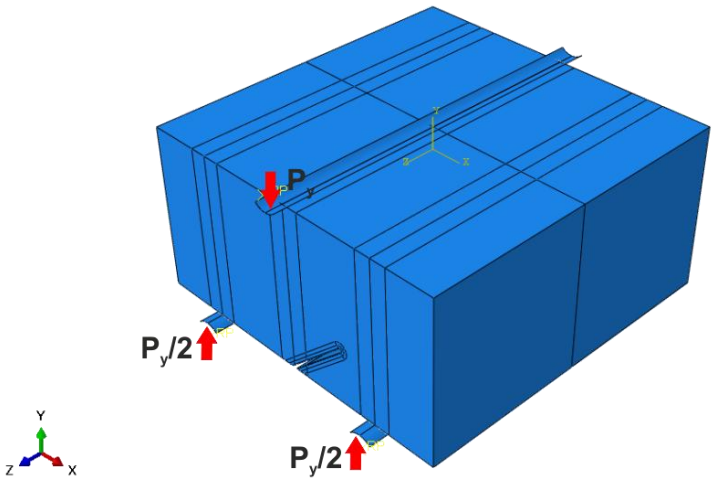

Figure 7.12 Representative prism of the modified SNDB model in 3D

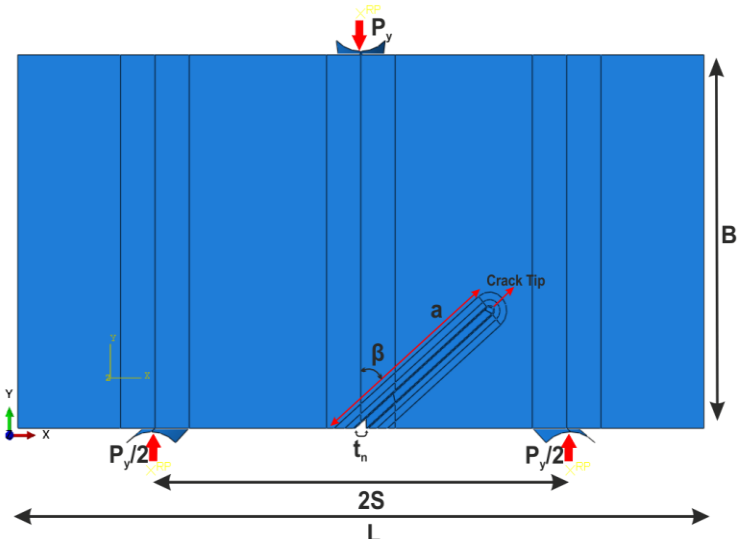

Figure 7.13 Plane strain mid-section and the geometric parameters of the 2D modified SNDB model

a: Notch Length

t_n: Notch Thickness

2S: Span Distance

W: Length/2

B: Specimen Thickness

L: Length

β: Notch Angle from Vertical

Stress intensity factor results that are computed by 2D Modified SNDB geometry, 3D rectangular prism SNDB, and 3D disc type SNDB models are compared. These are named as 2D SNDB Rectangular, 3D SNDB Prismatic, and 3D SNDB Disc models, and results are organized accordingly.

Material properties for both 2D and 3D modeling work for SNDB specimen geometry are kept the same and for linear elastic material they are Young's modulus E= 200 MPa and Poisson's ratio υ= 0.3. Young modulus is kept low here to better visualize the notch deformations and specimen model deformations in the interpretation of results. This way, any undesired asymmetric deformation and/or rotation and penetration of hard contact rollers to the specimen model can easily be detected, controlled and manipulated in the models, and precaution can be taken to apply necessary fixations to stop such movements.

As it was stated and proven before, when a low E value is used the load is applied through rigid rollers, value of E has no effect on the SIF results described as case 1 condition of loading before. Using a high value of E for the model material, on the other hand, can lead to model instabilities due to the frictional characteristics of the roller contacts. In such cases, rollers can slide apart from the load application point instead of penetrating and transferring the load correctly into the specimen model. For such models where a high E is going to be the input, case 2 boundary condition and loading without rollers are recommended.

In order to compare results of SIF computations between 3D disc type SNDB model, 3D rectangular prism SNDB and 2D Modified SNDB geometry, various 2D and 3D models were generated. In 3D rectangular prism SNDB and 2D Modified SNDB modeling geometries, models were constructed with 100 mm length (L), a=25 mm blunted notch with thickness t_n=1 mm , model thickness B=50 mm and for different crack angles (β=20, 30, 40, 48, 50, 60 in degrees) at constant S/W=0.6 span ratios. In addition, to make comparison between the SIF

results of seam crack and blunted notch in 2D, 2D Modified SNDB geometry with β=20°crack or notch angle was modeled with seam crack and blunted notch (Figure 7.14).

On the other hand, in 3D SNDB Disc modeling, models were constructed with D=100 mm diameter, a=25 mm initial blunted notch length of thickness t_n=1 mm, thickness B=50 mm for different crack angles (β=20, 30, 40, 50, 51 60 in degrees) at constant S/W=0.6 span ratios.

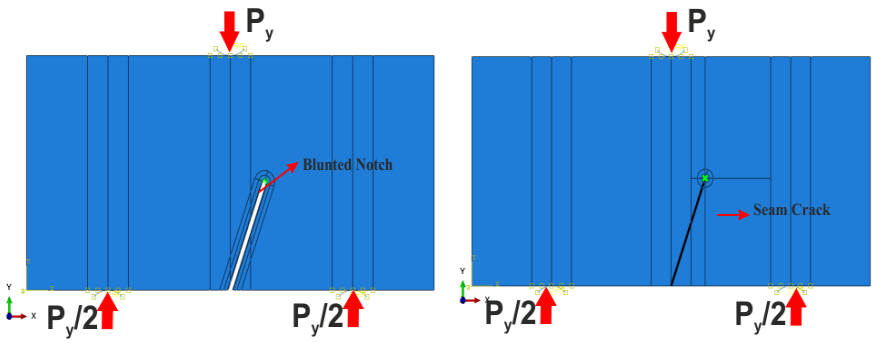

Figure 7.14 Section view of the 2D modified SNDB model with blunted and seam crack

Eight nodal linear brick type finite elements with reduced integration were employed for meshing of 3D SNDB and 3D Modified SNDB models. On the other hand, 2D Modified SNDB Models were constructed by using CPE8 (Second Order Quadrilateral Plane Strain Elements). In order to increase the computation accuracy approximately ≈120.000 brick elements (C3D8R) in 3D Modified SNDB models and ≈ 2500 plane strain elements in 2D models were used. Numbers of contours in the contour integral region around the crack front were set equal to 13 for all models.

Results of the analyses with the 3D SNDB Disc models, 3D Modified SNDB Prismatic Models and 2D Modified SNDB Rectangular Models are presented in terms of stress intensity factors K_I, K_{II}, and Crack Propagation Direction (CPD) for different notch angles are tabulated in Tables 7.5, 7.6, and 7.7, respectively.

Table 7.5 3D SNDB disc model SIF results

$\beta°$	K_I Pa $\sqrt{m}$	K_{II} Pa $\sqrt{m}$	Crack Propagation Direction ^{o}
20	83.08	-35.85	37.00
30	52.59	-39.13	48.23
40	24.56	-35.78	58.20
50	1.61	-28.59	68.14
51	-0.40	-27.69	68.96
60	-15.54	-19.10	56.06

Table 7.6 3D modified SNDB prismatic model SIF results

$\beta°$	K_I Pa $\sqrt{m}$	K_{II} Pa $\sqrt{m}$	Crack Propagation Direction ^{o}
20	78.84	-37.57	39.14
30	46.09	-40.55	51.04
40	17.72	-35.50	61.31
48	-0.07	-28.85	69.15
50	-3.80	-26.67	67.88
60	-18.16	-16.55	49.40

Table 7.7 2D modified SNDB rectangular model SIF results

$\beta°$	K_I Pa $\sqrt{m}$	K_{II} Pa $\sqrt{m}$	Crack Propagation Direction ^{o}
20	80.63	-37.11	38.42
20*	79.55	-36.43	38.31
30	47.52	-39,67	50.19
40	18.64	-35.58	60.91
48	0.54	-28.43	70.17
50	-3.29	-26,62	68.18
60	-18.03	-15.86	51.07

*= 2D Modified SNDB Model with seam crack

Using Equations 7.3 and 7.4 (Karakaş, 2011) normalized SIF results for 3D SNDB Disc model that are tabulated in Table 7.8, were calculated.

$$Y_{II} = \frac{K_{II\ ABAQUS}\pi DB}{Px\sqrt{\pi a}} \tag{7.3}$$

$$Y_I = \frac{K_{I\ ABAQUS}\pi DB}{Px\sqrt{\pi a}} \tag{7.4}$$

Table 7.8 Dimensionless stress intensity factors for 3D SNDB disc model

$\beta°$	Y_I	Y_{II}
20	4.66	-2.01
30	2.95	-2.19
40	1.38	-2.01
50	0.09	-1.60
51	-0.02	-1.55
60	-0.87	-1.07

Using Equations 7.5 and 7.6 normalized SIF results for 3D Modified SNDB Prismatic Model and 2D Modified SNDB Rectangular Model that are tabulated in Table 7.9 and Table 7.10 were calculated.

$$Y_{II} = \frac{K_{II\ ABAQUS}\pi LB}{Px\sqrt{\pi a}} \tag{7.5}$$

$$Y_{I} = \frac{K_{I\ ABAQUS}\pi LB}{Px\sqrt{\pi a}} \tag{7.6}$$

Table 7.9 Dimensionless stress intensity factors for 3D modified SNDB prismatic model

$\beta°$	Y_I	Y_{II}
20	4.42	-2.11
30	2.58	-2.27
40	0.99	-1.99
48	0.00	-1.62
50	-0.21	-1.49
60	-1.02	-0.93

Table 7.10 Dimensionless stress intensity factors for 2D modified SNDB rectangular model

$\beta°$	Y_I	Y_{II}
20	4.52	-2.08
20*	4.46	-2.04
30	2.66	-2.22
40	1.04	-1.99
48	0.03	-1.59
50	-0.18	-1.49
60	-1.01	-0.89

*= 2D Modified SNDB Rectangular Model with seam crack

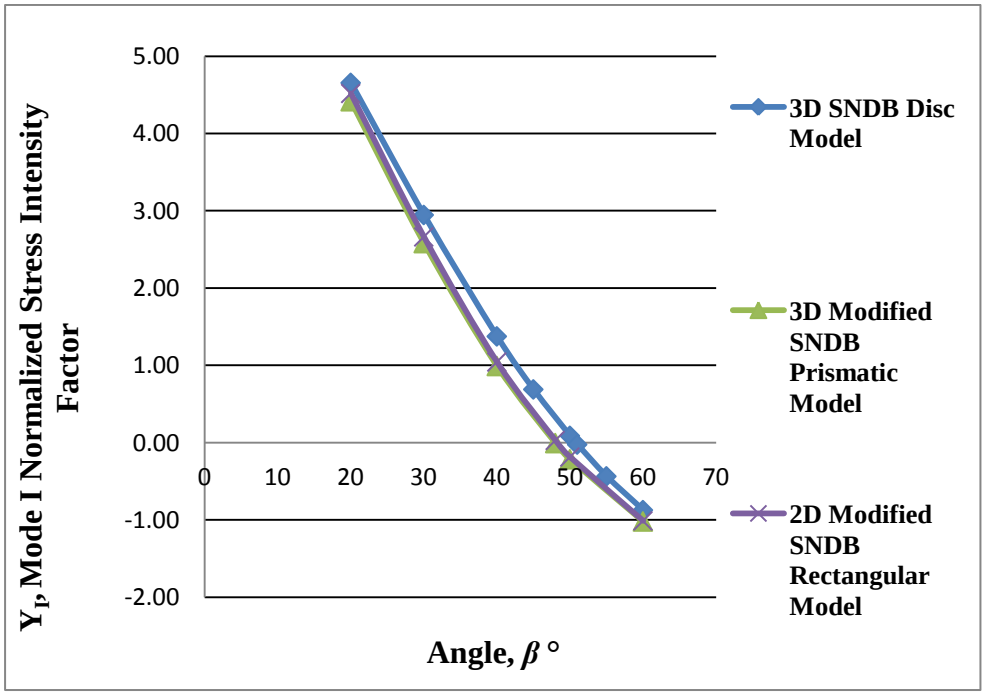

Figure 7.15 Graphical representations of Y_I results for different SNDB geometries

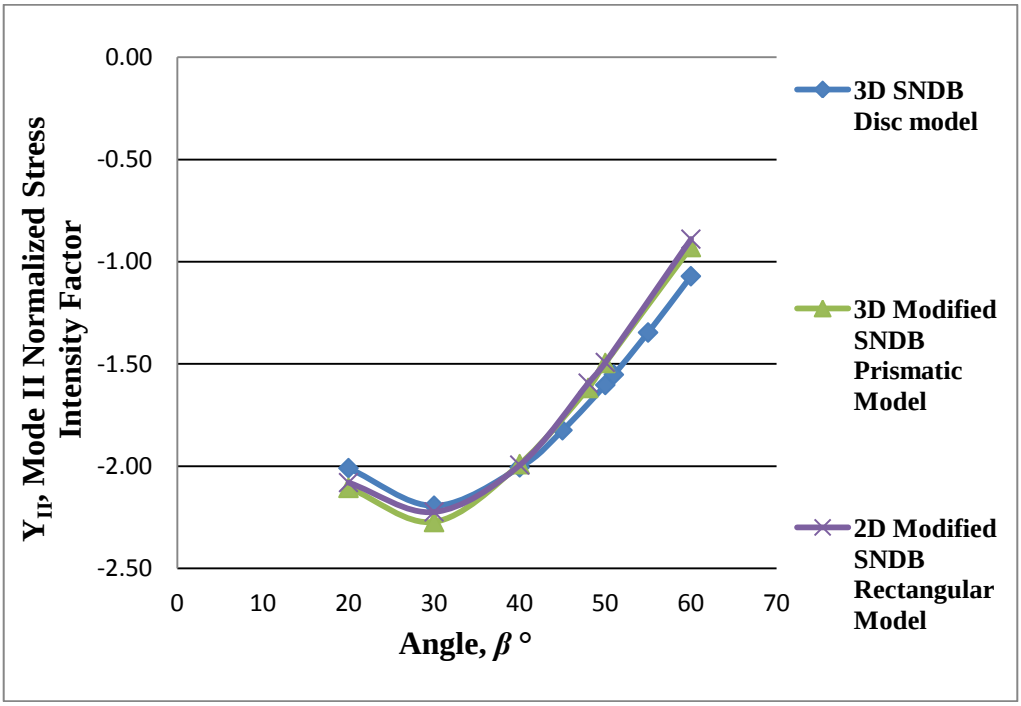

Figure 7.16 Graphical representations of Y_{II} results for different SNDB geometries

As it can be seen from Figure 7.15 and 7.16, 2D Modified SNDB Rectangular and 3D Modified SNDB Prismatic models reached pure mode II condition approximately at 48° crack angle from vertical. However, 3D SNDB Disc model reached this situation at 51°. In addition, Y_I and Y_{II} results that were obtained for Modified SNDB 2D and 3D models are compatible and showing the same trend. However, Y_I and Y_{II} results for 3D SNDB Disc model are slightly different from Modified SNDB models and in Figure 7.16, it is seen that Modified SNDB models were initially yielded higher Y_{II} values. However, after 40° crack angle from vertical Modified SNDB models changed their trends and reached the Y_{II} value at 60° that is lower than 3D SNDB Disc model.

7.4 Stress intensity factor calculations for CSTBD (cracked straight through Brazilian disc) specimen

CSTBD (Cracked Straight through Brazilian Disc) specimen geometry, depicted in Figure 7.17, is the third core-based specimen geometry that is investigated in the modeling work. In order to demonstrate real experimental conditions likewise in SCB and SNDB modeling, blunted notches are employed in CSTBD 2D and 3D modeling. Regarding the effect of model dimensions (2D or 3D) for K_I and K_{II} SIF computations, 2D and 3D CSTBD models were generated by using the dimensions and mechanical properties tabulated in Table 7.11.

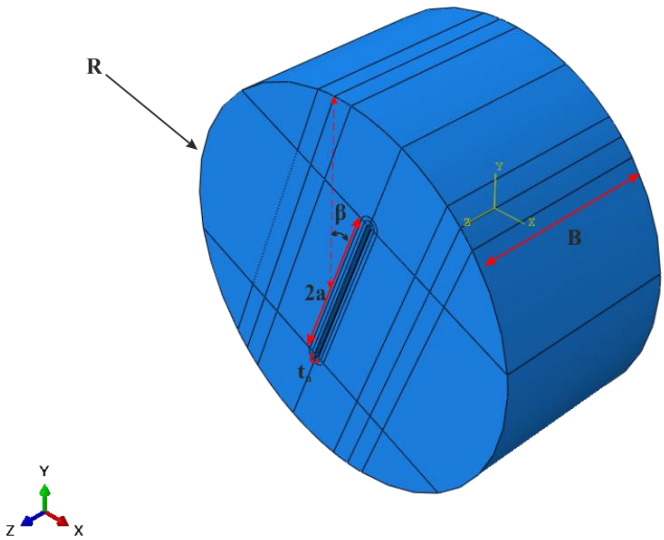

Figure 7.17 3D CSTBD model geometry

Table 7.11 Dimensional and mechanical properties of the 2D and 3D CSTBD models

Dimensions and Mechanical Properties	**Values**
Radius of the specimen, R	50 mm
Diameter of the specimen, D	100 mm
Thickness of the specimen, B	50 mm
Notch thickness, t_n	1 mm
Notch length, 2a	50 mm
Crack angle from vertical, β^o	23 ^{o}
Load, P_y	1 N
Young's modulus, E	200 MPa
Poisson's ratio, υ	0.3
a/R	0.5
B/D	0.5

For pure mode II condition, the required notch angle was calculated as 23° from the vertical loading axis, based on Fowell and Xu (1993) estimation. To adopt similar boundary conditions and the loading both in 2D and 3D models, analytical rigid shell units were attached to the upper and lower parts of the specimens. Upper shell was fixed in all directions from the reference point. Lower shell was initially fixed in all directions, then in Step 1 fixing in u_2 direction (y-direction) was set free and a unit load (P_y= 1N) was applied from its reference point as shown in Figure 7.18. In addition, interaction coefficient of friction between specimens and rigid shell load transfer units was set as 0.4.

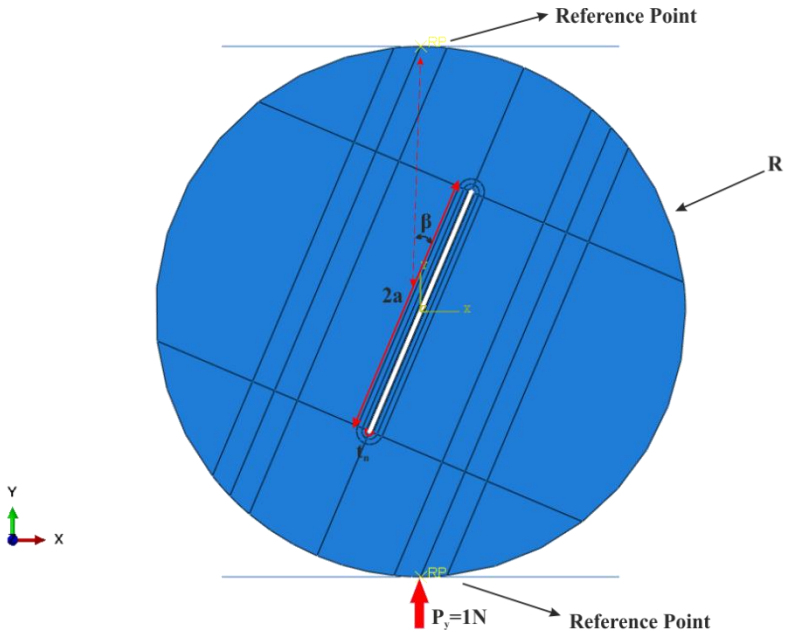

Figure 7.18 2D CSTBD model geometry

Eight nodal linear brick type finite elements with the choice of the reduced integration technique were employed for the mesh construction of 3D CSTBD models. 2D CSTBD model was developed by using CPE8 (Continuum Plane Strain Eight Node) elements. In order to increase the computation accuracy approximately ≈ 95000 brick elements (C3D8R) in 3D CSTBD models and ≈ 4000 plane strain elements in 2D CSTBD models were used. Number of contours in the contour integral region around the notch front was set equal to 13 for the models.

After running the 2D and 3D CSTBD models, K_I, K_{II} SIF results and Crack Propagation Directions (CPD) were found as:

2D Plane Strain Case

For Crack 1

K_I = 0.19 Pa $\sqrt{m}$ K_{II} = -78.46 Pa $\sqrt{m}$

Crack Propagation Direction = 70.48^o

For Crack 2

K_I = 0.18 Pa $\sqrt{m}$ K_{II} = -78.48 Pa $\sqrt{m}$

Crack Propagation Direction = 70.49^o

3D Case

For Crack 1

K_I = 0.82 Pa $\sqrt{m}$ K_{II} = -78.89 Pa $\sqrt{m}$

Crack Propagation Direction = 70.32^o

For Crack 2

K_I = 0.84 Pa $\sqrt{m}$ K_{II} = -78.79 Pa $\sqrt{m}$

Crack Propagation Direction: = 70.31^o

As it is seen from the results of both cases, no significant difference was observed in K_I and K_{II} SIF results. Hence, in order to reduce the computation time and modeling construction efforts, entire CSTBD geometries throughout the thesis were modeled by using the CPE8 (Second Order Quadrilateral Plane Strain) elements in 2D.

Notches with different thicknesses were inserted to the Brazilian type core specimens by many researchers in their CSTBD type tests. Notch thickness analyses here were conducted by using different notch thicknesses varying as 1

mm, 1.5 mm, 2 mm, 2.5 mm and 3 mm. Model specifications other than the notch thickness were tabulated in 7.11.

In order to analyze the effect of notch thickness on K_I and K_{II} SIF results, mesh density and number of contours in the contour integral region were set equal for all cases. After the computations on the notch thickness models, K_I, K_{II} and Crack Propagation Directions for various model cases were found as:

Table 7.12 K_I, K_{II} and SIF results for the various notch thicknesses on the CSTBD specimen models

		t_n 1 mm	t_n 1.5 mm	t_n 2 mm	t_n 2.5 mm	t_n 3 mm
Crack 1	K_I Pa $\sqrt{m}$	0.19	0.48	0.78	1.07	1.39
	K_{II} Pa $\sqrt{m}$	-78.46	-79.44	-80.43	-81.47	-82.44
	Crack Propagation Direction ^{o}	70.48	70.41	70.34	70.28	70.20
Crack 2	K_I Pa $\sqrt{m}$	0.18	0.47	0.76	1.08	1.39
	K_{II} Pa $\sqrt{m}$	-78.48	-79.48	-80.47	-81.47	-82.44
	Crack Propagation Direction ^{o}	70.49	70.42	70.35	70.28	70.21

As given in Table 7.12, approximately 5% difference in the results of K_{II} SIF estimations was observed between the specimens with 1 mm notch thickness and 3 mm notch thickness. In order to simplify and generalize the results of notch thickness effect analyses, K_I and K_{II} SIF values for Crack 1 were normalized according to the formulas based on Fowell and Xu's proposals as:

$$\boldsymbol{Y_I} = \frac{\boldsymbol{K_I} \times \boldsymbol{B} \times \sqrt{\boldsymbol{R}}}{\boldsymbol{P}} \tag{7.7}$$

$$\boldsymbol{Y_{II}} = \frac{\boldsymbol{K_{II}} \times \boldsymbol{B} \times \sqrt{\boldsymbol{R}}}{\boldsymbol{P}} \tag{7.8}$$

Table 7.13 Dimensionless SIF values for the various notch thicknesses on the CSTBD specimen models

	t_n 1 mm	t_n 1.5 mm	t_n 2 mm	t_n 2.5 mm	t_n 3 mm
$\boldsymbol{Y_I}$	0.00	0.01	0.01	0.01	0.02
$\boldsymbol{Y_{II}}$	-0.88	-0.89	-0.90	-0.91	-0.92

Normalized Y_{II} SIF results in Table 7.13 versus t_n/a are plotted in Figure 7.19 for the various blunted notch thicknesses. Moreover, for the comparison purposes normalized Y_{II} SIF value of Fowell and Xu's (1993)' work is added to the graph.

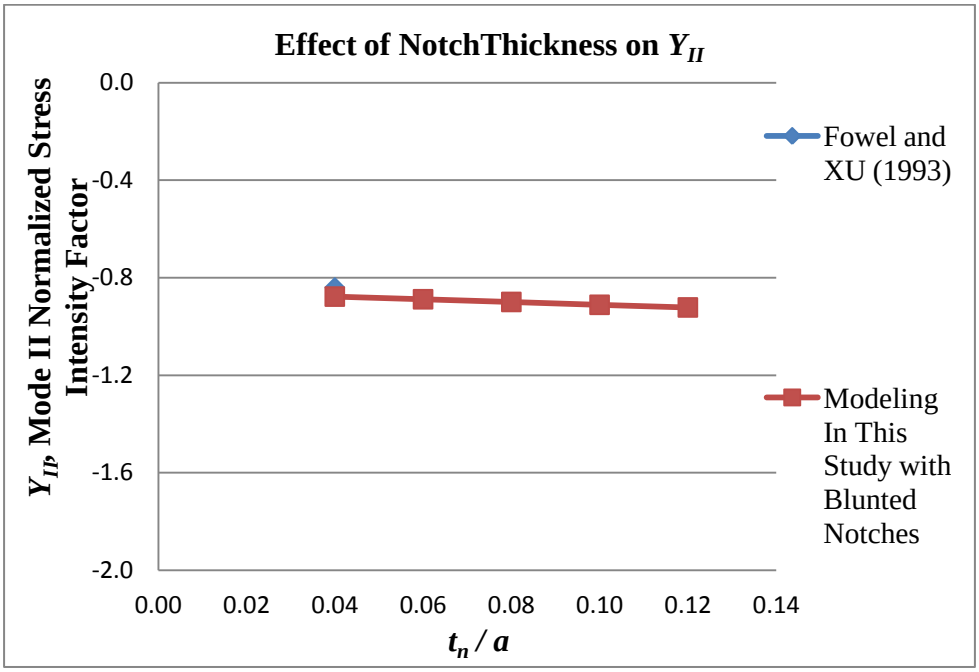

Figure 7.19 Normalized *SIF* Y_{II} results versus t_n/a

Around 4.5% difference in Y_{II} is observed between the specimens with1mm (t_n/a =0.04) notch thickness and 3 mm (t_n/a = 0.12) notch thickness.

7.5 Undeformed and deformed shapes of different core-based specimen geometries

In order to show the modeling accuracy and the effect of loading differences on the core-based specimen geometries, undeformed and deformed shapes of Brazilian disc type (CSTBD) specimen models, semi-circular disc (SCB) models, and the circular plate type (SNDB) specimen models are depicted in Figures 7.20, 7.21, 7.22. 7.23, 7.24 and 7.25. It can be seen from the figures that SCB and SNDB specimens are dominated by the tensile stress fields. On the other hand, compressive stress fields prevail in the CSTBD specimen models.

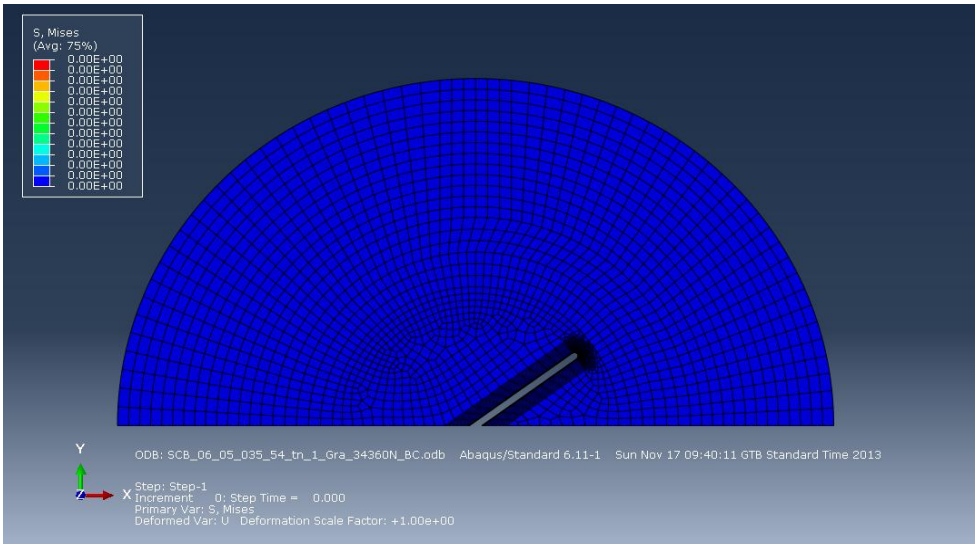

Figure 7.20 Undeformed shape of the SCB (semi-circular disc) specimen model

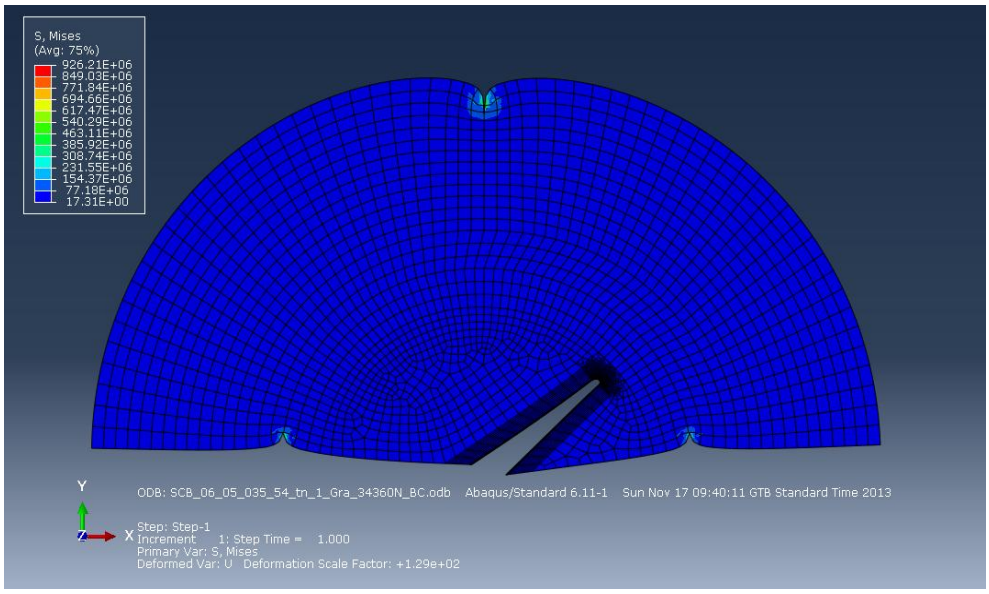

Figure 7.21 Deformed shape of the SCB (semi-circular disc) specimen model

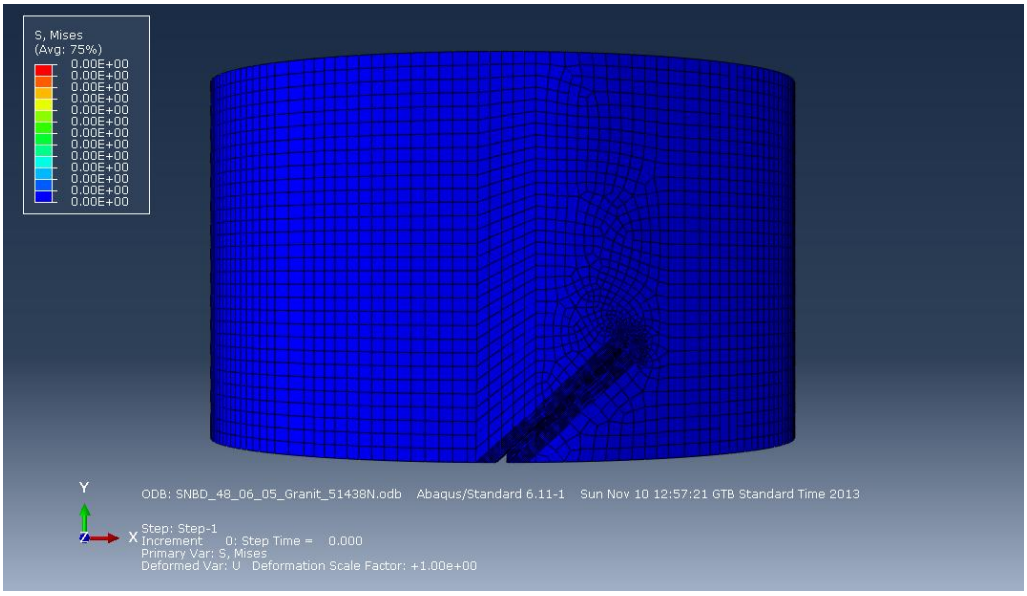

Figure 7.22 Undeformed shape of the SNDB (circular plate disc) specimen model

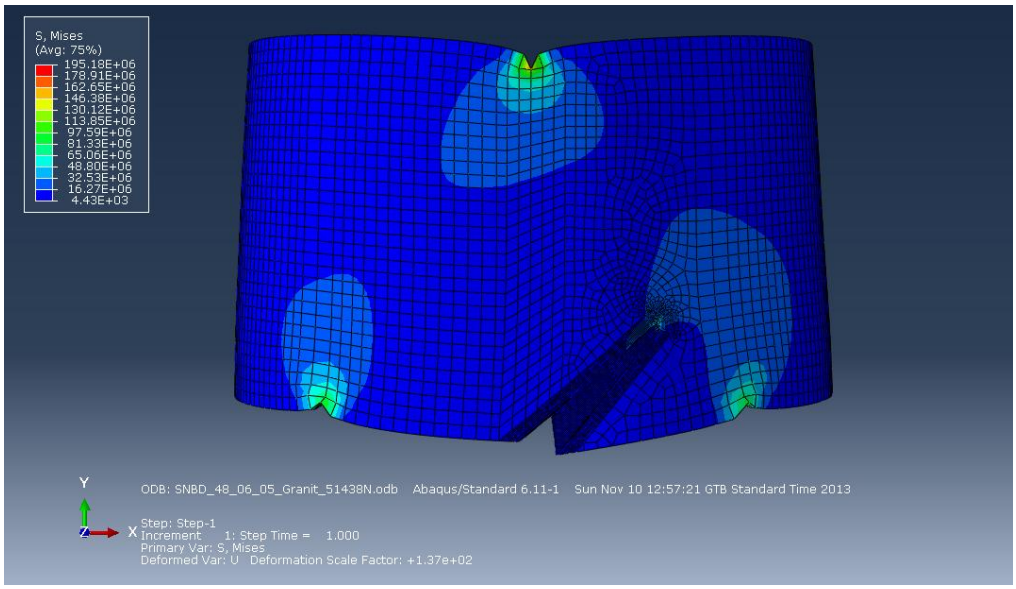

Figure 7.23 Deformed shape of the SNDB (circular plate disc) specimen model

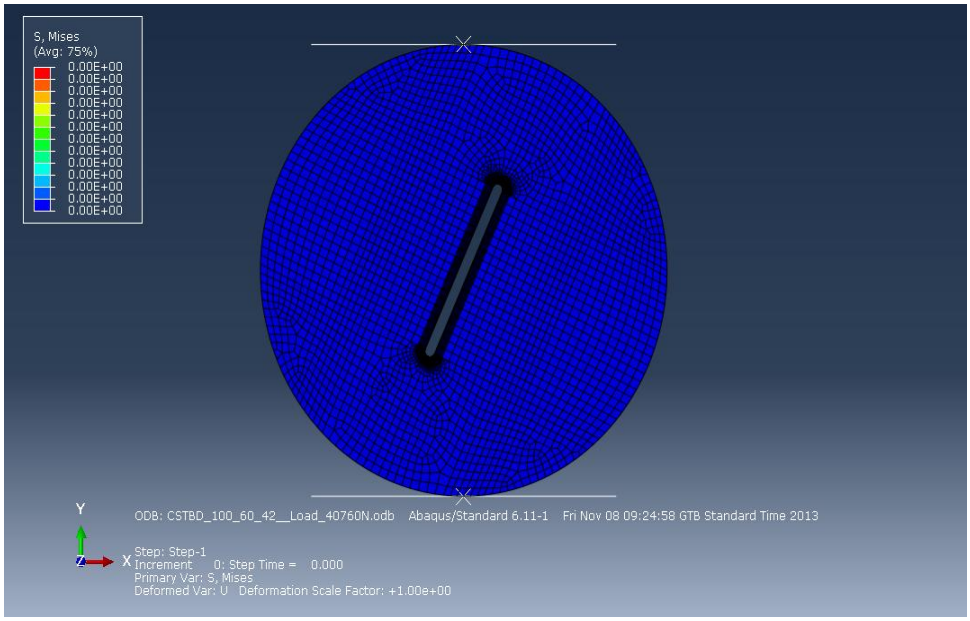

Figure 7.24 Undeformed shape of the CSTBD (Brazilian disc) specimen model

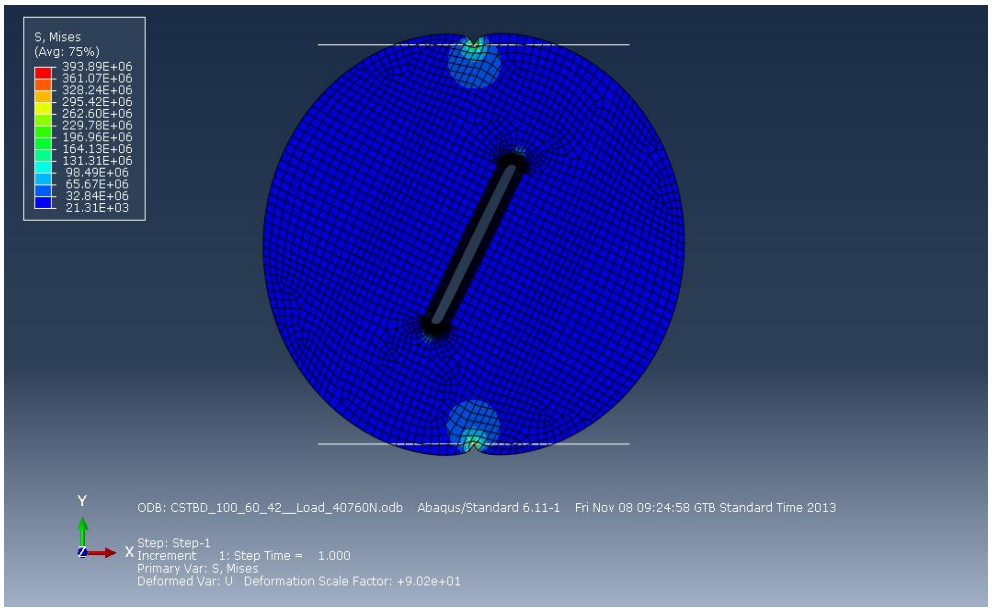

Figure 7.25 Deformed shape of the CSTBD (Brazilian disc) specimen model

CHAPTER 8

EXPERIMENTAL WORK & FRACTURE TOUGHNESS DETERMINATION

Fine grained gabbro blocks were used for the preparation of core specimens. This rock was imported from India by Aşan Granite Ltd. to use in decoration works. In order to minimize the effect of rock matrix heterogeneity on fracture toughness, this rock was preferred because of its relatively isotropic and homogeneous texture. All core specimens were prepared by machining the discs using high-pressure water jets at Aşan Granite Ltd. facilities in Temelli, Ankara. Semi-circular bending type specimens (SCB) were further halved by using rotary impregnated diamond saw and polished in Rock Mechanics Laboratory of Mining Eng. Dept. of Middle East Technical University.

In order to compare and assess which mode II core-based testing method best represents the stress state of originally defined pure mode II condition of the pure shear plate problem, three different specimen geometries are tried for mode II fracture toughness tests. Semi-Circular Disc specimens (SCB) and Circular plate (SNDB) specimens under three-point bending, and Brazilian Disc (CSTBD) specimens under concentrated compressive loads are used in this experimental work.

For presenting the mechanical and physical properties of the rock type selected, density, Brazilian indirect tensile strength, uniaxial compressive strength, and the deformability tests were conducted on the fine grained gabbro core specimens.

8.1 Rock properties

In order to determine the tensile strength of the gabbro, indirect tensile strength tests on six Brazilian Disc samples with B/D=0.5-1 were carried out according to ISRM (1978) suggested method. All Brazilian disc specimens were prepared with an approximate core diameter of 42 mm. Summary of the indirect tensile strength test data and results were tabulated below in Table 8.1.

Table 8.1 Results of indirect Brazilian type tensile strength tests

Name of the Specimen	**Diameter mm**	**Thickness mm**	**Weight gr**	**Density gr/cm^3**	**σ_t MPa**
Brazilian 1	41.81	23.77	100.04	3.07	15.98
Brazilian 2	41.82	23.95	100.45	3.05	15.55
Brazilian 3	41.80	23.58	98.29	3.04	10.23
Brazilian 4	41.83	22.83	94.92	3.03	10.67
Brazilian 5	41.80	24.11	101.1	3.06	8.75
Brazilian 6	41.83	23.76	98.22	3.01	9.01
Average ± STD	41.82 ± 0.01	23.67 ± 0.45	98.84 ± 2.24	3.04 ± 0.02	11.70 ± 3.23

Figure 8.1 Brazilian disc specimen in the indirect tensile strength test

Figure 8.2 Brazilian disc specimens after the tests

In order to determine the mechanical properties like Elastic Modulus, Poisson's Ratio, and the UCS (Uniaxial Compressive Strength) of the gabbro, a series of uniaxial compression tests were performed according to ISRM (1979) suggested

method. These tests were conducted on six samples of gabbro by using MTS 815 servo-controlled hydraulic testing machine in Mining Engineering Department of Middle East Technical University.

MTS 815 loading frame is equipped with an external 500 kN load cell with ±0.25 kN accuracy and two external displacement transducers (LVDT) of 1 cm travel capacity. Displacement transducers are used to measure the vertical displacement to be used in the vertical strain computations. A circumferential strain measurement apparatus with an extensometer is attached to the specimens to measure the circumferential deformation and lateral strain that is used in the determination of Poisson's Ratio.

Considering the high strength and competency of the rock type selected, and the loading capacity of the MTS 815 loading frame, relatively small diameter BX type core specimens were used in these tests. All UCS specimens were prepared with an approximate core diameter of 42 mm and their length/diameter ratios were set to $L/D \geq 2$.

Uniaxial compression and deformability test data, and the relevant results of the tests on the gabbro rock are given below in Table 8.2.

Table 8.2 Uniaxial compression and deformability test data and the results

Name of the Specimen	**Diameter mm**	**Length mm**	**Weight gr**	**Density gr/cm^3**	**σ_c MPa**	**E GPa**	**υ**
UCS-G1	41.81	96.67	409.30	3.08	254.95	40.99	0.13
UCS-G2	41.83	97.95	417.42	3.10	213.80	38.14	0.12
UCS-G3	41.81	94.78	401.71	3.09	242.48	41.10	0.12
UCS-G5	41.80	92.52	395.31	3.11	208.48	35.54	0.11
UCS-G6	41.81	94.88	401.50	3.08	216.23	38.73	0.10
Average ± STD	41.81 ± 0.01	95.36 ± 2.06	405.05 ± 8.51	3.09 ± 0.01	227.19 ± 20.33	38.90 ± 2.30	0.11 ± 0.01

Figure 8.3 Specimen under uniaxial compression equipped with circumferential extensometer

Stress-strain response shows quite a linear trend on macro-scale for the rock type selected in the testing program as seen in the Figure 8.4. Fine-grained homogeneous nature of this rock minimizes the effects of nonlinearity-related problems in the fracture toughness testing. It should be pointed out that effect of nonlinear nature of the internal structure on the notch tip stress state becomes increasingly noticeable around the sharp tips of the notches and the propagating cracks for the notched specimens. Based on this discussion, the choice of a fine grained gabbro rock type with a homogeneous nature and minimized nonlinearity is justified for the testing work.

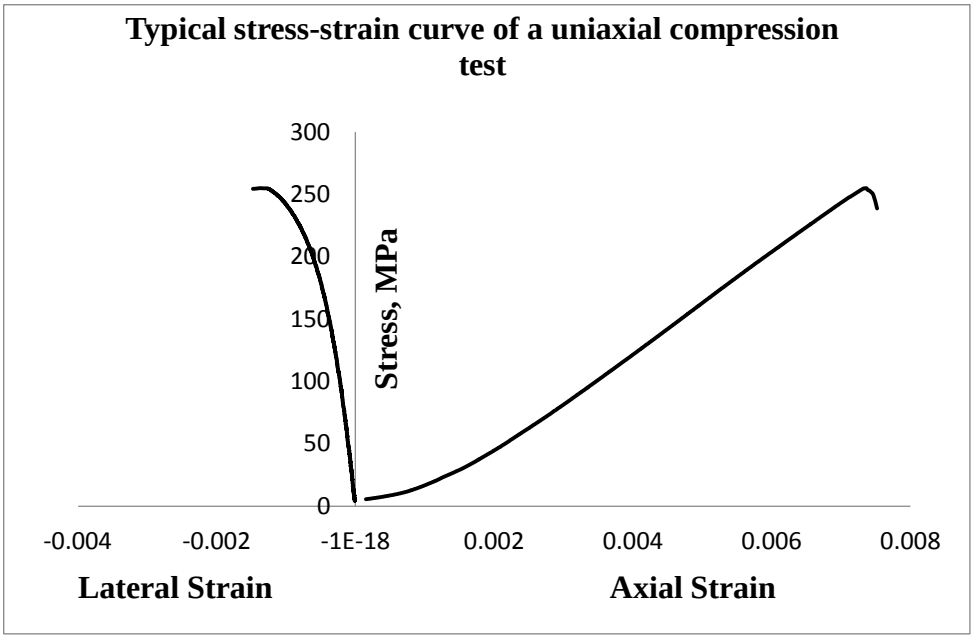

Figure 8.4 A typical stress-strain curve for a gabbro specimen under uniaxial compression

8.2 Fracture toughness testing

Although computational methods are very useful in fracture mechanics, they cannot replace experiments. Techniques such as finite element analysis and boundary integral elements rely on continuum theory. A continuum does not contain voids, micro cracks, second-phase particles, grain boundaries, dislocations, atoms, or any of the other microscopic or submicroscopic features that control fracture behavior in engineering materials. (Anderson, 1991) Therefore, in order to determine the real behavior of specimens under applied loads, experiments are necessary to interpret the results that are attained from simulation work.

Fracture toughness experiments were carried out on different core-based specimen geometries. To measure the displacement, two linear displacement transducers 10 mm capacity with ± 0.005 mm accuracy were used. For data acquisition, Testbox

1001 Data Acquisition System was used. This system has 16-bit resolution at 8 samples per second sampling rate per channel. Basic function of Testbox 1001 is analog to digital conversion of rather slowly changing signals (static/quasi-static) produced by various sensors, and then transfer of this digital data to the computer for further analysis.

8.2.1 Mode II fracture toughness determination with SCB specimen

In pure mode I and pure mode II SCB testing, initial vertical or angled notches were cut into center of half discs that have approximately 100 mm diameter and B=60 mm specimen thicknesses. Before the cutting application desired pure mode II loading angles (according to its *a/R* and *S/R* ratios) where K_I SIF is approximately zero were calculated by ABAQUS software. In ABAQUS modeling, loading angle β=54° that is given in Lim et al. (1994), was taken into consideration. After running the model that is designed with an angle from vertical β=54° for *S/R*=0.5 and *a/R*=0.352, pure mode II condition was believed to be achieved. In all ABAQUS models, material properties (E=38.9 GPa and υ=0.11) of gabbro were used.

In pure mode I SCB testing, vertical notches (β=0°) with a 20 mm initial notch length were machined into the center of half SCB discs. For all pure mode I specimen geometries, span ratios of *S/R*=0.6 was kept constant. 0.0016 mm/sec loading rate was applied in a displacement controlled way.

During specimen preparation all SCB discs were machined according to their cutting angle by circular diamond saw. Then, specimen geometries were recorded separately by using digital caliper. In order to separate the specimens in a convenient way, coding was generated according to the rule explained below in Figure 8.5. In order to increase statistical quality, two or three tests for gabbro rock were conducted under pure mode I and pure mode II loading conditions.

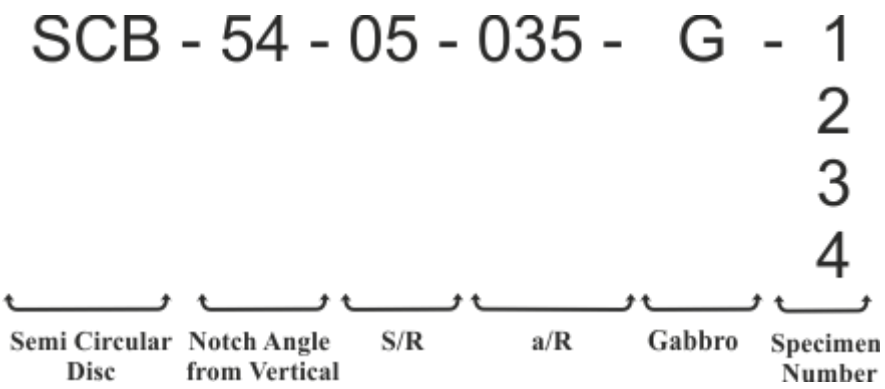

Figure 8.5 SCB specimen coding

Specimen dimensions used both in pure mode I and pure mode II tests with SCB method for gabbro are listed in Table 8.3.

Table 8.3 Dimensions of SCB gabbro specimens used for pure mode I and pure mode II fracture toughness tests

Specimen Code	Notch Thickness (t_n) (mm)	Notch Angle (β^o)	R (mm)	a (mm)	B (mm)	a/R
SCB-0-06-04-G-3	0.91	0	49.09	19.50	59.22	0.40
SCB-0-06-04-G-4	0.84	0	49.24	19.50	59.84	0.40
SCB-0-06-04-G-5	0.82	0	49.30	20.00	59.92	0.41
SCB-54-05-035-G-1	0.90	54	49.55	17.50	60.59	0.35
SCB-54-05-035-G-2	0.89	54	49.09	17.55	59.64	0.36

After recording the dimensions of all specimens, they were inserted and positioned in the loading frame with respect to the three-point bending load application rollers as it is shown in Figure 8.6.

Dimensionless Y_I and Y_{II} stress intensity factor values were obtained for 2D SCB specimen geometries by using ABAQUS software. Dimensionless Y_I and Y_{II} SIF values, failure loads and K_{Ic}, and K_{IIc} values of gabbro specimens according to their loading angles were found and tabulated in Table 8.4. In addition, during Y_I, Y_{II} SIF calculations, and fracture toughness (K_{Ic} and K_{IIc}) calculations of SCB specimens, Equations 8.1, 8.2, 8.3 and 8.4 were used respectively.

$$\boldsymbol{Y_I = \frac{K_I}{\frac{P}{2RB} \times \sqrt{\pi a}}} \tag{8.1}$$

$$\boldsymbol{Y_{II} = \frac{K_{II}}{\frac{P}{2RB} \times \sqrt{\pi a}}} \tag{8.2}$$

$$\boldsymbol{K_{Ic} = \frac{P \times \sqrt{\pi a}}{2RB} Y_I} \tag{8.3}$$

$$\boldsymbol{K_{IIc} = \frac{P \times \sqrt{\pi a}}{2RB} Y_{II}} \tag{8.4}$$

Figure 8.6 Configuration for pure mode I and pure mode II loading of SCB specimens

Table 8.4 Fracture toughness results for tests on SCB specimens

Specimen Code	Notch Angle (β^o)	Y_I	Y_{II}	P_{cr} (kN)	K_{Ic} MPa $\sqrt{m}$	K_{IIc} MPa $\sqrt{m}$
SCB-0-06-04-G-3	0	3.73	0.00	11.84	1.88	-
SCB-0-06-04-G-4	0	3.78	0.00	10.61	1.68	-
SCB-0-06-04-G-5	0	3.74	0.00	10.95	1.74	-
SCB-54-05-035-G-1	54	0.04	0.69	34.49	-	0.92
SCB-54-05-035-G-2	54	0.04	0.67	34.22	-	0.92

8.2.2 Mode II fracture toughness determination with SNDB specimen

In SNDB testing (Alkılıçgil, 2006), three-point bending load is applied to a circular plate type core disc specimens. Angular or vertical straight notches were machined at the center of the each specimen (Figure 8.7). As it was mentioned in previous chapters, in order to achieve pure mode II loading condition (K_I approximately zero) and determine the desired angle for this situation, numerical modeling with ABAQUS was conducted. In all models, material properties (E=38.9 GPa and υ=0.11) that are determined for fine grained gabbro were used.

Figure 8.7 Edge notch machining with angle setter and digital caliper

In experimental testing program with SNDB specimens, fine grained gabbro specimens that have 100 mm diameters (D) and 60 mm thicknesses (B) were used. Span distance which is $2S$=60 mm (S/R=0.60) was kept constant for all specimens. 0.0016 mm/sec loading rate was applied in a displacement controlled way.

According to ABAQUS modeling pure mode II condition was achieved β=48º notch angle from vertical for specimen that has 25 mm (a/R= 0.5) initial notch length.

In order to determine mode I fracture toughness property (K_{Ic}), pure mode I specimens that have vertical notches (β=0°) were prepared with a 20 mm (a/R= 0.4) initial notch length were machined into the center of SNDB discs.

During specimen preparation all SNDB discs were machined by circular diamond saw with notches according to their pre-determined angle from vertical. Then, specimen geometries were measured and recorded by using digital caliper. In order to separate the specimens in a convenient way, coding was generated according to the rule explained below in Figure 8.8. In order to increase statistical accuracy four or five tests for the gabbro rock were conducted for pure mode I and pure mode II loading conditions.

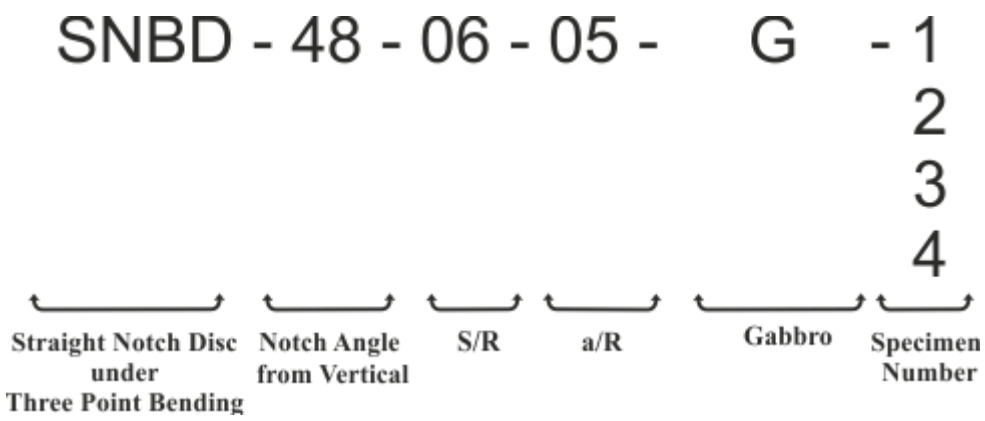

Figure 8.8 SNDB specimen coding

Specimen dimensions used both in pure mode I and pure mode II tests with SNDB method for gabbro are listed in Table 8.5.

Table 8.5 Dimensions of SNDB gabbro specimens used for pure mode I and pure mode II fracture toughness tests

Specimen Code	Notch Thickness (t_n) (mm)	Notch Angle (β^o)	R (mm)	a (mm)	B (mm)	a/R
SNDB-0-06-04-G-1	1.04	0	49.34	21.00	59.80	0.43
SNDB-0-06-04-G-2	1.00	0	49.29	21.17	60.06	0.43
SNDB-0-06-04-G-3	1.02	0	49.27	19.70	60.36	0.40
SNDB-0-06-04-G-4	0.99	0	49.18	20.00	58.81	0.41
SNDB-48-06-05-G-1	0.88	48	49.30	23.67	59.87	0.48
SNDB-48-06-05-G-2	0.88	48	49.47	25.33	60.68	0.51
SNDB-48-06-05-G-3	0.93	48	49.29	24.00	60.83	0.49
SNDB-48-06-05-G-4	0.85	48	49.32	24.33	60.70	0.49
SNDB-48-06-05-G-5	0.74	48	49.34	25.50	60.01	0.52

After recording the dimensions of all specimens,, specimens were placed in the loading frame with three-point bending load application rollers as it is shown Figure 8.9.

Figure 8.9 Position of SNDB core specimens under pure mode I and pure mode II loading

Dimensionless Y_I and Y_{II} SIF values of 3D SNDB specimen geometries were obtained using ABAQUS software. Pure shear condition for the SNDB geometry that are listed in Table 8.6 was achieved around 48° angle. Dimensionless Y_I, Y_{II}

SIF values, and K_{Ic} and K_{IIc} values of gabbro specimens according to their loading angles were found and tabulated in Table 8.7. In addition, during Y_I, Y_{II} SIF calculations and fracture toughness (K_{Ic} and K_{IIc}) calculations of SNDB specimens, Equations 8.5, 8.6, 8.7 and 8.8 were used respectively.

$$\boldsymbol{Y_I = \frac{K_I \times \pi \times D \times B}{P \times \sqrt{\pi a}}} \tag{8.5}$$

$$\boldsymbol{Y_{II} = \frac{K_{II} \times \pi \times D \times B}{P \times \sqrt{\pi a}}} \tag{8.6}$$

$$\boldsymbol{K_{Ic} = \frac{P}{\pi \times D \times B}\sqrt{\pi a} \times Y_I} \tag{8.7}$$

$$\boldsymbol{K_{IIc} = \frac{P}{\pi \times D \times B}\sqrt{\pi a} \times Y_{II}} \tag{8.8}$$

Table 8.7 Fracture toughness results for SNDB specimens

Specimen Code	Notch Angle (β^o)	Y_I	Y_{II}	P_{cr} (kN)	K_{Ic} MPa $\sqrt{m}$	K_{IIc} MPa $\sqrt{m}$
SNDB-0-06-04-G-1	0	4,03	0,00	34,48	1,93	-
SNDB-0-06-04-G-2	0	4,03	0,00	38,50	2,15	-
SNDB-0-06-04-G-3	0	4,20	0,00	40,28	2,25	-
SNDB-0-06-04-G-4	0	4,05	0,00	37,01	2,07	-
SNDB-48-06-05-G-1	48	0,03	1,56	45,45	-	1,04
SNDB-48-06-05-G-2	48	0,03	1,53	46,87	-	1,07
SNDB-48-06-05-G-3	48	0,03	1,57	49,18	-	1,12
SNDB-48-06-05-G-4	48	0,03	1,56	61,21	-	1,40
SNDB-48-06-05-G-5	48	0,03	1,50	54,49	-	1,25

8.2.3 Mode II fracture toughness determination with CSTBD specimen

In CSTBD testing program, core specimens of Fine Grained Gabbro with diameter *D*=100 mm and thickness *B*=60mm were prepared with five different notches machined internally with lengths between *2a*=32 mm to 72 mm. Internal notches were machined at the center of the discs by water jets available in the company with commercial title of Aşan Granite Ltd. Facilities, (Figure 8.10).

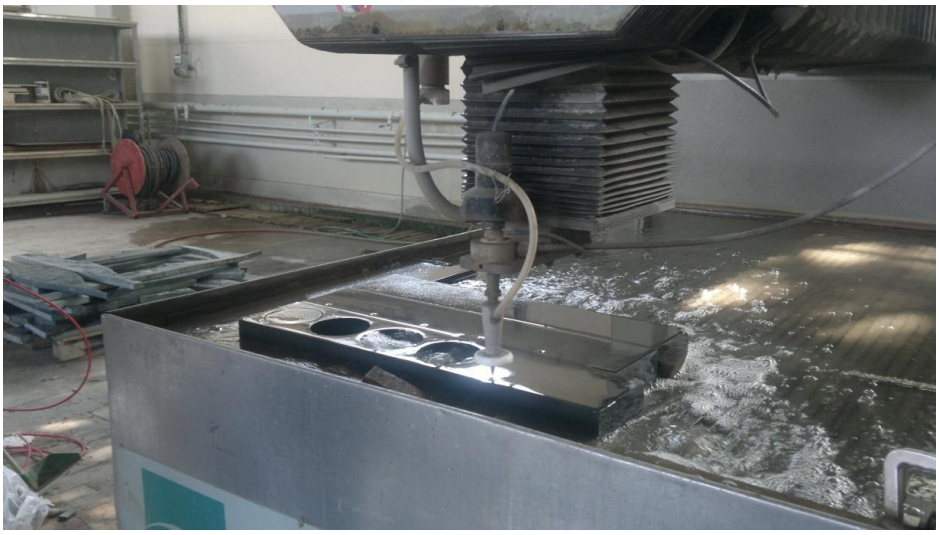

Figure 8.10 Preparation of CSTBD core specimens with high-pressure water jet

After shaping the discs, dimensions of the specimen geometries were measured sensitively and recorded by using digital caliper before the experiments. With respect to the loading axis of compressively applied concentrated load, internal notches were machined with certain angles, assuring pure mode II loading angle requirements based on the work of Fowell and Xu (1993).

In order to verify these loading angles expectedly producing pure mode II condition at the notch tip, specimen geometry for each notch length group was modeled and checked with ABAQUS software before the testing. Results

obtained from ABAQUS modeling work were observed to be in harmony with the suggestions of Fowell and Xu (1993).

Brazilian type compressive load application lines at the top and bottom boundaries of the CSTBD specimen were marked with respect to the pre-determined pure mode II angle of the preliminary internal notch. By using these precise markings, the specimen was positioned and aligned accurately in the loading frame, (Figure 8.11). The compressive loading was applied to the CSTBD disc in a displacement-controlled way with a rate of 0.0016 mm/sec.

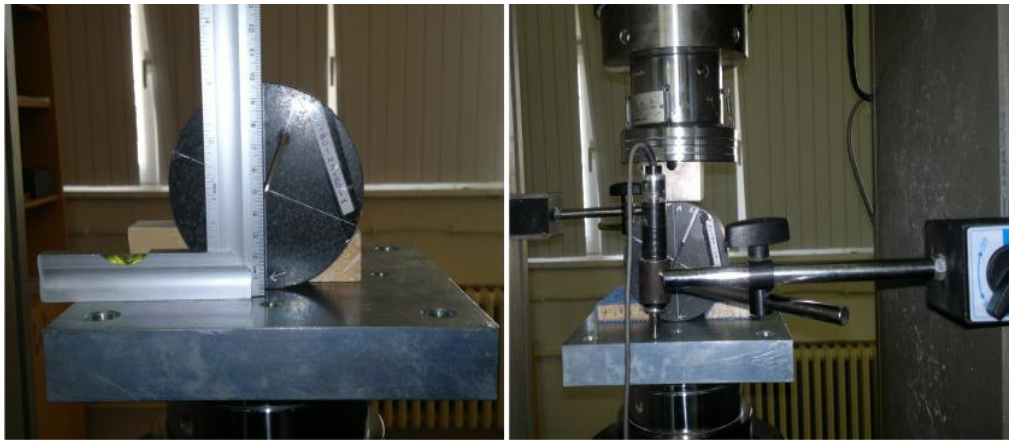

Figure 8.11 Positioning and alignment of the internally notched CSTBD disc with respect to the compressive load application axis

Before the test program, each specimen was coded as in Figure 8.12. Aim of the coding was to identify and distinguish the specimens with different notch length in a proper manner.

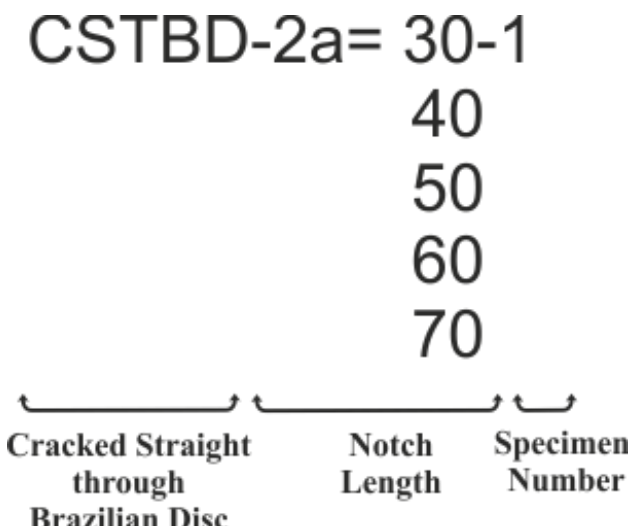

Figure 8.12 Coding for notched CSTBD specimen discs

In order to increase statistical quality of the results, preparation of six specimens was targeted initially for each notch length group. However, because of the practical difficulties related to the specimen surface preparation and machining an internal notch at desired thickness and position by high-pressure water jet application, some specimens had irregularities. These irregularities caused meaningless fracturing at inconvenient crack propagation angles in some tests. Crack propagation from a fracture mechanics point of view proceeded locally in meaningless directions and orientations with respect to the applied compressive loading ends. Results of such tests were dropped from the data processing work.

Dimensional details of all CSTBD specimens tested and resulted in meaningful way are tabulated in Table8.8, according to the coding procedure described above.

Table 8.8 CSTBD specimen dimensions

Specimen Code	Notch Thickness (t_n) (mm)	R (mm)	a (mm)	B (mm)	a/R	t_n/a
Specimens 2a=30-1	2,55	49,38	16,16	60,19	0,33	0,16
Specimens 2a=30-2	2,51	49,38	16,14	60,01	0,33	0,16
Specimens 2a=30-3	2,54	49,35	16,12	60,77	0,33	0,16
Specimens 2a=30-4	2,58	49,26	16,11	60,94	0,33	0,16
Specimens 2a=30-5	2,59	49,20	16,11	60,97	0,33	0,16
Specimens 2a=30-6	2,54	49,32	16,13	60,49	0,33	0,16
Specimens 2a=40-1	2,57	49,30	21,01	60,47	0,43	0,12
Specimens 2a=40-2	2,50	49,11	20,84	60,35	0,42	0,12
Specimens 2a=40-3	2,60	49,26	21,09	60,35	0,43	0,12
Specimens 2a=40-4	2,55	49,43	21,09	60,56	0,43	0,12
Specimens 2a=40-5	2,56	49,27	21,02	60,76	0,43	0,12
Specimens 2a=40-6	2,56	49,41	21,08	60,56	0,43	0,12
Specimens 2a=50-2	2,63	49,09	25,99	60,34	0,53	0,10
Specimens 2a=50-4	2,59	49,42	25,99	61,04	0,53	0,10
Specimens 2a=60-1	2,77	49,26	30,91	59,33	0,63	0,09
Specimens 2a=60-2	2,70	49,35	30,94	59,12	0,63	0,09
Specimens 2a=60-3	2,66	49,26	31,03	59,09	0,63	0,09
Specimens 2a=60-4	2,68	49,31	30,97	59,15	0,63	0,09
Specimens 2a=60-5	2,70	49,37	31,04	59,53	0,63	0,09
Specimens 2a=70-1	2,40	49,51	35,88	60,90	0,72	0,07
Specimens 2a=70-2	2,51	49,35	35,90	60,67	0,73	0,07
Specimens 2a=70-3	2,68	49,32	35,98	60,82	0,73	0,07
Specimens 2a=70-4	2,57	49,25	35,95	60,19	0,73	0,07
Specimens 2a=70-5	2,55	49,42	35,76	60,50	0,72	0,07
Specimens 2a=70-6	2,46	49,39	35,86	60,97	0,73	0,07

Representative 2D plane strain models were generated for particular notch length groups. All representative 2D models were designed with notch thickness t_n =2.5 mm and specimen thickness B=60 mm. 2D model dimensions and pure mode II loading angle proposed by Fowell and Xu (1993) are presented in Table 8.9.

Table 8.9 Representative CSTBD 2D model dimensions for each notch length group

2D Model Code	*a* (mm)	*2a* (mm)	*D* (mm)	Proposed angles for pure mode II condition (β^o)
Group 2a=30 mm	16	32	100	26,9
Group 2a=40 mm	21	42	100	24,9
Group 2a=50 mm	26	52	100	22,5
Group 2a=60 mm	31	62	100	19,6
Group 2a=70 mm	36	72	100	16,3

Example 2D plane strain models with preliminary notch lengths of 32 mm, 52 mm, and 72 mm group are illustrated in Figure 8.13. In all models, material properties are used as E=38.9 GPa and υ=0.11 from mechanical properties testing work on Fine Grained Gabbro. Initial notch angles (β) for 2D models are adopted from the work of Fowell and Xu (1993). Notches are inserted to the model geometries with the proposed angles in Table 8.9 to generate pure mode II condition.

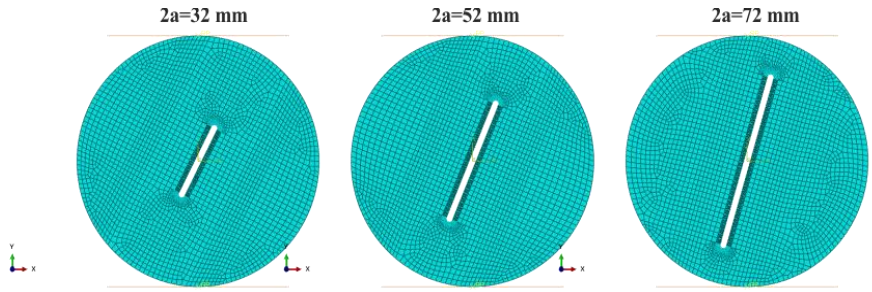

Figure 8.13 Example section views of 2D models for some notch length groups

After running the 2D Plane Strain representative models with ABAQUS, results by using the dimensionless forms of Equation 8.9 and 8.10 written below are presented in Table 8.10. Dimensionless mode I SIF denoted as Y_I and dimensionless mode II SIF as Y_{II} of modeling work results, and the Y_{II} results of pure mode II based on Fowel and Xu (1993) are listed in the table as well as crack propagation angles.

$$\boldsymbol{Y_I} = \frac{\boldsymbol{K_I} \times \boldsymbol{B} \times \sqrt{\boldsymbol{R}}}{\boldsymbol{P}} \tag{8.9}$$

$$\boldsymbol{Y_{II}} = \frac{\boldsymbol{K_{II}} \times \boldsymbol{B} \times \sqrt{\boldsymbol{R}}}{\boldsymbol{P}} \tag{8. 10}$$

Table 8.10 CSTBD 2D Model's Y_{II} results compared to the previous work

2D Model Code	Fowell and Xu pure mode II angle (β^o)	Fowell and Xu pure mode II dimensionless SIF Y_{II}	a/R	ABAQUS Y_I	ABAQUS Y_{II}	ABAQUS Crack Propagation Direction Angle ^{o}
Group 2a=30 mm	26.9	0.59	0.32	0.01	0.63	70.33
Group 2a=40 mm	24.9	0.72	0.42	0.01	0.78	70.30
Group 2a=50 mm	22.5	0.87	0.52	0.01	0.95	70.28
Group 2a=60 mm	19.6	1.05	0.62	0.02	1.17	70.16
Group 2a=70 mm	16.3	1.29	0.72	0.03	1.49	70.01

Graphical views of the results are illustrated in Figure 8.14. Y_{II} versus a/R results are plotted in dimensionless forms. Polynomial functions of fifth order provide good fits to the results of the previous work and modeling work here. Fitted functions are marked on the figure with compatible color-coding for the curves of the different cases considered.

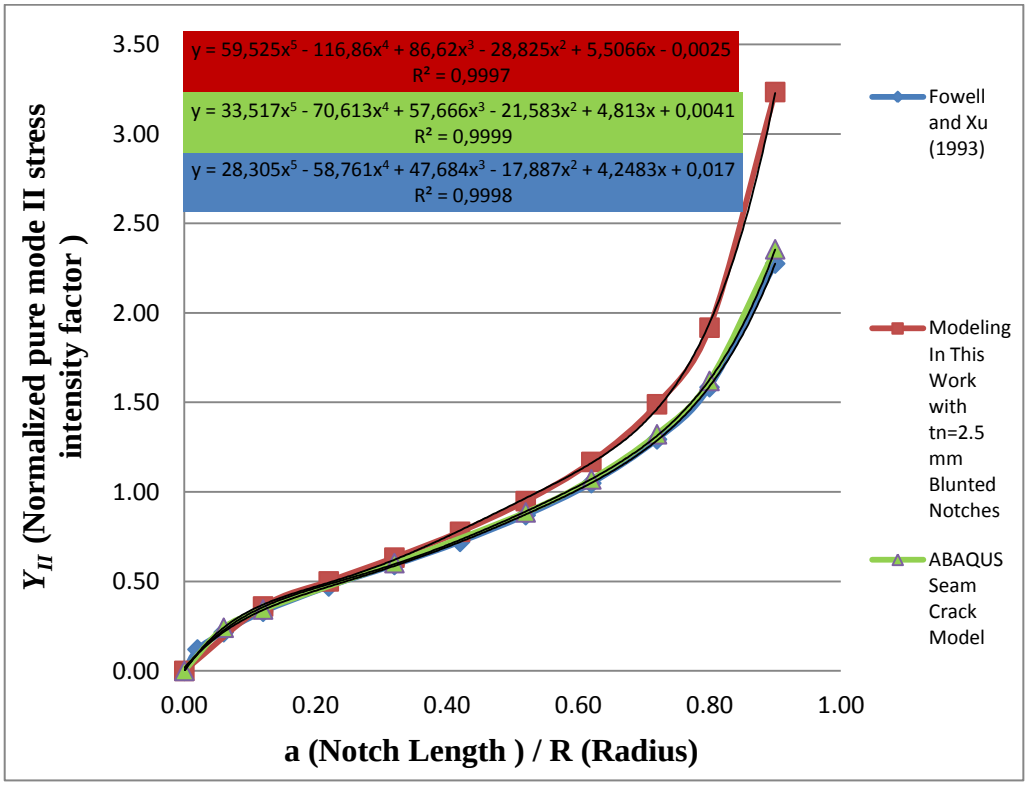

Figure 8.14 Y_{II} comparisons between the modeling work here and Fowell & Xu (1993)

Figure 8.14 demonstrates Y_{II} values for blunted notches, seam crack, and results of Fowell and Xu's fifteenth order polynomial equation (Equation 4.8 of Chapter 4). Some more models with extreme values of initial notch lengths (2a=6mm, 2a=12 mm, 2a=22 mm, 2a=80mm, 2a=90mm) are added to the analyses here to smoothly represent the functional variations in this figure.

For the estimation of Y_{II}, ABAQUS seam crack analyses results and results of Fowell & Xu's fifteenth order polynomial equation (4.8) for various *a/R* ratios match closely. However, in order to reduce complexity associated with estimation based on polynomial equation of order fifteen, new 5th order polynomial equation is proposed here as derived from ABAQUS seam crack Y_{II} analysis.

On the other hand, for determination of Y_{II} values for 2.5 mm blunted notch, similar 5th order polynomial equation is the best fit to the results of this case. One of the most important practical attractiveness of these new 5th order polynomial equations is that they have smaller residual values and they are in simpler functional forms compared to the polynomial equation of fifteenth order proposed by Fowell and Xu (1993).

As it is seen form Figure 8.14, a difference around 6 % is observed initially for notch length of a/R=0.32 between the Y_{II} stress intensity factor results of t_n=2.5 mm blunted notch case and seam crack case. However, this difference changes significantly to around %15.5 when the notch is close to the specimen boundary (a/R=0.72).

In Table 8.11, SIF and fracture toughness results for CSTBD specimens that have various initial notches are presented. In Table 8.12, summary of results is given based on the averaging process for a/R groups. During fracture toughness calculations to show the effect of blunted notches on Y_{II} results, Y_{II} results obtained from Fowell and Xu's fifteenth order polynomial equation and ABAQUS Y_{II} results of blunted notches with t_n=2.5 mm are listed in the table.

In fracture toughness calculations Equation 8.11 are used.

$$\boldsymbol{K_{IIc} = \frac{P_{cr}}{B \times \sqrt{R}} Y_{II}} \tag{8. 11}$$

P_{cr} is the load at the initiation of the mode II crack from the preliminary notch.

Table 8.11 SIF and fracture toughness results for CSTBD specimens

Specimen Code	Fowell and Xu (β^o)	Fowell and Xu (1993) Y_{II}	ABAQUS Y_{II}	P_{cr} (kN)	K_{IIc} Fowell and Xu MPa $\sqrt{m}$	K_{IIc} MPa $\sqrt{m}$
Specimens 2a=30-1	26.8	0.60	0,63	51,11	2,29	2,41
Specimens 2a=30-2				54,70	2,46	2,58
Specimens 2a=30-3				49,38	2,19	2,30
Specimens 2a=30-4				47,72	2,12	2,22
Specimens 2a=30-5				50,16	2,23	2,34
Specimens 2a=30-6				48,21	2,15	2,26
Specimens 2a=40-1	24.7	0.73	0,78	42,07	2,28	2,44
Specimens 2a=40-2				42,47	2,31	2,48
Specimens 2a=40-3				41,90	2,29	2,44
Specimens 2a=40-4				41,16	2,23	2,38
Specimens 2a=40-5				39,84	2,16	2,30
Specimens 2a=40-6				37,14	2,01	2,15
Specimens 2a=50-2	22.3	0.89	0,95	29,04	1,92	2,06
Specimens 2a=50-4				29,37	1,90	2,06
Specimens 2a=60-1	19.4	1.07	1,17	24,14	1,95	2,15
Specimens 2a=60-2				23,42	1,90	2,09
Specimens 2a=60-3				24,40	1,99	2,18
Specimens 2a=60-4				24,94	2,02	2,22
Specimens 2a=60-5				23,36	1,88	2,07
Specimens 2a=70-1	16.1	1.32	1,49	15,17	1,46	1,67
Specimens 2a=70-2				15,14	1,48	1,67
Specimens 2a=70-3				16,10	1,58	1,78
Specimens 2a=70-4				15,87	1,57	1,77
Specimens 2a=70-5				16,54	1,60	1,83
Specimens 2a=70-6				16,83	1,63	1,85

Table 8.12 Average P_{cr}, SIF and fracture toughness results for CSTBD specimens

Specimen Code	P_{cr} (kN)	Average K_{IIc} Fowell and Xu MPa $\sqrt{m}$	Average K_{IIc} MPa $\sqrt{m}$
2a=30	50.21	2.24	2.35
2a=40	40.76	2.21	2.37
2a=50	29.20	1.91	2.06
2a=60	24.05	1.95	2.14
2a=70	15.94	1.55	1.76

In Figure 8.15 critical load values for all CSTBD mode II fracture tests with different notch lengths are given. For the overall evaluation of test results targeted *a/R* groups are *2a*=32, 42, 52, 62 and 72 mm. Organizing the results according to average critical load for each group, a logarithmic functional form fitted can provide the critical load estimation for any *a/R* ratio not included in the groups above. As seen in Figure 8.16, quality of the fit is quite good for the critical load estimations for such cases.

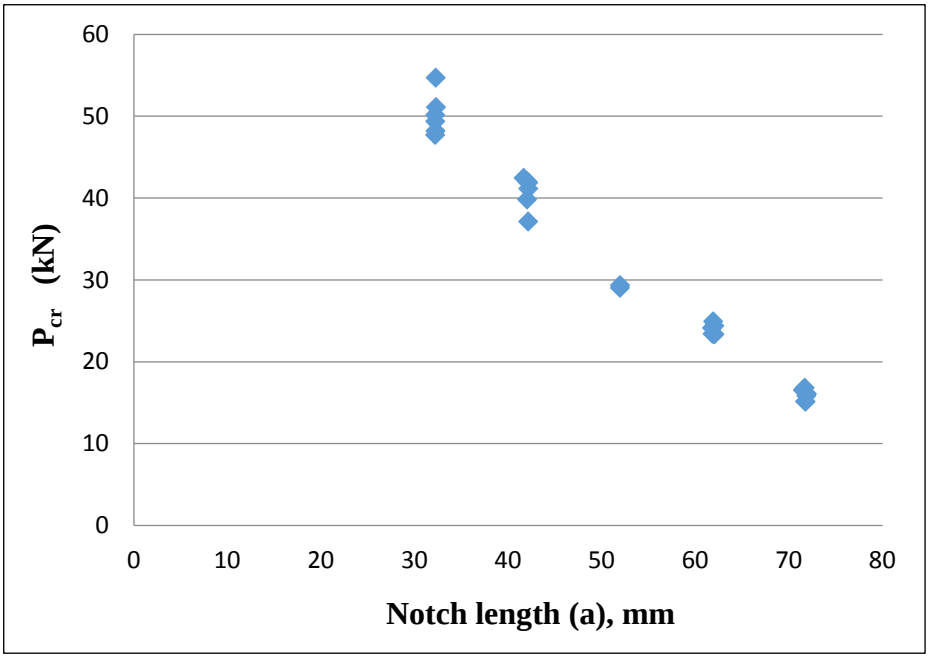

Figure 8.15 P_{cr} versus notch length

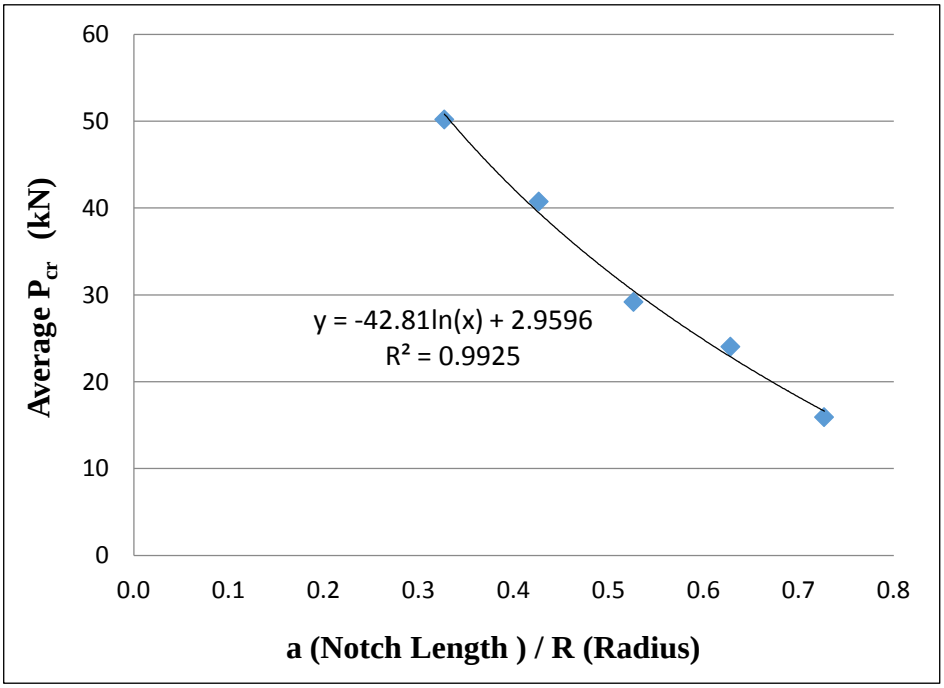

Figure 8.16 Average P_{cr} values versus grouped *a/R* entries

Figure 8.17 and 8.18 are generated to understand the behavior of the mode II fracture toughness against *a/R*. As it is seen from Figure 8.17 and 8.18 that, a decreasing trend is observed on K_{IIc} values of CSTBD specimens when *a/R* ratio gets close to 0.80; with higher *a/R* ratios initial notch tip and crack initiation location gets closer to the free boundary of the specimen. On the other hand, significant gradient change on correlation curve is observed when the *a/R* ratio is around 0.72. This situation can be interpreted as a boundary influence on shear mode fracture toughness. It should be reminded here that as the notch tip is close to the free boundary it is also in the neighborhood of the concentrated compressive load applied vertically at a point on the boundary.

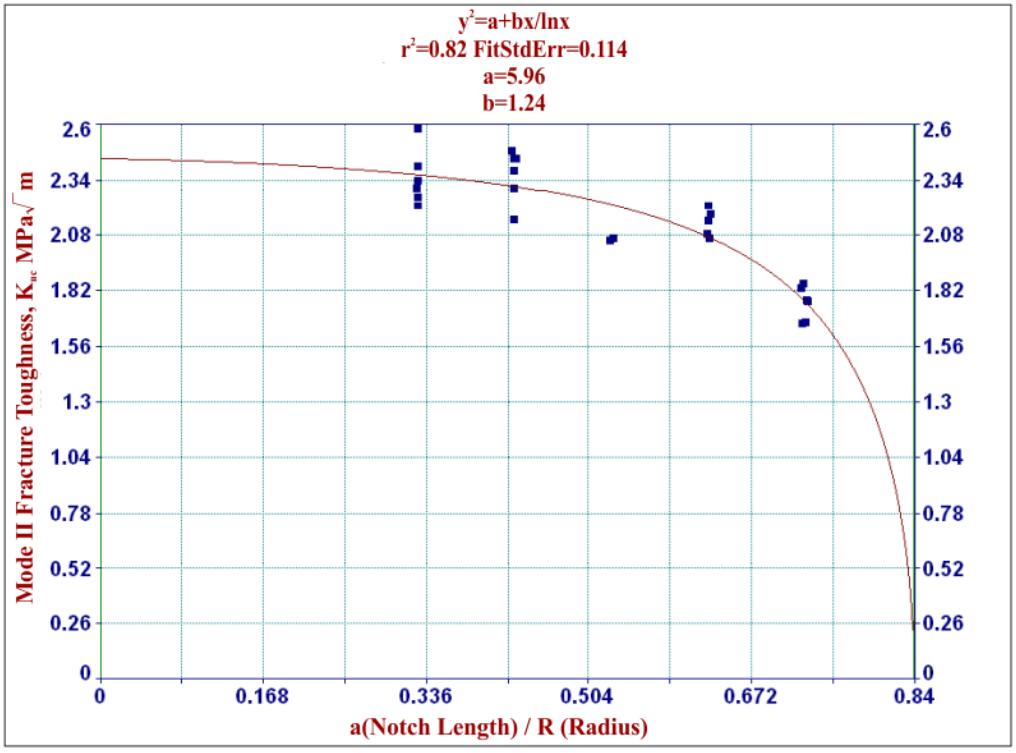

Figure 8.17 K_{IIc} versus *a/R* for all CSTBD Tests

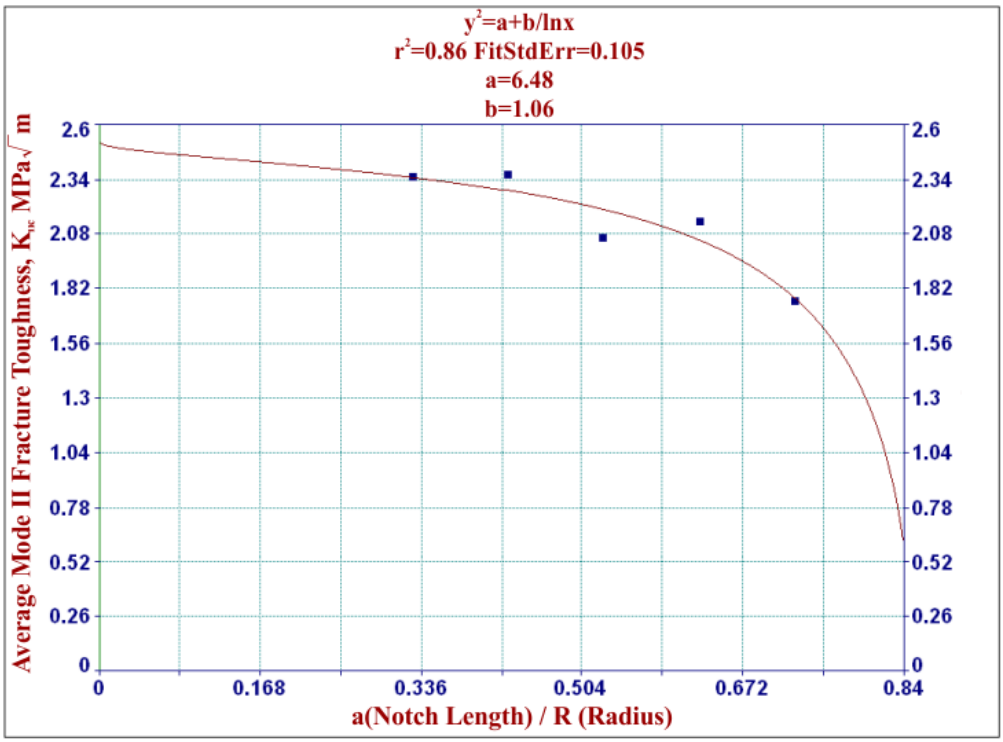

Figure 8.18 Averaged K_{IIc} versus group averaged *a/R* ratios

In Figure 8.17 results of all CTSBD tests are included. Group averaging is done to increase the quality of the data processing and fitting correlation function as in Figure 8.18. In fact R^2 value for the fitted functional form for this type of data processing increases from around 0.82 to 0.86.

It can be concluded from Figure 8.18 that in order to get reliable shear mode fracture toughness results from CTSBD experiments, experiments have to be made between *a/R*=0.2 and *a/R*=0.42 interval. With *a/R* values higher than *a/R*=0.42, shear mode fracture toughness value is negatively affected because the notch approaches to the specimen boundary.

Equation 8.12 extracted from the fitted functional form of Figure 8.17 for all test results is valid for mode II fracture toughness calculation of CSTBD method with the limitation imposed as *a/R* ≤0.84.

$$\boldsymbol{K_{IIc}{}^{2} = 5.96 + 1.24 \times \frac{a/R}{ln(a/R)}} \tag{8.12}$$

Interpretation of test data with a better quality can be done by considering the fitted functional form for the grouped average results of Figure 8.18. For this case, fitted functional form involves *ln(a/R)* term again in the denominator as appears in Equation 8.13 below.

$$\boldsymbol{K_{IIc}{}^{2} = 6.48 + \frac{1.06}{ln(a/R)}} \tag{8.13}$$

A common singularity in both equations are represented by *ln(a/R)* term in the denominator of second term of these equations. At the limit, as *a/R* approaches zero which means that there is no detectable crack or notch in macroscale.

x= *a/R*=0

$$\boldsymbol{\lim_{x\to 0} \frac{x}{\ln(x)}} \tag{8.14}$$

$$\boldsymbol{\lim_{x\to 0}(x) = 0 \text{ and } \lim_{x\to 0}(lnx) = -\infty} \tag{8.15}$$

Then, the second term in K_{IIc} expression tends to:

$$\boldsymbol{\frac{0}{-\infty} = 0} \tag{8.16}$$

K_{IIc} tends to square root of coefficient 6.48 as in Equation 8.13. This means that there is no crack or notch in macro scale, and thus resistance against mode II cracking is high with values of square root of 5.96 and 6.48 as observed in Equations 8.12 and 8.13, respectively. Concentrating on the fitted form of Equation 8.12, K_{IIc} is found as the square root of the coefficient 5.96. This value is calculated as K_{IIc}=2.44 MPa√m. This is an upper limit for the mode II fracture toughness of this rock with no notch or crack in macro scale exists in the core specimen. It can be interpreted as the mode II toughness value representing the internal microstructure of rock with inherent grain boundary cracks and micro defects.

K_{IIc} becomes zero around approximately a/R =0.80 in both Equations 8.12 and 8.13. Specimen boundary is now too close to the notch tip and there is no resistance offered by the specimen in terms the toughness K_{IIc} anymore.

In summary of the test results on CSTBD type core-based specimen geometries, a logarithmic functional form best represents the variation of mode II fracture toughness (K_{IIc}) with preliminary notch length/specimen radius ratio (a/R). As a/R approaches zero K_{IIc} tends to micro mechanical representative value of K_{IIc}=2.44 MPa√m. For a/R around 0.80, K_{IIc} tends to zero, since the notch tip is positioned too close to the specimen boundary. For such a notch length and position, it is concluded that CSTBD testing does not yield reliable results for mode II fracture toughness, considering the proximity and influence of the free boundary and the concentrated compressive load. To avoid the boundary influence issue in CSTBD testing, it is recommended to apply preliminary notches with a/R between 0.30 and 0.40.

CHAPTER 9

STRESS ANALYSES AROUND THE NOTCHES OF DIFFERENT SPECIMEN GEOMETRIES

For rock fracture mechanics testing, core-based specimens with different loading configurations and initial notch geometries are commonly used for pure K_{Ic} and K_{IIc} testing. The reason for the preference of cylindrical core samples can be attributed to the borehole exploration drilling work. In drilling work, boreholes are circular in section and rock samples obtained are in pieces of cylindrical cores.

In the current testing practice, there are different pure mode II core-based specimens with the various loading configurations such as the three-point bending and the Brazilian type indirect compression used in K_{IIc} testing. CSTBD, CCNBD, SCB, PTS, and DECBD are the well-known and widely used core-based specimens in the mode II fracture toughness testing work.

Fracture toughness tests on the cylindrical core specimens of relatively homogeneous gabbro have been conducted on the core-based specimen geometries of SCB, SNDB and CSTBD methods. Results in terms of existing stress fields around the notches and the propagating cracks are analyzed and compared in this section.

Testing results for fracture toughness with these methods show significant differences for K_{Ic} and K_{IIc} values. By analyzing the stress gradients and distributions around the initial notches, it is attempted to explain the differences of the K_{IIc} results achieved with different testing methods and specimen geometries. Stress gradients and distributions for different core-based specimen geometries are compared to the ones observed for a plate under pure mode II shear loading which

is the fundamental problem geometry that constitutes the original definition of the pure shear loading mode on a crack.

In order to initiate the pure K_{II} mode crack, initial notches with certain lengths and inclinations with respect to the loading ends are needed for all three geometries considered here. For the different testing geometries and the loading configurations, required inclination and position of the initial notch relative to the load application ends are different. Decision of the right inclination and the position with respect to the applied loading has been made based on the modeling work here. In order to apply the real experimental data in the modeling work, material properties (E=38.9 GPa and υ=0.11) that had been found for the gabbro rock were used.

9.1 Geometrical details and the critical load levels for the stress analyses of the specimen models

The semi-circular disc type, SCB model geometry proposed by Lim et al. (1994) is for a core sample of 100 mm diameter with plane strain thickness of 60 mm. With a loading span of 60 mm (S/R = 0.5), the pure mode II condition is attained at angle of 54 degrees from vertical load application axis with an initial notch of length a=17.6 mm (a/R=0.35) and the blunted notch thickness of t_n=1 mm.

The SCB model was constructed in 2D by using the CPE8 (Continuum Plane Strain Eight Node) second order quadrilateral elements available in the software. In order to apply the real critical load levels observed in the related tests of SCB specimens, the average maximum crack initiation load of P_{cr}=-34.36 kN of the experimental work was applied to a SCB model geometry used in the stress distribution analyses.

After analyzing the SCB model with ABAQUS, the average stress intensity factors K_I, K_{II}, and the Crack Propagation Direction (CPD) were found as:

K_I = -0.049 MPa $\sqrt{m}$ K_{II} = -0.920 MPa $\sqrt{m}$ CPD = 69.52^o

The circular plate type SNDB model geometry was constructed with a core specimen of 100 mm diameter, a thickness of 60 mm, and a span of 60 mm (*S/R* =0.6). With this geometry, the pure mode II state at the notch front was attained with an initial notch angle of 48 degrees from the vertical load application axis, an initial notch length *a*=25 mm (*a/R*=0.5), and the blunted notch thickness of t_n=1 mm.

Because of its complex geometry, the SNDB model was developed in 3D by using the C3D8R (Continuum Eight Node Brick Elements with Reduced Integration) elements of the modeling software. Again, in order to generate the stresses under the real load levels of the testing work, and investigate the stress distributions around the SNDB model notch front under the related critical load, the model was constructed and analyzed under an averaged maximum load of P_{cr}=-51.44 kN of the five tests on the SNDB circular plate type core specimens.

After analyzing the SNDB model with ABAQUS, the average stress intensity factors K_I, K_{II}, and the Crack Propagation Direction (CPD) from the vertical loading axis were found as:

K_I = -0.020 MPa $\sqrt{m}$ K_{II} = -1.180 MPa $\sqrt{m}$ CPD = 70.03^o

Having very low K_I values from the models of both SCB and SNDB methods shows the success of the modeling work here. Ideally, the mode I SIF is supposed to be zero for a model of the notched pure shear geometry.

For the analyses of the Brazilian disc type CSTBD model, the model was constructed for a core specimen with a 100 mm diameter and a thickness of 60 mm. The model reached the pure mode II state at the notch front at a notch angle of 24.9° from the vertical load application axis for an initial notch length of $2a$=42 mm or a=21 mm (a/R=0.42), and the blunted notch thickness of t_n=2.5 mm.

Contrary to other specimen geometries, CSTBD model was loaded under Brazilian type of compression. The CSTBD model was developed in 2D by using the CPE8 (Continuum Plane Strain Eight Node) second order quadrilateral elements of the software. In order to simulate the action of the experimentally determined loading at the crack propagation state and investigate the stress distributions around the notches of the CSTBD Brazilian disk type models, models were constructed and analyzed under an average maximum load of P_{cr}=40.76 kN of the six tests available for the particular notch length.

After analyzing the CSTBD model with ABAQUS, the average stress intensity factors K_I, K_{II}, and the Crack Propagation Direction (CPD) were found as:

$K_I = 0.027$ MPa $\sqrt{m}$ $\quad$ $K_{II} = -2.360$ MPa $\sqrt{m}$ $\quad$ CPD= 70.31^o

Again, mode I SIF is nearly zero indicating that the quality of the modeling is high, and the modeling work is quite successful to simulate pure mode II condition for the Brazilian disk type geometry briefly named as CSTBD.

For comparison of the stress distributions of the different mode II core-based specimen geometries, various reference paths named as the stress paths are constructed parallel to the notch plane and ahead of the notch front. Based on the findings of the modeling work for the different specimen geometries, the mode II

crack propagation direction (CPD) with respect to the initial notch plane is available as an output of the related model. Paths originating around the notch tip region at certain angles and following the crack propagation direction with respect to the notch plane are also added for the stress analyses following the possible crack propagation front.

9.2 Comparison of the results with different geometries and the loading methods

Geometric details and important results of the fracture toughness testing work with various core-based specimen geometries are summarized in Table 9.1. For all the tests involving these different geometries, cylindrical cores had a diameter of D=100 mm and the out of plane thickness of 60 mm.

Table 9.1 Summary of the results of the fracture toughness tests on the gabbro rock with the different specimen geometries

	SCB	SNDB	CSTBD
t_n (Notch Thickness, mm)	1	1	2.5
a or *2a* (Initial Notch Length, mm)	a=17.6	a=25	2a=42
β^o Initial Notch Angle from Vertical	54°	48°	24.9^o
Applied Loading Type	3-point bending with 2S=50 mm	3-point bending with 2S=60 mm	Concentrated Brazilian Type Compressive
a/R	0.35	0.50	0.42
B/D	0.60	0.60	0.60
P_{cr}	34.36 kN	51.44 kN	40.76 kN
Average K_{Ic} $MPa\sqrt{m}$	1.77± 0.10	2.10±0.14	2.27*
Average K_{IIc} $MPa\sqrt{m}$	0.92± 0.00	1.18±0.15	2.37±0.12
K_{IIc} / K_{Ic}	0.52	0.56	1.04*

(*) results are estimated based on the previous work as explained below.

Due to the difficulties in machining of the notches by the water jets and the limited number of specimens available for the gabbro rock, mode I fracture toughness tests could not be conducted directly on the CSTBD specimens. All the available CSTBD specimens were used in K_{IIc} testing. In order to estimate the entry for the CSTBD in the table, K_{Ic} value of the gabbro was computed from the logarithmic relationship of Equation 9.1 proposed by Tutluoglu and Keles (2011).

$$K_{Ic(SNDB)} = 0.5 \ln\left(\frac{B}{R}\right) + K_{Ic\ (SCB)} \tag{9.1}$$

Equation 9.1 is for the estimation of the K_{Ic} values of the testing on the circular plate type SNDB specimens. By using the K_{Ic} value of SCB testing results and considering the *B/R* ratio of the circular plate type geometry of SNDB, a good quality estimation of mode I fracture toughness is possible. Adopting the expression of Tutluoglu and Keles (2011), sufficiently high value of *B/R* ratio, which is equal or greater than 2.7, should be employed to minimize the core specimen boundary influence on K_{Ic} values. Then, the K_{Ic} result approaches to the results that would have been obtained by the ISRM suggested CCNBD method.

By using the K_{Ic} value of SCB for the gabbro in this work and taking the *B/R* ratio as 2.7 in the equation, K_{Ic} value of CSTBD specimen is estimated as 2.27 MPa√m. With this estimation process, K_{IIc} / K_{Ic} ratio of the CSTBD gabbro specimen is around 1.04. This result is impressively compatible with the results of the original work by Awaji and Sato (1978) in which K_{IIc} / K_{Ic} ratio of the CSTBD tests were reported to be approximately around this value for marble, graphite and plaster, as given in Table 4.3 of Chapter 4.

P_{cr} values in Table 9.1 represent the average load values of different tests at the point of unstable crack initiation for that particular test. These critical loads are applied in the models to investigate and compare the distribution of stress

gradients and stress components around the preliminary notches of different core-based specimen geometries at the initiation of the crack around the preliminary notches machined.

Shear mode fracture toughness values from the three-point bending type tests of SCB and SNDB are 2 to 2.5 times lower than the value K_{IIc}=2.37 MPa√m found by the CSTBD testing with the Brazilian type compressive loading. Result of the SNDB method testing gives K_{IIc}=1.18 MPa√m which is about 30% higher than the result of the SCB testing work. With K_{IIc}=0.92 MPa√m, SCB method produces the lowest result in this testing work for the determination of mode II fracture toughness. It can be concluded that among the three-point bending type testing methods employed here, SNDB method yields comparatively closer value to the results of CSTBD testing.

Comparing the K_{IIc} / K_{Ic} ratio of 0.52 found by the SCB testing work here to the results of the other researchers, similar trends are observed related to this ratio. In Aliha and Ayatollahi (2011) this ratio is again low with a value of 0.40 for Iranian White Marble. K_{IIc} / K_{Ic} ratio is 0.49 for Johnstone mudstone given in Lim et al., (1994). In summary, K_{IIc} / K_{Ic} ratio of the SCB testing here is quite compatible with the ones previously found.

9.3 Analyses of the distribution of stresses around the notches of the different geometries

In stress distribution analyses, various stress components (normal stresses S_{11}', S_{22}', S_{33}', shear stress S_{12}' and von Mises stress) were generated for the models of the different specimen geometries by assigning various stress analyses paths around the preliminary notches and the crack propagation directions.

Some of the paths are positioned parallel to the long axis of the notch (Paths 1 and 2). Distance along the normal to the Path 1 and notch axis is 1 mm. This normal distance is 2 mm for the Path 2. Path 3 starts directly from the initial notch tip. Along the paths global co-ordinate system is rotated or transformed into local co-ordinate system. In this local system that involves *x* axis parallel to the notch plane (*q* vector direction) and *y* axis perpendicular to the notch plane, stress and displacement components can be studied with respect to the primed local coordinate system.

Path 4 is generated along the estimated crack propagation directions of the models of different core-based specimen geometries. A local primed coordinate system to the Path 4 is again assigned which is approximately oriented around 70° counterclockwise from the notch plane of the different specimen geometries. This local system is defined by an *x*-axis perpendicular to the crack propagation direction (CPD) and *y*-axis parallel to the crack propagation direction (CPD).

After assigning a local coordinate system, distance along any path is defined by a length variable *d* and/or its dimensionless form *d/a* for presenting the stress variations at different positions around the initial notch plane.

Owing to the individual machining processes, initial notch lengths can be slightly different for the SCB, SNDB, and CSTBD specimen geometries used in this work. Average initial notch lengths for the SCB, SNDB and CSTBD specimen geometries were measured to be around 17.6 mm, 25 mm and 21 mm, respectively. The specimen models were constructed accordingly to be consistent. Slight differences appearing in couple of mm's in the initial notch lengths are not expected to effect the global treatment and comparison of the results.

In presenting the results of the stress distribution analyses, it proves to be useful to employ dimensionless forms for the stress components located on the vertical scale of the plots. The dimensionless form is constructed by a functional form involving the relevant stress component times the square root of the notch length a in the numerator, and the fracture toughness K_{IIc} in the denominator. An example for such normalization is given in the form as $(S_{11}' \times \sqrt{a})/K_{IIc}$ which represents the dimensionless normal stress parallel to the notch plane for the paths 1, 2, and 3, referring to the particular local system assigned to these paths. The same form represents the dimensionless normal stress perpendicular to Path 4, which is along the estimated crack propagation direction. This way, effect of the geometry and load application related differences on the stresses around the notches of the three core-based based specimen models analyzed is minimized; quality of the results for comparison purposes is increased.

For all three testing geometries, stress components that are effective in the initiation of a mode II crack have high variations or gradients around the immediate neighborhood of the machined notch tip. That is why stress distribution analyses are concentrated to this region. For parallel paths to the notch, stress variation plots of dimensionless forms as $[(S_{11}' \times \sqrt{a})/K_{IIc}, (S_{22}' \times \sqrt{a})/K_{IIc}, (S_{33}' \times \sqrt{a})/K_{IIc}, (S_{12}' \times \sqrt{a})/K_{IIc}, (S_{Mises}' \times \sqrt{a}) / K_{IIc}]$ versus d/a are started from a position of $-a/2$ in the back of the notch tips and extended to $+a/2$ ahead of the notch tips.

9.3.1 Stress distributions along Path 1 for the different core-based specimen geometries

In stress distribution analyses, various stress components (S_{11}', S_{22}', S_{33}', S_{12}' and *Mises Stress*) along the different paths were generated for the semi-circular disc (SCB), the circular plate type (SNDB) and the Brazilian disc type (CSTBD) core-based specimen model geometries. Position and geometric details of Path 1 on the

different core-based specimen geometries are illustrated in Figures 9.1, 9.2 and 9.3.

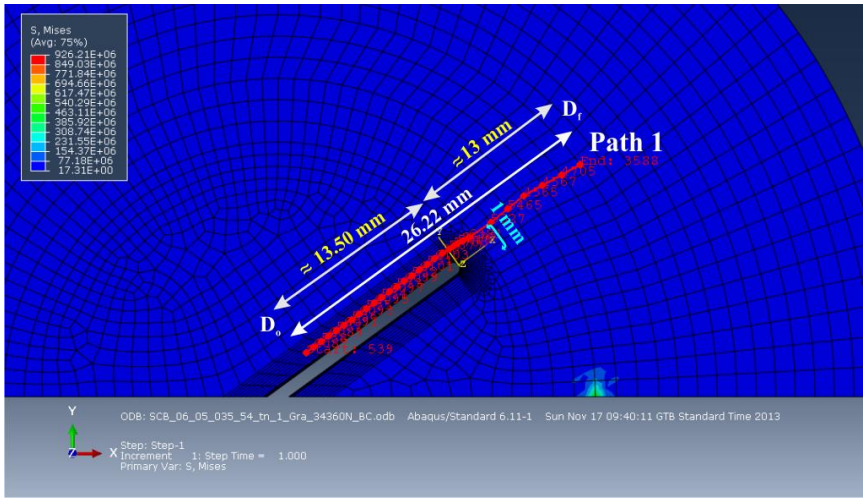

Figure 9.1 Position and geometric details of Path 1 on the semi-circular disc (SCB) specimen model

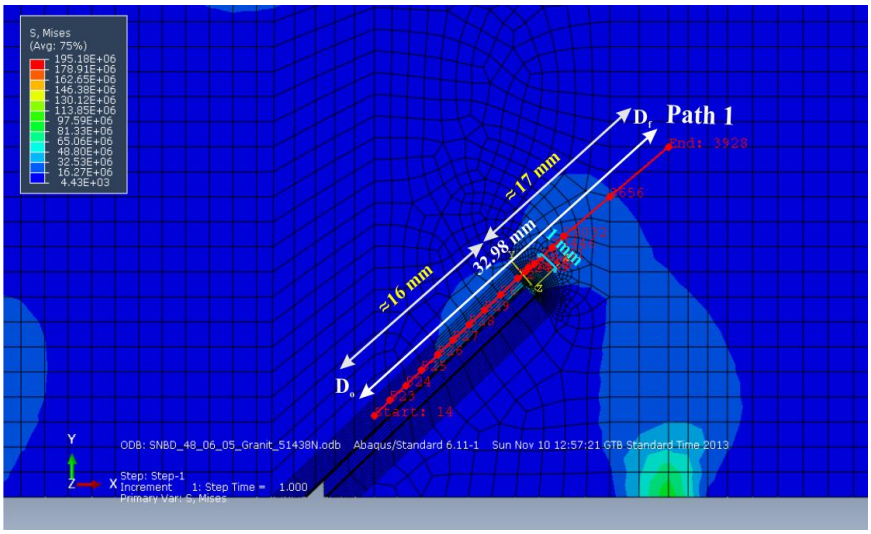

Figure 9.2 Position and geometric details of Path 1 on circular plate type (SNDB) specimen model

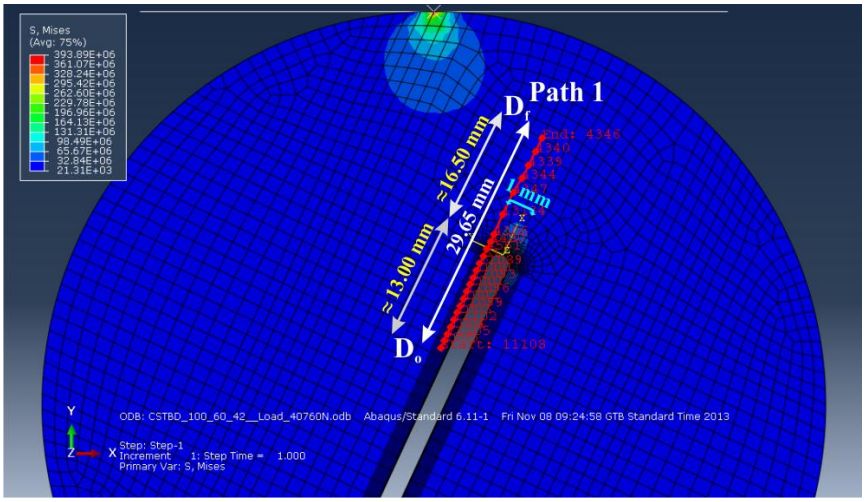

Figure 9.3 Position and geometric details of Path 1 on the Brazilian disc type (CSTBD) specimen model

Path 1 covers an overall distance of around *d*=30 mm for each specimen geometry; approximately 15 mm portion is located over the notch plane and the remaining portions represent the regions over and ahead of the notch tip and the notch front. These distance assignments are marked in the figures related to the analyses of the stresses around and ahead of the initial notch plane of the model geometries considered.

In order to compare the stress components along Path 1, stress distribution graphs are generated for the core-based specimen geometries and presented in Figures 9.4, 9.5, 9.6, 9.7 and 9.8 respectively. Notch front vicinity is circled and marked on the related plots in these figures.

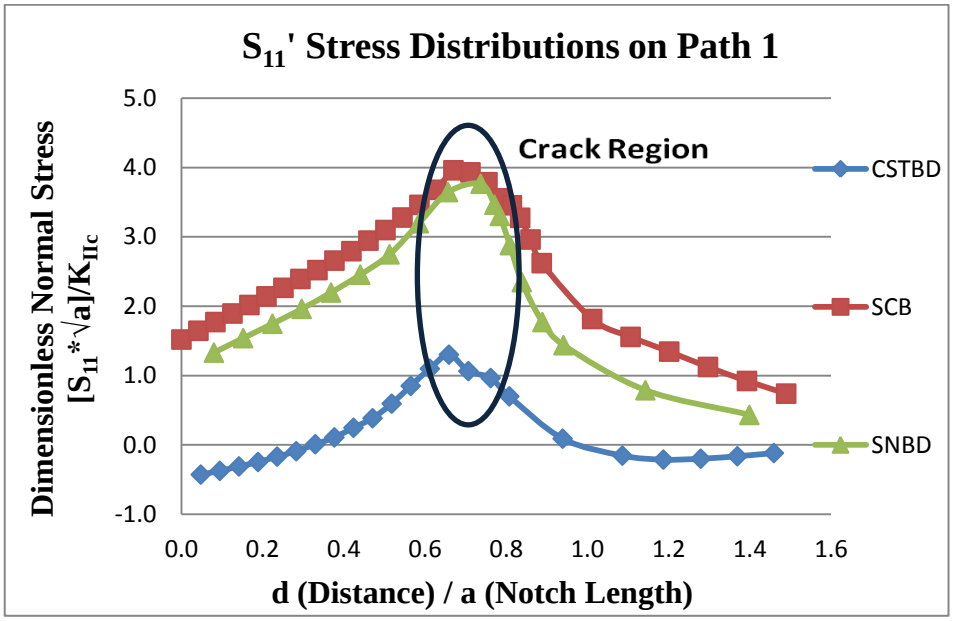

Figure 9.4 Dimensionless S_{11}' normal stress distribution vs. *d / a* (Distance / Notch Length) ratio along Path 1

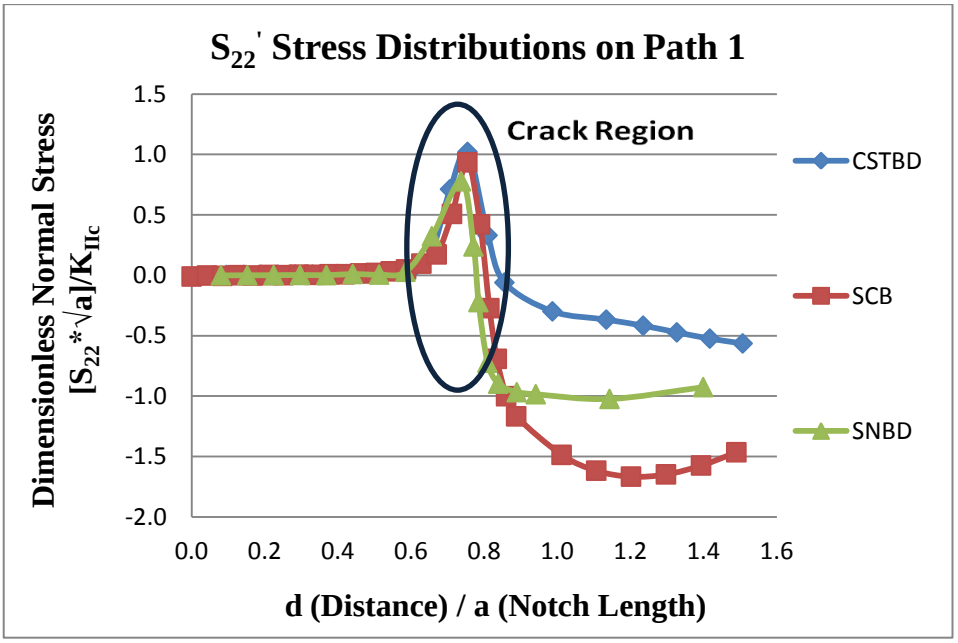

Figure 9.5 Dimensionless S_{22}' stress distribution vs. *d* (Distance) / *a* (Notch Length) along Path 1

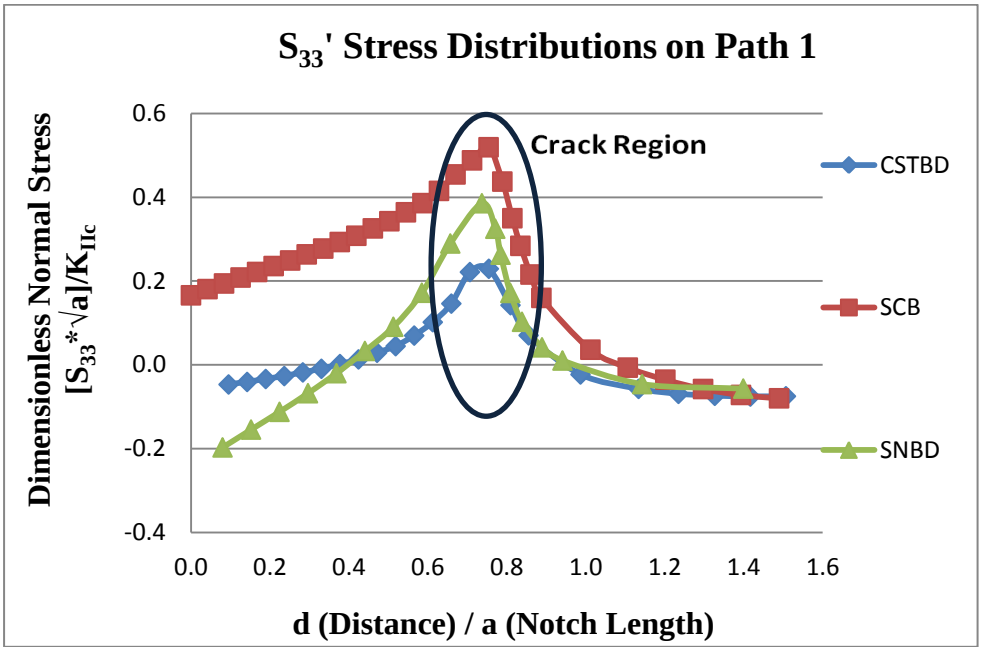

Figure 9.6 Dimensionless S_{33}' stress distribution vs. *d* (Distance) / *a* (Notch Length) along Path 1

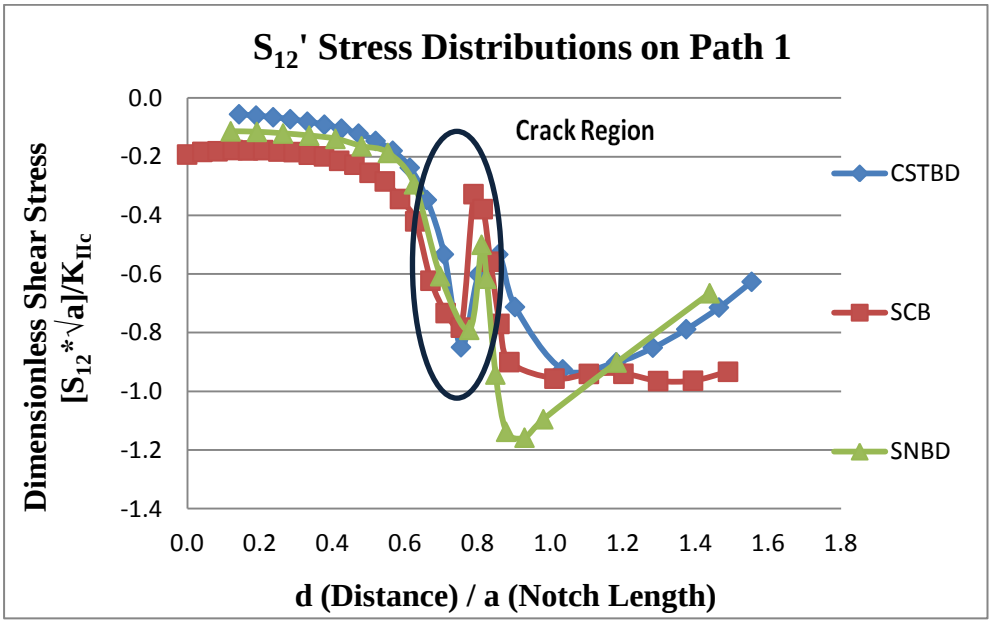

Figure 9.7 Dimensionless S_{12}' stress distribution vs. *d* (Distance) / *a* (Notch Length) along Path 1

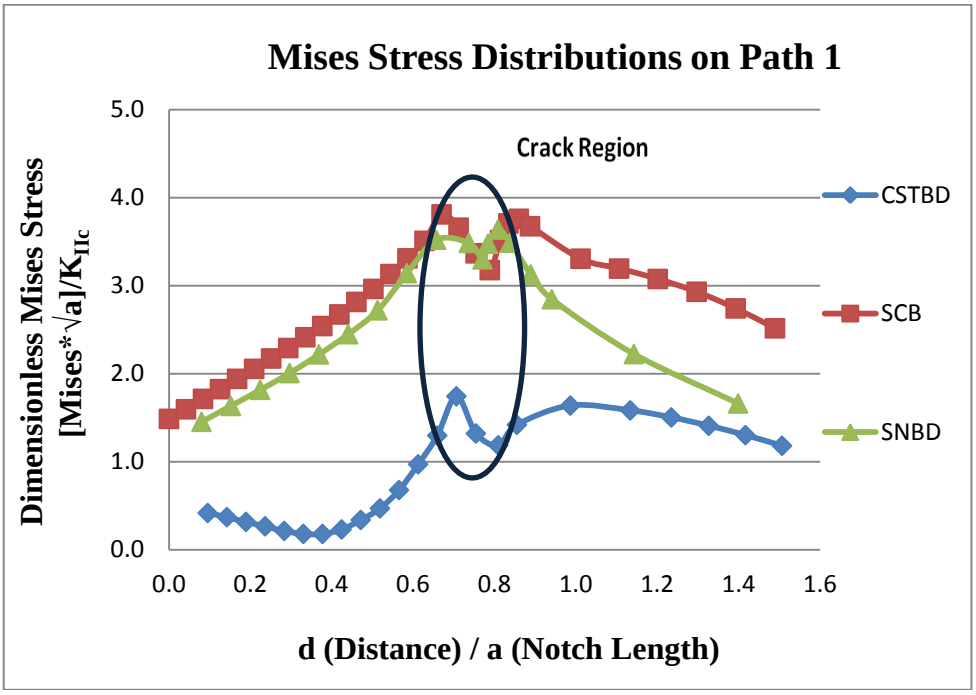

Figure 9.8 Dimensionless *Mises* stress distribution vs. *d* (Distance) / *a* (Notch Length) along Path 1

In Figures 9.4, 9.5, 9.6, 9.7 and 9.8 along Path 1 main difference in the stress distributions of different model geometries are observed for the S_{11}' which is the normal stress component parallel to the notch plane. Von Mises stresses are also significantly different for various core-based specimen geometries. Parallel to the initial notch tip, S_{11}' stresses for the SNDB and the SCB specimens are in more tension than CSTBD specimen. This case can be attributed to the loading configuration. For the SCB and SNDB specimen geometries, loading is generated by the three-point bending loading configuration. However, for the CSTBD specimen loading is Brazilian type compression, and this situation significantly affects S_{11}' stress distribution parallel to the notch tip.

On the other hand, Mises stress distribution proportional to the damaging J_2 stress invariant shows that, for the SNDB and SCB specimen models Mises stress is about two times higher than the one for the CSTBD model. As it is known, von

Mises yield criterion depends on the distortion energy hypothesis; this means that if the equivalent von Mises stress is higher than the yield strength of the material, material fails. This may be interpreted as a larger size of FPZ (Fracture Process Zone) around the notch and propagating crack tips for these bending type specimen geometries. Larger failed zone or plastic zone around the notch and propagating crack tip can result in lower values of fracture toughness.

9.3.2 Stress distributions along Path 2 for different core-based specimen geometries

In Figure 9.9, 9.10 and 9.11 position and geometric details of the Path 2 for the different core-based specimen geometries are illustrated.

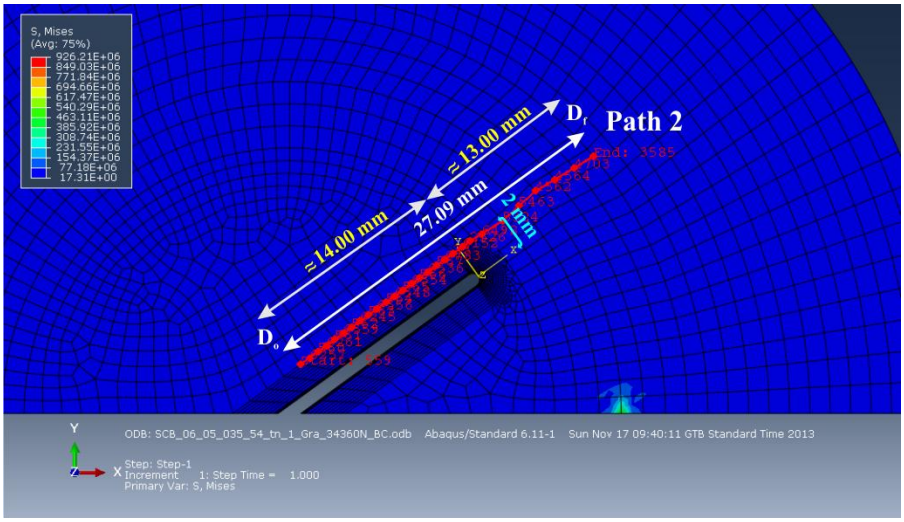

Figure 9.9 Position and geometric details of Path 2 on SCB specimen model

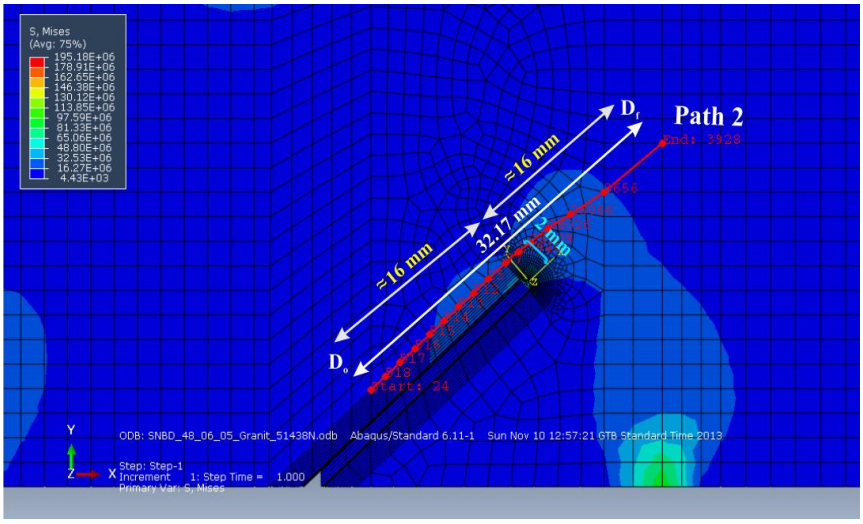

Figure 9.10 Position and geometric details of Path 2 on SNDB specimen model

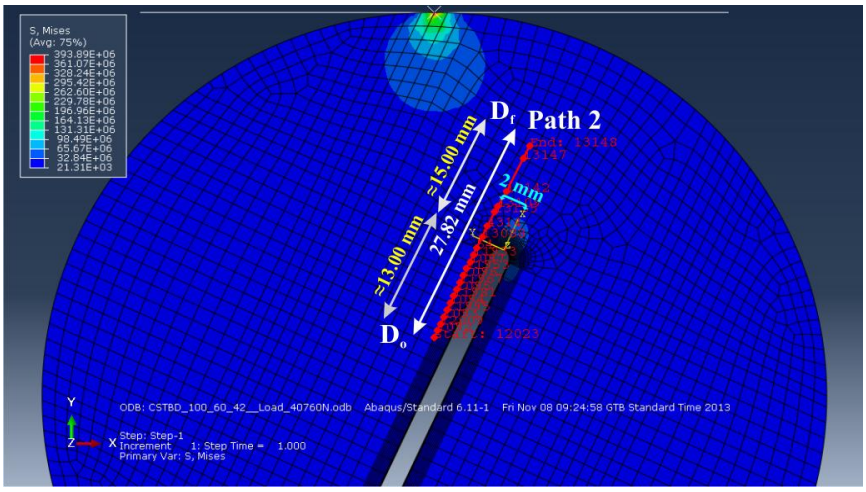

Figure 9.11 Position and geometric details of Path 2 on CSTBD specimen model

Path 2 covers an overall distance of around *d*=30 mm for each specimen geometry; approximately 14 mm portion is located over the crack plane and the remaining portions represent the region over and ahead of the crack tip and its front. These distance assignments are marked in the figures related to the analyses of the stresses around and ahead of the initial notch plane.

As discussed for the Path 1, similar stress distribution trends can be observed for the Path 2. In order to focus the reader on the important stress differences, *Mises* and S_{11}' stress distributions are graphed in Figure 9.12 and 9.13.

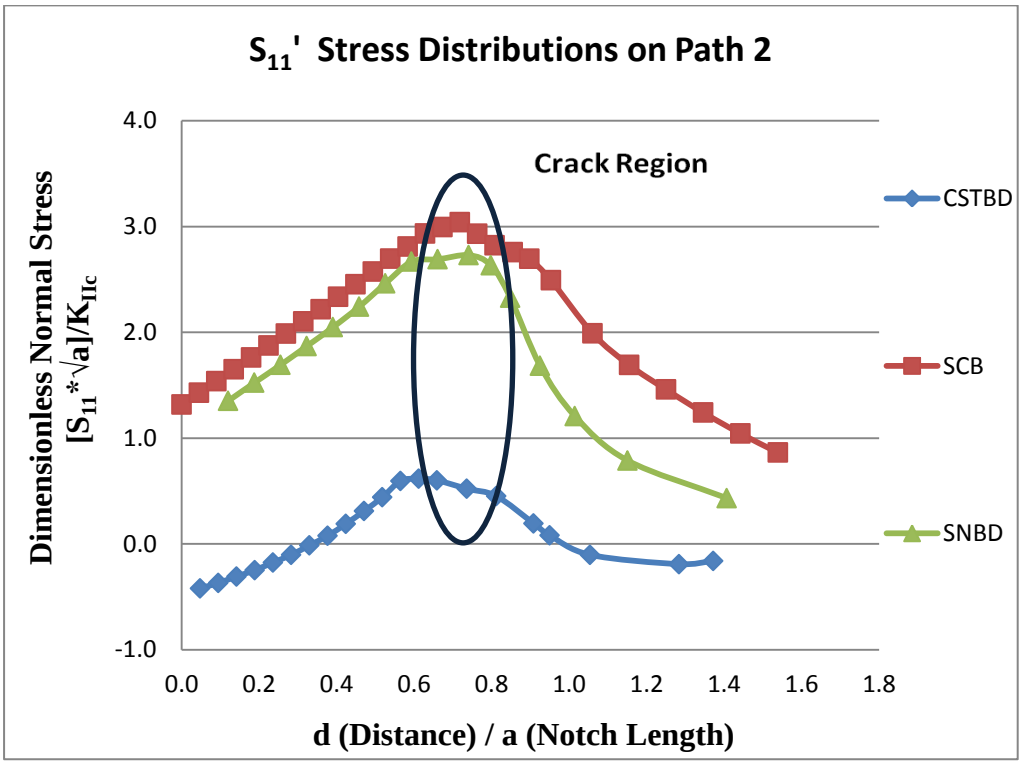

Figure 9.12 Dimensionless S_{11}' stress distribution vs. *d* (Distance) / *a* (Notch Length) along Path 2

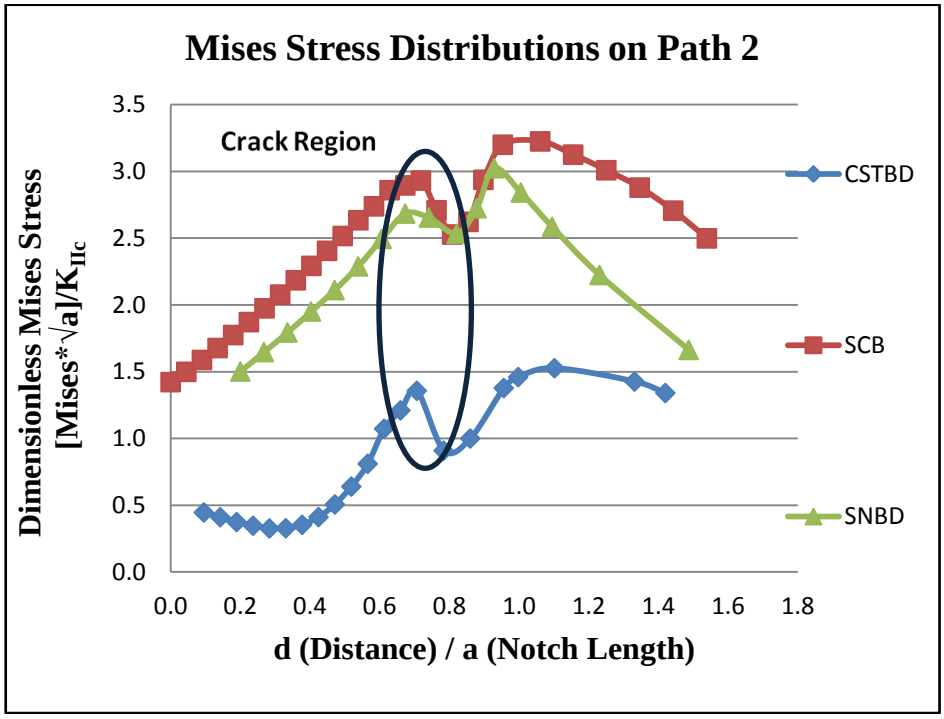

Figure 9.13 Dimensionless *Mises* stress distribution vs. *d* (Distance) / *a* (Notch Length) along Path 2

Analyzing the trends in Figures 9.12 and 9.13, similar trends but slightly lower stress concentrations are observed around the notches of all specimen models, compared to the trends for the Path 1. The trend for the stress difference ratios ($S_{11}'_{(SCB)} / S_{11}'_{(CSTBD)} = 4\ S_{11}'_{(SNDB)} / S_{11}'_{(CSTBD)} = 4$) for the component S_{11}' and for the von Mises stress are almost the same as the ones of the Path 2. The reason for slightly decreased stress entries can be attributed to the increased distance (2 mm) between the Path 2 and the notch plane.

9.3.3 Stress distributions along Path 3 for the different core-based specimen geometries

In Figures 9.14, 9.15 and 9.16 position and geometric details of Path 3 for different core-based specimen geometries are illustrated.

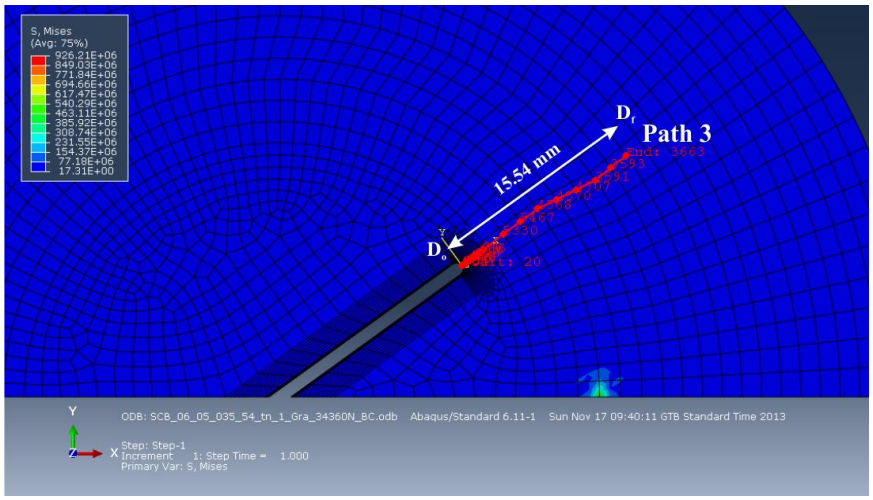

Figure 9.14 Position and geometric details of Path 3 on SCB specimen model

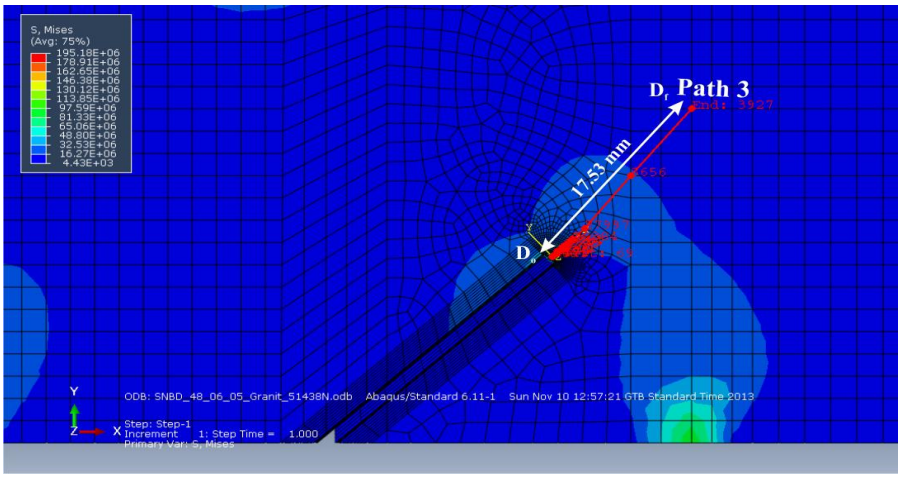

Figure 9.15 Position and geometric details of Path 3 on the SNDB specimen model

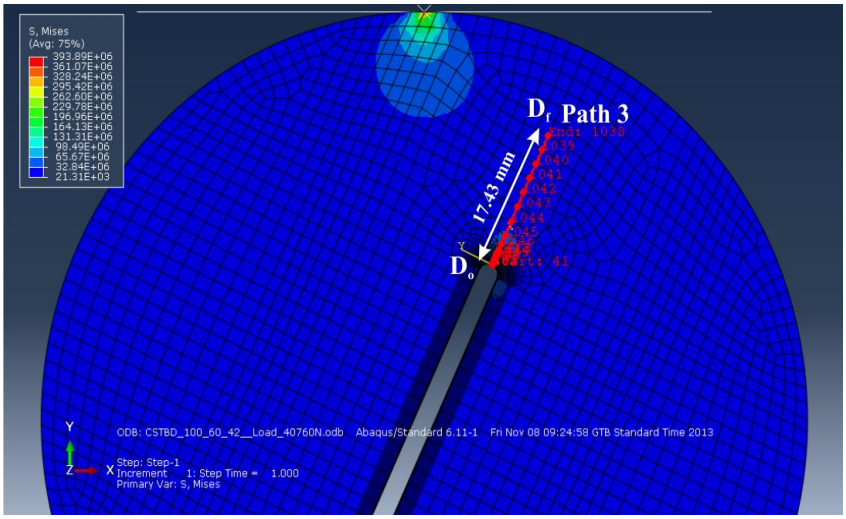

Figure 9.16 Position and geometric details of Path 3 on the CSTBD specimen model

Being straightly ahead of the notch tip, Path 3 is an important path for the stress distribution analyses. This is because interpretation of results based on the original definition of K_{II} and its associated analytical solutions give the tendencies along the notch or crack front for the stress components at the vicinity of the notch or crack tip. Original stress distribution tendencies can be estimated by using Equations 3.14, 3.15, 3.16 and 3.17 for the mode II loading conditions.

From Equations 3.14, 3.15, 3.16 and 3.17, mode II stress components (S_{11}', S_{22}', S_{33}', and S_{12}') can be calculated at the crack tip (where $r \rightarrow 0$ and θ=0), as 0, 0, 0 and - ∞, respectively. However, numerical modeling solutions are approximate solutions, and as the notch or crack tip is approached, stress gradients are too high and depending on the mesh and the mesh construction techniques accuracy of the solutions may decrease around the sharp front of the notch or crack.

As seen in Figure 9.17, some of the S_{12}' stress values positioned at the notch tip or at the starting point of the path are significantly affected by the high stress variations; they show large fluctuations at the immediate notch-tip modeling

elements of the blunted notch. This situation continues until *d/a*=0.08. Such stress values at these elements have been treated as inaccurate compared to the analytical solution. In order to examine the real S_{12}' stress distribution behavior, these values have been dropped to refine the overall stress distribution behavior.

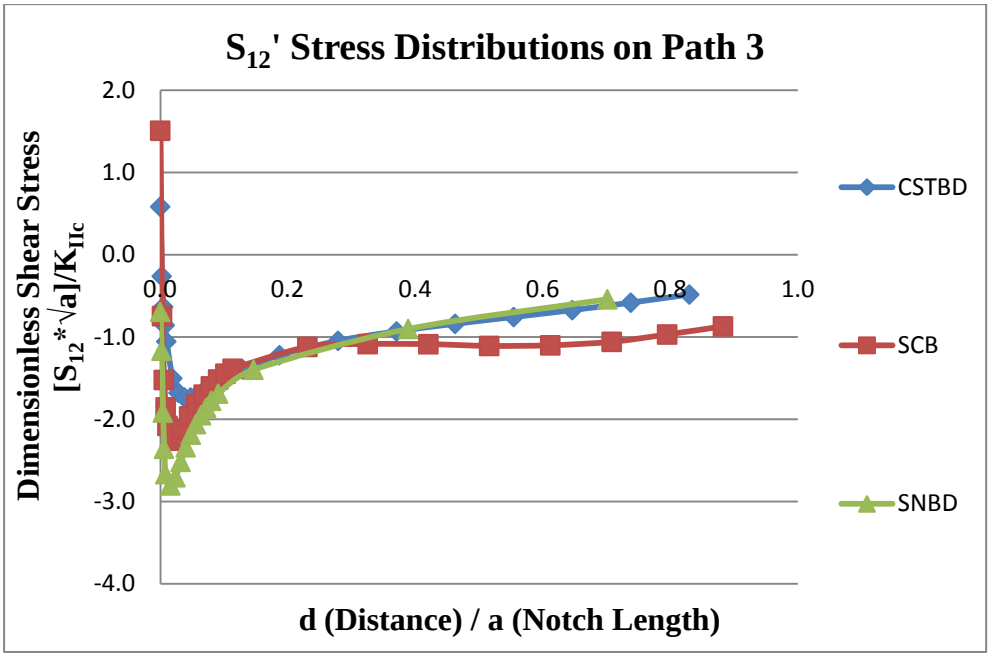

Figure 9.17 Dimensionless S_{12}' stress distribution vs. *d* (Distance) / *a* (Notch Length) along Path 3

The stress distributions are reprocessed in the refined style avoiding the modeling inaccuracies related to the curved notch tip. Results in the refined style are plotted again in Figures 9.18, 9.19, 9.20, 9.21 and 9.22.

As seen from the Figure 9.18, S_{11}' stress for the CSTBD specimen is compressive with a very low value. Analytical trend indicates a zero stress state in this sense. On the other hand, S_{11}' stresses for the SCB and SNDB indicate tension with magnitudes much higher than the compressive stress of the CSTBD specimen model.

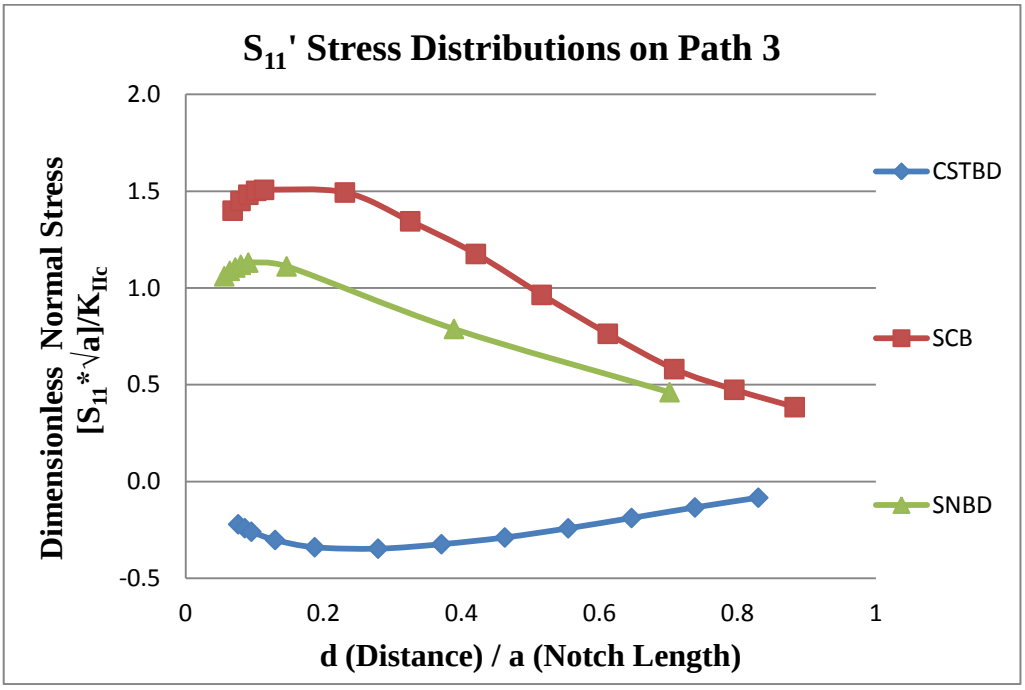

Figure 9.18 Dimensionless S_{11}' stress distribution vs. *d* (Distance) / *a* (Notch Length) along Path 3 after the data refinement

Similar comments can be made for S_{22}' distribution in Figure 9.19. In this case, all stress magnitudes are in the compression side. Although, CSTBD S_{22}' stress values show a tendency to becoming more compressive with increasing *d/a*, its values are much lower than the SCB and SNDB S_{22}' stress values. Again, CSTBD stresses are the closest to the analytical solution tendencies.

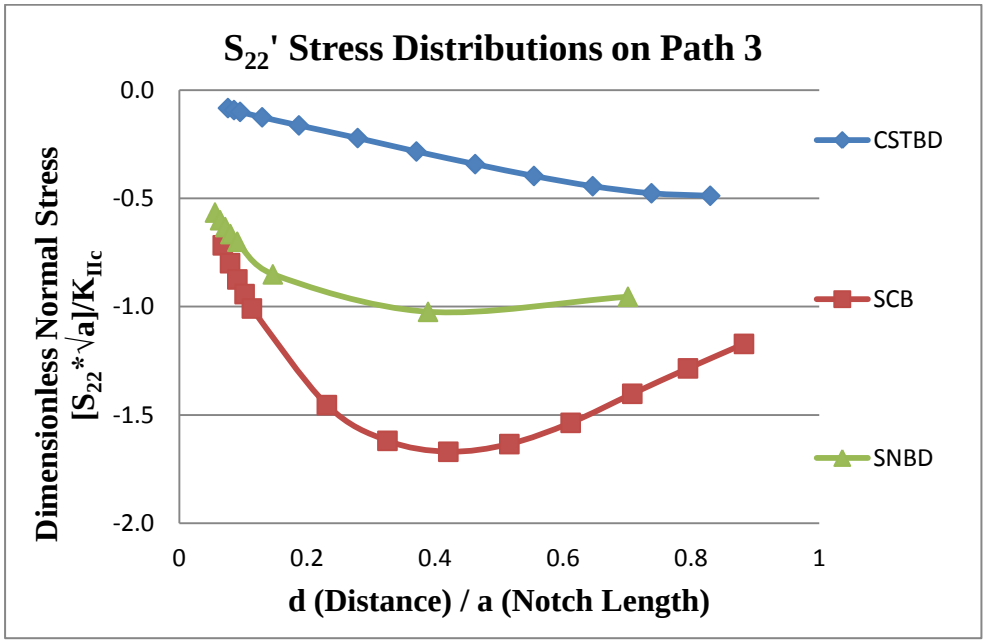

Figure 9.19 Dimensionless S_{22}' stress distribution vs. *d* (Distance) / *a* (Notch Length) along Path 3 after the data refinement

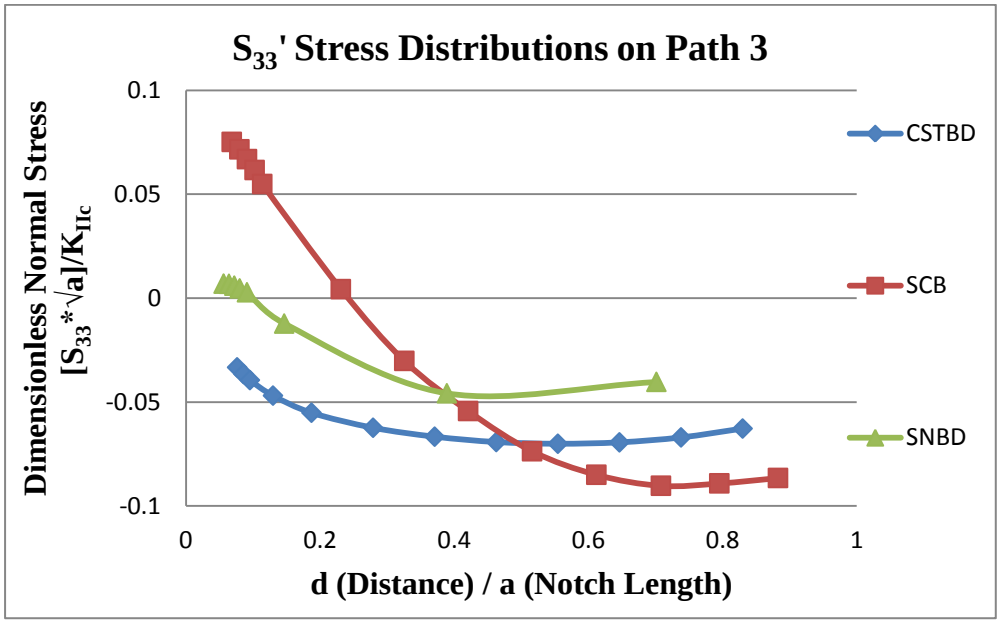

Figure 9.20 Dimensionless S_{33}' stress distribution vs. *d* (Distance) / *a* (Notch Length) along Path 3 after the data refinement

Distribution of the shear stress S_{12}' along the Path 3 following the notch plane was analyzed for the SCB, SNDB, and CSTBD core-based test specimen geometries in Figure 9.21.

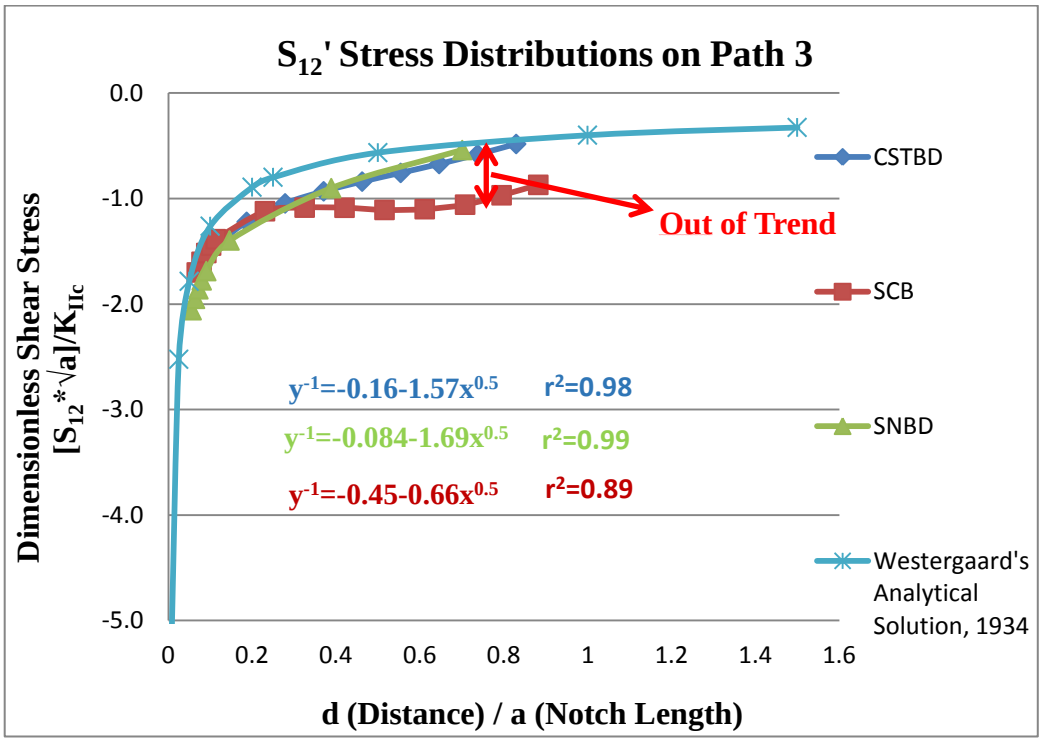

Figure 9.21 Dimensionless S_{12}' stress distribution vs. *d* (Distance) / *a* (Notch Length) along Path 3 after the data refinement

For comparison, a curve for the analytical solution of Westergaard for the shear stress variation along that path was also inserted to the Figure 9.21. Distance variable *d* along the path corresponds to the radial distance *r* of the analytical solution. In terms of the path distance variable *d*, analytical solution for the S_{12} reads as:

$$S_{12} = \frac{K_{II}}{\sqrt{2\pi d}} \tag{9.2}$$

This expression equivalently represents the $1/(r)^{1/2}$ singularity form of the stress distribution of the analytical solution, being replaced as $1/(d)^{1/2}$. As the distance d approaches zero that is as the notch or crack tip is approached, shear stress tends to infinity along the related trend curve in the Figure 9.21.

For a dimensionless plotting effort, vertical and horizontal scales are manipulated. Coefficient 2π was dropped from the governing expression of the vertical scale as in the case of previous plots for the stress distribution analyses. The vertical scale variable took the following form:

$$\frac{S_{12} * \sqrt{a}}{K_{IIC}} \tag{9.3}$$

Horizontal scale was applied as the ratio of the distance over the crack length (d/a) in Figure 9.21. As reported before, different K_{IIc} results were obtained for the different testing methods and the geometries. With the normalization of the vertical scale as above, no matter what value is entered for K_{IIc} variation trends of the stress distribution curves in the Figure 9.21 become independent of the individual test result of a particular core-based geometry. This way, independent comparisons of the trends of the different methods and the associated geometries become possible.

A perfect numerical modeling for observing the exact stress distribution around a notch or crack tip is obviously not possible. In Figure 9.21, stress distribution trend corresponding to the SNDB and CSTBD geometries shows very much parallel tendency to the stress distribution curve of the analytical solution. The trend curves of these three are almost coincident. Of course, there is a level distance between the curves, corresponding to the different stress intensities of the different geometries considered.

The parallel tendency however, becomes questionable as the specimen boundary is approached. For SNDB and CSTBD geometries, deviation from the general trend starts at around *d/a* of 0.5-0.6. As the specimen boundary is approached, this deviation becomes more pronounced at around *d/a=0.7*. This deviation close to the boundary is expected, referring to the boundary influence issue related to the core-based specimen geometries.

On the other hand, stress distribution trend along the notch front of SCB geometry model shows noticeable deviation and fluctuation from the analytically expected behavior. This deviation is observed very early, even *d/a* around 0.25.

Comparing the von Mises stress trend around the notch tip, for all specimen geometries this stress shows a decreasing trend along Path 3. Von Mises stress at the notch tip is about 30% higher for SCB and SNDB specimen geometries compared to CSTBD geometry. This situation is depicted in Figure 9.22. An interesting observation is that von Mises stress distribution trend curves are almost parallel for CSTBD and SNDB while SCB curve shows some undulations and deviations from the general trend.

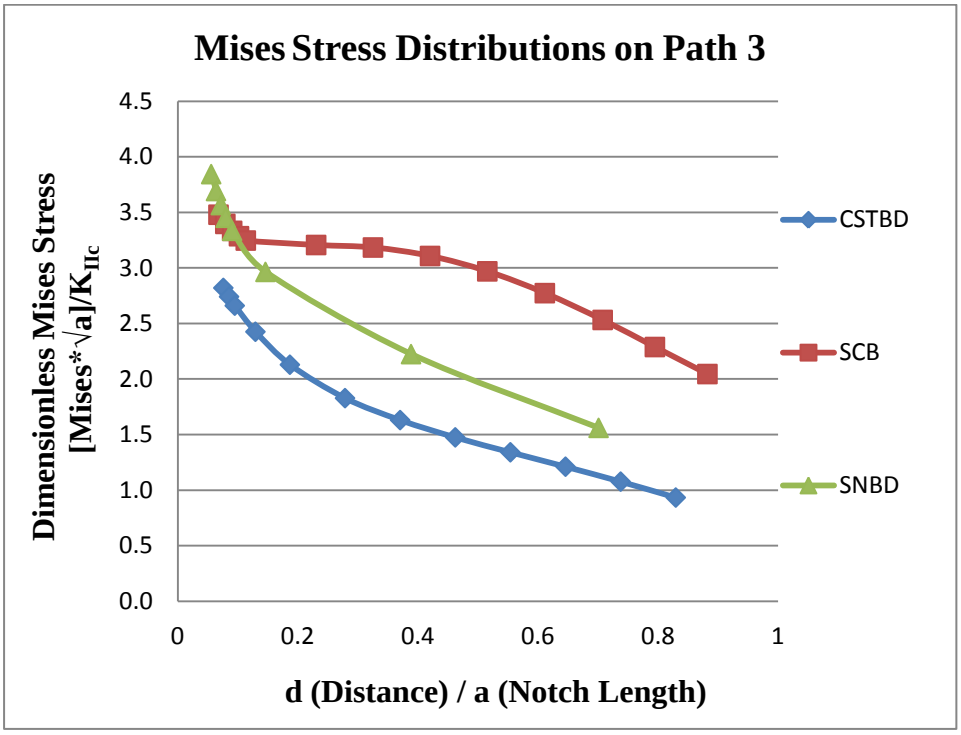

Figure 9.22 Dimensionless Mises stress distribution vs. *d* (Distance) / *a* (Notch Length) along Path 3 after the data refinement

9.3.4 Stress distributions along Path 4 for the various specimen models

In Figures 9.23, 9.24 and 9.25 position and geometric details of Path 4 for different specimen geometries are illustrated. A local primed coordinate system to the Path 4 is again assigned which is approximately oriented around 70° degree counterclockwise from the notch plane. As illustrated in the Figures 9.23, 9.24 and 9.25, this local system is defined by an x-axis perpendicular to the crack propagation direction (CPD) and y-axis parallel to the crack propagation direction (CPD).

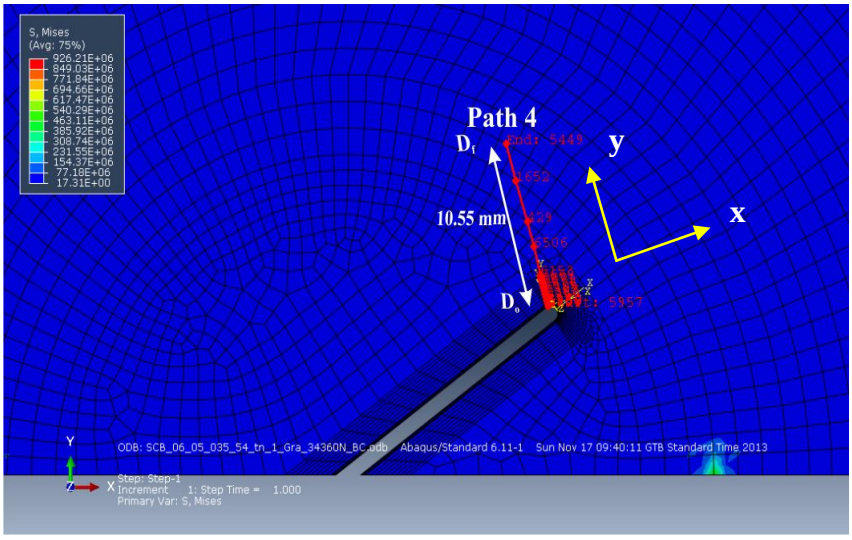

Figure 9.23 Position and geometric details of the Path 4 on the SCB specimen model

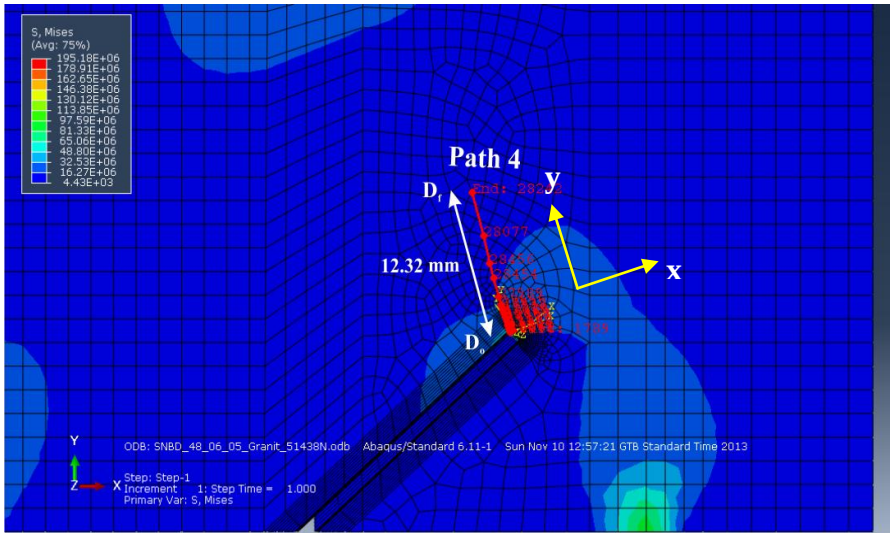

Figure 9.24 Position and geometric details of the Path 4 on the SNDB specimen model

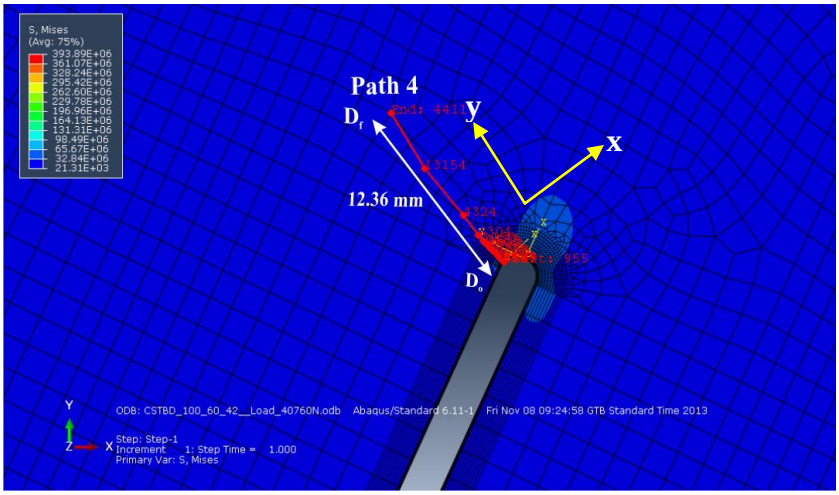

Figure 9.25 Position and geometric details of the Path 4 on the CSTBD specimen model

In order to compare the stress components along Path 4 for the different specimen models, stress distribution graphs in the dimensionless forms in terms of the stresses are generated for the models in Figures 9.26, 9.27, 9.28, 9.29 and 9.30.

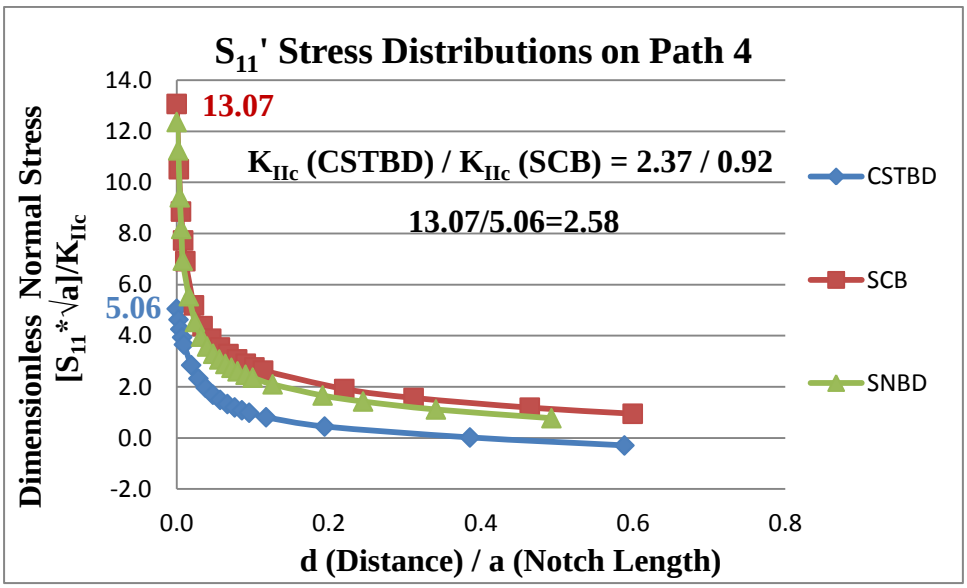

Figure 9.26 Dimensionless S_{11}' stress distribution vs. *d* (Distance) / *a* (Notch Length) along Path 4

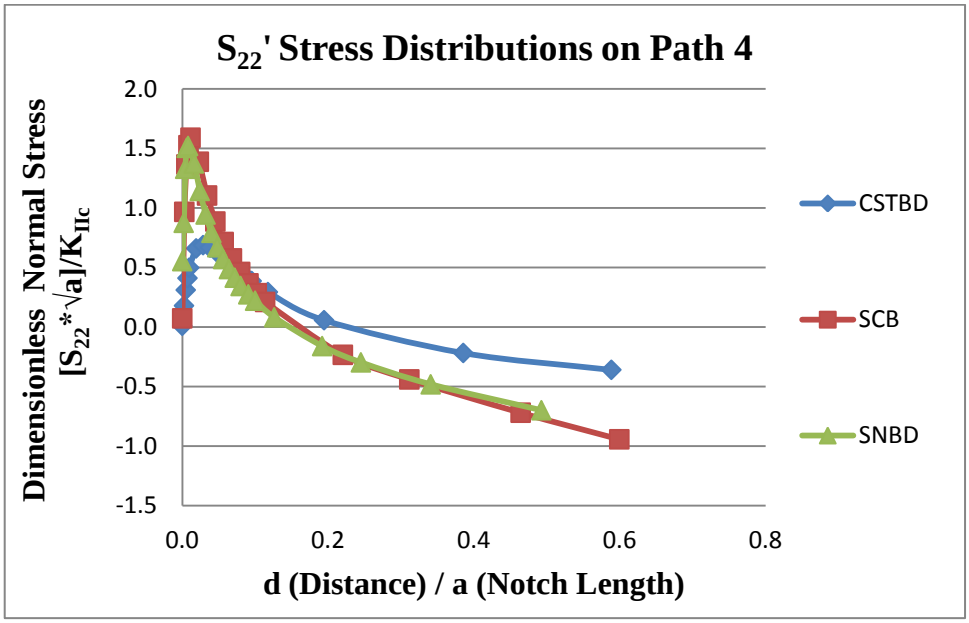

Figure 9.27 Dimensionless S_{22}' stress distribution vs. *d* (Distance) / *a* (Notch Length) along Path 4

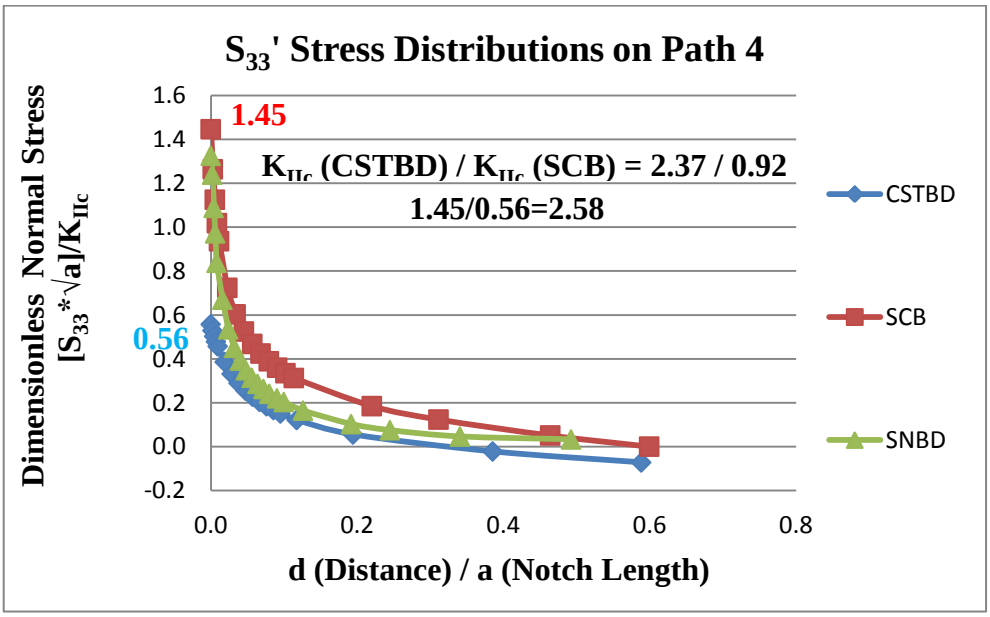

Figure 9.28 Dimensionless S_{33}' stress distribution vs. *d* (Distance) / *a* (Notch Length) along Path 4

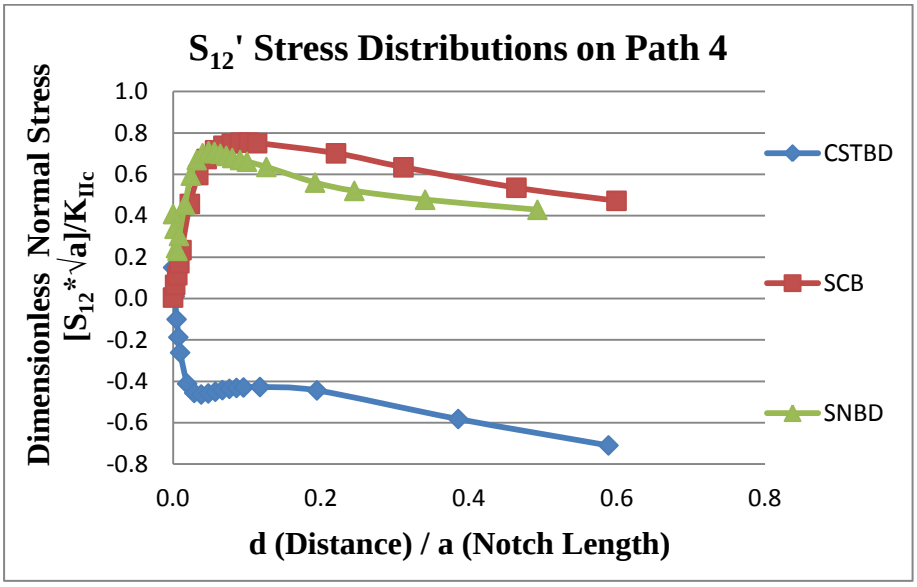

Figure 9.29 Dimensionless S_{12}' stress distribution vs. *d* (Distance) / *a* (Notch Length) along Path 4

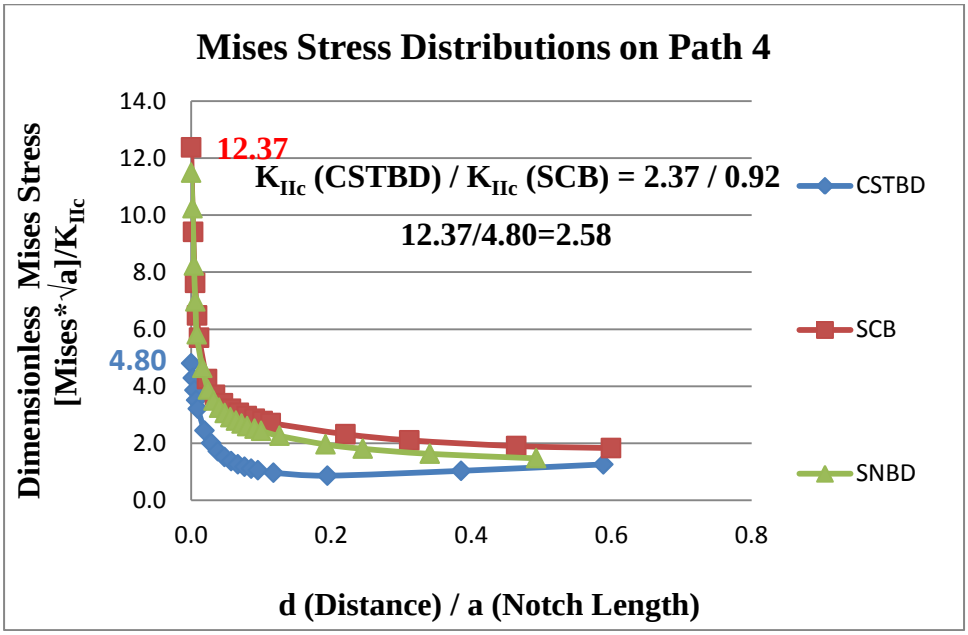

Figure 9.30 Dimensionless *Mises* stress distribution vs. *d* (Distance) / *a* (Notch Length) along Path 4

As reported before, the shear mode fracture toughness ratio for the CSTBD and SCB specimens has been found as 2.58, (K_{IIc} (CSTBD) / K_{IIc} (SCB) = 2.37 / 0.92 =2.58). In Figure 9.26, S_{11}' stress value of the CSTBD specimen model at the starting point of the Path 4 is 5.06. On the other hand, S_{11}'stress of the SCB specimen model at the starting point is 13.07. If these two values are divided as 13.07/5.06, the ratio 2.58 is obtained. This difference between the models of the two specimens along the crack propagation direction is interestingly parallel with the ratio of shear mode fracture toughness obtained from the tests on the SCB and CSTBD specimens.

Moreover, the same ratio is observed for the S_{33}' stress distributions and the *Mises* stress distributions in Figures 9.28 and 9.30. The von Mises stress values at the starting point of the Path 4 for the CSTBD and SCB specimens are computed as 4.80 and 12.37, respectively. The ratio found by dividing those two values equals to 2.58. S_{11}' normal stress which is perpendicular to the Path 4 is in tension for all the specimen models. By comparing these two ratios, the intensity of tension in the CSTBD specimen model is 2.58 times smaller than the one in the SCB specimen model.

This situation can be interpreted as that the crack can easily propagate with relatively low fracture energy input along the direction of Path 4 for the SCB specimens, because of the relatively high tension along the Path 4. On contrary to the SCB specimen, 2.58 times lower tension along the Path 4 is observed for the CSTBD specimen model. Hence, the crack needs more energy to propagate in the case of the CSTBD specimen for propagation towards the maximum principal stress direction which is the concentrated load application point of the Brazilian type loading configuration. Shear mode fracture toughness difference between the testing results with the CSTBD and SCB specimens for the same rock can be explained with the arguments above.

9.4 Stiffness comparison for different core-based specimen geometries

In experiments, displacements were recorded by using the vertically positioned displacement transducers. In order to compare the stiffness (k_f) values of the specimens, load-displacement plots in Figure 9.31 was prepared. Stiffness is computed as the slope of the tangent line at the 50% of the fracturing load. Values computed this way are presented in Table 9.2 below.

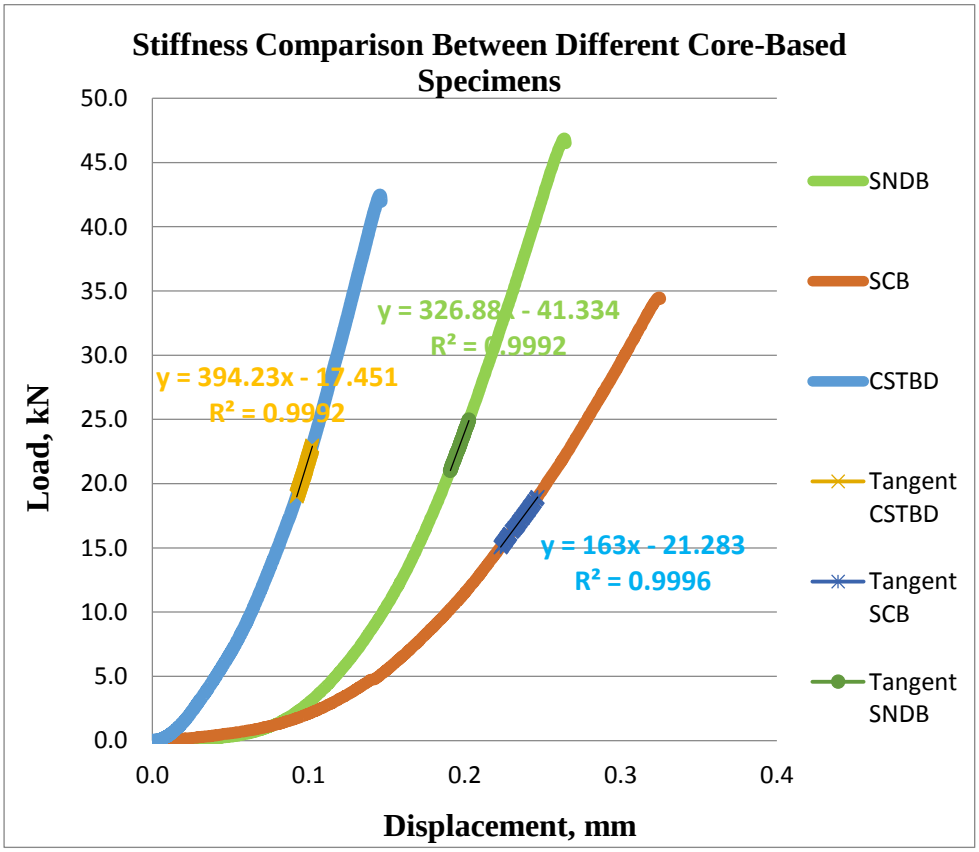

Figure 9.31 Stiffness comparisons between different core-based specimens

As it is seen from Figure 9.30, highest stiffness was obtained for the Brazilian Disc (CSTBD) specimen. The lowest stiffness was associated with the semi-circular disc (SCB) specimen geometry. The stiffness of the circular-plate type (SNDB) specimen geometry lies in the between the two. The CSTBD specimen

geometry is about 2.5 times stiffer than the semi-circular disc (SCB) specimen geometry. It is interesting to note the surprisingly close relationship between the stiffness ratio and the shear mode fracture toughness ratio of the CSTBD and SCB specimens which is around 2.58. Based on the experimental work, mode II fracture toughness ratio is computed as K_{IIc} (CSTBD) / K_{IIc} (SCB) = 2.37 / 0.92 =2.58 and the stiffness ratio is computed as k_f (CSTBD) / k_f (SCB) = 394 / 163 =2.41.

Table 9.2 Stiffness values for different core-based specimen geometries

	SCB	SNDB	CSTBD
Stiffness (kN/mm)	$129.60_{(2)}$ ± 47.31	$319.73_{(5)}$ ± 38.90	$401.00_{(6)}$ ± 80.45

Having a medium stiffness and being stiffer than the commonly-employed three-point bend geometry of SCB in fracture toughness testing, the circular-plate type SNDB specimens may prove to be a challenging three-point bending type specimen. In order to come out with supportive evidence, further research is needed about this argument.

9.5 Comparison of stress distributions along the paths between different core-based specimen models and pure shear plate model

After analyzing and comparing stress distributions for individual core-based mode II type specimens, the same stress paths were again generated for the specimen geometries under investigation and pure shear plate model. To investigate which specimen geometry shows similar trends as in the originally defined pure shear plate model.

Pure shear plate model under mode II loading based on the original definition of the related loading mode had the dimensions and the loading levels given in Table 9.3 in which details related to the SCB, SNDB and CSTBD geometries are also given.

Table 9.3 Dimensions and the loading levels applied to the 2D centrally notched plate under pure mode II loading

Dimensions and loading levels	Values
Width of the plate, *2W*	0.84 m
Height of the plate, *2H*	0.84 m
Plane Strain Thickness of the plate, *B*	0.504 m
Crack (seam-type) length of the plate, *2a*	42 mm
Notch thickness for CSTBD, t_n	2.5 mm
Notch thickness for SNDB and SCB, t_n	1 mm
Traction Stress on the plate for CSTBD, τ	9.22 MPa
Traction Stress on the plate for SCB, τ	3.58 MPa
Traction Stress on the plate for SNBD, τ	4.59 MPa
Young's modulus, *E*	38.9 GPa
Poisson's ratio, υ	0.11

Loading levels represented by traction stress entries in the table are set based on the K_{IIc} determined from the related test crack initiation load labeled as P_{cr}.

K_{IIc} for SNDB specimen has been determined as 1.18 MPa $\sqrt{m}$. After substituting this value into the Equation 9.2 as the K_{II} stress intensity factor entry, traction stress τ to be applied on the pure shear model plate is calculated as 4.59 MPa for an initial notch length of *2a*=42 mm.

$$K_{II} = \tau\sqrt{\pi a} \tag{9.4}$$

Traction stress τ for SCB and CSTBD model geometries have been computed in the same way by using the K_{IIc} results of these testing methods.

9.5.1 Stress distribution comparisons between CSTBD and pure shear plate model on Path 1

In Figures 9.32 and 9.33 position and geometric details of Path 1 for CSTBD and Pure Shear Plate Model geometries are illustrated.

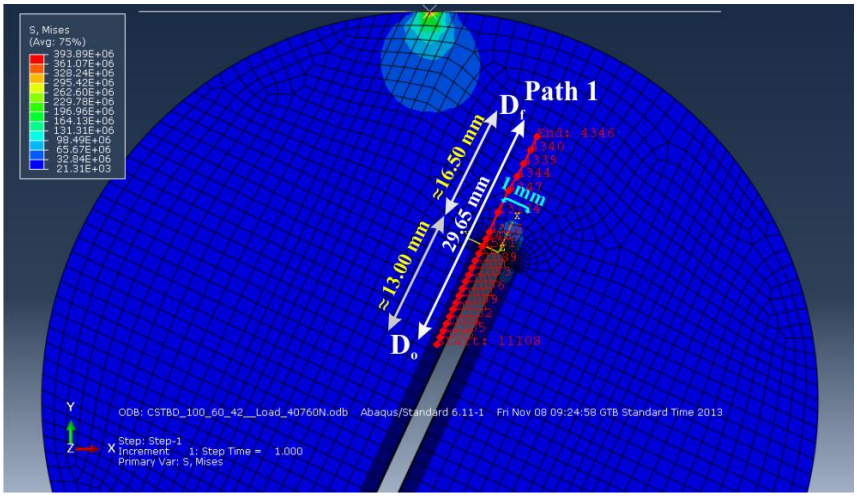

Figure 9.32 Position and geometric details of Path 1 on CSTBD specimen model

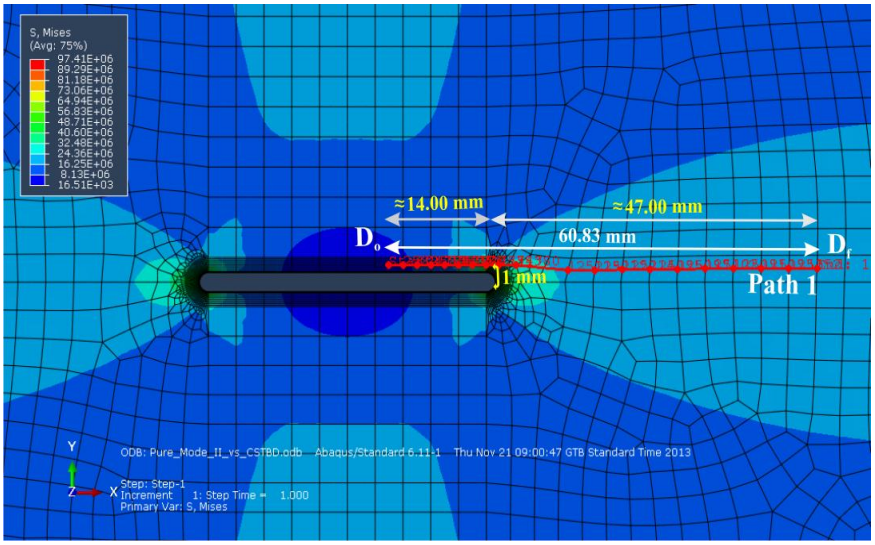

Figure 9.33 Position and geometric details of Path 1 on pure shear plate model

For stress analyses around the initial notch in terms of normal stress components of S_{11}', S_{22}', S_{33}' and the shear stress component of S_{12}', Path 1 is assigned parallel to the crack plane. As it is seen above in Figures 9.32 and 9.33, distance along the normal to the crack plane and the assigned path is about 1 mm away from the crack surface. Path 1 covers an overall distance of around d=30 mm for CSTBD specimen and *d*=60 mm for Pure Shear Plate Model. These distance assignments are marked in the figures related to the analyses of the stresses around and ahead of the initial notch plane.

In order to compare various stress components on Path 1, normalized stress variations along normalized paths in terms of *d/a* plots are generated for CSTBD specimen and Pure Shear Plate Model in Figures 9.34, 9.35, 9.36, 9.37 and 9.38 respectively. Notch tip regions are marked and highlighted in these figures.

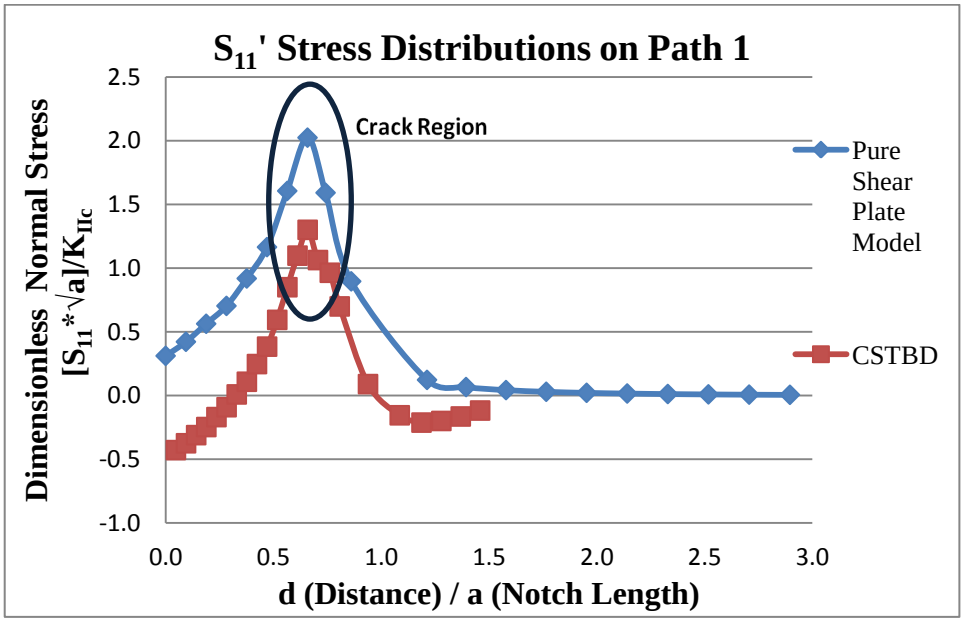

Figure 9.34 Dimensionless S_{11}' stress distribution vs. *d* (Distance) / *a* (Notch Length) along Path 1

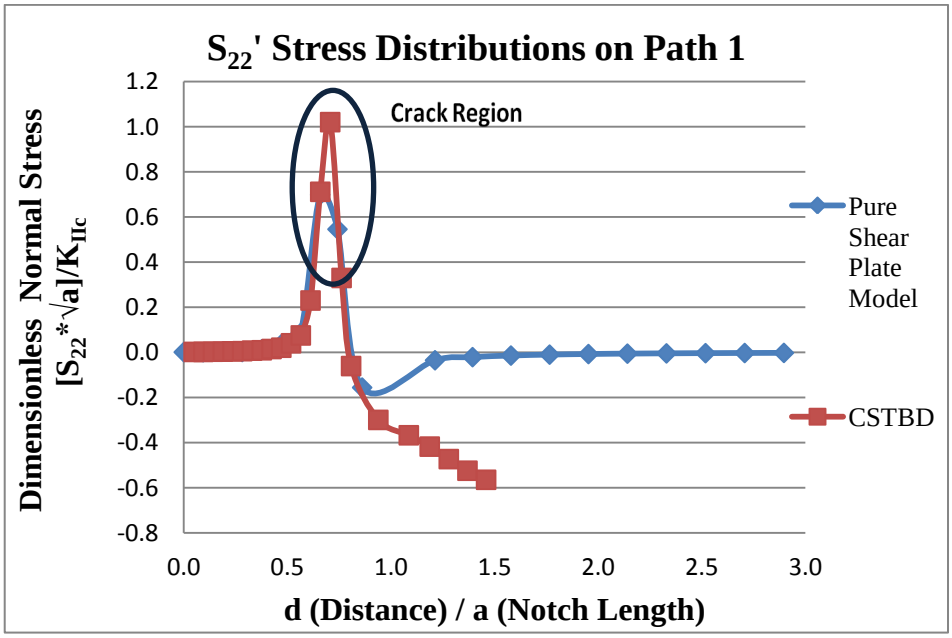

Figure 9.35 Dimensionless S_{22}' stress distribution vs. *d* (Distance) / *a* (Notch Length) along Path 1

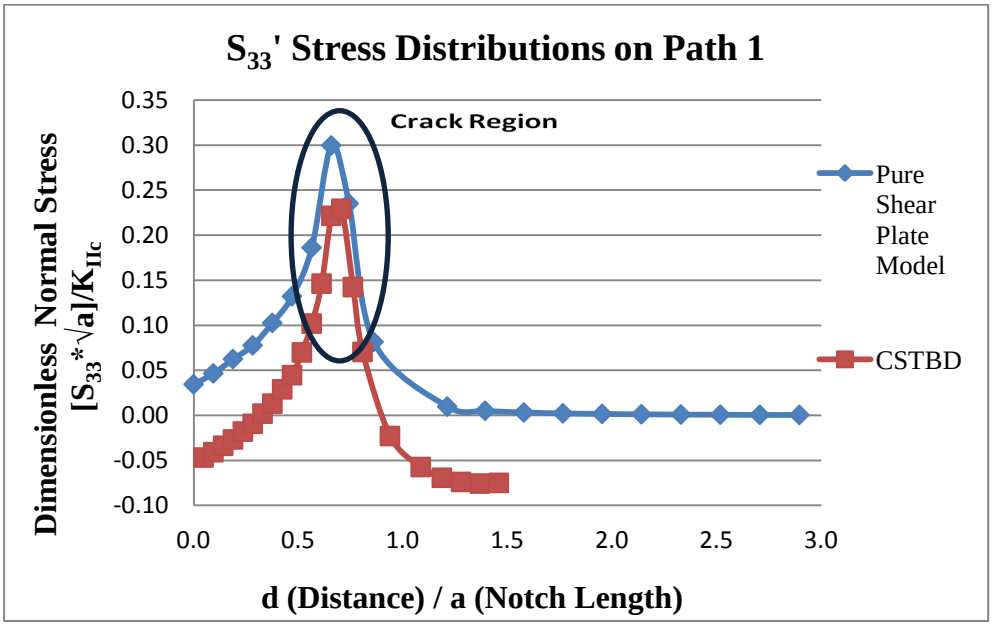

Figure 9.36 Dimensionless S_{33}' stress distribution vs. *d* (Distance) / *a* (Notch Length) along Path 1

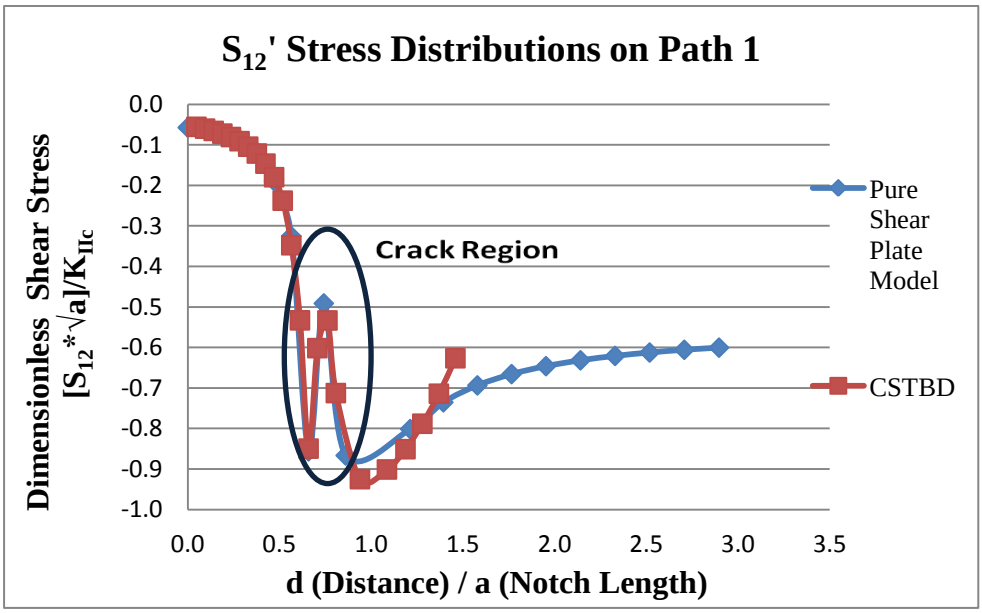

Figure 9.37 Dimensionless S_{12}' stress distribution vs. *d* (Distance) / *a* (Notch Length) along Path 1

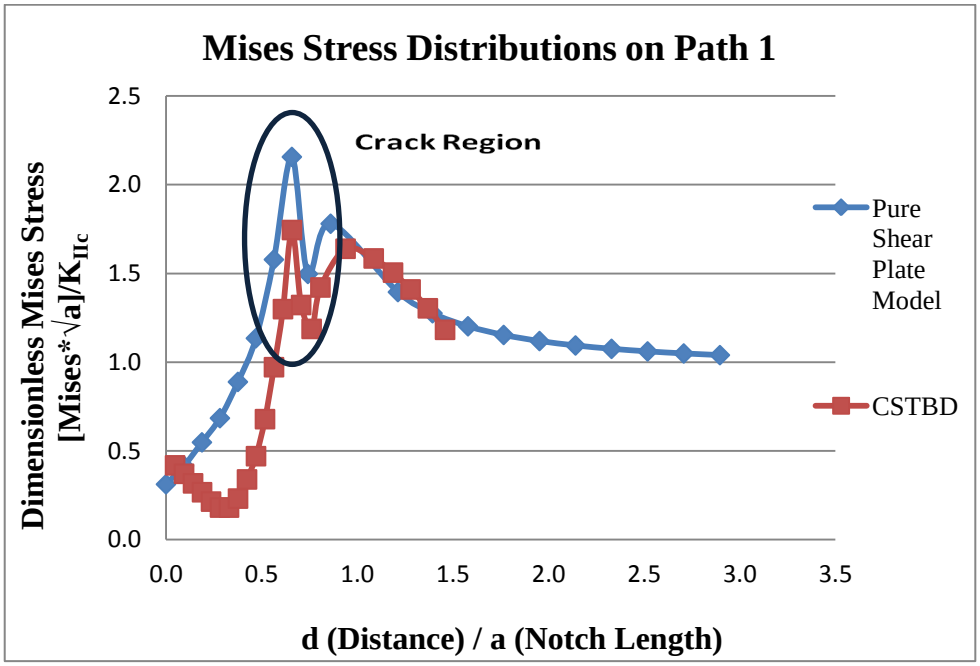

Figure 9.38 Dimensionless *Mises* stress distribution vs. *d* (Distance) / *a* (Notch Length) along Path 1

9.5.2 Stress distribution comparisons between CSTBD and pure shear plate model on Path 2

In Figures 9.39 and 9.40 position and geometric details of Path 2 for CSTBD specimen and Pure Shear Plate Model geometries are illustrated.

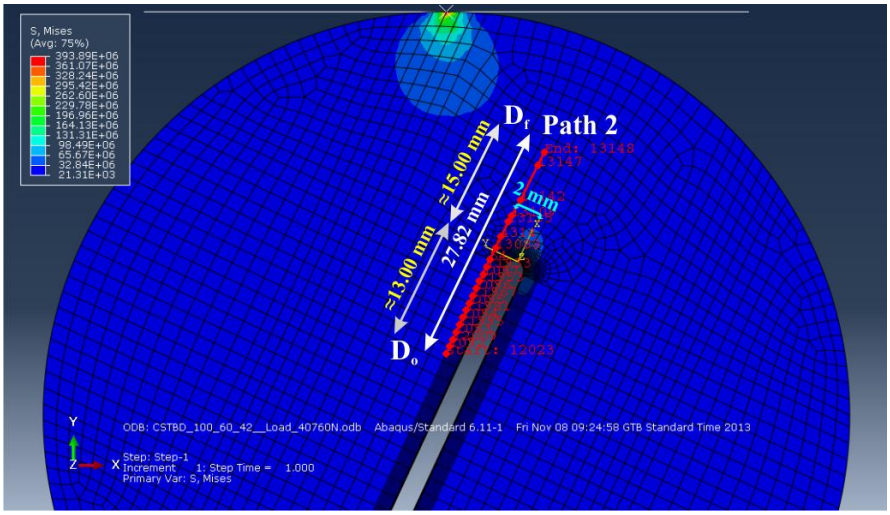

Figure 9.39 Position and geometric details of Path 2 on CSTBD specimen model

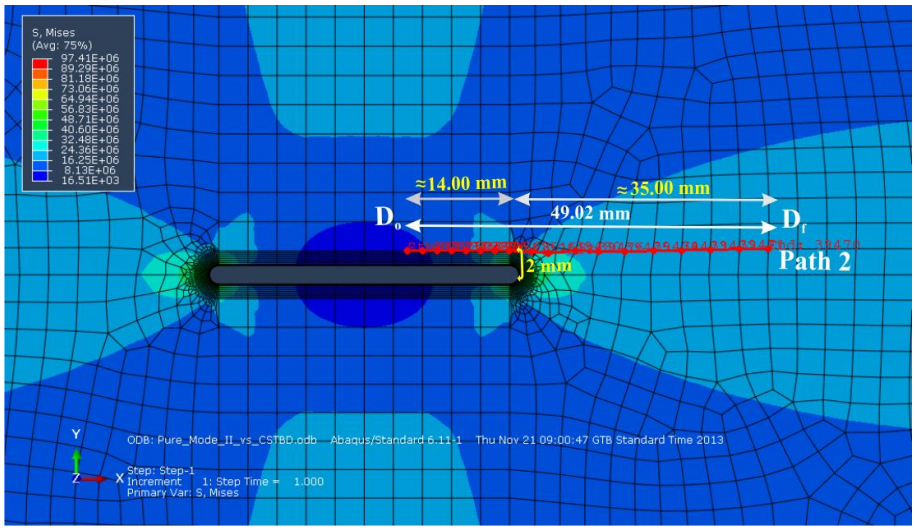

Figure 9.40 Position and geometric details of Path 2 on Pure Shear Plate Model

For stress analyses around the initial notch in terms of normal components of S_{11}', S_{22}', S_{33}' stresses and the shear component of S_{12}' stress, Path 2 is assigned parallel to the crack plane. As it is seen above in Figures 9.39 and 9.40 distance along the normal to the crack plane and the assigned path is about 2 mm away from the crack surface. Path 2 covers an overall distance of around *d*=28 mm for CSTBD specimen and *d*=49 mm for Pure Shear Plate Model respectively. These distance assignments are marked in the figures related to the analyses of the stresses around and ahead of the initial notch plane.

In order to compare various stress components on Path 2, normalized stress variations along normalized paths in terms of *d/a* plots are generated for CSTBD specimen and Pure Shear Plate Model in Figures 9.41, 9.42, 9.43, 9.44 and 9.45 respectively. Notch tip regions are marked and highlighted in these figures.

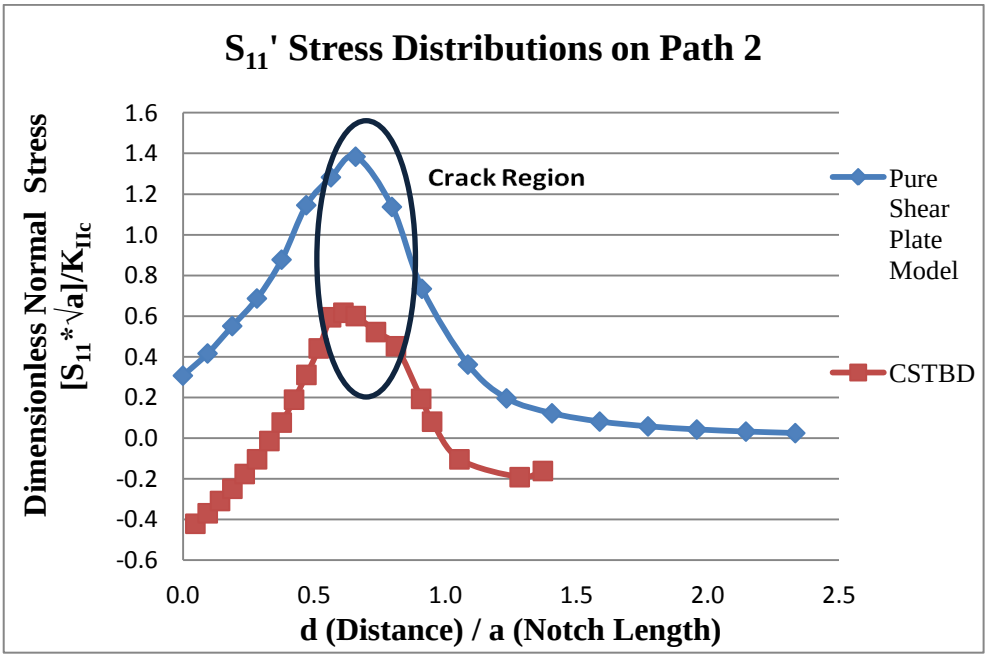

Figure 9.41 Dimensionless S_{11}' stress distribution vs. *d* (Distance) / *a* (Notch Length) along Path 2

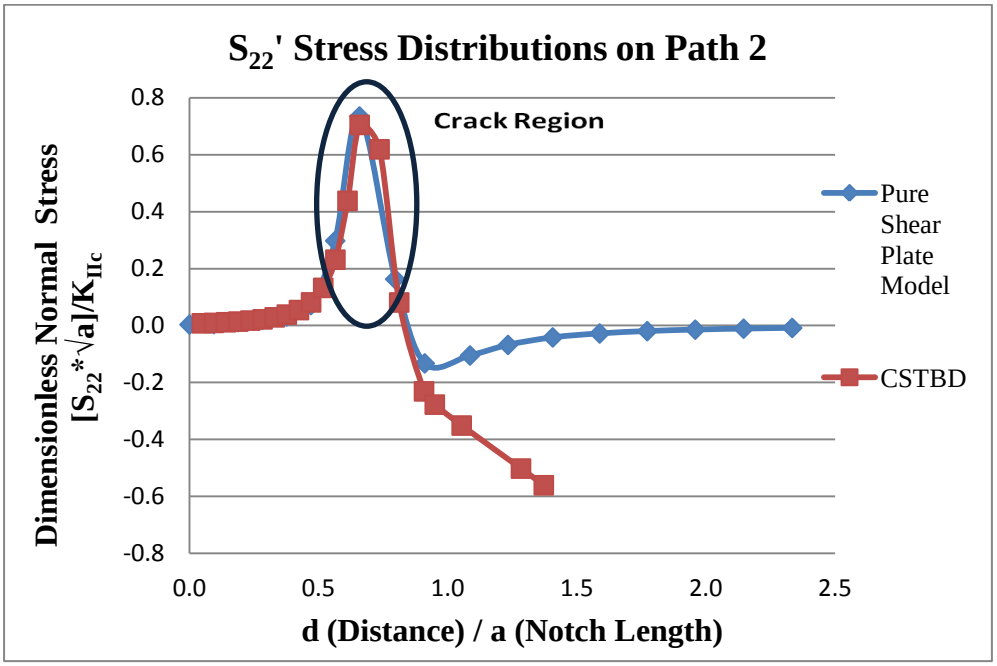

Figure 9.42 Dimensionless S_{22}' stress distribution vs. *d* (Distance) / *a* (Notch Length) along Path 2

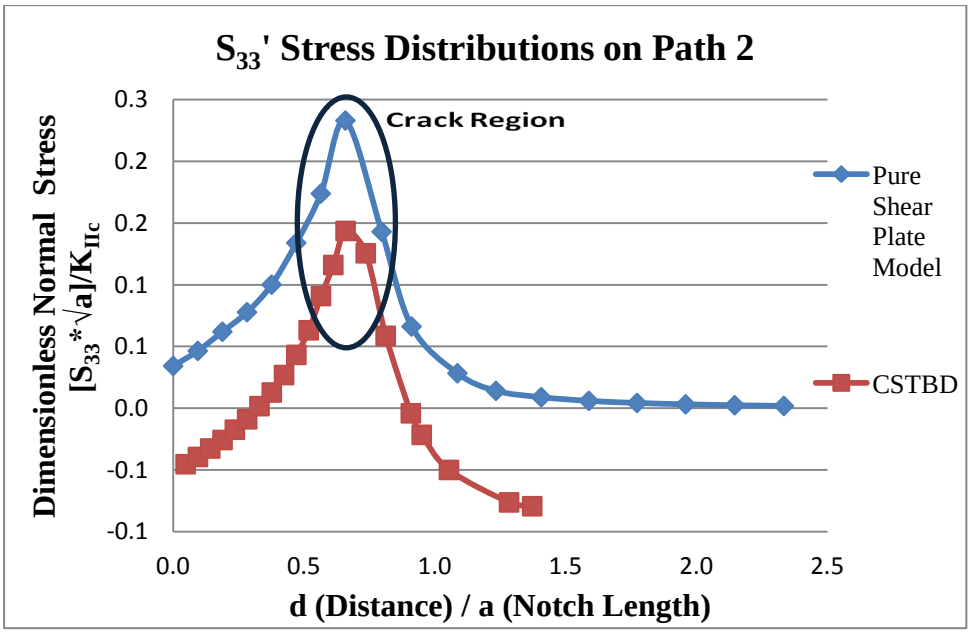

Figure 9.43 Dimensionless S_{33}' stress distribution vs. *d* (Distance) / *a* (Notch Length) along Path 2

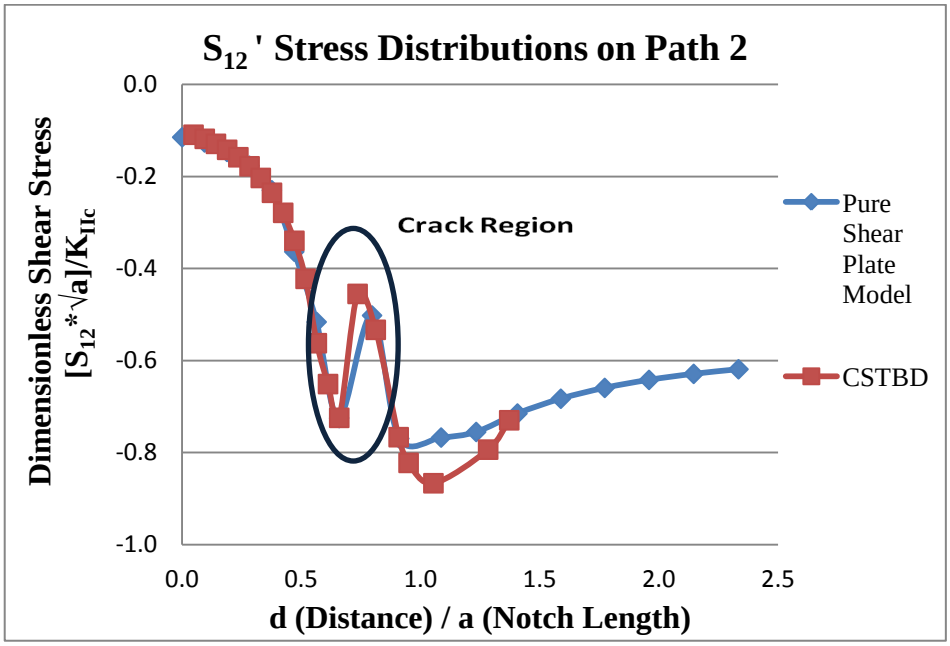

Figure 9.44 Dimensionless S_{12}' stress distribution vs. *d* (Distance) / *a* (Notch Length) along Path 2

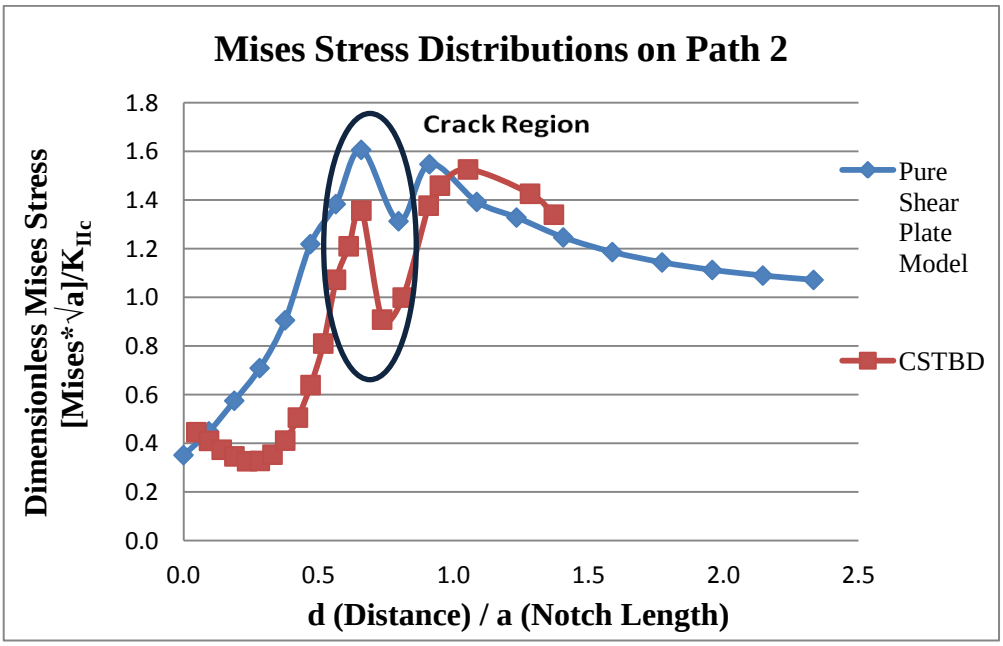

Figure 9.45 Dimensionless *Mises* stress distribution vs. *d* (Distance) / *a* (Notch Length) along Path 2

9.5.3 Stress distribution comparisons between CSTBD and pure shear plate model on Path 3

In Figures 9.46 and 9.47 position and geometric details of Path 3 for CSTBD specimen and Pure Shear Plate Model geometries are illustrated.

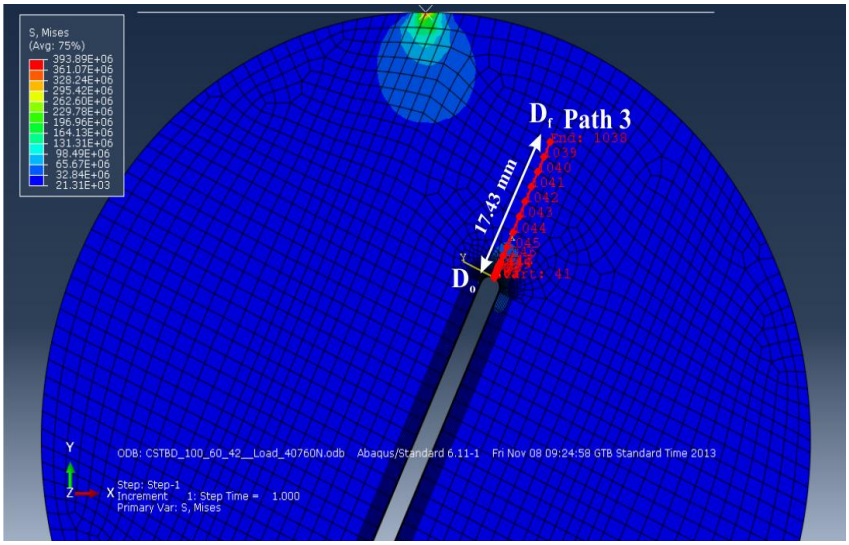

Figure 9.46 Position and geometric details of Path 3 on CSTBD specimen model

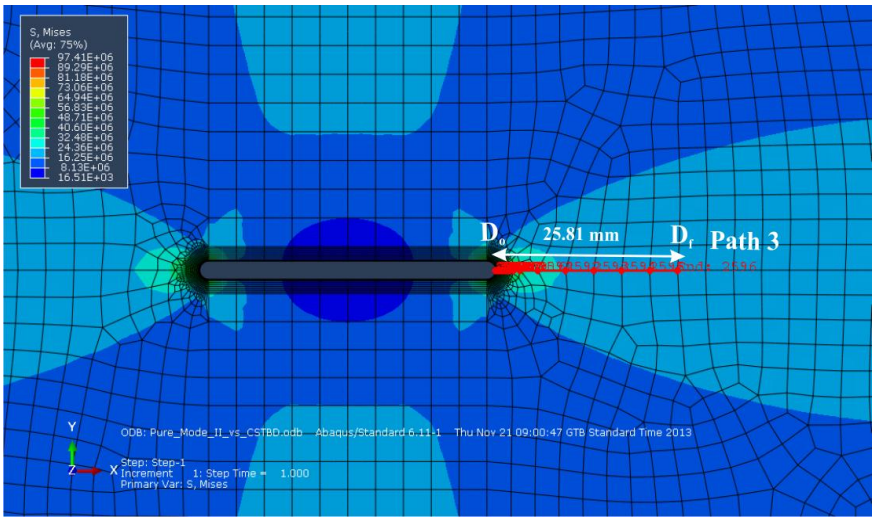

Figure 9.47 Position and geometric details of Path 3 on Pure Shear Plate Model

For stress analyses around the initial notch in terms of normal components of S_{11}', S_{22}', S_{33}' stresses and the shear component of S_{12}' stress, Path 3 starts at the notch tip where the local reference system is positioned and extends to the outer boundary of the specimen parallel to the plane of the initial notch. Path 3 is marked in the in Figures 9.46 and 9.47 related to the analyses of the stresses ahead of the initial notch plane.

In order to compare various stress components on Path 3, normalized stress variations along normalized paths in terms of *d/a* plots are generated for CSTBD specimen and Pure Shear Plate Model in Figures 9.48, 9.49, 9.50, 9.51 and 9.52 respectively.

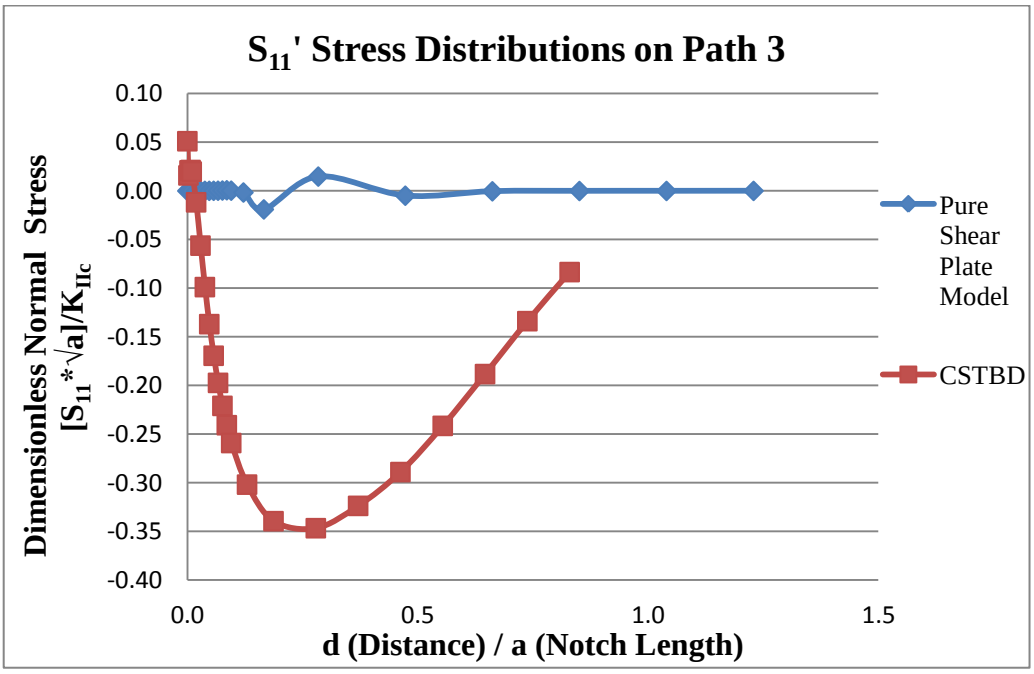

Figure 9.48 Dimensionless S_{11}' stress distribution vs. *d* (Distance) / *a* (Notch Length) along Path 3

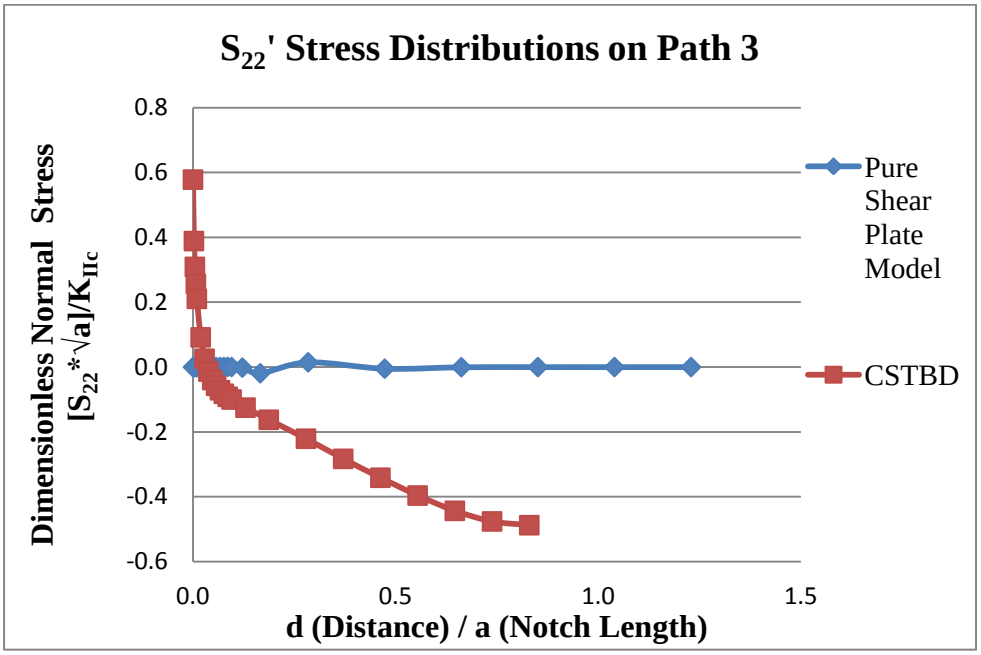

Figure 9.49 Dimensionless S_{22}' stress distribution vs. *d* (Distance) / *a* (Notch Length) along Path 3

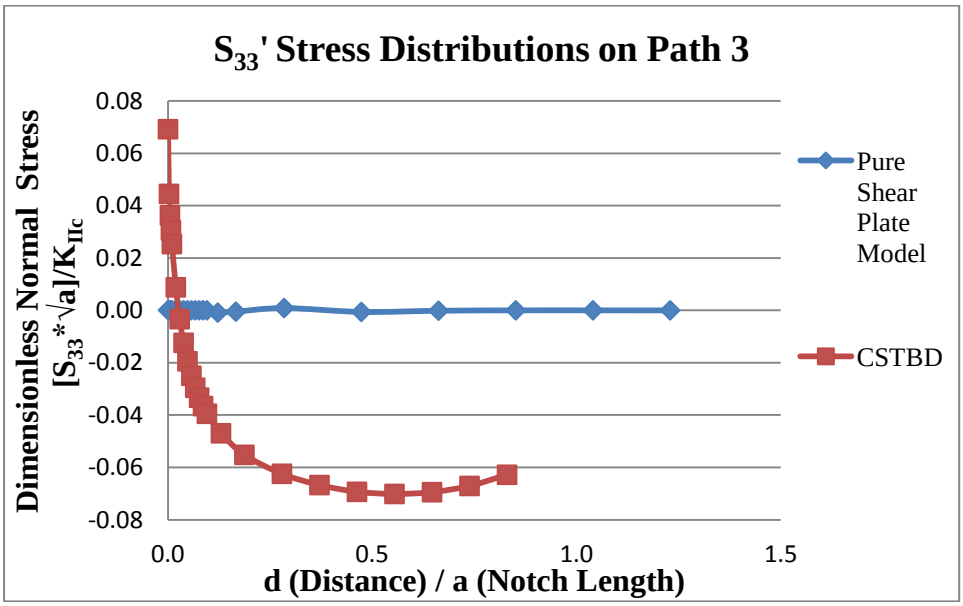

Figure 9.50 Dimensionless S_{33}' stress distribution vs. *d* (Distance) / *a* (Notch Length) along Path 3

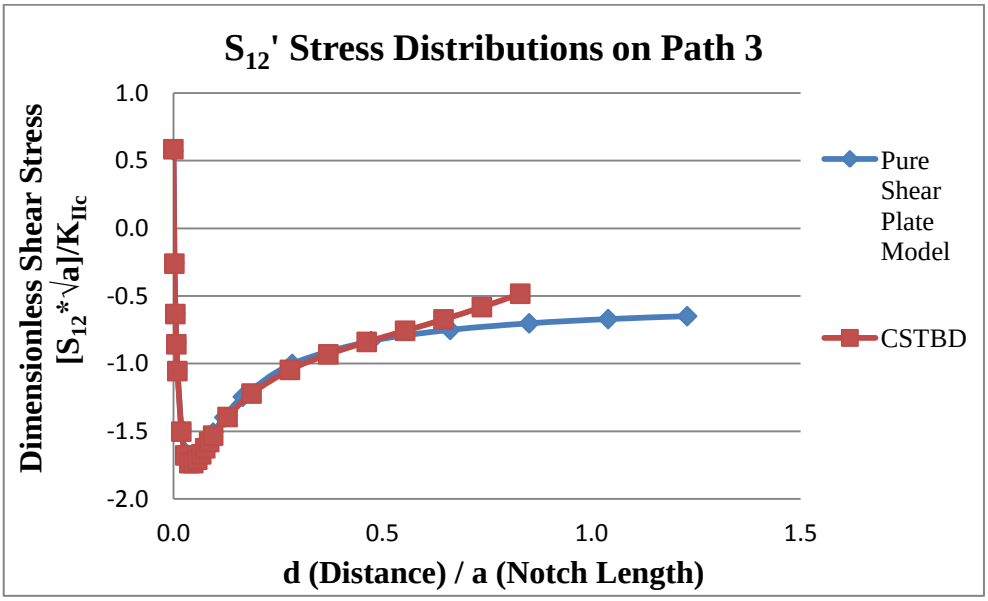

Figure 9.51 Dimensionless S_{12}' stress distribution vs. *d* (Distance) / *a* (Notch Length) along Path 3

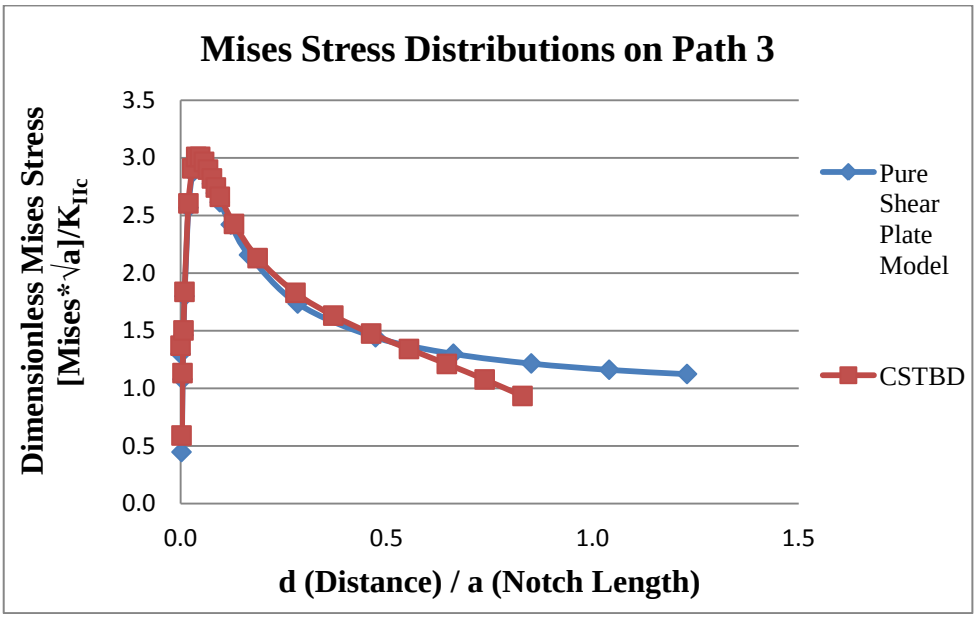

Figure 9.52 Dimensionless *Mises* stress distribution vs. *d* (Distance) / *a* (Notch Length) along Path 3

9.5.4 Stress distribution comparisons between CSTBD and pure shear plate model on Path 4

In Figures 9.53 and 9.54 position and geometric details of Path 4 for CSTBD specimen and Pure Shear Plate Model geometries are illustrated.

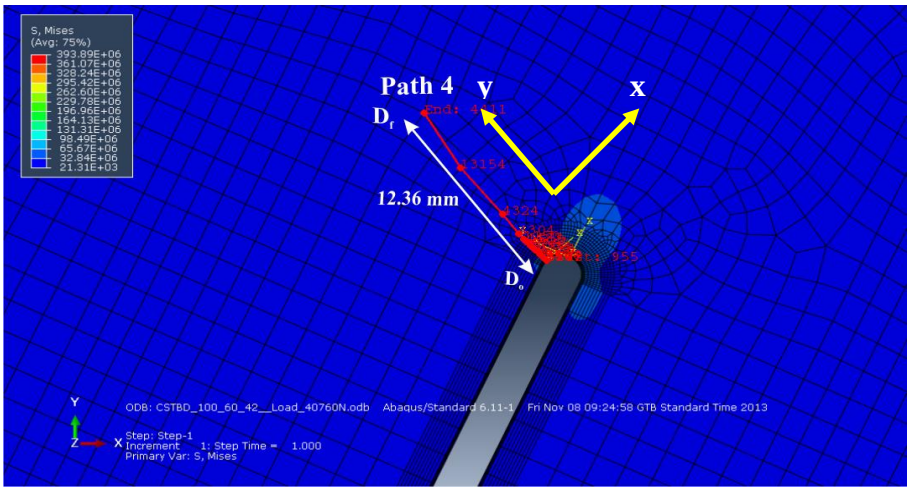

Figure 9.53 Position and geometric details of Path 4 on CSTBD specimen model

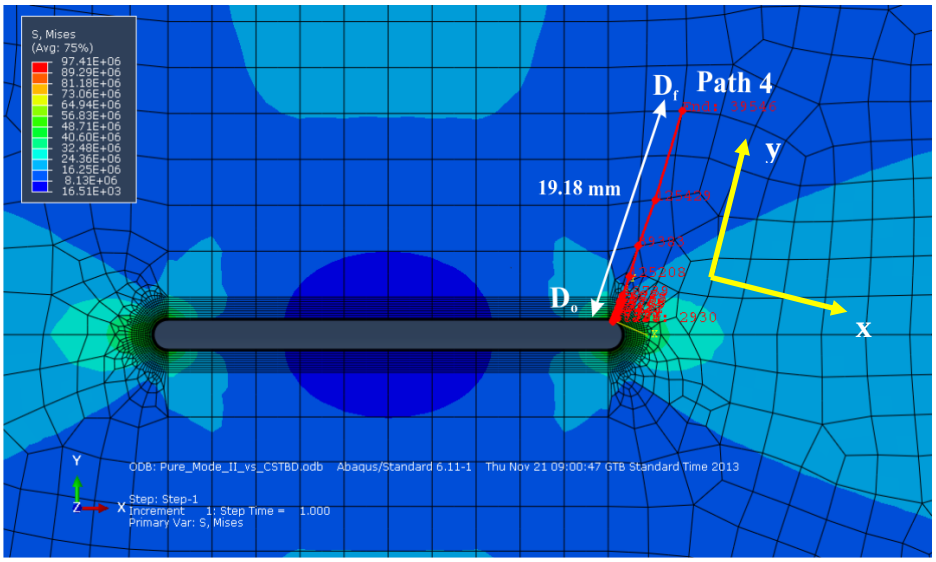

Figure 9.54 Position and geometric details of Path 4 on Pure Shear Plate Model

Path 4 was located near the notch tip where the notch was propagated. This path was generated after transforming the global coordinate system into local co-ordinate system approximately oriented around 70° degrees counterclockwise from the notch plane. As it is illustrated in Figures 9.53 and 9.54 this local system is defined by an x-axis perpendicular to the crack propagation direction (CPD) and y-axis parallel to the crack propagation direction (CPD).

In order to compare various stress components on Path 4, normalized stress variations along normalized paths in terms of a *d/a* plots are generated for CSTBD specimen and Pure Shear Plate Model in Figures 9.55, 9.56, 9.57, 9.58 and 9.59 respectively.

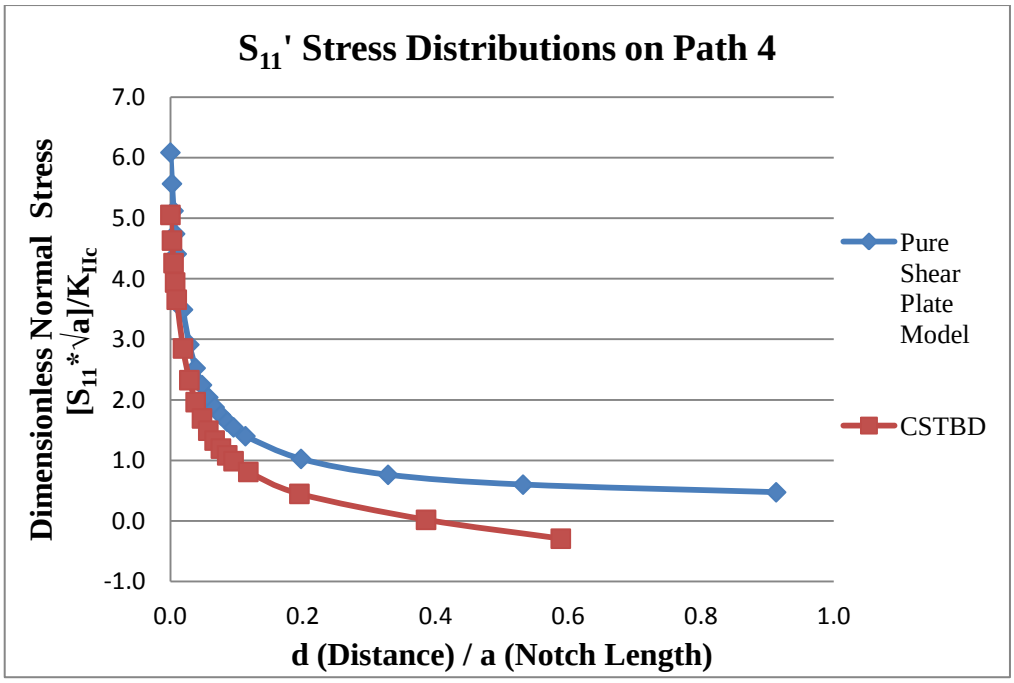

Figure 9.55 Dimensionless S_{11}' stress distribution vs. *d* (Distance) / *a* (Notch Length) along Path 4

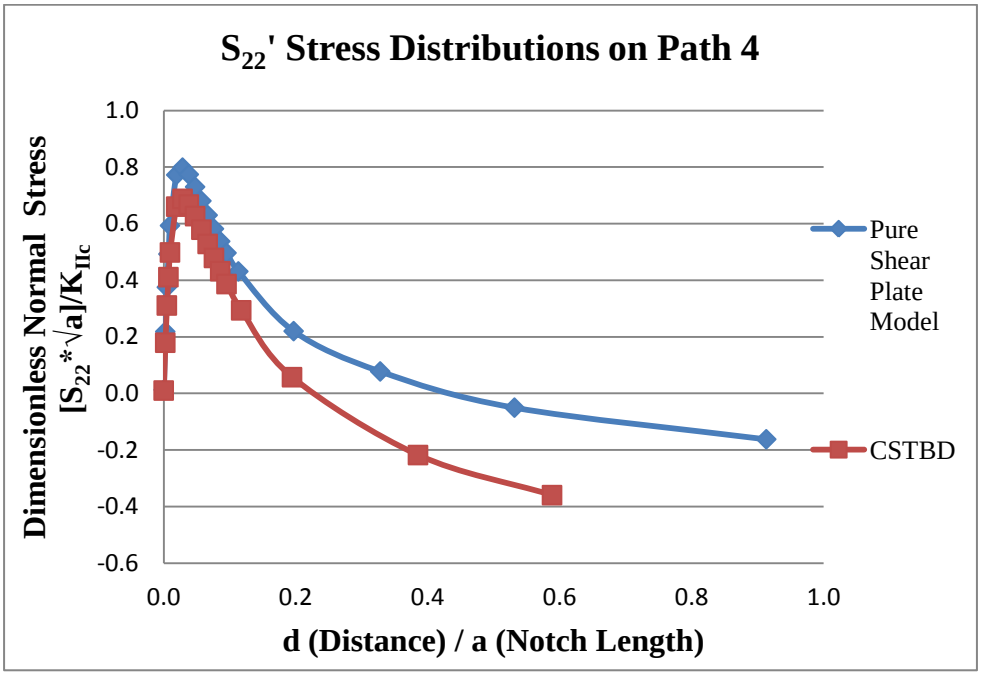

Figure 9.56 Dimensionless S_{22}' stress distribution vs. *d* (Distance) / *a* (Notch Length) along Path 4

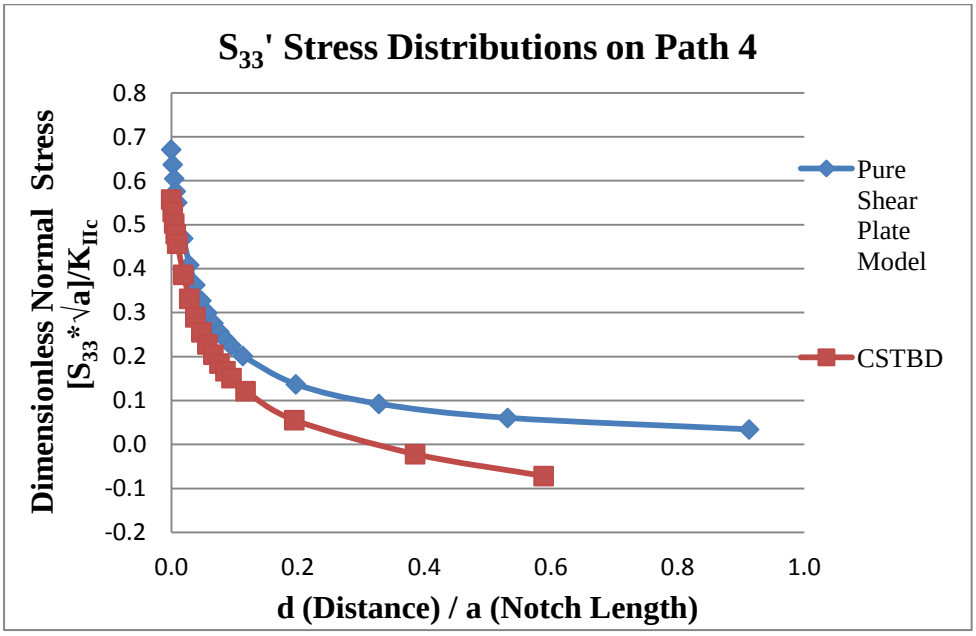

Figure 9.57 Dimensionless S_{33}' stress distribution vs. *d* (Distance) / *a* (Notch Length) along Path 4

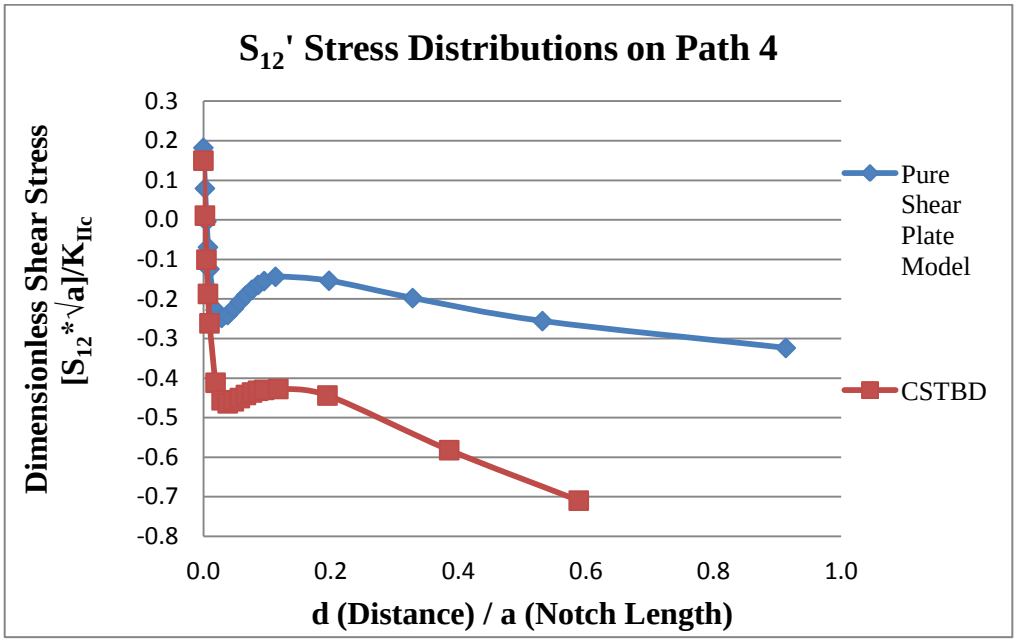

Figure 9.58 Dimensionless S_{12}' stress distribution vs. *d* (Distance) / *a* (Notch Length) along Path 4

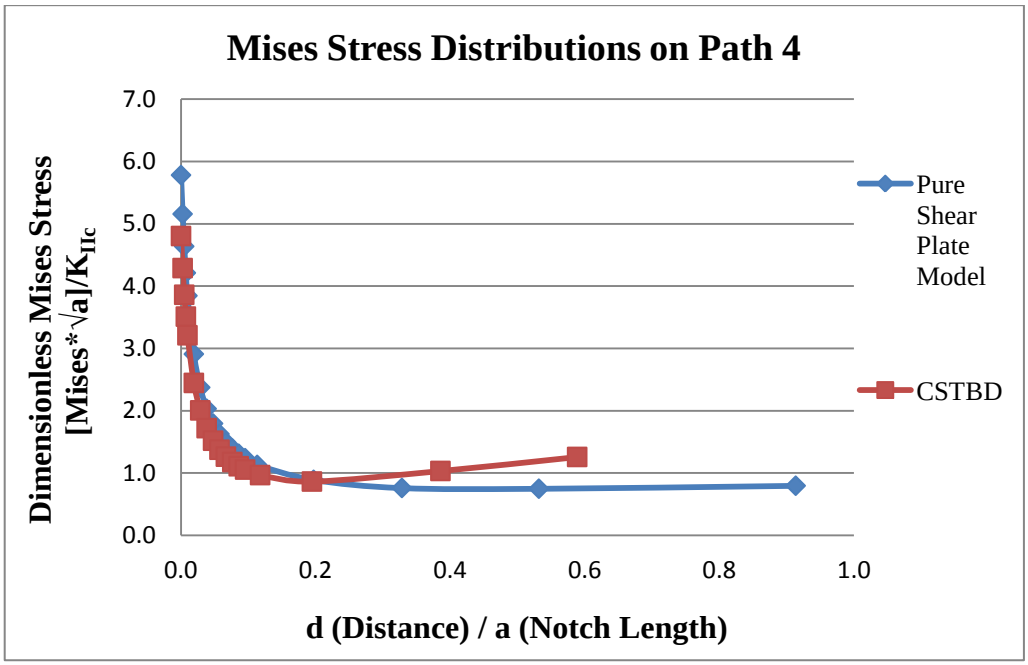

Figure 9.59 Dimensionless *Mises* stress distribution vs. *d* (Distance) / *a* (Notch Length) along Path 4

9.5.5 Stress distribution comparisons between SCB and pure shear plate model on path 1

In Figures 9.60 and 9.61 position and geometric details of Path 1 for SCB specimen and Pure Shear Plate Model geometries are illustrated.

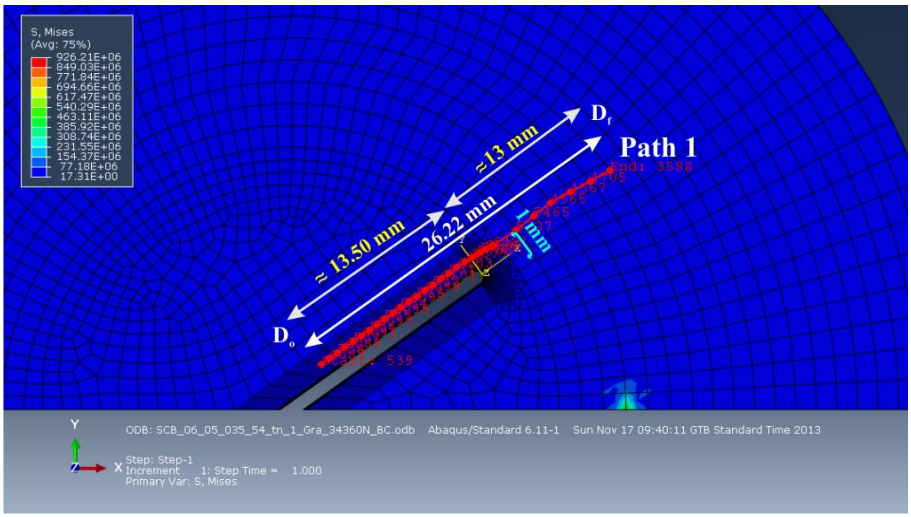

Figure 9.60 Position and geometric details of Path 1 on SCB specimen model

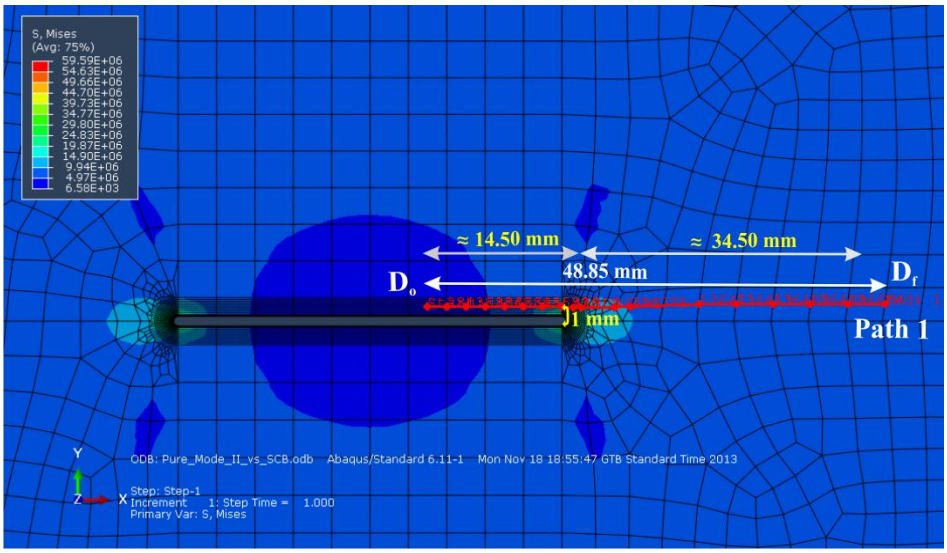

Figure 9.61 Position and geometric details of Path 1 on Pure Shear Plate Model

For stress analyses around the initial notch in terms of normal components of S_{11}', S_{22}' and S_{33}' stresses, and the shear component of S_{12}' stress, Path 1 is assigned parallel to the crack plane. As it is seen above in Figures 9.60 and 9.61 distance along the normal to the crack plane and the assigned path is about 1 mm away from the crack surface. Path 1 covers an overall distance of around *d*=26 mm for SCB specimen and *d*=49 mm for Pure Shear Plate Model. These distance assignments are marked in the figures related to the analyses of the stresses around and ahead of the initial notch plane.

In order to compare various stress components on Path 1, normalized stress variations along normalized paths in terms of *d/a* plots are generated for SCB specimen and Pure Shear Plate Model in Figures 9.62, 9.63, 9.64, 9.65 and 9.66 respectively. Notch tip regions are marked and highlighted in these figures.

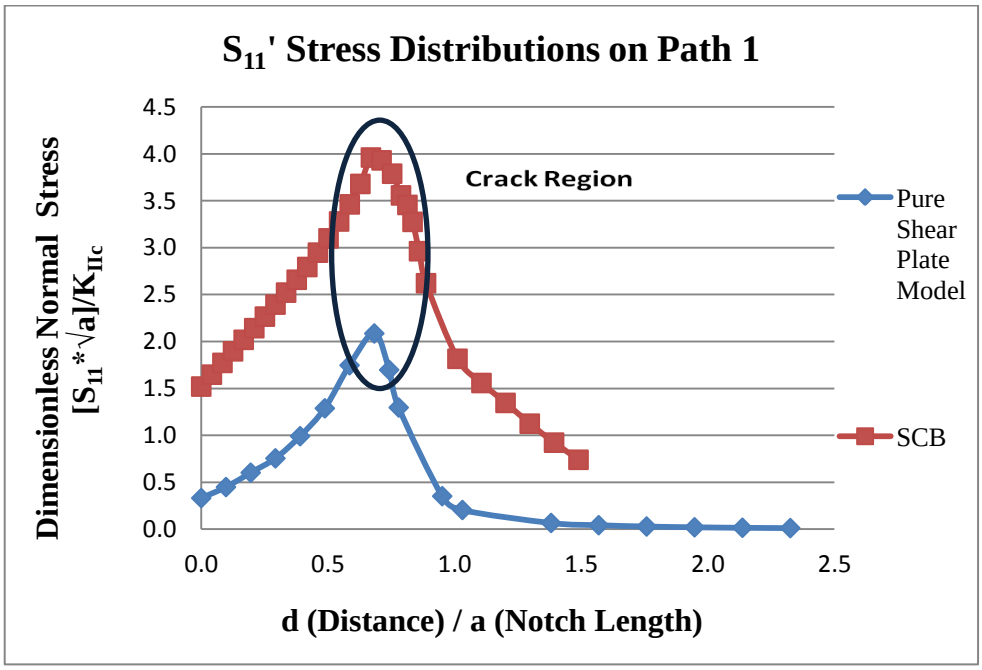

Figure 9.62 Dimensionless S_{11}' stress distribution vs. *d* (Distance) / *a* (Notch Length) along Path 1

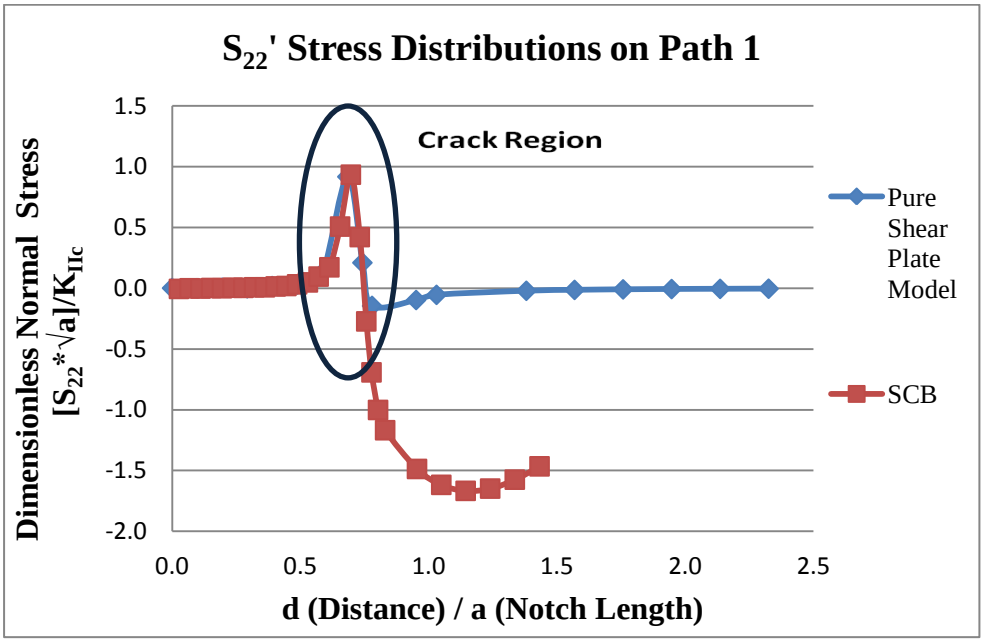

Figure 9.63 Dimensionless S_{22}' stress distribution vs. *d* (Distance) / *a* (Notch Length) along Path 1

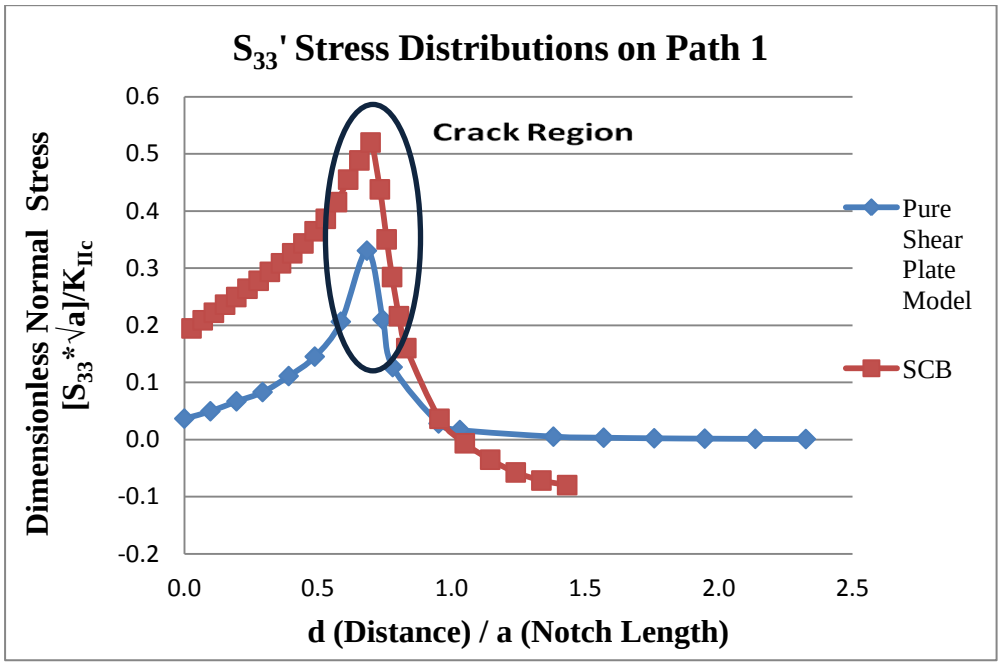

Figure 9.64 Dimensionless S_{33}' stress distribution vs. *d* (Distance) / *a* (Notch Length) along Path 1

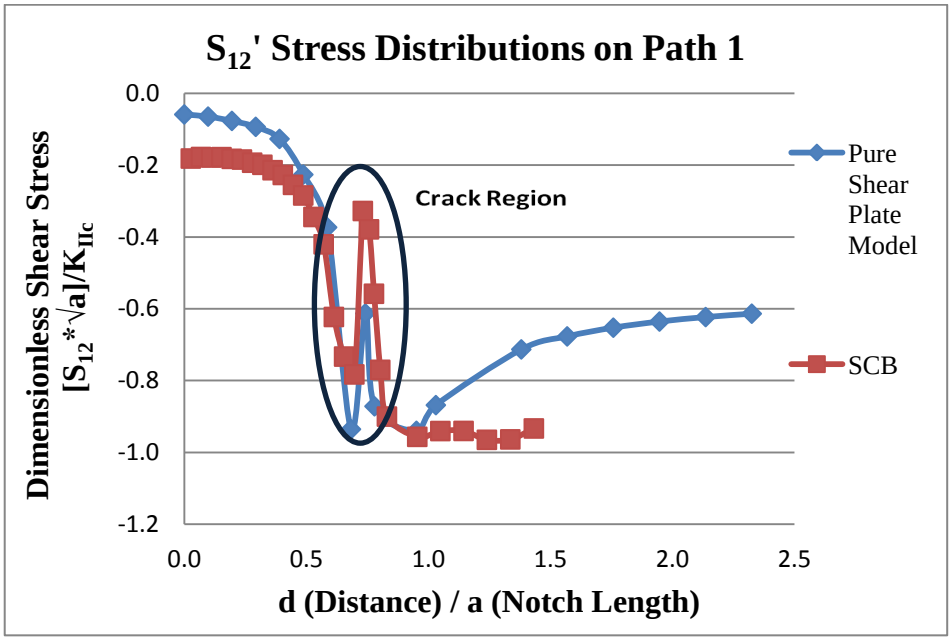

Figure 9.65 Dimensionless S_{12}' stress distribution vs. *d* (Distance) / *a* (Notch Length) along Path 1

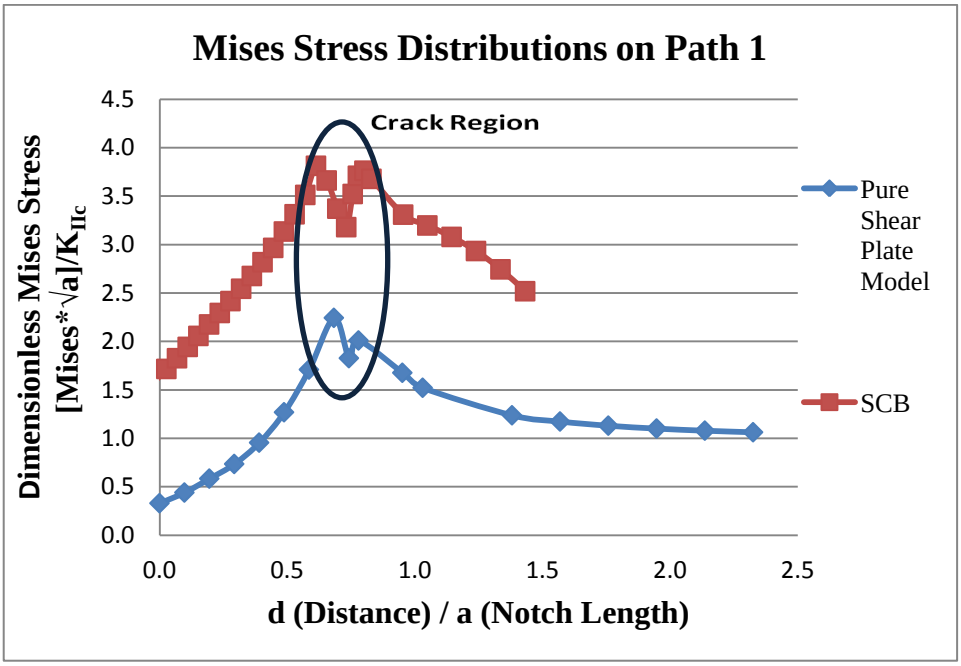

Figure 9.66 Dimensionless *Mises* stress distribution vs. *d* (Distance) / *a* (Notch Length) along Path 1

9.5.6 Stress distribution comparisons between SCB and pure shear plate model on path 2

In Figures 9.67 and 9.68 position and geometric details of Path 2 for SCB specimen and Pure Shear Plate Model geometries are illustrated.

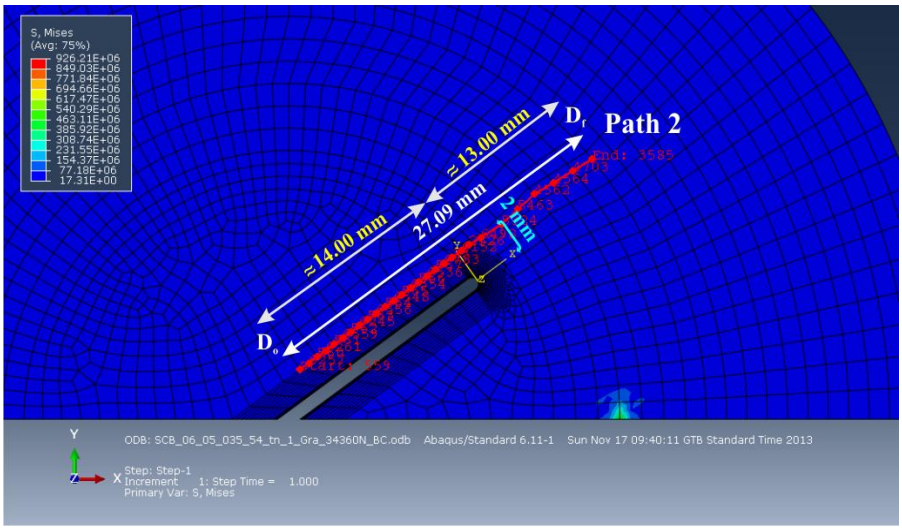

Figure 9.67 Position and geometric details of Path 2 on SCB specimen model

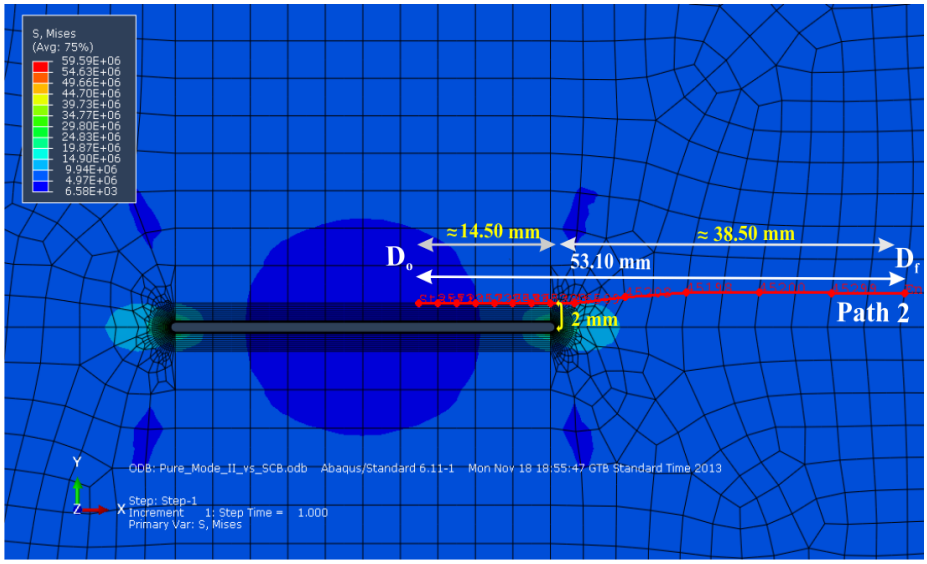

Figure 9.68 Position and geometric details of Path 2 on Pure Shear Plate Model

For stress analyses around the initial notch in terms of normal components of S_{11}', S_{22}', S_{33}' stresses and the shear component of S_{12}' stress, Path 2 is assigned parallel to the crack plane. As it is seen above in Figures 9.67 and 9.68 distance along the normal to the crack plane and the assigned path is about 2 mm away from the crack surface. Path 2 covers an overall distance of around *d*=27 mm for SCB specimen and *d*=53 mm for Pure Shear Plate Model respectively. These distance assignments are marked in the figures related to the analyses of the stresses around and ahead of the initial notch plane.

In order to compare various stress components on Path 2, normalized stress variations along normalized paths in terms of *d/a* plots are generated for SCB specimen and Pure Shear Plate Model in Figures 9.69, 9.70, 9.71, 9.72 and 9.73 respectively. Notch tip regions are marked and highlighted in these figures.

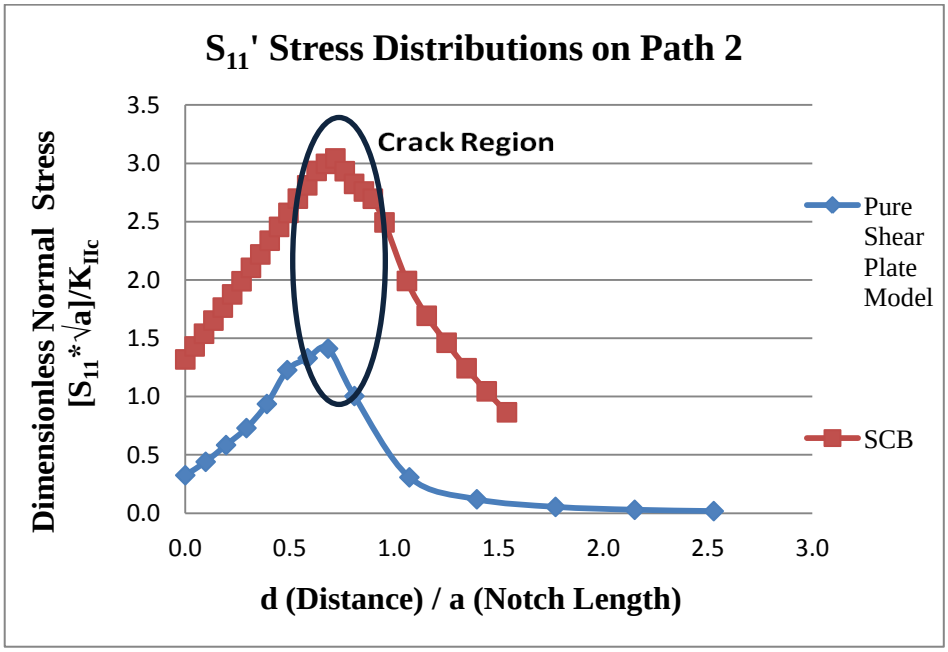

Figure 9.69 Dimensionless S_{11}' stress distribution vs. *d* (Distance) / *a* (Notch Length) along Path 2

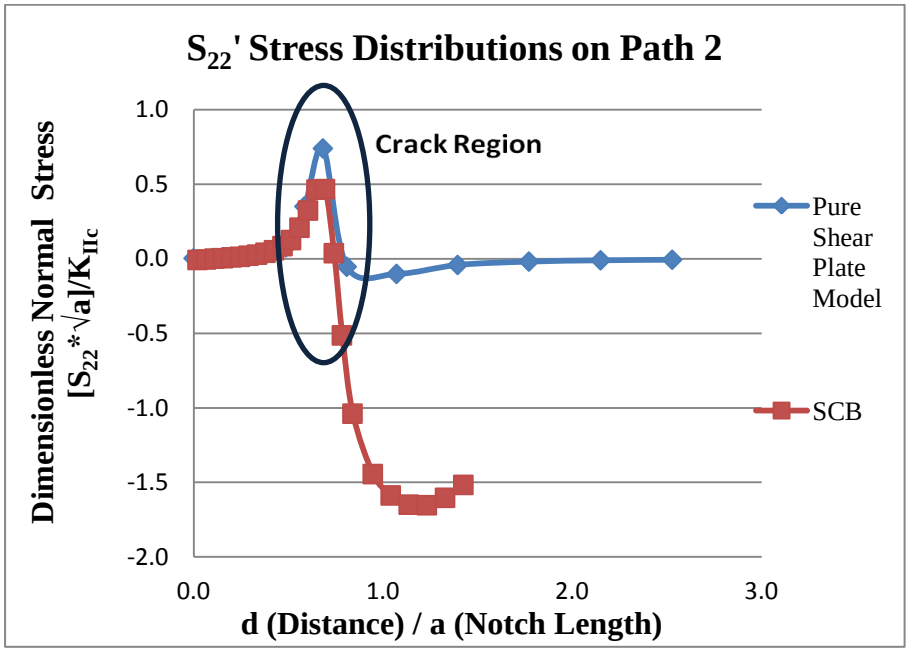

Figure 9.70 Dimensionless S_{22}' stress distribution vs. *d* (Distance) / *a* (Notch Length) along Path 2

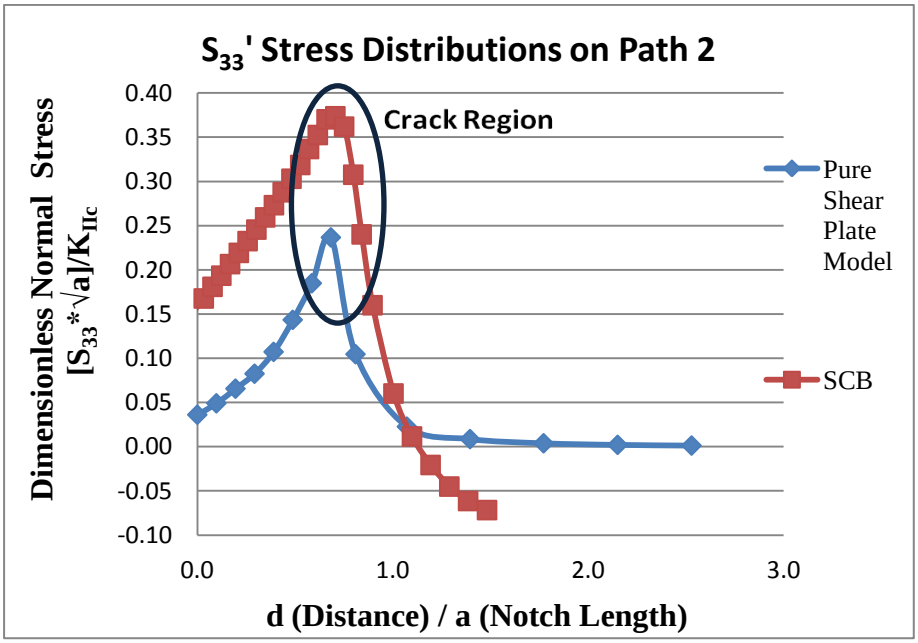

Figure 9.71 Dimensionless S_{33}' stress distribution vs. *d* (Distance) / *a* (Notch Length) along Path 2

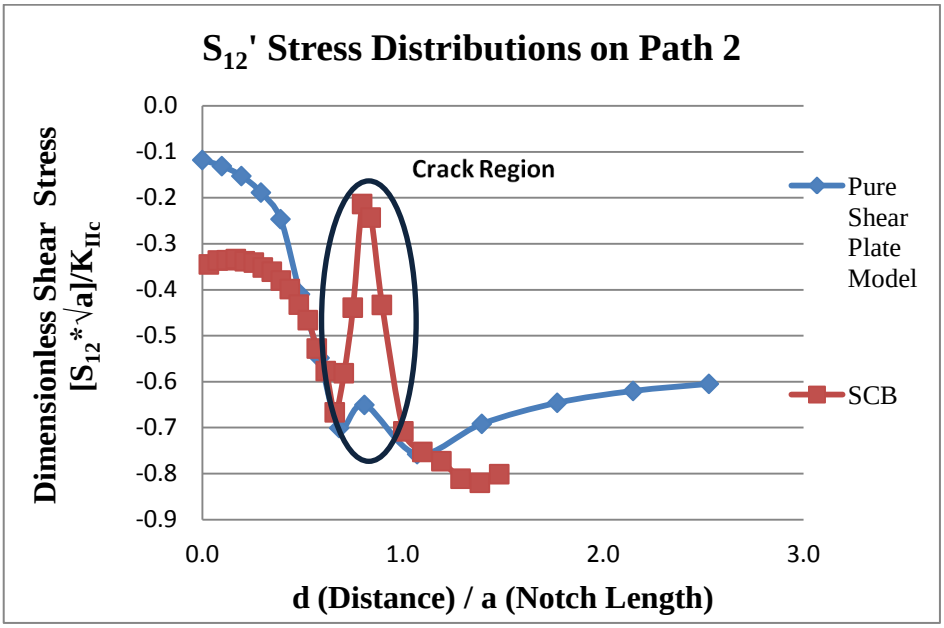

Figure 9.72 Dimensionless S_{12}' stress distribution vs. *d* (Distance) / *a* (Notch Length) along Path 2

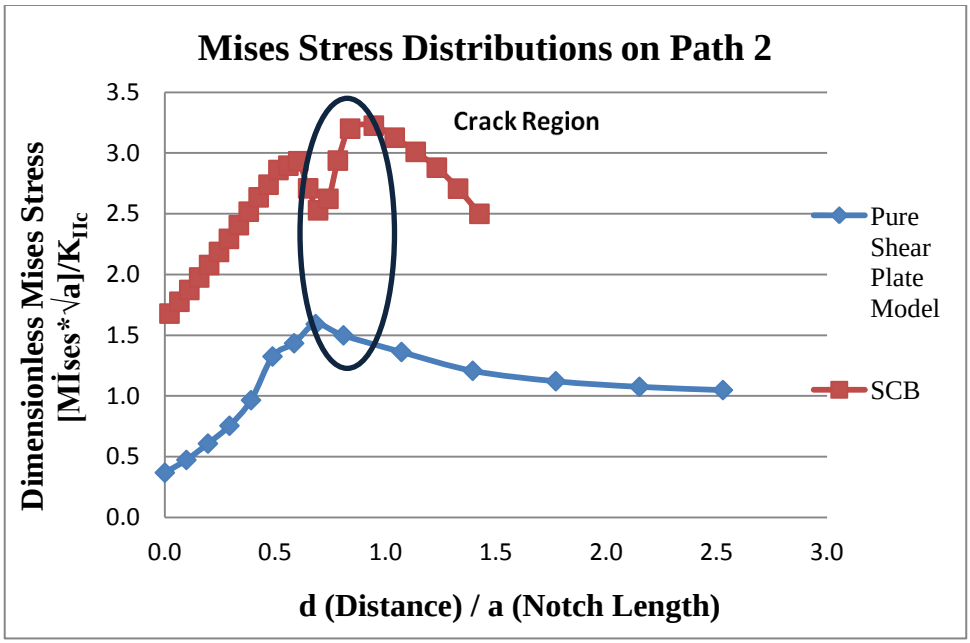

Figure 9.73 Dimensionless *Mises* stress distribution vs. *d* (Distance) / *a* (Notch Length) along Path 2

9.5.7 Stress distribution comparisons between SCB and pure shear plate model on path 3

In Figures 9.74 and 9.75 position and geometric details of Path 3 for SCB specimen and Pure Shear Plate Model geometries are illustrated.

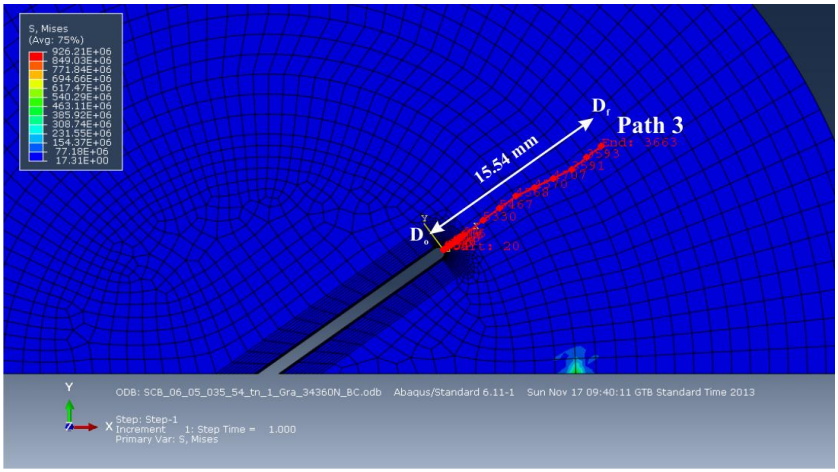

Figure 9.74 Position and geometric details of Path 3 on SCB specimen model

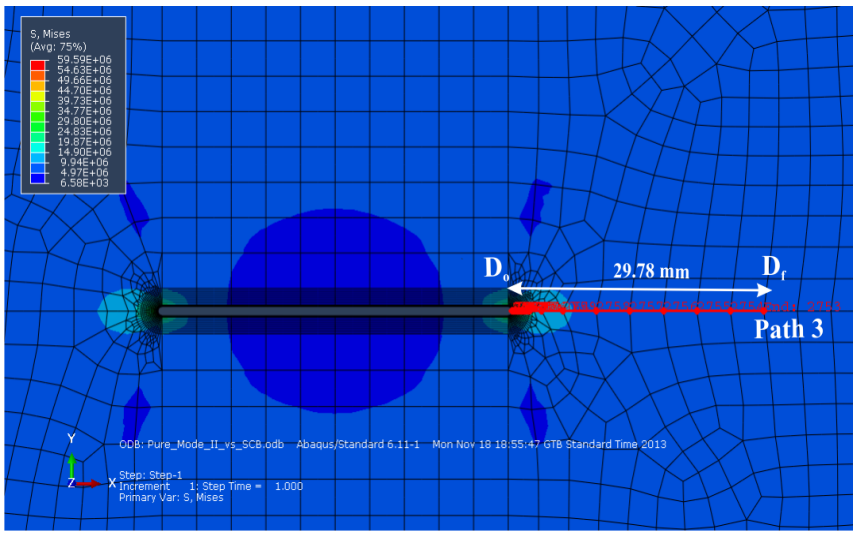

Figure 9.75 Position and geometric details of Path 3 on Pure Shear Plate Model

For stress analyses around the initial notch in terms of normal components of S_{11}', S_{22}', S_{33}' stresses and the shear component of S_{12}' stress, Path 3 starts at the notch tip where the local reference system is positioned and extends to the outer boundary of the specimen parallel to the plane of the initial notch. Path 3 is marked in the in Figures 9.74 and 9.75 related to the analyses of the stresses ahead of the initial notch plane.

In order to compare various stress components on Path 3, normalized stress variations along normalized paths in terms of *d/a* plots are generated for CSTBD specimen and Pure Shear Plate Model in Figures 9.76, 9.77, 9.78, 9.79 and 9.80 respectively.

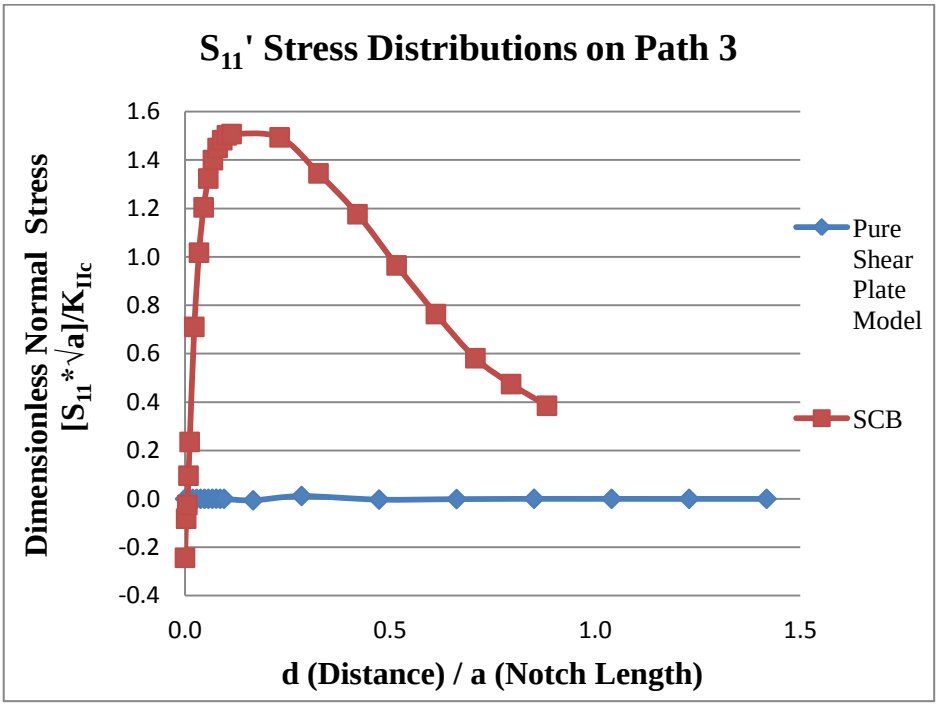

Figure 9.76 Dimensionless S_{11}' stress distribution vs. *d* (Distance) / *a* (Notch Length) along Path 3

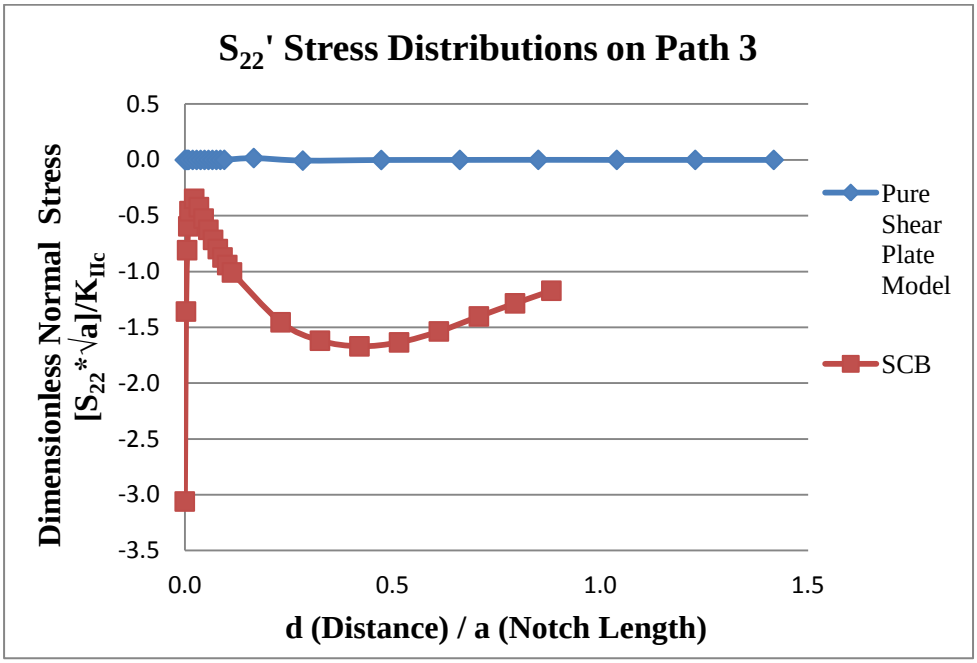

Figure 9.77 Dimensionless S_{22}' stress distribution vs. *d* (Distance) / *a* (Notch Length) along Path 3

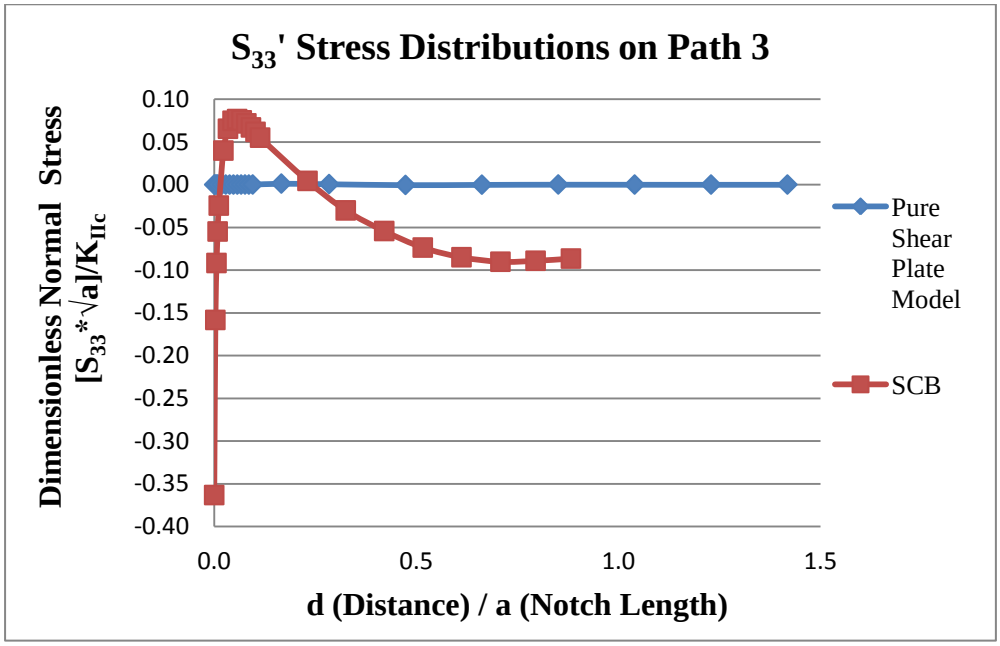

Figure 9.78 Dimensionless S_{33}' stress distribution vs. *d* (Distance) / *a* (Notch Length) along Path 3

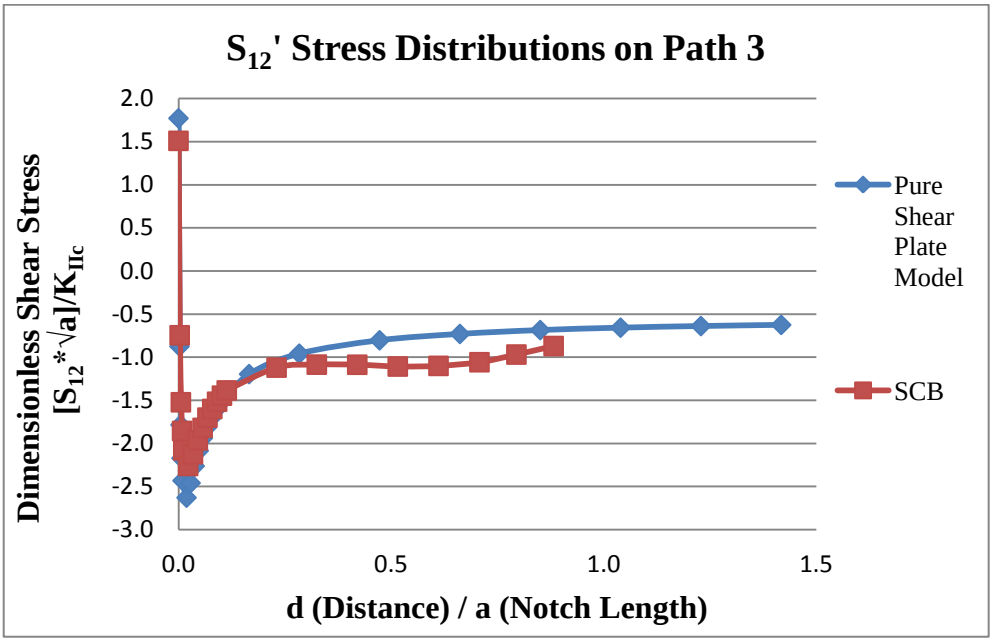

Figure 9.79 Dimensionless S_{12}' stress distribution vs. *d* (Distance) / *a* (Notch Length) along Path 3

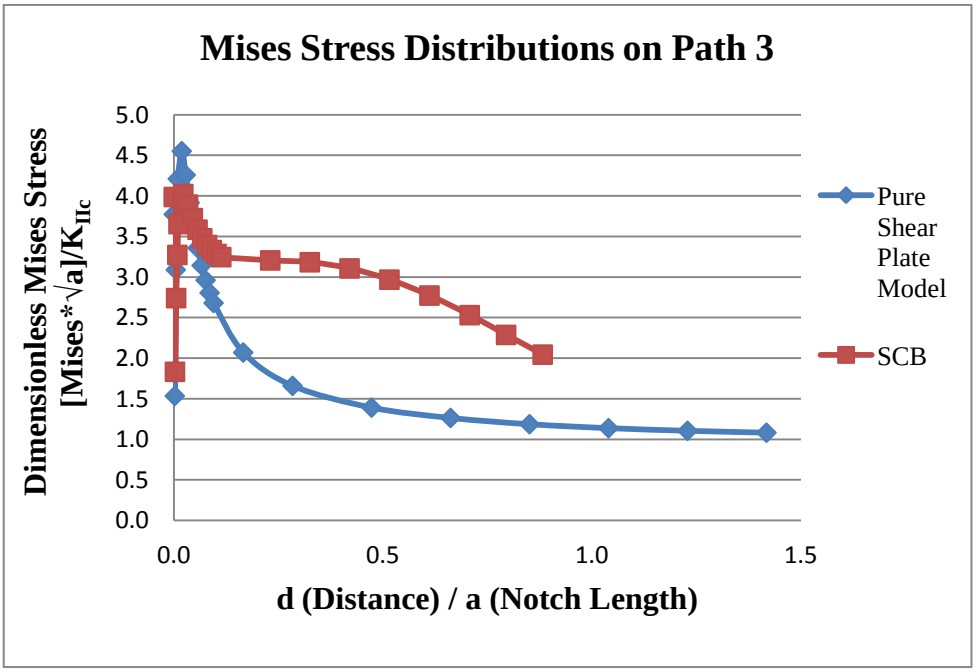

Figure 9.80 Dimensionless *Mises* stress distribution vs. *d* (Distance) / *a* (Notch Length) along Path 3

9.5.8 Stress distribution comparisons between SCB and pure shear plate model on path 4

In Figures 9.81 and 9.82 position and geometric details of Path 4 for SCB specimen and Pure Shear Plate Model geometries are illustrated.

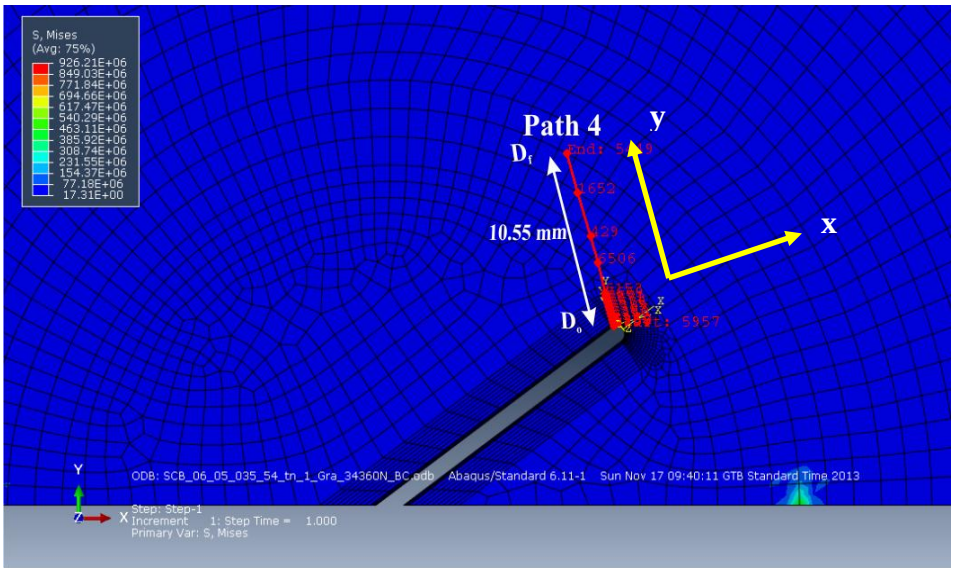

Figure 9.81 Position and geometric details of Path 4 on SCB specimen model

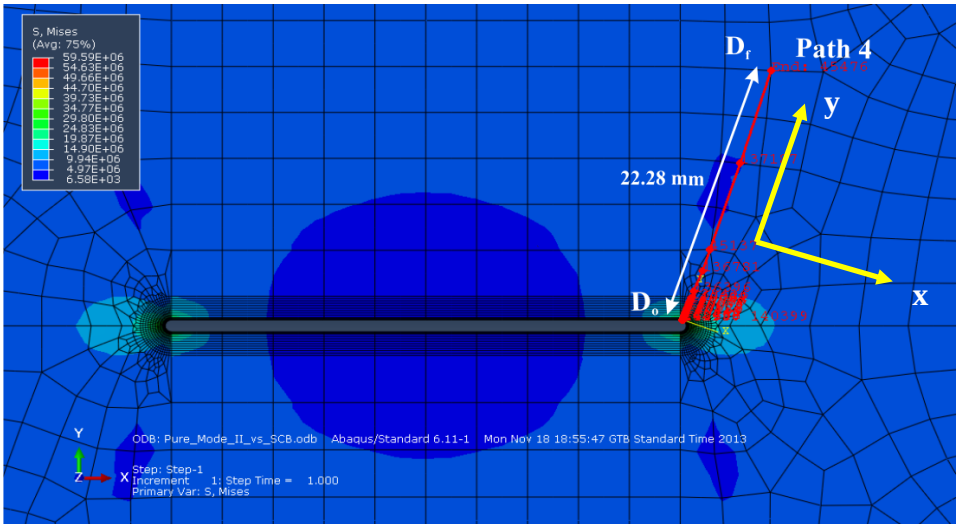

Figure 9.82 Position and geometric details of Path 4 on Pure Shear Plate Model

Path 4 was located near the notch tip where the notch was propagated. This path was generated after transforming the global coordinate system into local co-ordinate system approximately oriented around 70° degrees counterclockwise from the notch plane. As it is illustrated in Figures 9.53 and 9.54 this local system is defined by an x-axis perpendicular to the crack propagation direction (CPD) and y-axis parallel to the crack propagation direction (CPD).

In order to compare various stress components on Path 4, normalized stress variations along normalized paths in terms of a *d/a* plots are generated for SCB specimen and Pure Shear Plate Model in Figures 9.83, 9.84, 9.85, 9.86, and 9.87 respectively.

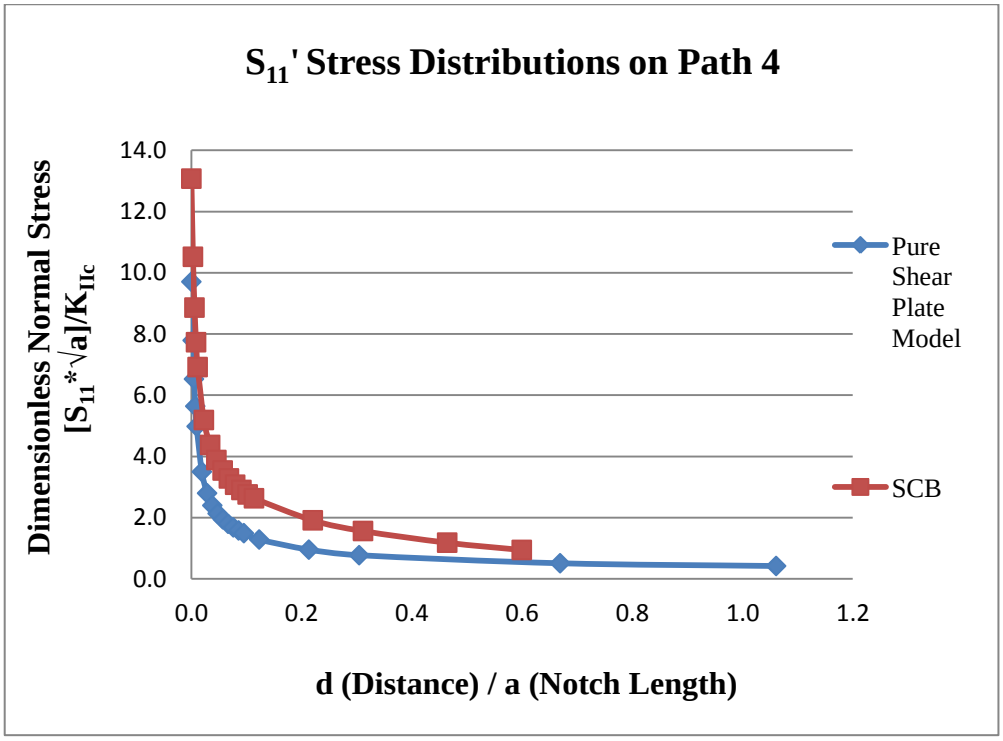

Figure 9.83 Dimensionless S_{11}' stress distribution vs. *d* (Distance) / *a* (Notch Length) along Path 4

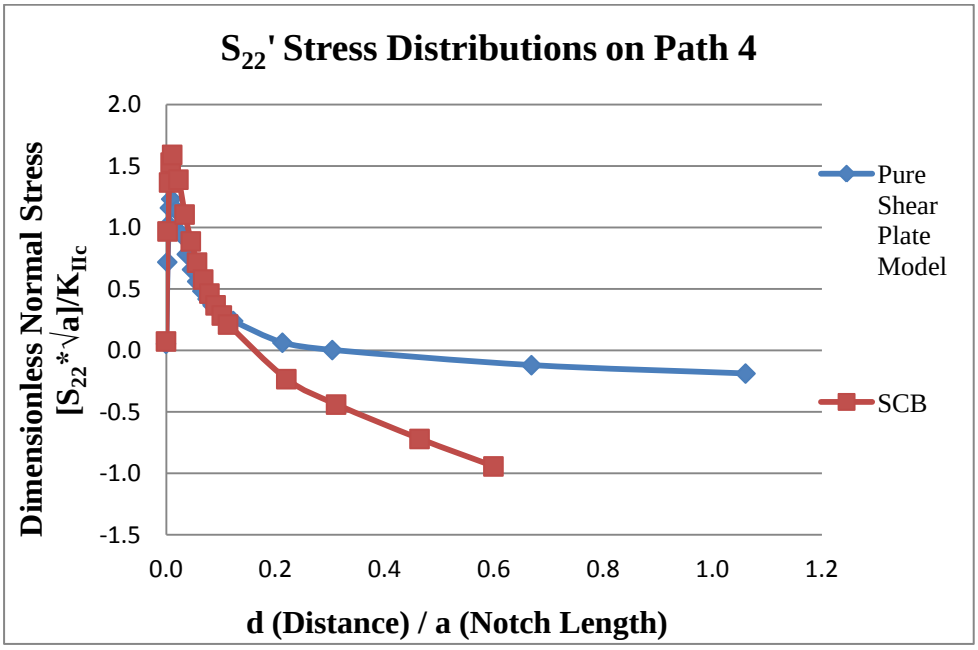

Figure 9.84 Dimensionless S_{22}' stress distribution vs. *d* (Distance) / *a* (Notch Length) along Path 4

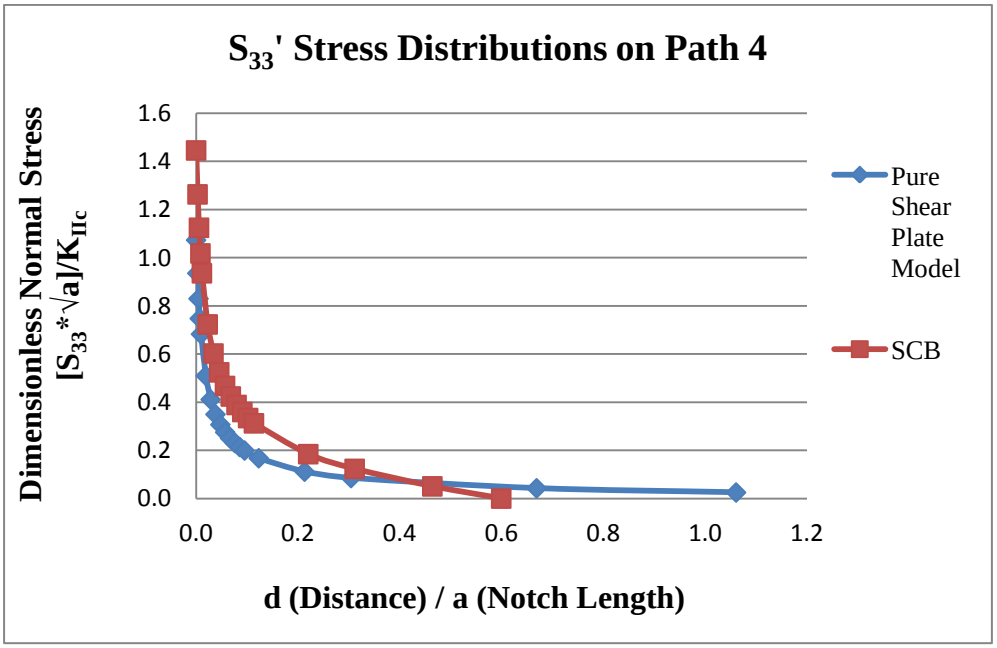

Figure 9.85 Dimensionless S_{33}' stress distribution vs. *d* (Distance) / *a* (Notch Length) along Path 4

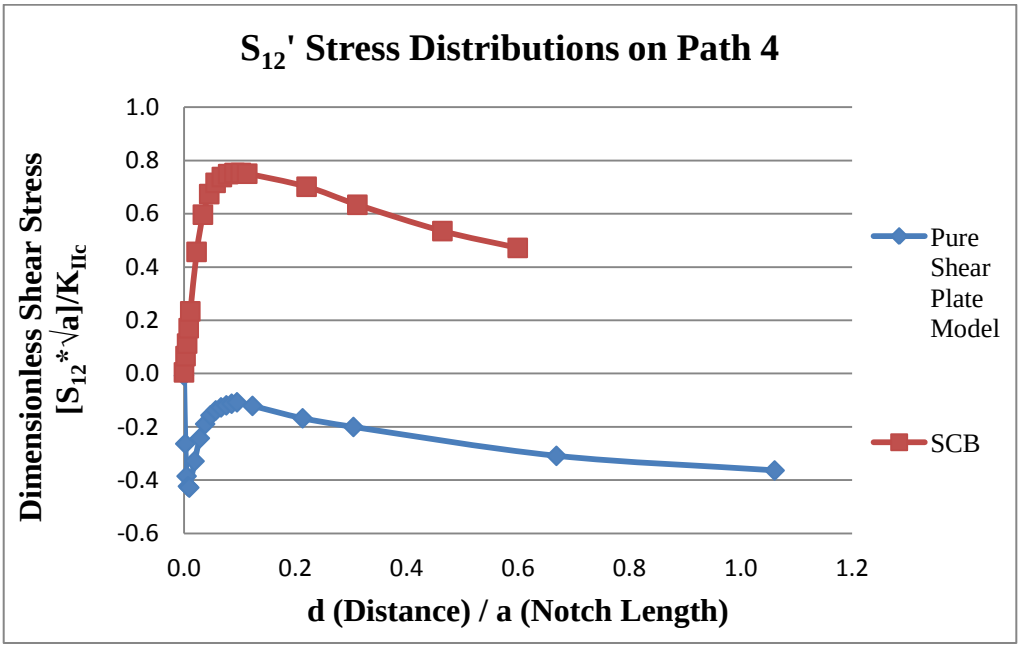

Figure 9.86 Dimensionless S_{12}' stress distribution vs. *d* (Distance) / *a* (Notch Length) along Path 4

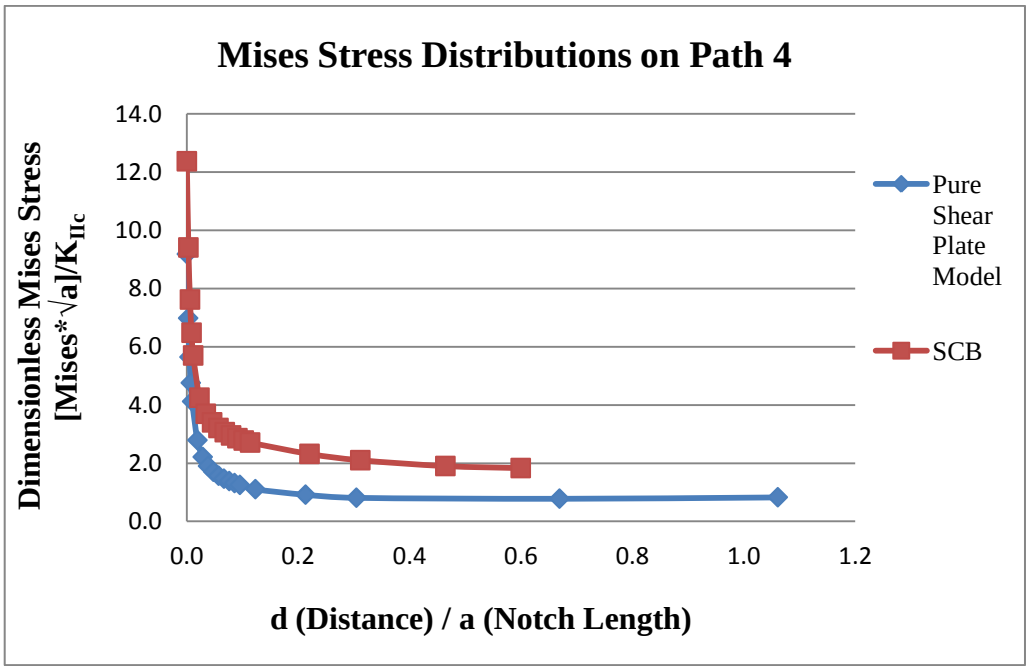

Figure 9.87 Dimensionless *Mises* stress distribution vs. *d* (Distance) / *a* (Notch Length) along Path 4

9.5.9 Stress distribution comparisons between SNDB and pure shear plate model on path 1

In Figures 9.88 and 9.89 position and geometric details of Path 1 for SNDB specimen and Pure Shear Plate Model geometries are illustrated.

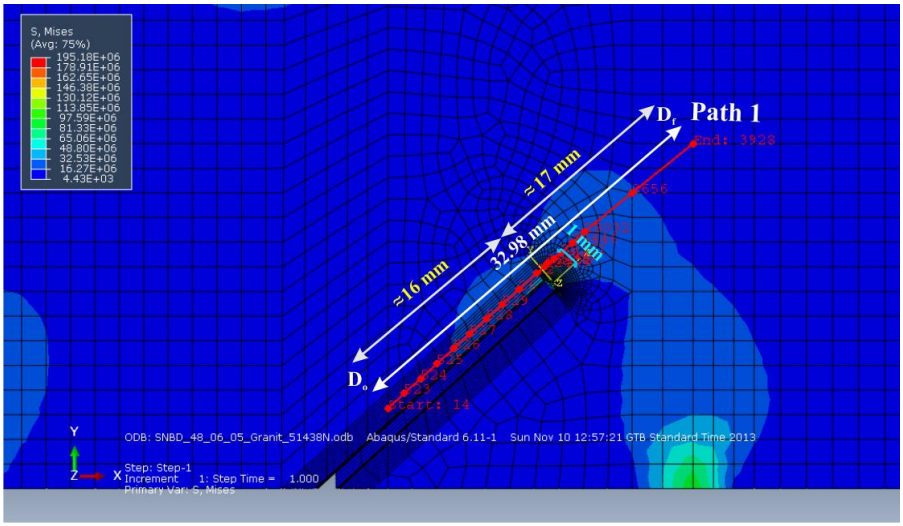

Figure 9.88 Position and geometric details of Path 1 on SNDB specimen

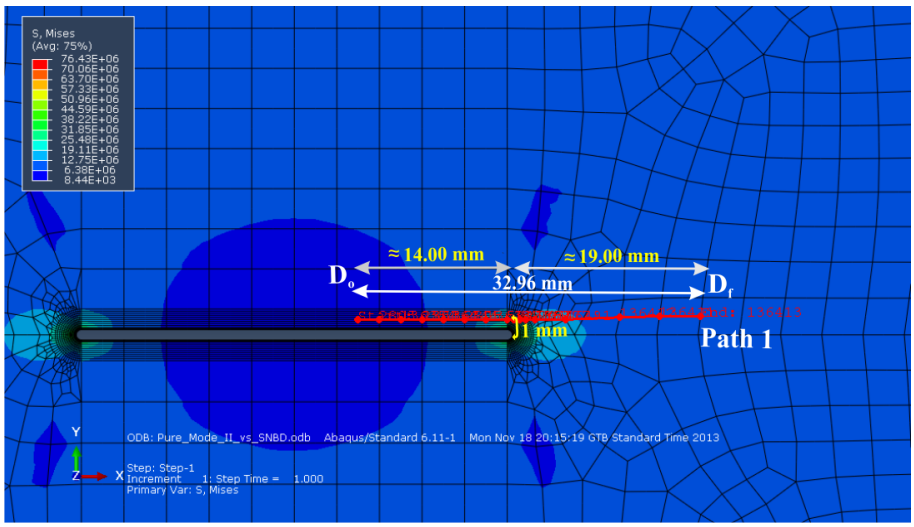

Figure 9.89 Position and geometric details of Path 1 on Pure Shear Plate Model

For stress analyses around the initial notch in terms of normal components of S_{11}', S_{22}', S_{33}' stresses and the shear component of S_{12}' stress, Path 1 is assigned parallel to the crack plane. As it is seen above in Figures 9.88 and 9.89 distance along the normal to the crack plane and the assigned path is about 1 mm away from the crack surface. Path 1 covers an overall distance of around *d*=33 mm for SNDB specimen and *d*=33 mm for Pure Shear Plate Model. These distance assignments are marked in the figures related to the analyses of the stresses around and ahead of the initial notch plane.

In order to compare various stress components on Path 1, normalized stress variations along normalized paths in terms of *d/a* plots are generated for SNDB specimen and Pure Shear Plate Model in Figures 9.90, 9.91, 9.92, 9.93 and 9.94 respectively. Notch tip regions are marked and highlighted in these figures.

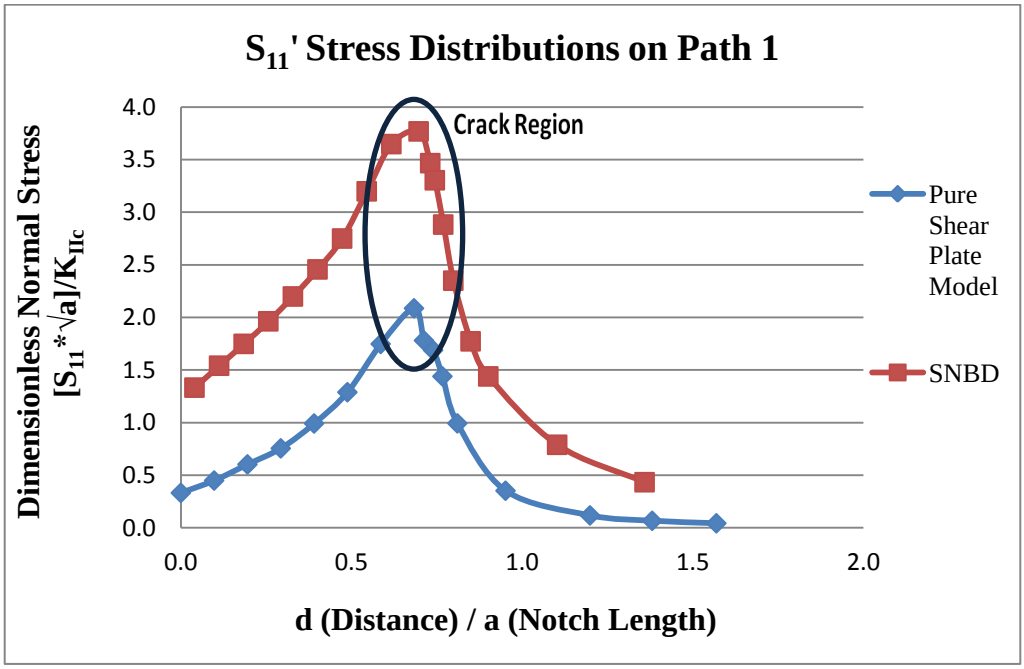

Figure 9.90 Dimensionless S_{11}' stress distribution vs. *d* (Distance) / *a* (Notch Length) along Path 1

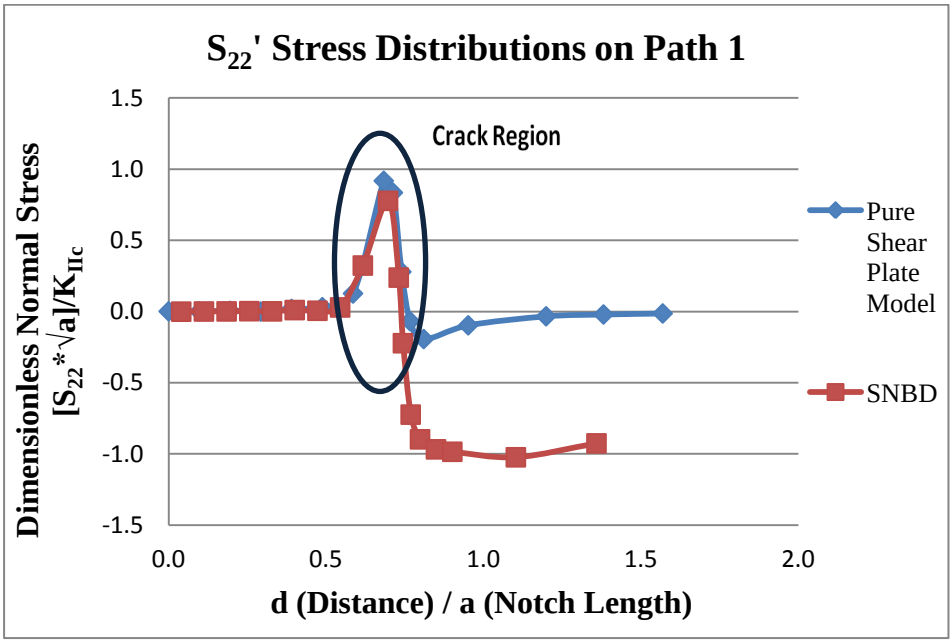

Figure 9.91 Dimensionless S_{22}' stress distribution vs. *d* (Distance) / *a* (Notch Length) along Path 1

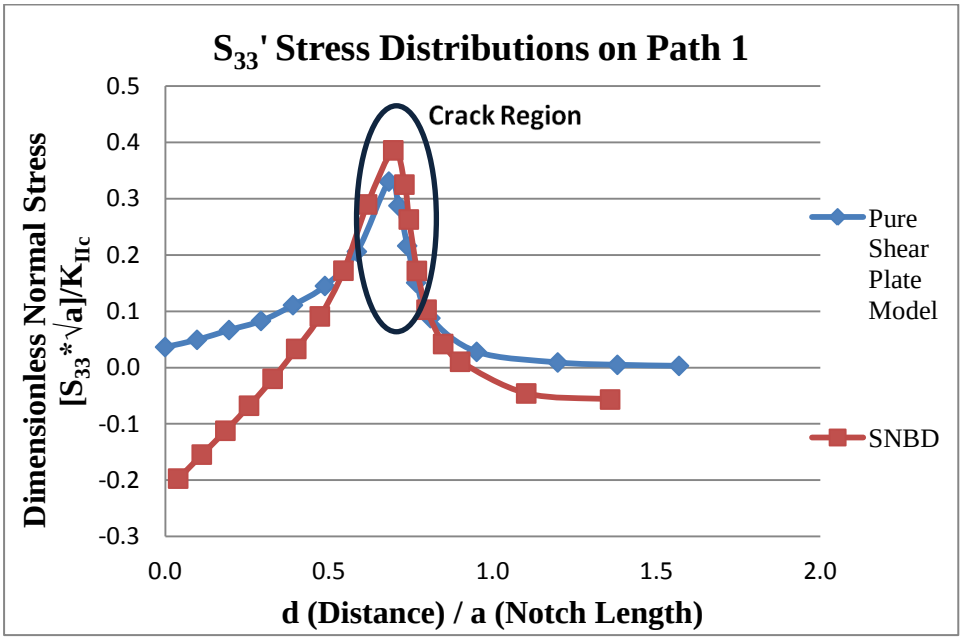

Figure 9.92 Dimensionless S_{33}' stress distribution vs. *d* (Distance) / *a* (Notch Length) along Path 1

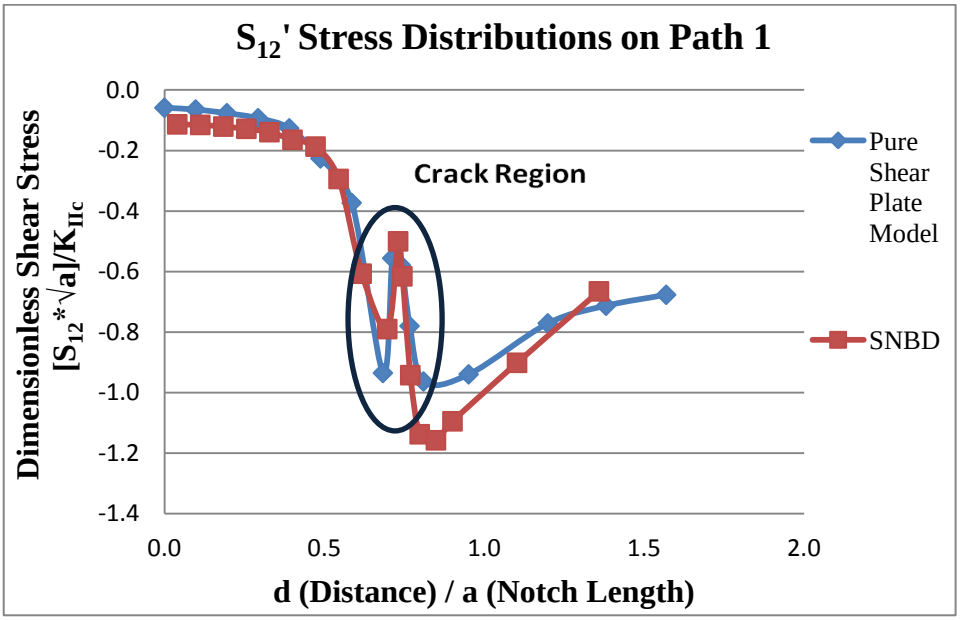

Figure 9.93 Dimensionless S_{12}' stress distribution vs. *d* (Distance) / *a* (Notch Length) along Path 1

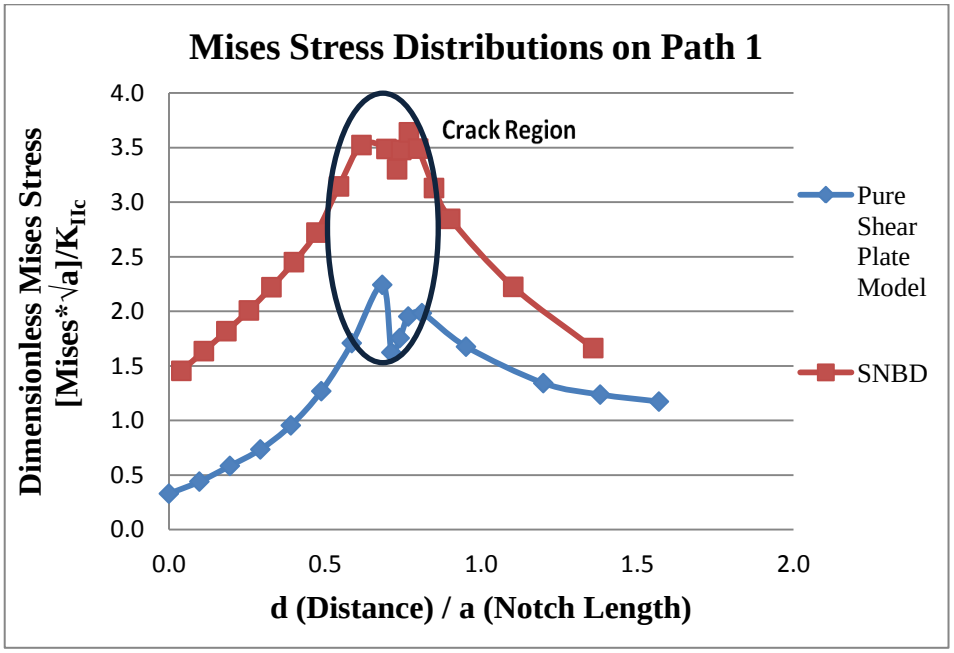

Figure 9.94 Dimensionless *Mises* stress distribution vs. *d* (Distance) / *a* (Notch Length) along Path 1

9.5.10 Stress distribution comparisons on path 2 between SNDB and pure shear plate model

In Figures 9.95 and 9.96 position and geometric details of Path 2 for SNDB specimen and Pure Shear Plate Model geometries are illustrated.

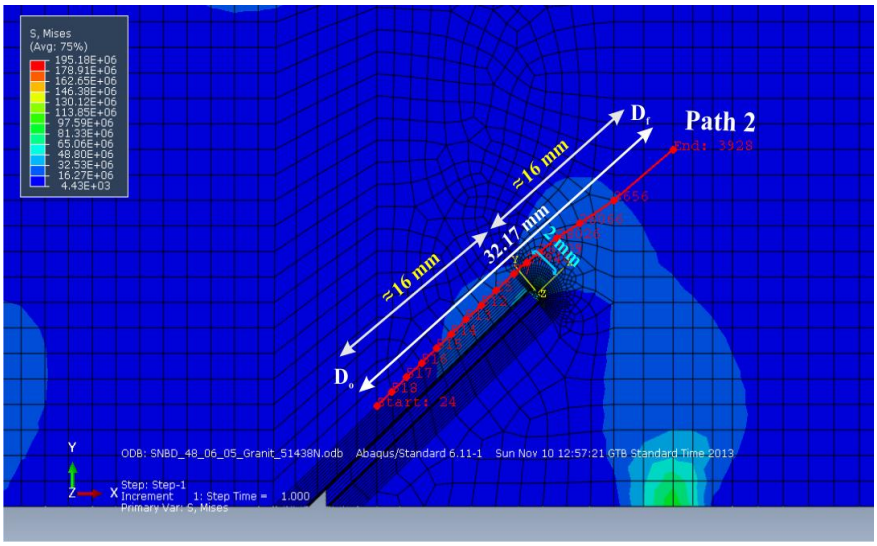

Figure 9.95 Position and geometric details of Path 2 on SNDB specimen model

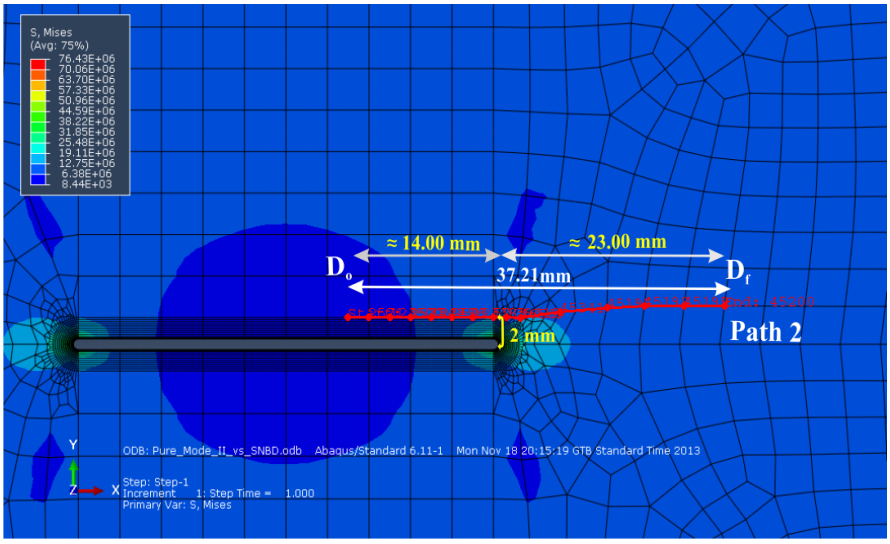

Figure 9.96 Position and geometric details of Path 2 on Pure Shear Plate Model

For stress analyses around the initial notch in terms of normal components of S_{11}', S_{22}', S_{33}' stresses and the shear component of S_{12}' stress, Path 2 is assigned parallel to the crack plane. As it is seen above in Figures 9.95 and 9.96 distance along the normal to the crack plane and the assigned path is about 2 mm away from the crack surface. Path 2 covers an overall distance of around *d*= 32 mm for SNDB specimen and *d*=37 mm for Pure Shear Plate Model respectively. These distance assignments are marked in the figures related to the analyses of the stresses around and ahead of the initial notch plane.

In order to compare various stress components on Path 2, normalized stress variations along normalized paths in terms of *d/a* plots are generated for SNDB specimen and Pure Shear Plate Model in Figures 9.97, 9.98, 9.99, 9.100 and 9.101 respectively. Notch tip regions are marked and highlighted in these figures.

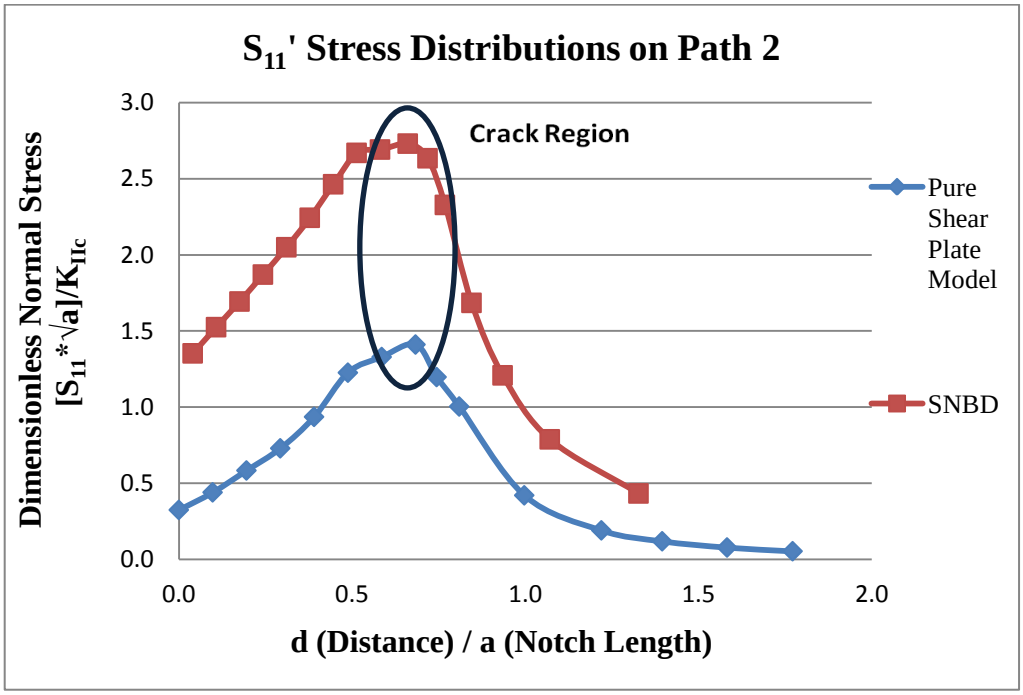

Figure 9.97 Dimensionless S_{11}' stress distribution vs. *d* (Distance) / *a* (Notch Length) along Path 2

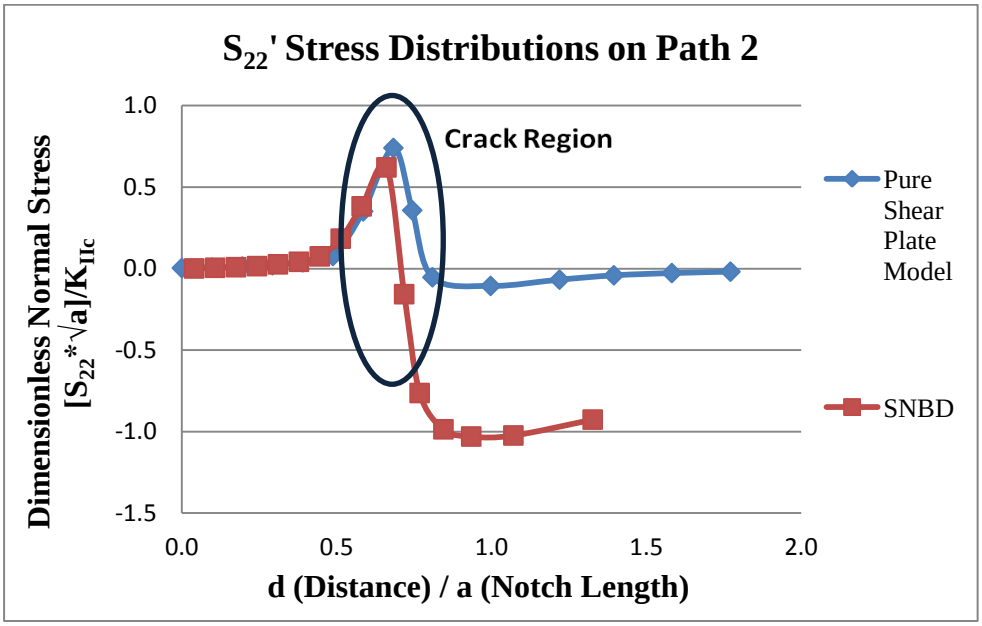

Figure 9.98 Dimensionless S_{22}' stress distribution vs. *d* (Distance) / *a* (Notch Length) along Path 2

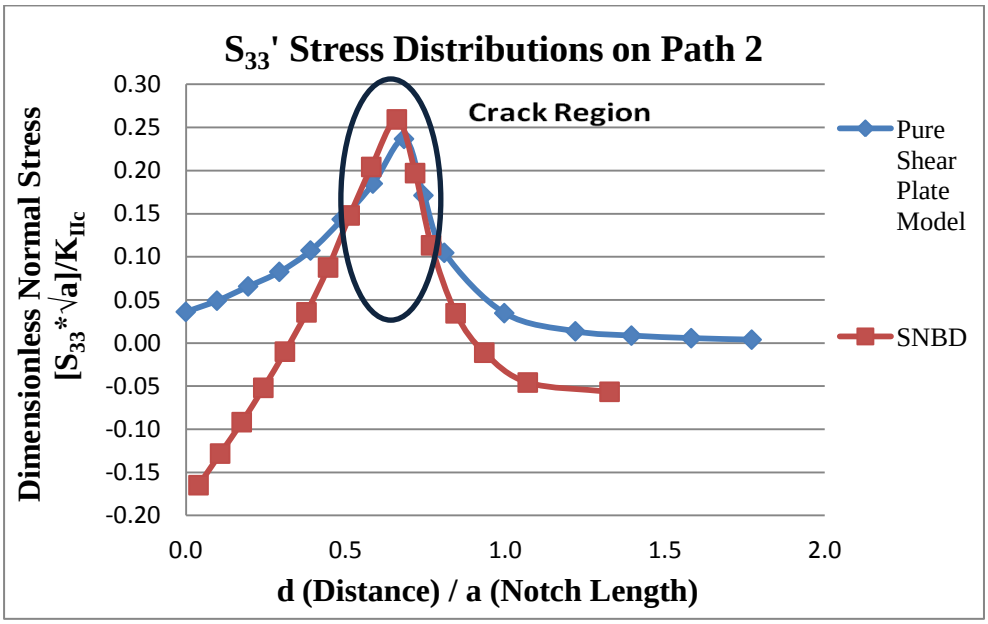

Figure 9.99 Dimensionless S_{33}' stress distribution vs. *d* (Distance) / *a* (Notch Length) along Path 2

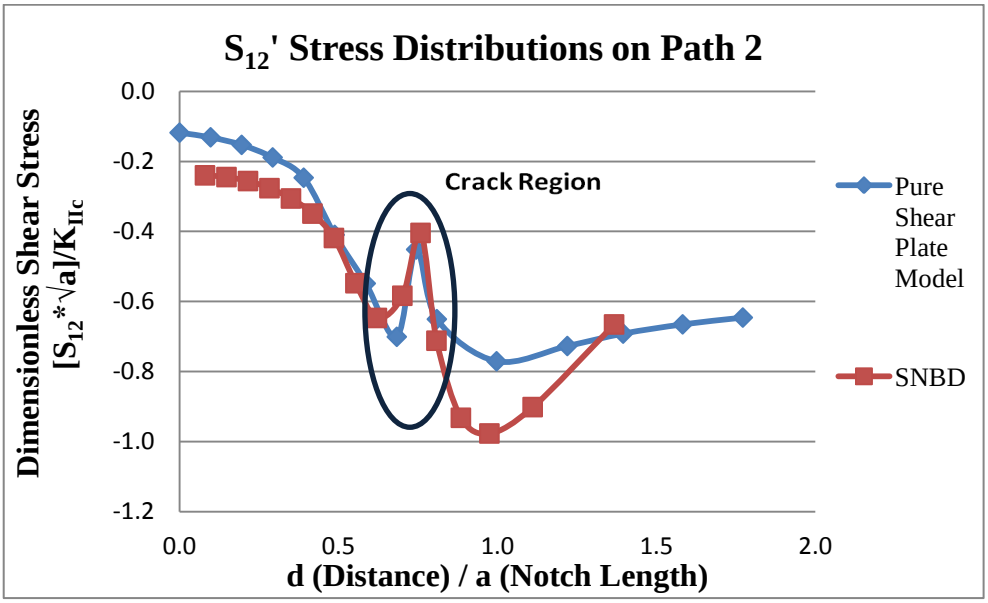

Figure 9.100 Dimensionless S_{12}' stress distribution vs. *d* (Distance) / *a* (Notch Length) along Path 2

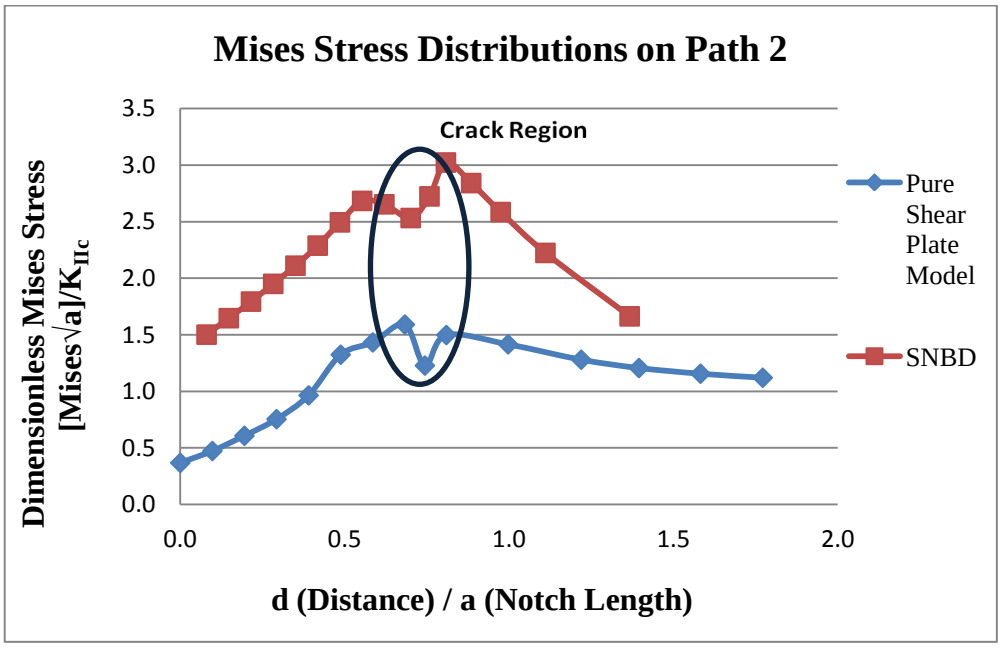

Figure 9.101 Dimensionless *Mises* stress distribution vs. *d* (Distance) / *a* (Notch Length) along Path 2

9.5.11 Stress distribution comparisons on path 3 between SNDB and pure shear plate model

In Figures 9.102 and 9.103 position and geometric details of Path 3 for SNDB specimen and Pure Shear Plate Model geometries are illustrated.

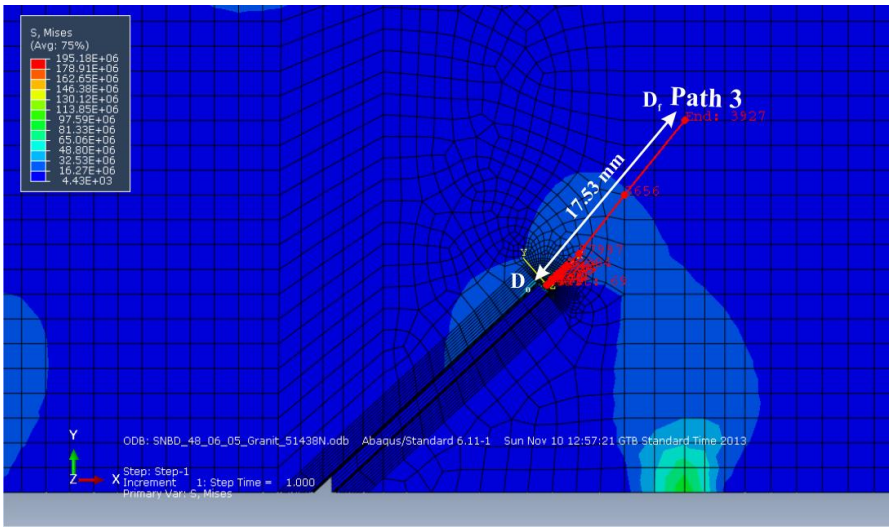

Figure 9.102 Position and geometric details of Path 3 on SNDB specimen

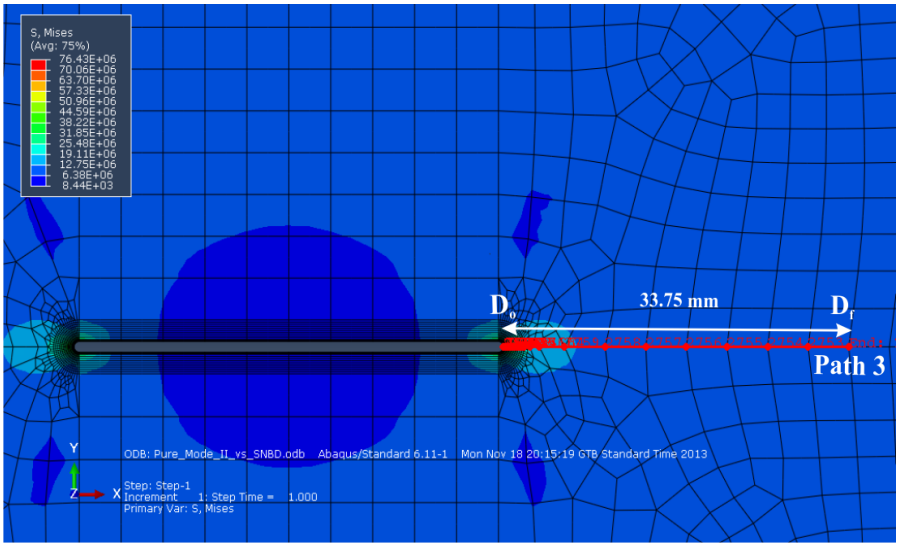

Figure 9.103 Position and geometric details of Path 3 on Pure Shear Plate Model

Path 3 starts at the notch tip where the local reference system is positioned and extends to the outer boundary of the specimen parallel to the plane of the initial notch. Path 3 is marked in Figures 9.102 and 9.103 related to the analyses of the stresses ahead of the initial notch plane.

In order to compare various stress components on Path 3, normalized stress variations along normalized paths in terms of *d/a* plots are generated for SNDB specimen and Pure Shear Plate Model in Figures 9.104, 9.105, 9106, 9.107 and 9.108 respectively.

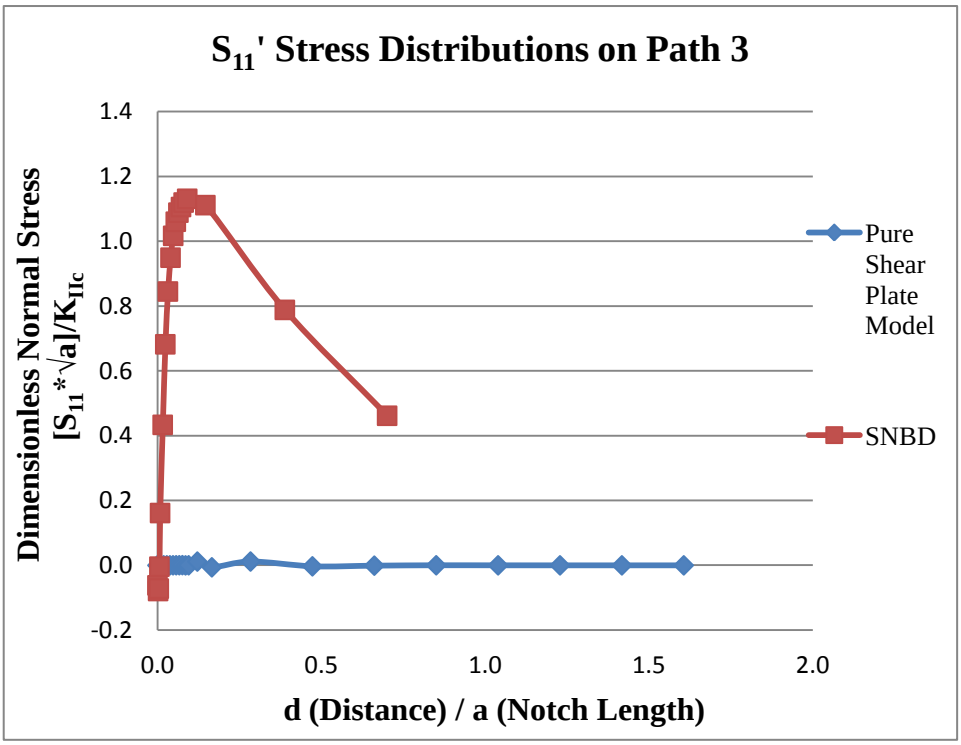

Figure 9.104 Dimensionless S_{11}' stress distribution vs. *d* (Distance) / *a* (Notch Length) along Path 3

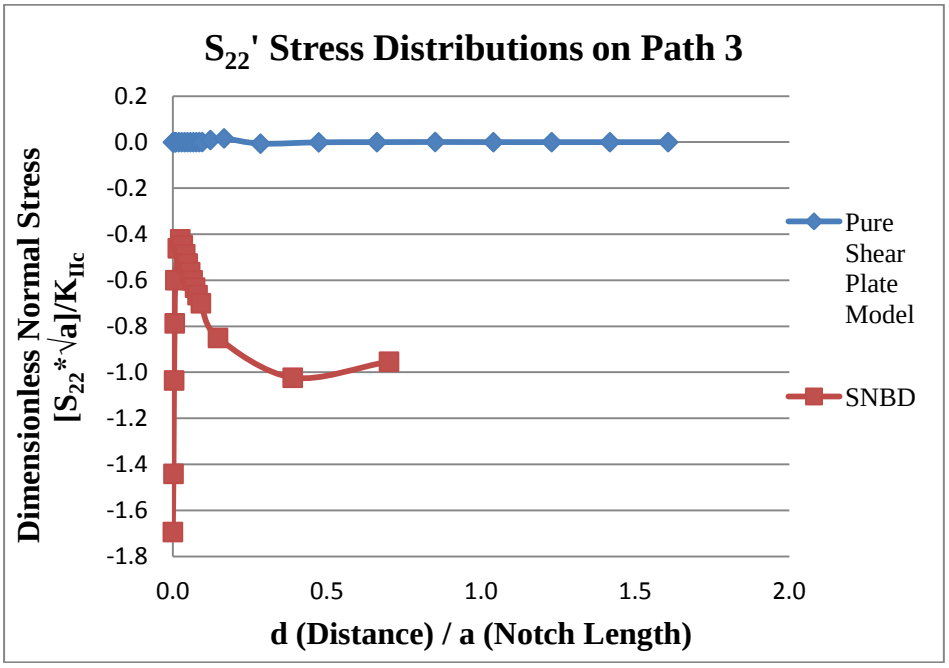

Figure 9.105 Dimensionless S_{22}' stress distribution vs. *d* (Distance) / *a* (Notch Length) along Path 3

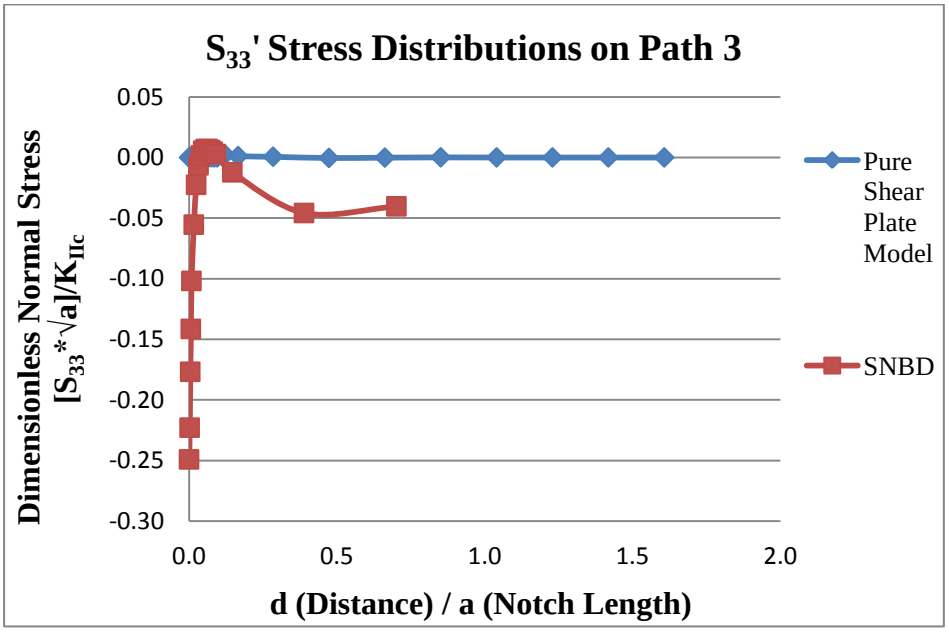

Figure 9.106 Dimensionless S_{33}' stress distribution vs. *d* (Distance) / *a* (Notch Length) along Path 3

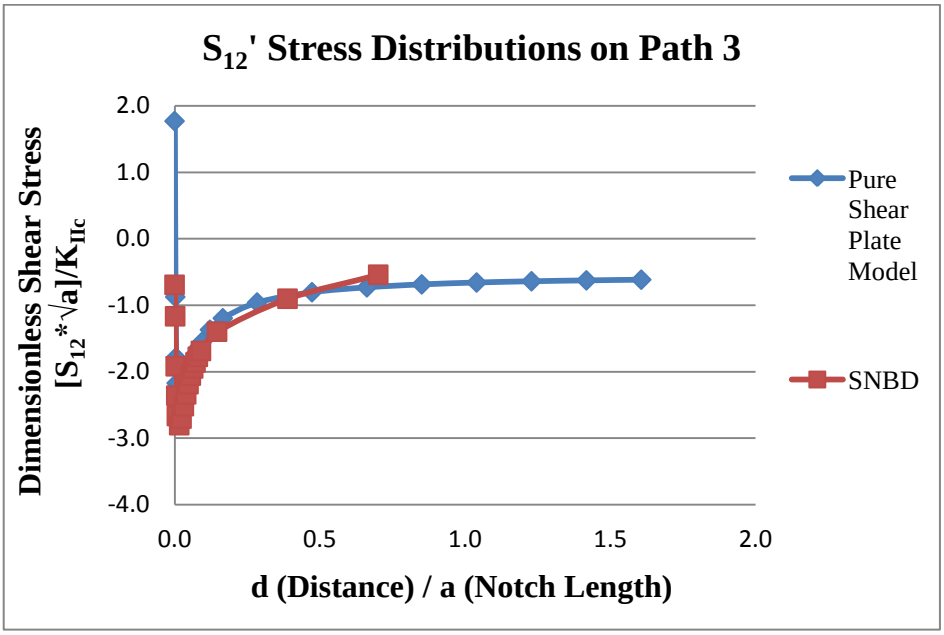

Figure 9.107 Dimensionless S_{12}' stress distribution vs. *d* (Distance) / *a* (Notch Length) along Path 3

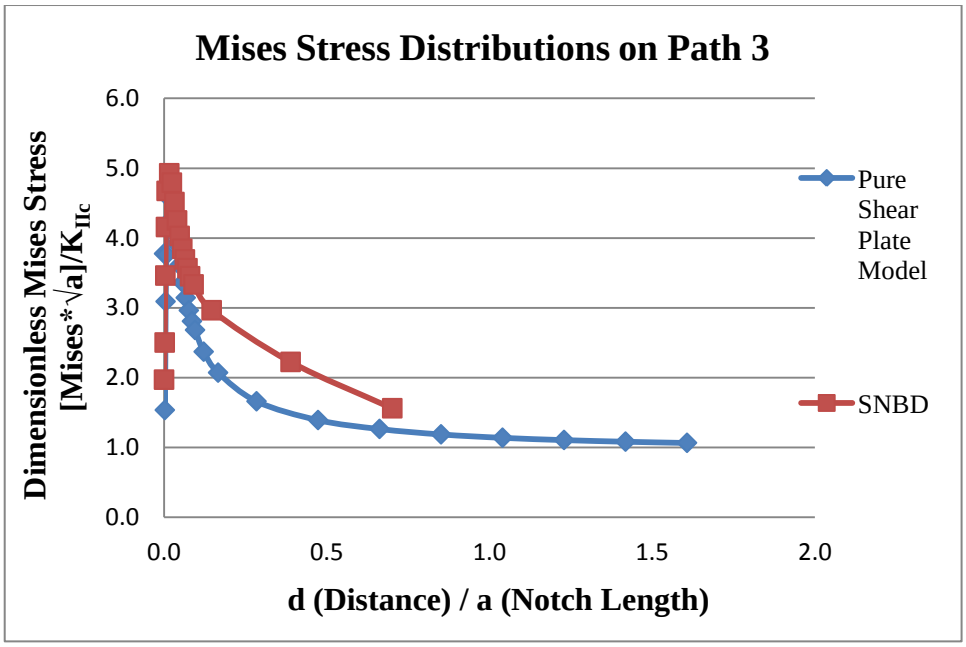

Figure 9.108 Dimensionless *Mises* stress distribution vs. *d* (Distance) / *a* (Notch Length) along Path 3

9.5.12 Stress distribution comparisons between SNDB and pure shear plate model on Path 4

In Figures 9.109 and 9.110 position and geometric details of Path 4 for SNDB specimen and Pure Shear Plate Model geometries are illustrated.

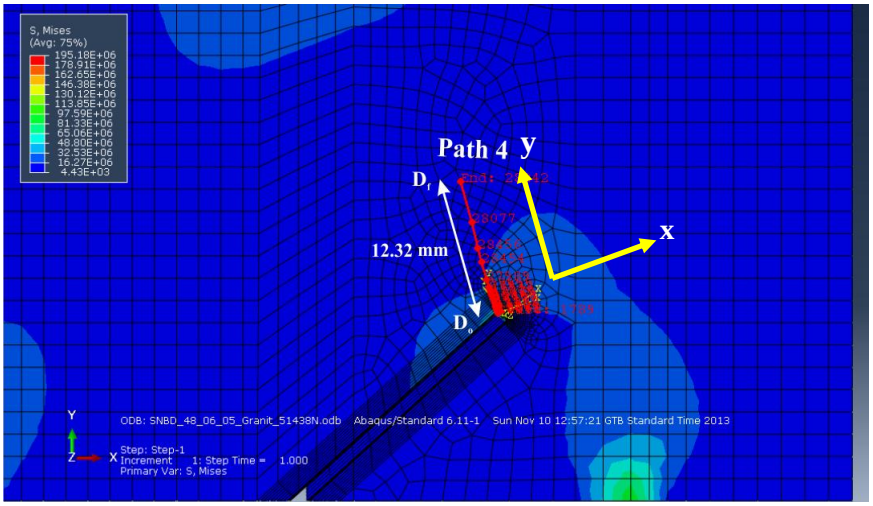

Figure 9.109 Position and geometric details of Path 4 on SNDB specimen

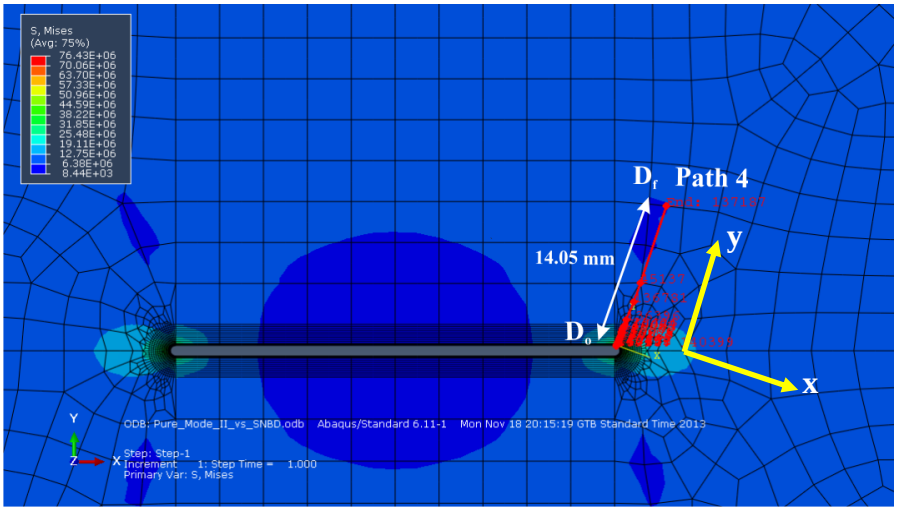

Figure 9.110 Position and geometric details of Path 4 on Pure Shear Plate Model

Path 4 was located near the notch tip where the notch was propagated. This path was generated after transforming the global coordinate system into local co-ordinate system approximately oriented around 70° degrees counterclockwise from the notch plane. As it is illustrated in Figures 9.109 and 9.110 this local system is defined by an x-axis perpendicular to the crack propagation direction (CPD) and y-axis parallel to the crack propagation direction (CPD).

In order to compare various stress components on Path 4, normalized stress variations along normalized paths in terms of a *d/a* plots are generated for SNDB specimen and Pure Shear Plate Model in Figures 9.111, 9.112, 9.113, 9.114 and 9.115 respectively.

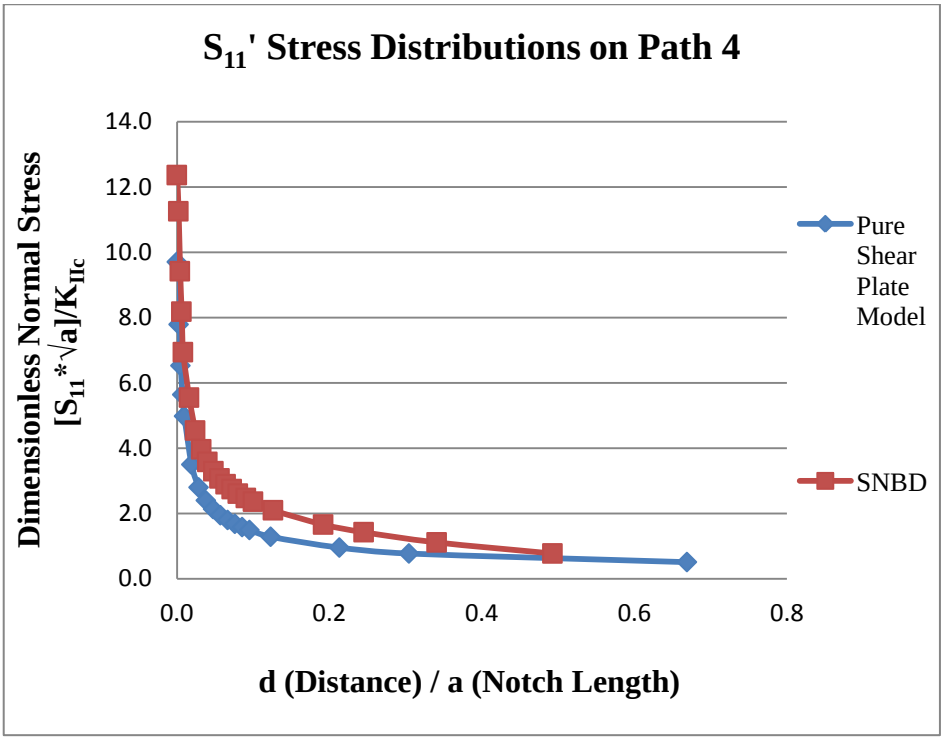

Figure 9.111 Dimensionless S_{11}' stress distribution vs. *d* (Distance) / *a* (Notch Length) along Path 4

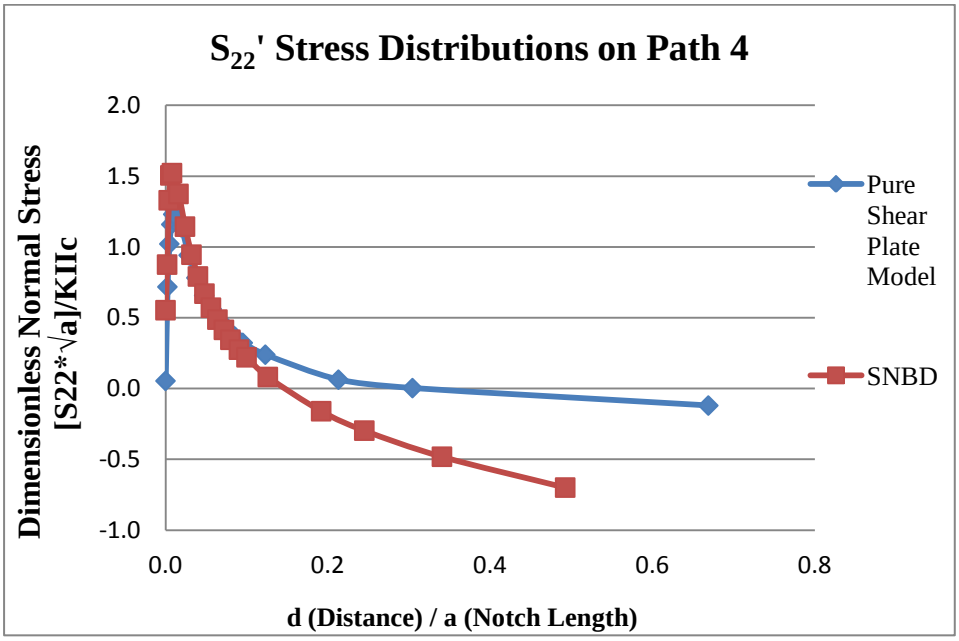

Figure 9.112 Dimensionless S_{22}' stress distribution vs. *d* (Distance) / *a* (Notch Length) along Path 4

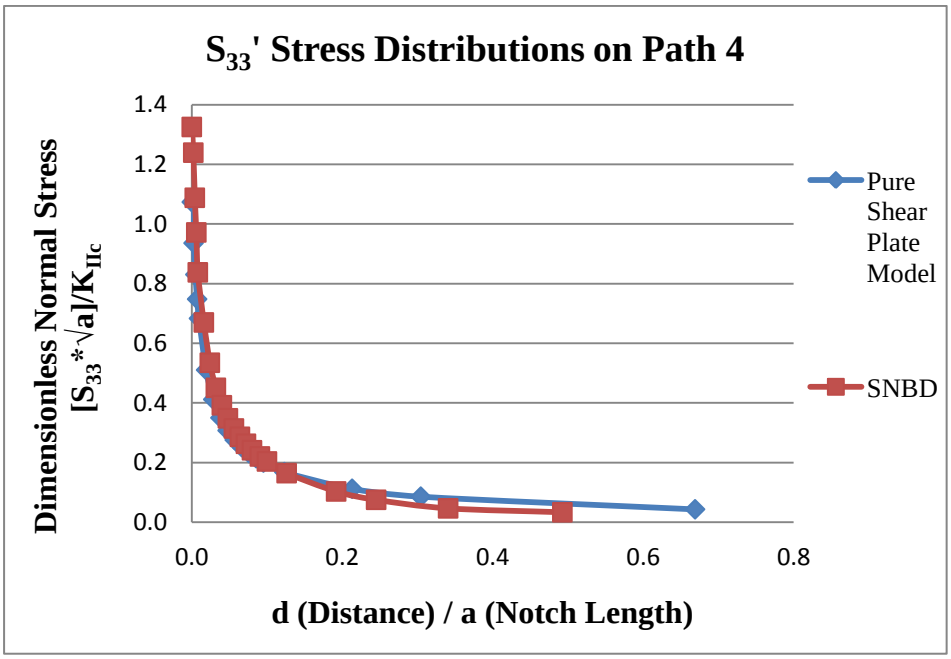

Figure 9.113 Dimensionless S_{33}' stress distribution vs. *d* (Distance) / *a* (Notch Length) along Path 4

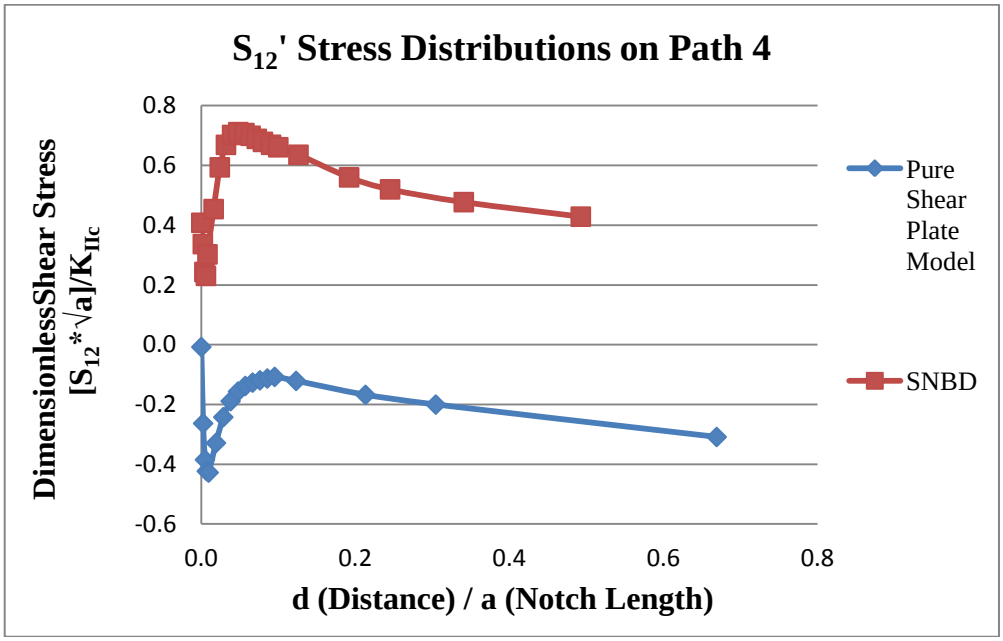

Figure 9.114 Dimensionless S_{12}' stress distribution vs. *d* (Distance) / *a* (Notch Length) along Path 4

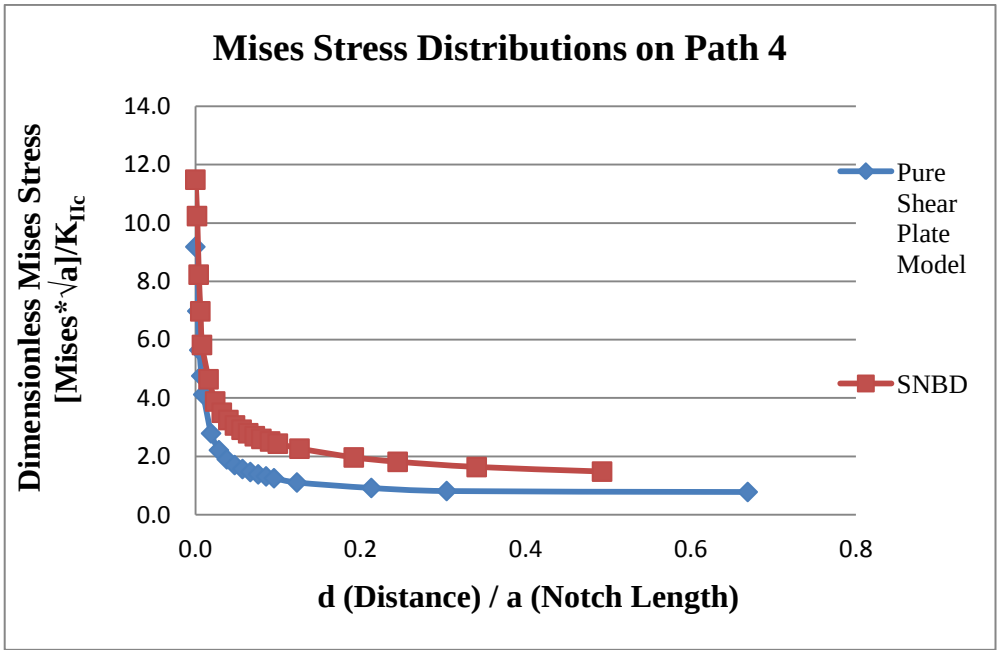

Figure 9.115 Dimensionless *Mises* stress distribution vs. *d* (Distance) / *a* (Notch Length) along Path 4

Summary of results for analyses of stress distributions around the preliminary notches of different core-based specimen geometries is discussed below.

The most similar stress state to the originally defined pure shear mode II loading configuration is satisfied by the CSTBD specimen geometry and the associated testing configuration. Von Mises stress which is proportional to the damaging component of J_2 invariant of deviator stress matrix is quite low for notches machined through CSTBD core specimen geometries. This minimizes the effects of the plastic zone or FPZ (Fracture Process Zone) on the mode II fracture toughness results. Presence of a FPZ zone reduces the fracture toughness as observed for the testing results with SCB and SNDB geometries and loading configurations. Boundary influence on fracture toughness testing is another issue related to the core-based testing with different methods. It is found that with initial notches machined with lengths less than a/R=0.5 to the CSTBD specimens produces results free from the issues discussed above.

9.6 Stress distribution on path 3 and path 4 for CSTBD specimens with initial notch length varying between 32 mm and 72 mm

CSTBD experiments have been conducted on specimens that have various initial notch lengths (32 mm, 42 mm, 52 mm, 62 mm and 72 mm). In terms of showing the stress variations during failure for particular notch length group, representative models tabulated in Table 9.4 have been loaded with average P_{cr}'s (maximum load) that are obtained after testing for particular notch length group. Average P_{cr} loads that are obtained after testing are listed in Table 9.4 below.

Table 9.4 Average P_{cr}'s for CSTBD specimens

Notch Length (*2a*), mm	Average P_{cr} (*kN*)
32	50,21
42	40,76
52	29,20
62	24,05
72	15,94

In order to show the stress variations on notch tips for CSTBD specimens that have initial notch lengths 32 mm to 72 mm, Path 3 and Path 4 are developed likewise in previous stress distribution analyses. Again, stresses were acquired according to the local co-ordinate systems for Path 3 and Path 4 that are along the notch plane direction and notch extension direction respectively.

In stress analysis around the initial notch, normalized S_{11}', S_{22}', S_{33}', S_{12}' and von Mises stresses are examined along normalized path distances (*d/a*).

Stress distribution of S_{11}' along the crack front for various initial notch lengths through CSTBD specimens is illustrated in Figures 9.116 and 9.117. Initial notches are 32 mm, 42 mm, 52 mm, 62 mm, and 72 mm respectively. As seen from the Figure 9.116, S_{11}' is zero right at the notch tip, as the distance *d/a* increases to attain values *d/a*=0.07 to *d/a*= 0.36, all S_{11}' values reach compressive maximums of -0.10 to -0.42, respectively for initial notch lengths extending in the range of 32 mm, 42 mm, 52 mm, 62 mm, and 72 mm.

This behavior is expected and the lowest compression is obtained for 72 mm initial notch lengths. This is explained by the crack front being too close to the free boundary and applied concentrated load.

Along Path 4 immediate crack front not much difference is observed between S_{11}' stresses for crack lengths extending 32 to 72 mm. S_{11}' is the tensile and tendency to unbounded *d/a*=0 which is notch tip. Around the distance from *d/a*, S_{11}' stresses show deviation from the common trend. Especially tensile stresses tend to zero for all initial notch lengths but this occurs around *d/a*=0.2 for 72 mm initial notch case and around *d/a*=0.40 for 32 mm notch case.

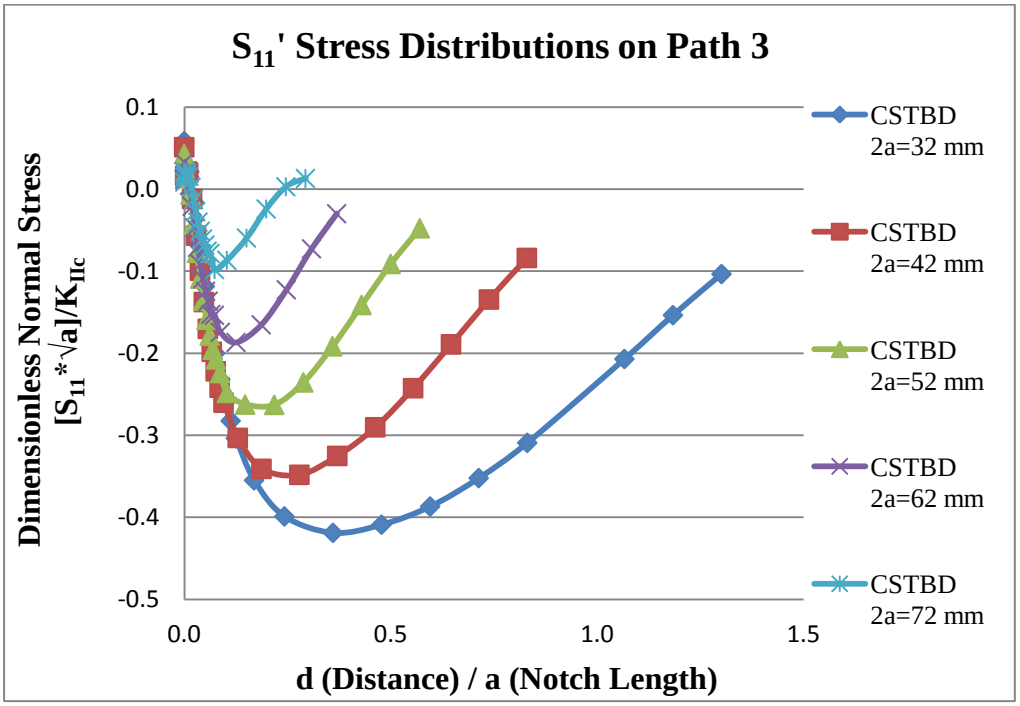

Figure 9.116 Dimensionless S_{11}' stress distribution vs. *d* (Distance) / *a* (Notch Length) along Path 3

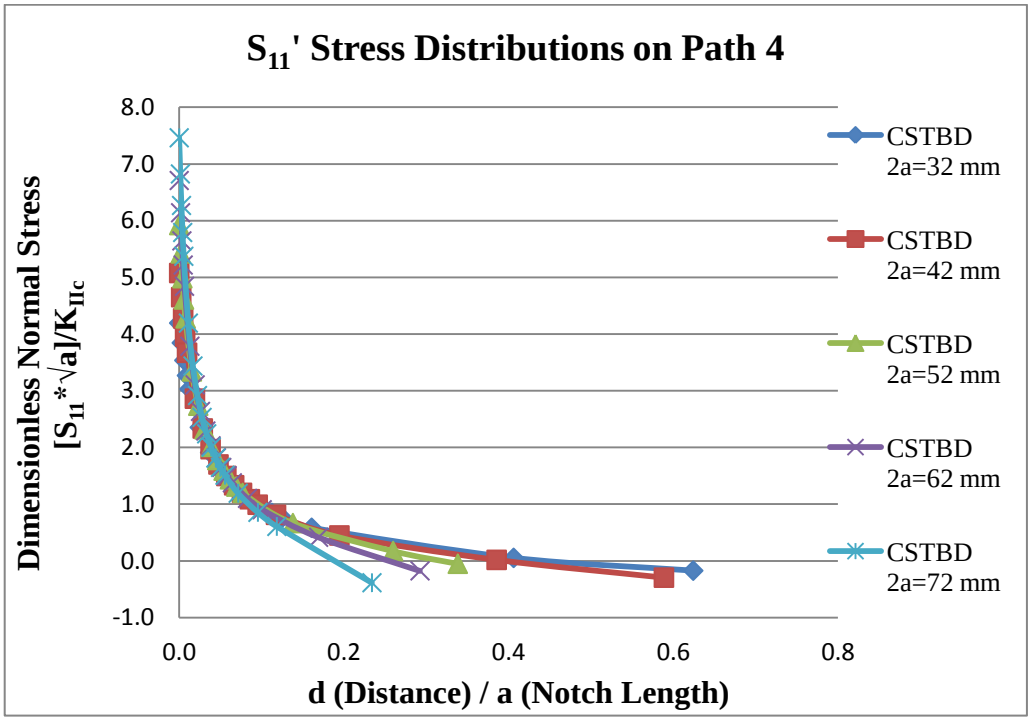

Figure 9.117 Dimensionless S_{11}' stress distribution vs. *d* (Distance) / *a* (Notch Length) along Path 4

As it will be mentioned in the upcoming paragraphs, stress values that are attained around *d/a*=0 to *d/a*= 0.08 are attributed as inaccurate stress values. Therefore, in order to understand the real stress behaviors for various initial notch length cases, those stress values are dropped from the stress distribution graphs hereafter. Refined stress distributions along Path 3 and Path 4 are plotted again in Figures 9.118 and 9.119.

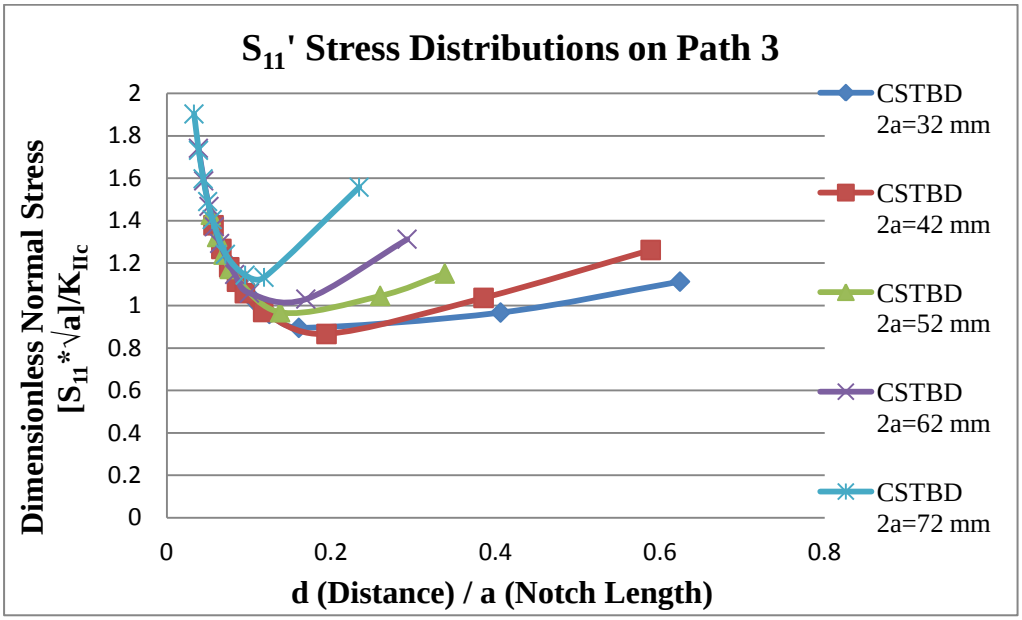

Figure 9.118 Dimensionless S_{11}' stress distribution vs. *d* (Distance) / *a* (Notch Length) along Path 3 after data refinement

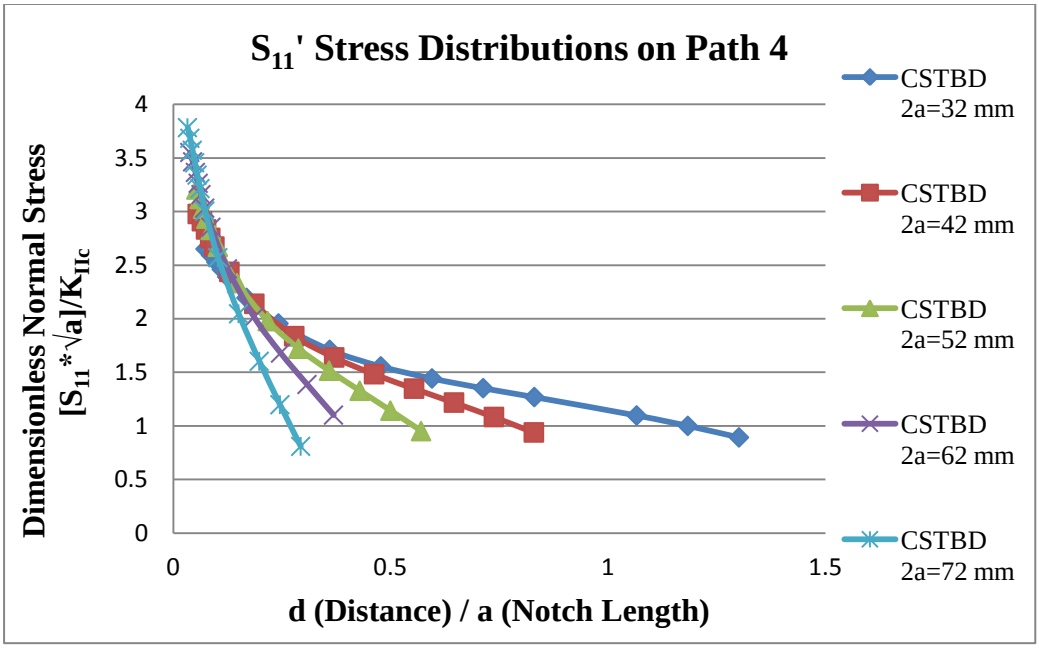

Figure 9.119 Dimensionless S_{11}' stress distribution vs. *d* (Distance) / *a* (Notch Length) along Path 4 after dropping problematic stress values

As seen in Figure 9.120, for S_{22}' stress distribution analysis along Path 3, right at the notch tip S_{22}' stresses for all notch lengths 32 mm to 72 mm are initially tensile around 0.2 to 0.6. Then point *d/a*=0.05 they turn to be compression and their compressive magnitudes are -0.40 at d/a=0.20, for 72 mm case. Around *d/a*=0.20 is -0.10 which is 4 times less compression for 32 mm initial notch length.

Parallel to the extending crack front (Path 4), stresses S_{22}' are tension around *d/a*=0.02 and the highest tension is around 1 for 72 mm notch case and around point 0.6 for 32 mm notch case. Then this compression tends become 0 at point *d/a*=0.10 for 32 mm notch length and *d/a*=0.35 for 72 mm notch length. After that, compression gradient on 72 mm notch length is steeply higher than 32 mm notch length.

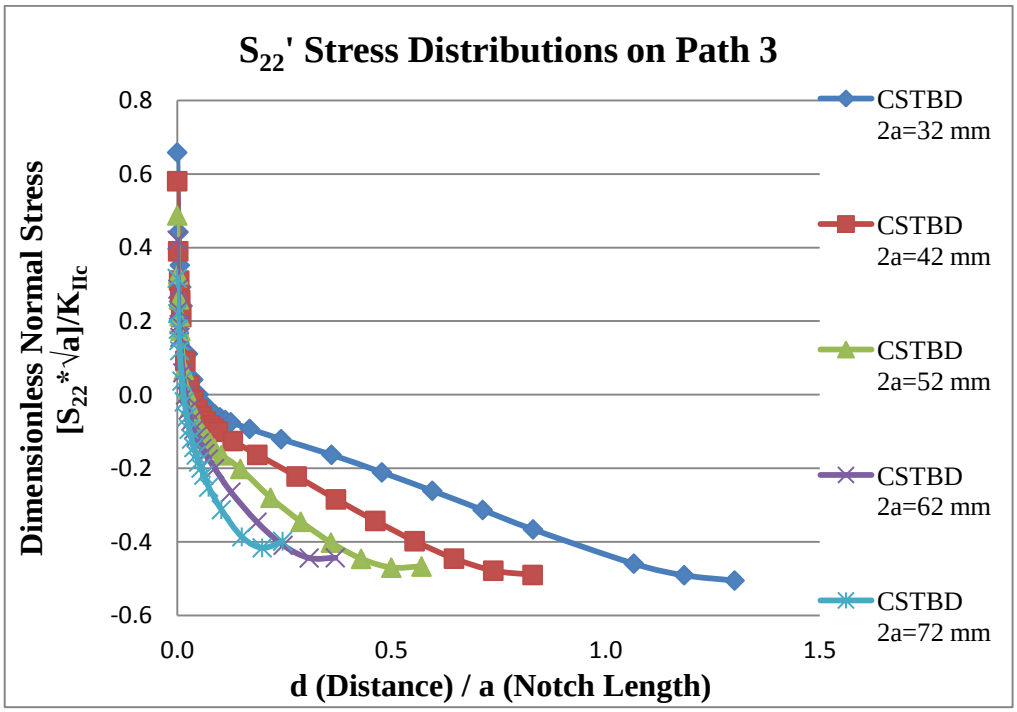

Figure 9.120 Dimensionless S_{22}' stress distribution vs. *d* (Distance) / *a* (Notch Length) along Path 3

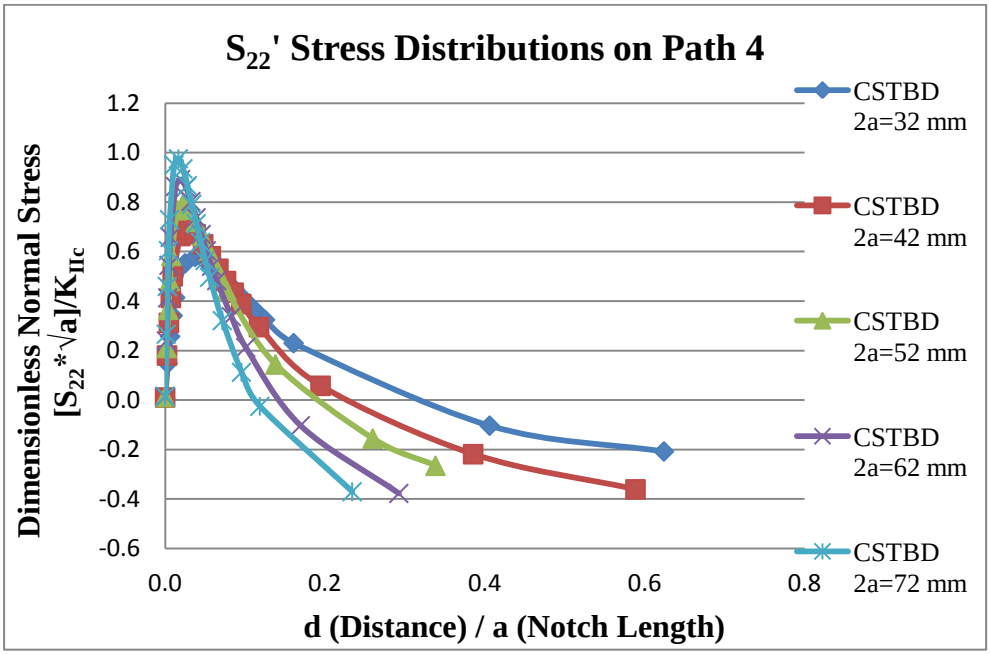

Figure 9.121 Dimensionless S_{22}' stress distribution vs. *d* (Distance) / *a* (Notch Length) along Path 4

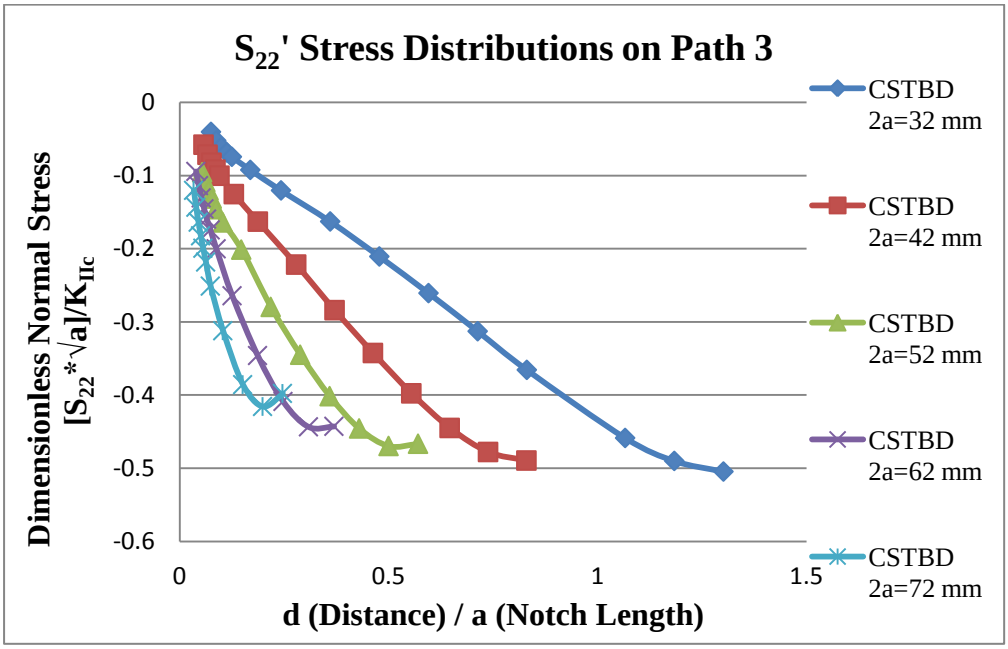

Figure 9.122 Dimensionless S_{22}' stress distribution vs. *d* (Distance) / *a* (Notch Length) along Path 3 after data refinement

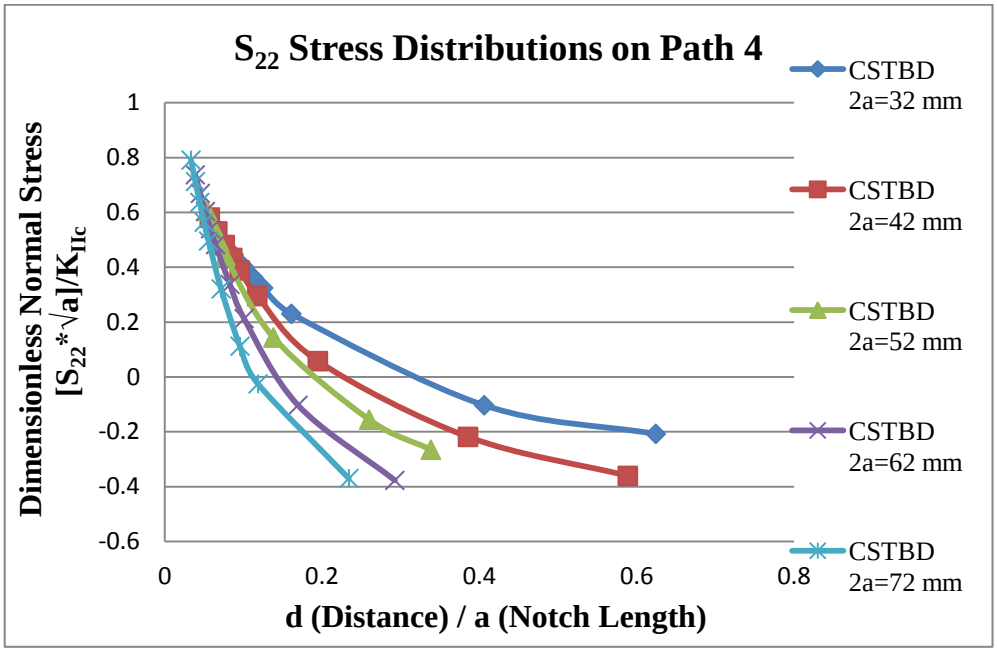

Figure 9.123 Dimensionless S_{22}' stress distribution vs. *d* (Distance) / *a* (Notch Length) along Path 4 after data refinement

As seen from Figure 9.124, S_{33}' confining stresses are initially tensile and the highest tensile magnitude around 0.08 is attained for 32 mm notch length at the notch tip. After *d/a*=0.01, all stresses turn into compression and the tendency to increase continues to -0.05 around *d/a*=0.20 for 72 mm notch length. However, this tendency continues to -0.07 around *d/a*=0.60 for 32 mm notch length.

In Figure 9.125, tensile confining stresses (S_{33}') dominate for all notch length groups on crack propagation direction. Highest tensile stress around 0.80 was obtained initially for 32 mm notch length. However, nearly 0.45 S_{33}' stress was initially attained for 32 mm notch length. In addition, gradient for tendency to compression is higher for 72 mm notch length. This situation easily seen in Figure 9.125 that, curve that belongs to 72 mm notch length reaches to zero around *d/a*=0.18 and curve that belongs to 32 mm notch length reaches to zero around *d/a*=0.40.

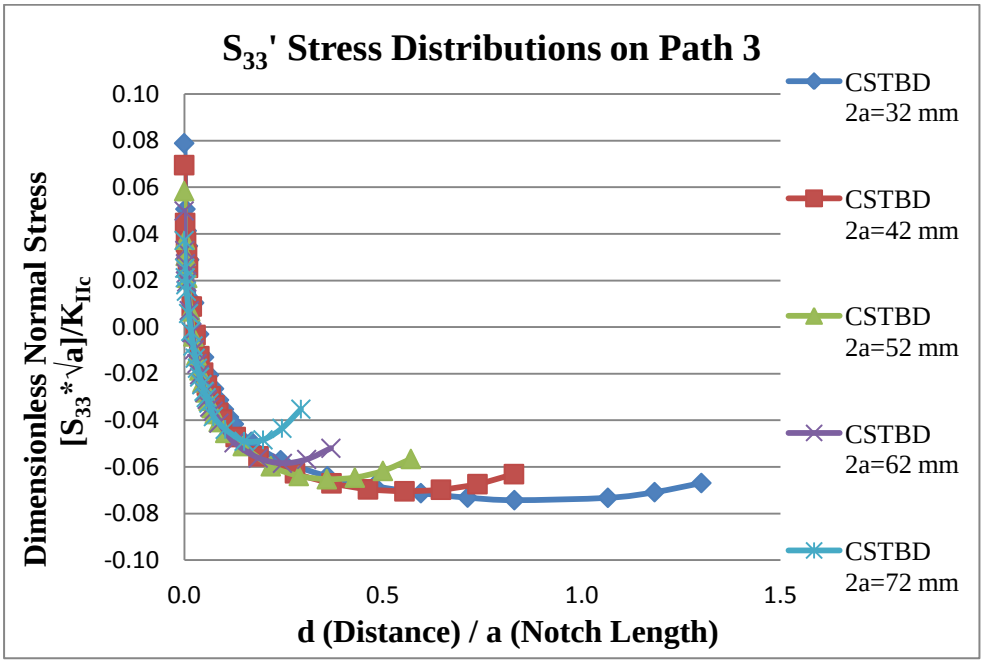

Figure 9.124 Dimensionless S_{33}' stress distribution vs. *d* (Distance) / *a* (Notch Length) along Path 3

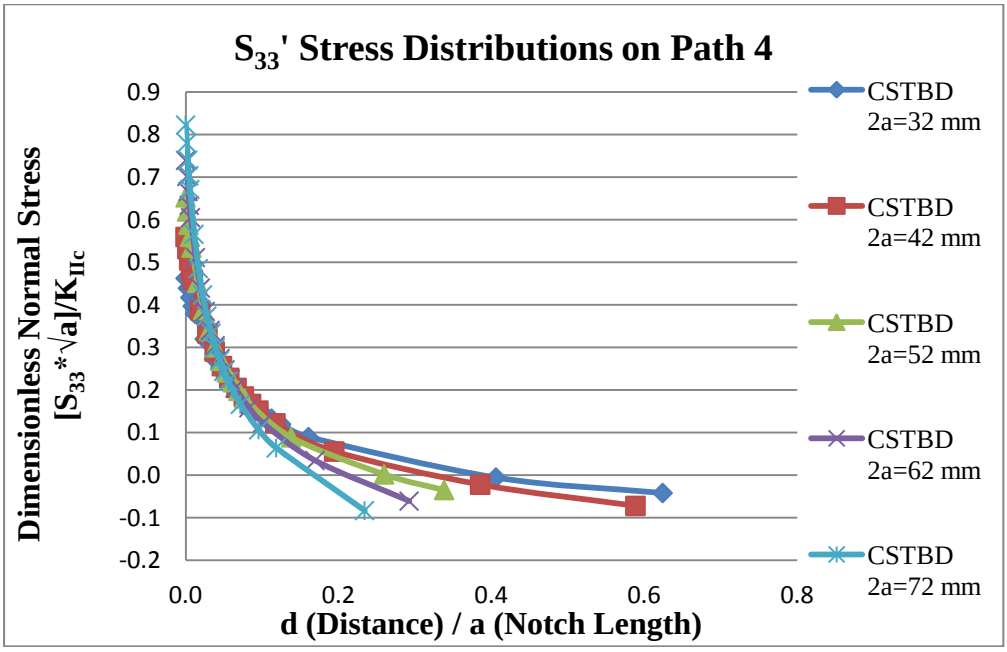

Figure 9.125 Dimensionless S_{33}' stress distribution vs. *d* (Distance) / *a* (Notch Length) along Path 4

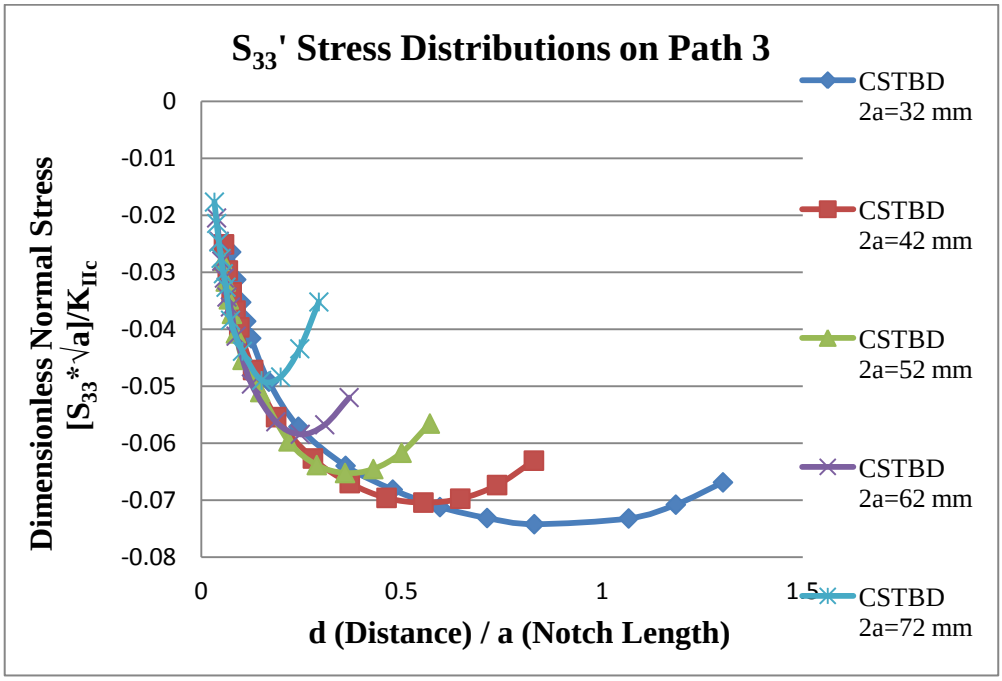

Figure 9.126 Dimensionless S_{33}' stress distribution vs. *d* (Distance) / *a* (Notch Length) along Path 3 after data refinement

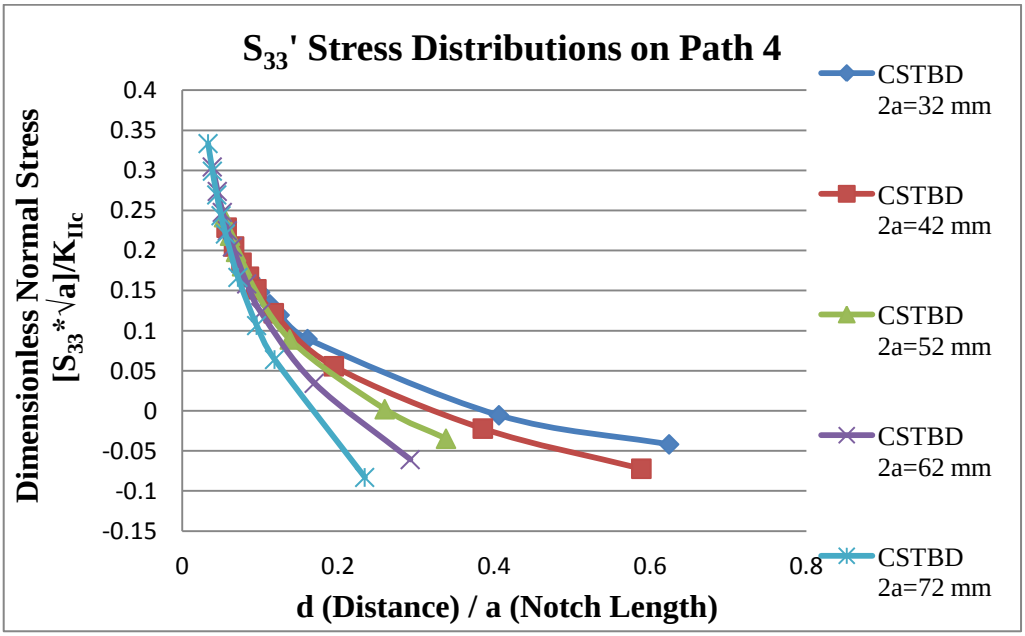

Figure 9.127 Dimensionless S_{33}' stress distribution vs. *d* (Distance) / *a* (Notch Length) along Path 4 after data refinement

As it is seen from Figure 9.128 that, along Path 3 analysis for S_{12}' stresses show that up to point d/a= 0.05 all S_{12}' stresses show singularity trends towards the notch tip d/a= 0 position. There are points within d/a=0 and d/a=0.05 for which stresses are presenting as an output of a program towards tendency to reach 0 as opposed to singular behavior that is predicted from analytical solutions. These points are attributed to the approximate values of numerical modeling and mesh design. They are considered inaccurate because of mesh construction and modeling and also blunted notch that has circular notch front shape influences accuracy at the notch tip and lead to such inaccurate results.

These parts are dropped from data processing. They do not show the right trend predicted by analytical solution. Best solutions have $1/\sqrt{r}$ singularity as then notch front approached. These points are omitted and remaining meaningful points are processed again curve fitted with proper singularity $1/\sqrt{x}$ curves became likewise in Figure 9.130. As it is seen from Figure 9.130 that, highest shear stress gradient is for 72 mm initial notch length case. The lowest shear stress gradient is for 32 mm notch case. Between those extreme notch length values, S_{12}' stress distributions for 42, 52 mm and 62 mm initial notch lengths are illustrated. Furthermore, curve fittings were associated for each initial notch length. As it can be seen from Figure 9.130 that, best curve fitting ($1/\sqrt{x}$) was attained for 32 initial notch length which gave the highest experimental fracture toughness value.

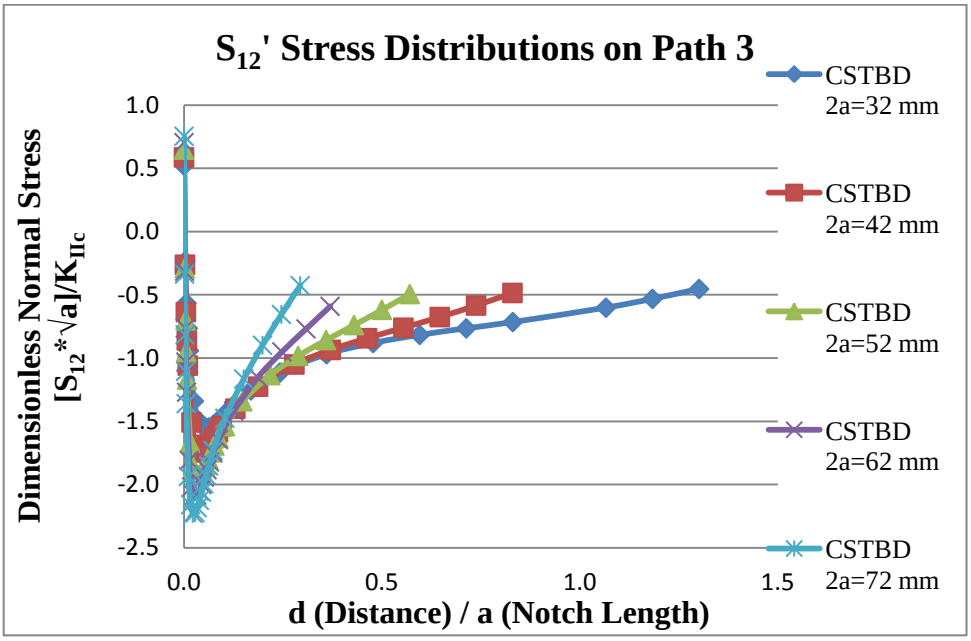

Figure 9.128 Dimensionless S_{12}' stress distribution vs. *d* (Distance) / *a* (Notch Length) along Path 3

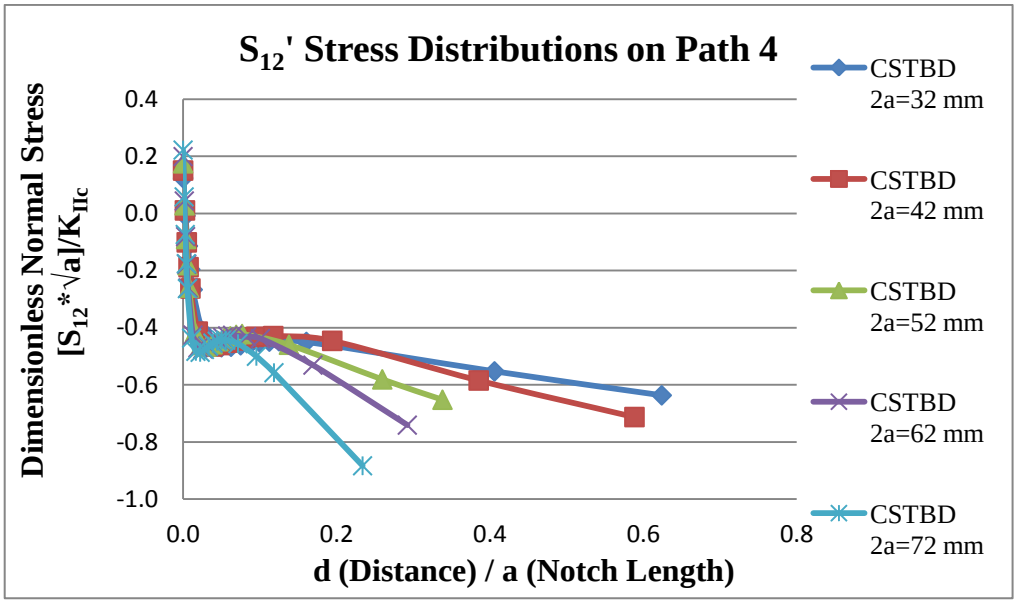

Figure 9.129 Dimensionless S_{12}' stress distribution vs. *d* (Distance) / *a* (Notch Length) along Path 4

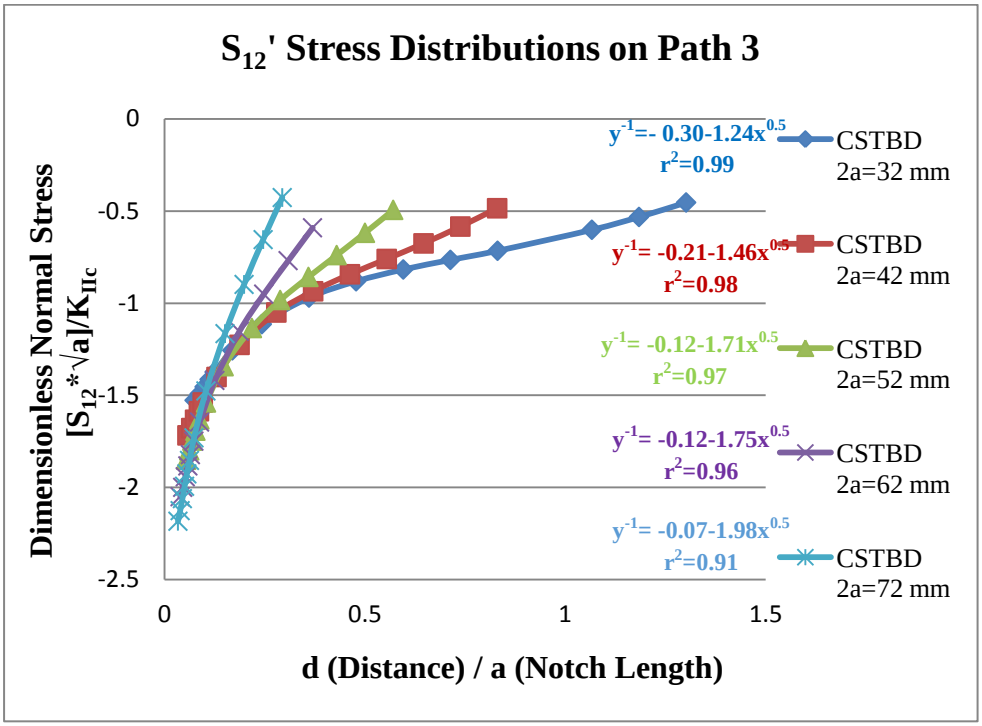

Figure 9.130 Dimensionless S_{12}' stress distribution vs. *d* (Distance) / *a* (Notch Length) along Path 3 after data refinement

After dropping the meaningless stress values that are too close to the notch tip, shear stress distributions along the crack propagation direction (Path 4) were generated in Figure 9.131. As it is seen from Figure 9.131 that, S_{12}' stresses are negative and the highest shear stress magnitude and gradient are observed for 72 mm initial notch length. As it is illustrated in Figure 9.131 that, S_{12}' stresses show tremendous variations for different initial notch length groups. Such that, the lowest gradient that is for 32 initial notch length case is very low and its average around -0.50 between *d/a*=0.10 to *d/a*=0.50.

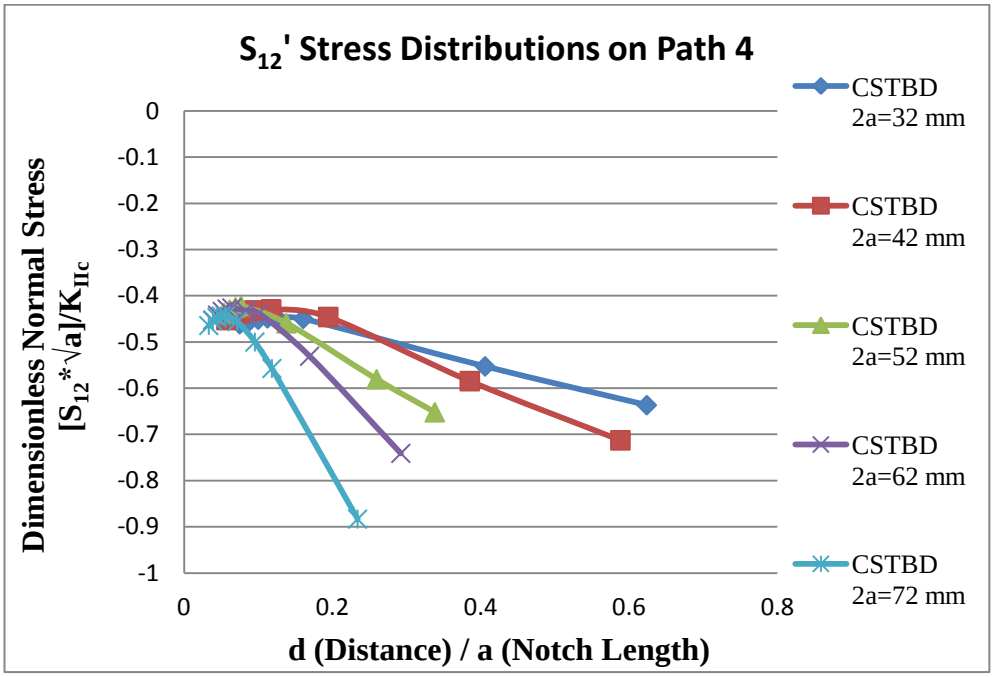

Figure 9.131 Dimensionless S_{12}' stress distribution vs. *d* (Distance) / *a* (Notch Length) along Path 4 after data refinement

On the other hand, to specify the best pure mode II notch length, stress distributions for extreme notch lengths (*2a*=22 mm and *2a*= 27 mm) were tried on CSTBD specimens. In order to determine the P_{cr} load values for extreme notch lengths, Equation that is illustrated in Figure 8.16 was used. Critical loads for extreme notch lengths for *2a*=22 mm and *2a*= 27 mm were estimated as 67.78 *kN* and 59.01 *kN* respectively.

In Figure 9.132, S_{12}' stress distributions for various CSTBD notch lengths versus Westergaard's analytical solution are compared. As it is seen from Figure 9.132 that, CSTBD specimen that has 22 mm notch length achieved the best trend considering Westergaard's analytical solution for the notch tip S_{12}' stresses. On the other hand, CSTBD specimen that has 72 mm notch length attained the worst trend regarding Westergaard's analytical solution.

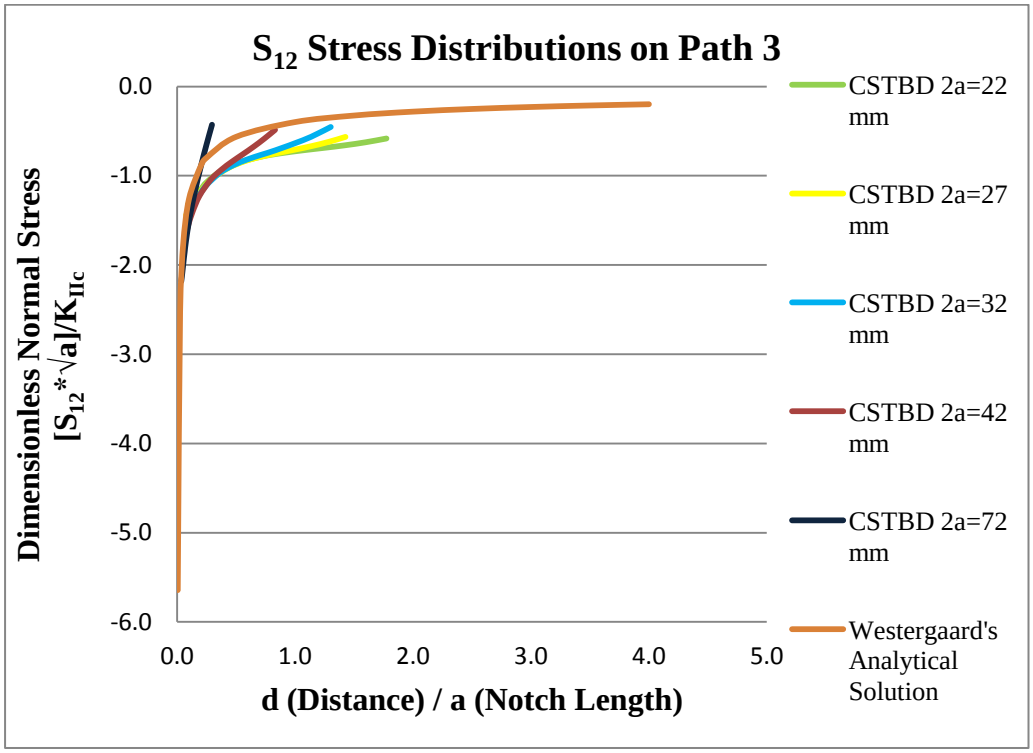

Figure 9.132 Dimensionless S_{12}' stress distribution vs. *d* (Distance) / *a* (Notch Length) along Path 3

Von Mises stress distribution output of ABAQUS corresponds to yield strength, σ_y. This is also called von Mises yield strength. During von Mises stress distribution analysis, as same in S_{12}' stress distribution analysis, invalid data entries too close to the notch tip were removed. As it was mentioned in above paragraphs, reason of these inaccurate datas can be attributed as meshing and roundness of notch. These inaccuracies are in stress distributions and von Mises stress distributions are unavoidable. Before removing inaccurate datas, plot of all datas were graphed in Figure 9.133 and 9.134. In Figure 9.135 and 9.136, curves are regenerated for Path 4 without these unavoidable datas.

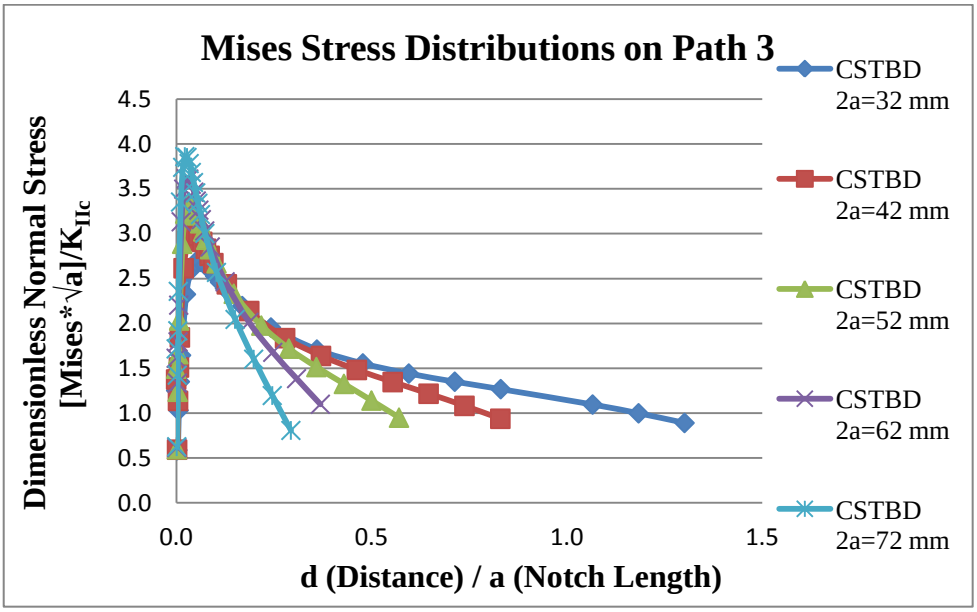

Figure 9.133 Dimensionless *Mises* stress distribution vs. *d* (Distance) / *a* (Notch Length) along Path 3

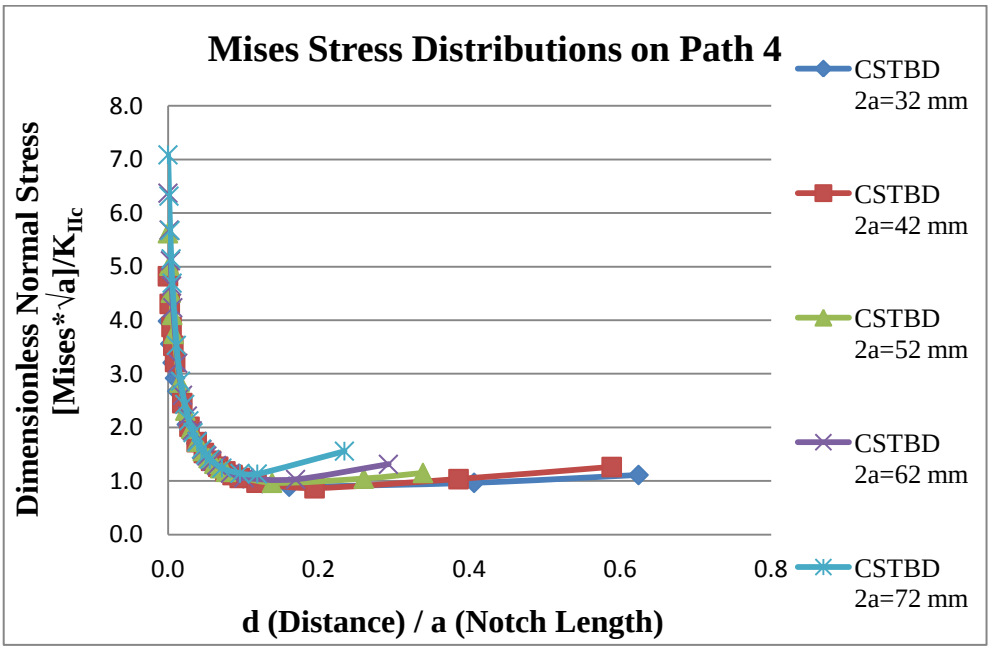

Figure 9.134 Dimensionless *Mises* stress distribution vs. *d* (Distance) / *a* (Notch Length) along Path 4

As it is seen in Figure 9.135 that, highest gradient and magnitude for von Mises stress distribution is observed in initial notch length 72 mm case. Mises stress takes the value around 3.78 at point *d/a*=0.03 and it reduces down to around *d/a*=0.4. The lowest von Mises stress distribution is observed for initial notch length 32 mm case. Mises stress takes the value around 2.65 at *d/a*=0.08. This reaches to 1 around *d/a*=1.2.

In Figure 9.136, along Path 4 crack extension direction all von Mises distributions tend to be infinitely high tension but highest value is for 72 mm around 7 and around 4 for 32 mm at the notch tip. These values are not be considered exact because of the uncertainties affect real stress magnitudes. Around *d/a*=0.1 for 32 mm notch case von Mises stress value are 1.05 and go to 1.11 around *d/a*=.0.62. However, for 72 mm initial notch case von Mises values are around 1.14 and go to 1.56 around *d/a*=0.23. There is an extensive yield zone along crack whose notch tip is too close to the notch free boundary. Boundary effect for crack length 62 mm was clearly observed in various notch lengths in CSTBD specimens.

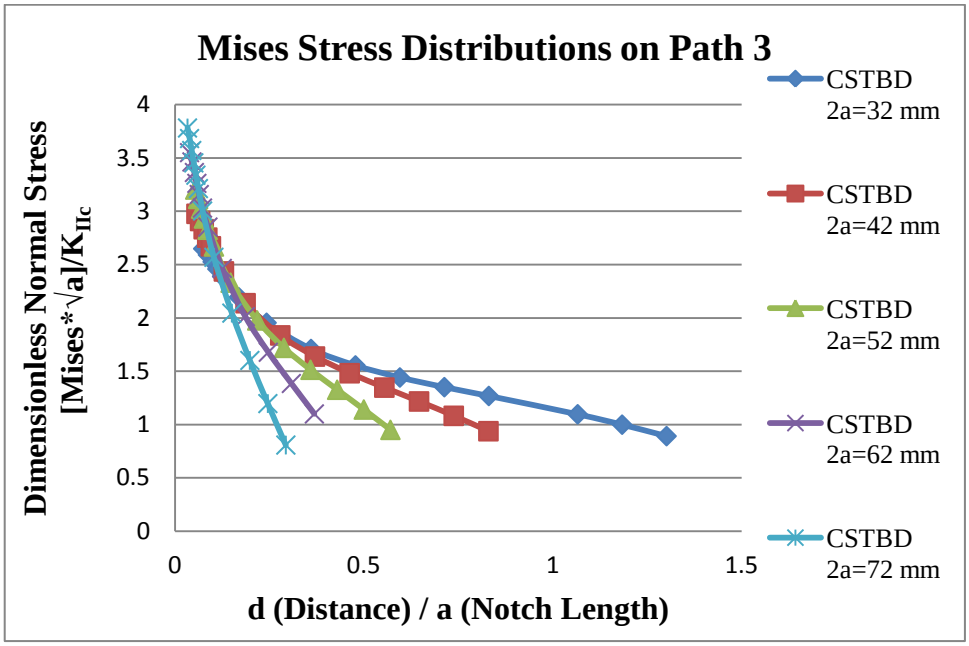

Figure 9.135 Dimensionless *Mises* stress distribution vs. *d* (Distance) / *a* (Notch Length) along Path 3 after data refinement

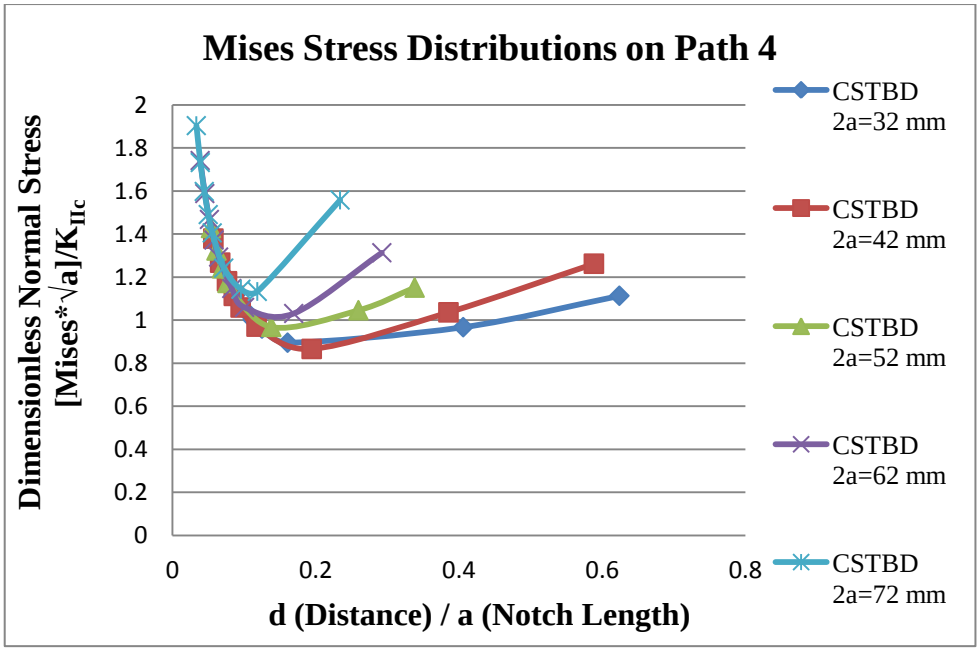

Figure 9.136 Dimensionless *Mises* stress distribution vs. *d* (Distance) / *a* (Notch Length) on Path 4 after data refinement

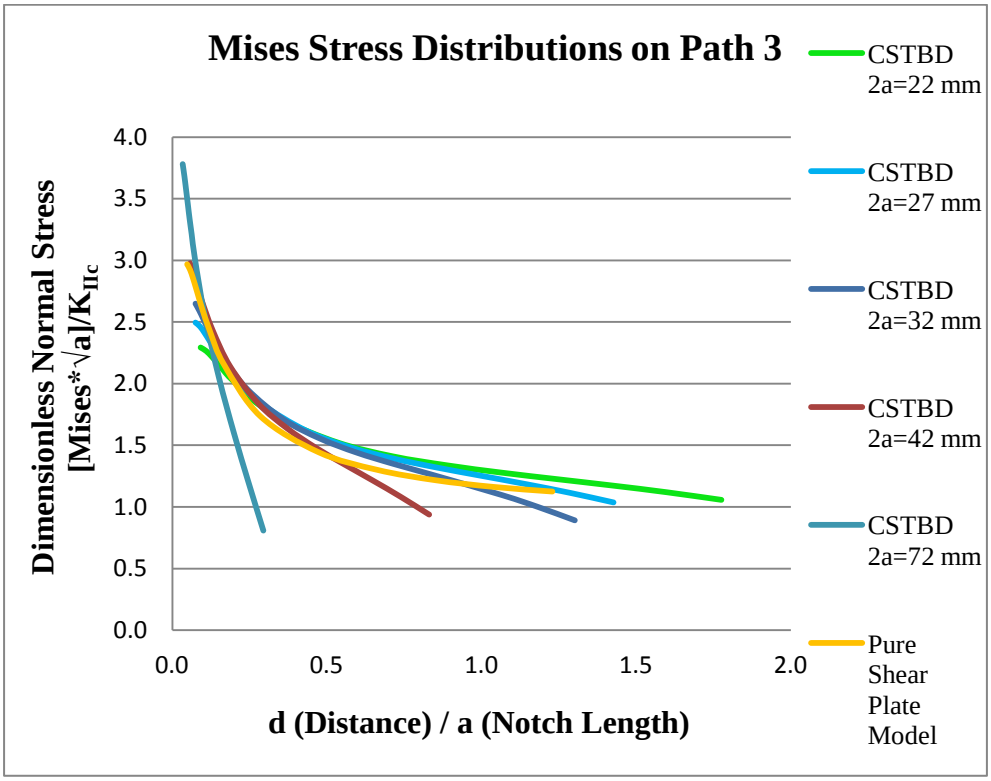

Figure 9.137 Dimensionless *Mises* stress distribution vs. *d* (Distance) / *a* (Notch Length) on Path 3

In Figures 9.137 and 9.138, *Mises* stress distributions along Path 3 and Path 4 for various notch lengths including extreme conditions (2a=22 mm and 2a=27 mm) are illustrated. Especially in Figure 9.137, best trend comparing with Pure Shear Plate Model was achieved with 2a=22 mm notch length CSTBD specimen model.

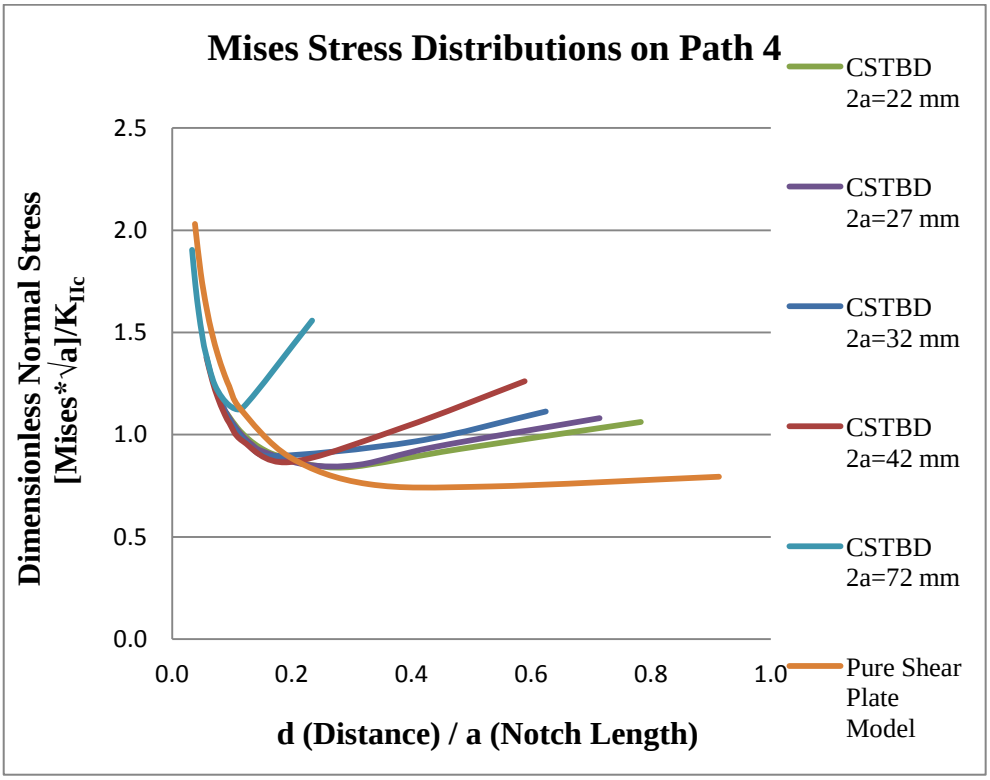

Figure 9.138 Dimensionless *Mises* stress distribution vs. *d* (Distance) / *a* (Notch Length) along Path 4

CHAPTER 10

CONCLUSIONS & RECOMMENDATIONS

For fracture testing of rock cores machining a notch is necessary to establish the conditions for the desired crack propagation. Simulating the machined notches by mechanical means like diamond saw or wire saw cutting were introduced in ABAQUS models. In stress intensity factor computations, seam cracks with no thickness and blunted notches with thicknesses were considered in the models. Results obtained from the pure shear plate models showed that machining a notch with a few mm finite thickness had only a minor effect of within 2.5 % on the computed stress intensity factor compared to the result of models with a seam crack.

Effect of variation of notch thickness on stress intensity factor computation for CSTBD model was investigated. CSTBD specimen model with a notch of medium length (2a=52 m) with varying notch thicknesses between 1-3 mm were generated. A difference of around 4.5% was observed in Y_{II} results of specimens with 1 mm (t_n/a =0.04) notch thickness and 3 mm (t_n/a = 0.12) notch thickness.

In this study, shear mode fracture toughness of a fine grained gabbro rock with different core-type specimen geometries (SCB, CSTBD, SNDB) were investigated. In order to minimize the effect of rock heterogeneity on fracture toughness, gabbro rock having a relatively homogeneous texture was used in the testing program.

Shear mode fracture toughness values from three-point bending type tests of SCB and SNDB are 2 to 2.5 times lower than the value K_{IIc}=2.37 MPa√m found by CSTBD testing with Brazilian type compressive loading. Result of SNDB method

testing gives K_{IIc}=1.18 MPa√m which is about 30% higher than the result of SCB testing work. With K_{IIc}=0.92 MPa√m, SCB method produces the lowest result in this testing work for the determination of mode II fracture toughness. It can be concluded that among the three-point bending type testing methods investigated here, SNDB method yields comparatively closer value to the results of CSTBD testing.

To investigate the reasons for having different fracture toughness values with these different testing geometries, modeling with ABAQUS finite element software was conducted on the specimen models of different geometries under their critical individual mode II fracturing loads. In these models, some geometric paths called stress paths were assigned to analyze the stress distributions developing ahead and around the preliminary notch and the notch tip vicinity of a particular specimen geometry.

It can be concluded from the stress path analyses that SCB and SNDB specimens are in more tension than CSTBD specimens. This situation can be easily seen on stress distribution paths that are ahead on notch tip and along fracture propagation direction. Functional forms involving expected crack tip singularity that is $1/\sqrt{r}$ term were fitted to the stresses along the notch front. It was observed that fitting quality is quite high for the stresses of SNDB and CSTBD geometries identified with correlation coefficient R^2 values of close to one. This was not the case for SCB specimen geometry, for which R^2=0.89 indicated a decreased quality of fitting process. Stresses for all specimen geometries approach to the $-\infty$ as $r \rightarrow 0$, which is the trend calculated by the analytical expressions. It was seen that stress distributions of the CSTBD and SNBD specimen geometries show the same trend with Westergaard's analytical solution. However, undulations and deviation from the general expected trend are observed for shear stress S_{12}' distribution along the notch front of SCB geometry.

On the other hand, along Path 4 which is along the fracture propagation direction, 2 to 2.5 times higher tensile stresses for SCB and SNDB specimen geometries than the stresses of CSTBD geometry along the same path. For SCB and SNDB type geometries under three-point bending load, high tensile stresses may result in the development of a larger volume of so-called yield zone or fracture process zone (FPZ); the fracture can easily propagate through this high tension zone along this path with lower resistance. The lack of resistance with higher possibility of tensile yielding on this path may result in lower shear mode fracture toughness values for SCB and SNDB specimen geometries compared to the CSTBD specimens under compressively applied loads.

The most similar stress state to the originally defined pure shear mode II loading configuration is satisfied by the CSTBD specimen geometry and the associated testing configuration. Von Mises stress which is proportional to the damaging component of J_2 invariant of deviator stress matrix is quite low for notches machined through CSTBD core specimen geometries. This minimizes the effects of the plastic zone or FPZ (Fracture Process Zone) on the mode II fracture toughness results. Presence of a FPZ zone reduces the fracture toughness as observed for the testing results with SCB and SNDB geometries and loading configurations. Boundary influence on fracture toughness testing is another issue related to the core-based testing with different methods. It is found that with initial notches machined with lengths less than a/R=0.5 to the CSTBD specimens produces results free from the issues discussed above.

Effect of initial notch lengths varying from 32 mm to 72 mm on fracture toughness values were investigated in CSTBD testing program. In summary of the test results on CSTBD type core-based specimen geometries, a logarithmic functional form best represents the variation of mode II fracture toughness (K_{IIc}) with preliminary notch length/specimen radius ratio (a/R). As a/R approaches zero K_{IIc} tends to micro mechanical representative value of K_{IIc}=2.44 MPa •(m)$^{1/2}$. For

a/R around 0.80, K_{IIc} tends to zero, since the notch tip is positioned too close to the specimen boundary. For such a notch length and position, it is concluded that CSTBD testing does not yield reliable results for mode II fracture toughness, considering the proximity and influence of the free boundary and the concentrated compressive load. To avoid the boundary influence issue in CSTBD testing, it is recommended to apply preliminary notches with *a/R* between 0.30 and 0.40.

For further work, measurements of stresses are recommended with the use of strain gauges on related paths in order to materialize and measure the stress distributions along different paths for different specimen geometries. Thus, comparisons can be done between the results that are obtained by the finite element analyses here and real experimental measurements. For CSTBD testing method, improvements in results are expected by using water jets of smaller diameter nozzles.

Three-point bending loading is commonly the preferred load application configuration in core-based testing work. In this sense, SNDB specimen geometry has a potential for improving the accuracy of fracture toughness measurements. This geometry shows indications of smaller boundary influence conditions, provided that specimens with smaller length notches and with larger thicknesses are employed in the testing work. A good thing about SNDB geometry is the flexibility to adjust the height of the circular plate type core specimen.

REFERENCES

ABAQUS Analysis User's Manual, Version 6.11 Documentation.

ABAQUS/CAE User's Manual, Version 6.11 Documentation.

ABAQUS, Inc., "Modeling Fracture and Failure with ABAQUS", 2006.

Alkılıçgil, Ç., "Development of a New Method For Mode I Fracture Toughness Test On Disc Type Rock Specimens", M.Sc. Thesis, METU, Ankara, 145p., 2006.

Alkılıçgil, Ç., "Development of Specimen Geometries For Mode I Fracture Toughness Testing with Disc Type Rock Specimen", PhD. Thesis, METU, Ankara, 172p., 2010.

Al-Shayea, N.A., Khan, K. and Abduljauwad, S.N., "Effects of Confining Pressure and Temperature on Mixed-Mode (I-II) Fracture Toughness of A Limestone Rock", Int. J. Rock. Mech. & Min. Sci., Vol.37, pp. 629 – 643, 2000.

Aliha M.R.M. and Ayatollahi M.R., "Mixed Mode I/II Fracture Evaluation of Marble Using SCB Specimen", Procedia Engineering, Vol. 10, pp. 311-318, 2011.

Aliha M.R.M. and Saghafi H., "The Effects of Thickness and Poisson's Ratio on 3D Mixed-Mode Fracture", Eng. Frac. Mech., Vol.98, pp. 15-28,2013

Aliha M.R.M., Sistaninia M., Smith D.J., Pavier M.J. and Ayatollahi M.R., "Geometry Effects and Statistical Analysis of Mode I Fracture In Guiting Limestone", Int. J. Rock. Mech. & Min. Sci., Vol. 51, pp. 128-135, 2012.

Ameri M., Mansourian A., Pirmohammad S., Aliha M.R.M. and Ayatollahi M.R. "Mixed mode fracture resistance of asphalt concrete mixtures", Eng. Fract. Mech., Vol. 93, pp 153-167, 2012.

Anderson, T.L., “Fracture Mechanics Fundamentals and Applications”, CRC, Florida, 1991.

Atkinson, C., Smelser, R.E. and Sanchez, J., “Combined Mode Fracture via The Cracked Brazilian Disk Test”, Int. J. Frac., Vol.18 (4), pp.279 – 291, 1982.

Awaji, H. and Sato, S., “Combined Mode Fracture Toughness Measurement by the Disk Test”, J. Eng. Materials and Tech., Vol. 100, pp. 175 – 182, 1978.

Ayatollahi M.R., Aliha M.R.M., and Hassani M.M., “Mixed Mode Brittle Fracture in PMMA-An Experimental Study Using SCB Specimens”, Mat. Sci. & Eng. A., Vol. 417, pp. 348-356, 2006.

Ayatollahi M.R. and Aliha M.R.M., “Wide Range Data for Crack Tip Parameters in Two Disc-Type Specimens under Mixed Mode Loading”, Compt. Mat. Sci., Vol. 38,pp. 660-670, 2007.

Ayatollahi M.R. and Torabi A.R., “Determination of Mode II Fracture Toughness for U-Shaped Notches Using Brazilian Disc Specimen”, Int. J. Rock. Mech. & Min.Sci., Vol.47, pp. 454 – 465, 2010.

Ayatollahi M.R. and Sistaninia M., “Mode II Fracture Study of Rocks Using Brazilian Disk Specimens”, Int. J. Rock. Mech. & Min.Sci., Vol.48, pp. 819 – 826, 2011.

Banks L., “Finite Elements and Fracture Mechanics Presentation”, The Dreszer Fracture Mechanics Laboratory Department of Solid Mechanics, Materials and Systems Tel Aviv University, Tel Aviv, 2003.

Backers, T., Stephansson, O. and Rybacki, E., “Rock Fracture Toughness Testing in Mode - II Punch Through Shear Test”, Int.J.Rock.Mech. & Min.Sci., Vol.39, pp. 755 – 769, 2002.

Backers T., “Fracture Toughness Determination and Micromechanics of Rock Under Mode I and Mode II Loading”, PhD. Doctoral Thesis, University of Potsdam, Germany, 95 p., 2004.

Backers, T., Dresen, G., Rybacki, E. and Stephansson, O., “New Data on Mode II Fracture Toughness of Rock from the Punch-Through Shear Test”, SINROCK2004, Int.J.Rock.Mech. & Min.Sci., Vol.41 (3), 1A-01, CD-ROM, 2004.

Backers T., “ISRM Suggested Method for the Determination of Mode II Fracture Toughness”, Rock Mech. & Rock Eng., Vol. 45, pp. 1011-1022, 2012.

Barrenblatt, G.I., “The Mathematical Theory of Equilibrium Cracks In Brittle Materials” Advances In Applied Mechanics”, Vol. 7, pp. 55-129, 1962.

Barton M. and Rajan S.D., “Finite Element Primer for Engineers”, Term Paper Presentation, The Graduate Engineering Course CEE598 Finite Elements for Engineers, Arizona State University, USA, 2000.

Bradley J. Dibble, MD., “What the Frack is Fracking Anyway?”, http://bradleydibble.authorsxpress.com/tag/hydraulic-fracturing/, last visited on 09 January 2014.

Chandler M., Meredith P. and Crawford B., “Experimental Determination of the Fracture Toughness and Brittleness of the Mancos Shale, Utah”, Geophysical Research Abstracts, Vol. 15, 2013.

Chen, F., Sun, Z. and Xu, J., “Mode I Fracture Analysis of The Double Edge Cracked Brazilian Disk Using a Weight Function Method”, Int.J.Rock.Mech. & Min.Sci., Vol. 38, pp. 475 – 479, 2001.

Chen, F., Cao, P. Rao, Q.H., Ma, C.D. and Sun, Z.Q., “A Mode II Fracture Analysis of Double Edge Cracked Brazilian Disk Using The Weight Function Method”, Int.J.Rock.Mech. & Min.Sci., Vol. 42, pp. 461 – 465, 2005.

Chong, K.P. and Kuruppu, M.D., “New Specimen For Fracture Toughness Determination of Rock and Other Materials”, Int.J. Frac. Vol.26, pp. 59 – 62, 1984.

Chong K. P., Kuruppu M. D. and Kuszmaul J. S. “Fracture toughness determination of layered materials”, Eng. Fract. Mech. 28, pp. 55-65, 1987.

Chong K. P., Kuruppu M. D. and Kuszmaul J. S., “Fracture Toughness Determination of Rocks with Core-Based Specimens”. SEM/RILEM Int. Conf. on Fracture of Concrete and Rocks, Texas, pp. 13-25, 1987.

Chong, K. P. and Kuruppu M. D. , “A New Specimen for Mixed-Mode Fracture Investigation of Geomaterials” Eng. Fract. Mech., Vol. 30, pp 701-712, 1988.

Clough, R. W., “The Finite Element Method in Plane Stress Analysis”, Proc. 2nd ASCE Conf. On Electronic Computation, Pittsburg, Pa.1960.

Cottrell, A. H., "Theoretical Aspects of Radiation Damage and Brittle Fracture In Steel Pressure Vessels." Steels for Reactor Pressure Circuits, A Symposium of the Iron and Steel Inst., Special Report No. 69, Vol. Nov.-Dec., pp. 281, 1960.

Deliac, E.P., “Optimization Des Machines D’abattage a Pics” PhD Thesis, University of Paris VI, Paris, 501 p., 1986.

Donovan, G. J., “Fracture Toughness Based Models for the Prediction of Power Consumption, Product Size and the Capacity of Jaw Crushers” PhD Thesis, Virginia Polytechnic Institute and State University, Blacksburg, 220 p., 2003.

Erdoğan, F., and Sih, G.H., “On the Crack Extension in Plates Under Plane Loading and Transverse Shear”, J. Basic Eng. Am. Soc. Mech. Engrs., Vol.85, pp. 519- 527, 1963.

Fowell, R.J. and Xu, C., “The Cracked Chevron Notched Brazilian Disc Test – Geometrical Considerations for Practical Rock Fracture Toughness Measurement”, Int.J.Rock.Mech. & Min.Sci., Vol.30, pp. 821 – 824, 1993.

Griffith, A.A., “The Phenomena of Rapture and Flow in Solids”, Phil.Trans.Roy.Soc. of London, Vol. A221, pp. 163-198, 1920/1921.

Griffith, A.A., “The Theory of Rupture”, Proc. of First Int. Cong. Appl. Mech., pp. 53-64, 1924.

GuoH., “Rock Cutting Studies Using Fracture Mechanics Principles” PhD. Thesis, University of Wollongong, Australia, 225 p., 1990.

Haberfield, C.M. and Johnston, I.W., “ Determination of The Fracture Toughness of A Saturated Soft Rock” , Can. Geotech. J., Vol.27, pp. 276 – 284, 1990.

Het K., “Effects Of Geometrical Factors on Fracture Toughness Using Semi-Circular Bending Type Specimens”, M.Sc. Thesis, METU, Ankara, 158p., 2008

Hood, M.C. and Roxborough, F.F., “Rock Breakage: Mechanical”, SME Mining Engineering Handbook, Second Edition, SME, H.L. Hartman (senior editor), Vol. 1, pp. 680-721, 1992.

Inglis, C.E., “Stresses in A Plate Due to The Presence of Cracks and Sharp Corners”, Trans. Inst, Naval Archit., Vol.55, pp.219-230, 1913.

ISRM, “Suggested Methods for Determining Tensile Strength of Rock Materials”, Int. J. Rock Mech. Min. Sci. & Geomech. Abstr., Vol. 15, pp. 99-103, 1978.

ISRM, “Suggested Methods for Determining the Uniaxial Compressive Strength and Deformability of Rock Materials”, Int. J. Rock Mech. Min. Sci. & Geomech. Abstr., Vol. 16, pp. 135-140, 1979.

Irwin, G.R., “Analysis of Stress and Strains Near the End of a Crack Traversing a Plate”, J. of Applied Mechanics, A.S.M.E., New York, 1957.

Jeu, S. J., T. L. Logan, and R. A. McBane. "Exploitation of Deeply Buried Coalbed Methane Using Different Hydraulic Fracturing Techniques In the Piceance Basin, Colorado and San Juan basin New Mexico." SPE Annual Technical Conference and Exhibition, 1988.

Jin Y., Yuan J., Chen M., Chen K.P., Lu Y., and Wang H., "Determination of Rock Fracture Toughness K_{IIc} and Its Relationship with Tensile Strength", Rock Mech. & Rock Eng., Vol. 44, pp. 621-627, 2011.

Karakaş, Ş. S., "Shear Mode Rock Fracture Toughness Determination with a Circular Plate Type Specimen under Three-Point Bending" PhD. Thesis, METU, Ankara, 127p., 2011.

Krishnan, G.R., Zhao, X.L., Zaman, M. and Roegiers, J.C., "Fracture Toughness a Soft Sandstone", Int. J. of Rock Mech. Min. Sci., Vol. 35, pp. 695-710, 1998.

Levén M. and Rickert D., "Stationary 3D Crack Analysis with ABAQUS XFEM for Integrity Assessment of Subsea Equipment" M.Sc. Thesis, Chalmers Unıversity of Technology, Göteborg, 77p., 2012.

Libatskii, L.L. and Kovichik, S.E., "Fracture of Discs Containing Cracks", Soviet Materials Science, Vol. 3, pp. 334-339, 1967.

Lim, I.L., Johnston, I.W., Choi, S.K., "Stress Intensity Factors For Semi-circular Specimens Under Three-Point Bending", Eng. Fract. Mech.. Vol.44 pp.363-382, 1993.

Lim, I.L., Johnston, I.W., Choi, S.K., Boland, J.N., "Fracture Testing of A Soft Rock with Semi-circular Specimens under Three-point Bending", Part 1-2, Int. J. Rock Mech. & Min. Sci. and Geomech. Abstr., Vol.31, pp.185-212, 1994.

Lim, I.L., Johnston, I.W. and Choi, S.K., "Assessment of Mixed-mode Fracture Toughness Testing Methods for Rock", Int. J. Rock Mech. & Min. Sci. and Geomech. Abstr., Vol.31 (3), pp.265 – 272, 1994.

Lode, W., Versuche Über den Einfuss der Mittleren Hauptspannung auf das Fliessen der Metalle Eisen Kupfer und Nickel. Zeitung Phys., Vol. 36, pp. 913–939, 1926.

Mises, V. R., “Mechanik der Festen Körper Im Plastisch Deformablen Zustand”, Göttin. Nachr. Math. Phys., Vol. 1, pp. 582–592, 1913.

MTS System Catalogue, 1992.

Phase 2, User’s Manual, 2010.

Rice, J.R., “A Path Independent Integral and the Approximate Analysis of Strain Concentration by Notches and Cracks.” Journal of Applied Mechanics, Vol. 35, pp.379-386, 1968.

Rao, Q., Sun, Z., Stephansson, O., Li, C. and Stillborg, B., “Shear Fracture (Mode II) of Brittle Rock”, Int.J.Rock.Mech. & Min.Sci., Vol. 40, pp. 355 – 375, 2003.

Schmidt, R. A., "Fracture Mechanics of Oil Shale-Unconfined Fracture Toughness, Stress Corrosion Cracking, and Tension Test Results." The 18th US Symposium on Rock Mechanics (USRMS), 1977.

Senseny, P. E., and T. W. Pfeifle. "Fracture Toughness of Sandstones and Shales." The 25th US Symposium on Rock Mechanics (USRMS), 1984.

Shetty, D.K., Rosenfield, A.R. and Duckworth, W.H., “Mixed-Mode Fracture of Ceramics in Diametral Compression”, J. Am. Ceram. Soc., Vol. 69 (6), pp. 437-443, 1986.

Sih, G.C., “Handbook of Stress-Intensity Factors”, Lehigh University, Bethlehem, 1973.

Suo Z., “ES 247 Fracture Mechanics”, http://imechanica.org/node/7448, last visited on 23 December 2013.

Tada H., Paris P.C., and Irwin G.R., “The Stress Analysis of Cracks Handbook”, Del Research Cooperation, Hellertown, 1973.

TestBox 1001 System brochure, www.teknikdestek.com.tr, last visited on 28 December 2013.

Thiercelin M., Jeffrey R.G., Naceur B. K. and Schlumberger D. “Influence of Fracture Toughness on the Geometry of Hydraulic Fractures”, Society of Petroleum Engineers, 1989.

Tutluoglu T and Keles C., “Mode I Fracture Toughness Determination with Straight Notched Disk Bending Method”, Int.J.Rock.Mech. & Min.Sci., Vol.48, pp. 1248 – 1261, 2011.

Wang, C.H., “Introduction to Fracture Mechanics, Lecture Notes.”, Public Release Melbourne, 1996.

Watkins, J., “Fracture Toughness Test For Soil-Cement Samples In Mode II”, Int. J. Fracture, Vol. 23, pp. 135- 138, 1983.

Wells, A.A., “Unstable Crack Propagation in Metals: Cleavage and Fast Fracture”, Proceedings of the Crack Propagation Symposium, Vol 1, Paper 84, Cranfield, UK, 1961.

Westergaard. H.M., “Stresses at a crack, size of the crack and the bending of reinforced concrete”, Prov. American Concrete Institute, Vol.30, pp. 93-102, 1934.

Whittaker, B.N., Singh, R.N., Sun, G., “Rock Fracture Mechanics-Principles, Design and Applications”, Elsevier, Amsterdam, 1992.

Williams, M., “On The Stress Distribution at The base of A Stationary Crack”, Journal of Applied Mechanics, ASME 24(1), pp. 109-114, 1957.

Zienkiewicz, O.C. and Cheung Y.K., “The Finite Element Method in Continuum and Structural Mechanics”, McGraw Hill, 1967.

APPENDIX A

PETROGRAPHICAL ANALYSIS

According to petro-graphical analyses that were conducted in Geological Engineering Department of Ankara University, rock was determined and named as Gabbro. Rock consists of plagioclase, pyroxene, and little amounts of opaque minerals, biotite, and amphibole. In addition, plagioclase minerals generally have polysynthetic duplication and small amount of textures with zones. Pyroxene minerals constitute big amount of main mafic minerals of rock. Types of pyroxenes are described as clino-pyroxene and furthermore cleavages and inclined extinctions were observed. Biotite and amphibole minerals generally appear as weathering materials. General texture of rock was described as holocyrstalline texture. During thin section analysis, ophitic texture that is typically occurred for gabbrotic rocks was observed.

Generally, plagioclase minerals that compose of rock weren't show any weathering. However, uralitization was observed in pyroxene minerals. It can be seen easily that edge of some pyroxene minerals transformed into amphibole minerals. Entire biotite minerals that are existed of trace amounts in rock, are observed likewise some of them are totally opaqued form and some of them are partially opaqued form.

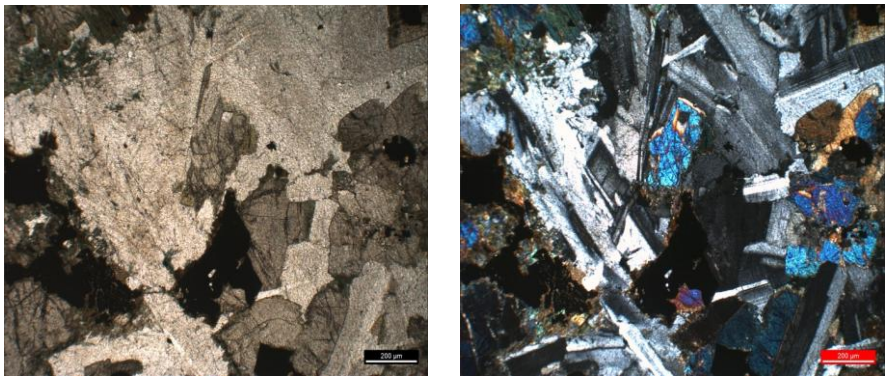

Figure A.1 General views of thin section and ophitic texture

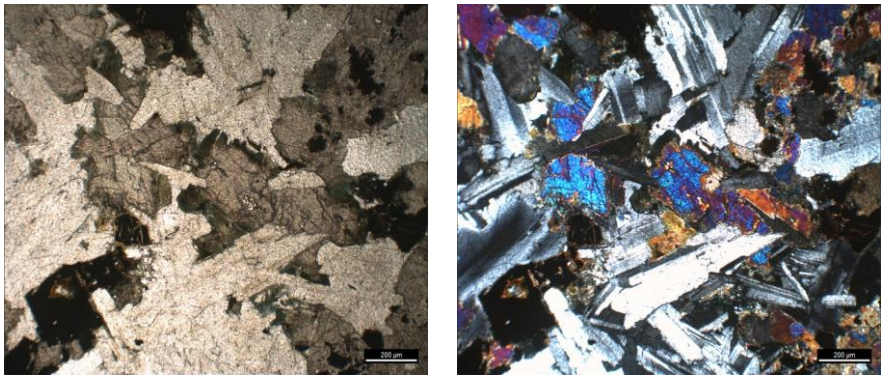

Figure A.2 Pyroxene, plagioclase and opaqued biotite minerals observed in thin section

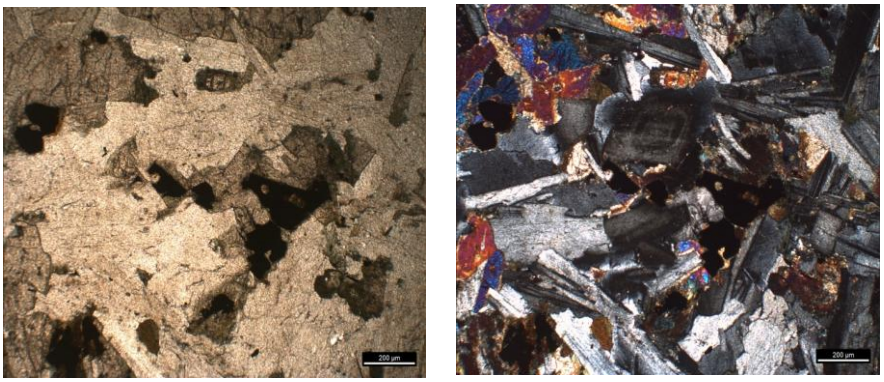

Figure A.3 Plagioclase and opaqued biotite minerals that have zones in textures

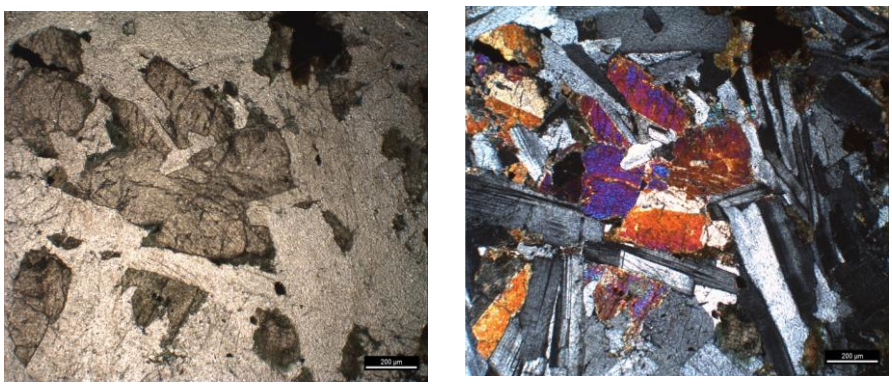

Figure A.4 Amphibol generation after uralitization that is observed in pyroxenes

APPENDIX B

SPECIMEN PHOTOS AFTER EXPERIMENTS

B.1 CSTBD Specimen Photos after Mode II Experiments

Figure B.1 CSTBD specimens (fine grained gabbro) after experiments

Figure B.2 Shear surfaces on CSTBD gabbro specimen after experiment

Figure B.3 CSTBD gabbro specimen with 2a=52 mm initial notch after experiment

Figure B.4 CSTBD gabbro specimen fractured along desired path

Figure B.5 CSTBD gabbro specimen fractured along undesired path

B.2 SNDB Specimen Photos after Mode I & Mode II Experiments

Figure B.6 SNDB gabbro specimens after mode I experiments

Figure B.7 SNDB gabbro specimens after mode II experiments

B.3 SCB Specimen Photos after Mode I & Mode II Experiments

Figure B.8 SCB gabbro specimens after mode I experiments

Figure B.9 SCB gabbro specimens after mode II experiments

CIRRICULUM VITAE

PERSONEL INFORMATION

Surname, Name: Het, Kıvanç
Nationality: Turkish (TC)
Date and Place of Birth: 29 September 1980, Ankara
Marital Status: Single
Phone: +90 312 540 17 61
Fax: +90 312 540 17 75
email: kivanchet@gmail.com; hetk@tki.gov.tr

EDUCATION

Degree	Institution	Year of Graduation
MS	METU Mining Engineering	2008
BS	HU Mining Engineering	2004
High School	Atatürk Anadolu High School, Ankara	1998

WORK EXPERIENCE

Year	Place	Enrollment
2007-Present	Turkish Coal Enterprises	Mining Engineer
2003-June	Aktürk A.Ş.	Intern Engineering Student
2002-June	Set Italcementi Group	Intern Engineering Student

FOREIGN LANGUAGES

Fluent English

HOBBIES

Movies, Travelling, Real Time & Turn-Based Strategy PC Games, Playing Chess, Fitness, Swimming, Running.